Charles University in Prague
Faculty of Mathematics and Physics

DOCTORAL THESIS

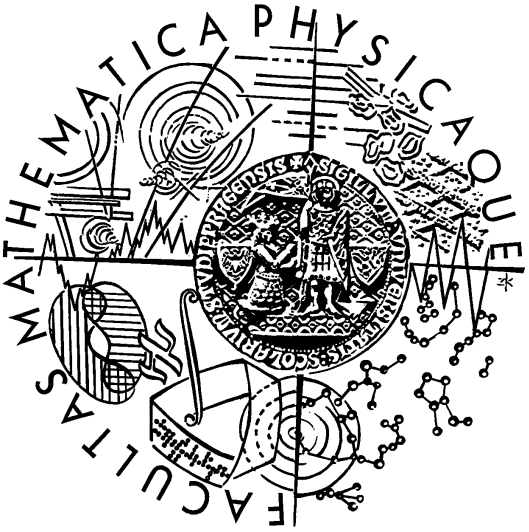

Petr Nečesal

Study of Interactions of Cosmic Rays at Ultra-high Energies

Institute of Physics AS CR, v. v. i.

Supervisor: prof. Jan Řídký, DrSc.

Study programme: Physics
Specialization: Subnuclear Physics

Prague 2014

Acknowledgement

I would like to express my great gratitude to my supervisor prof. Jan Řídký for his guidance and valuable discussions, patience and overall support. In particular, I especially thank him for choosing the subject, for convincing me to be a part of a top class experiment, the Pierre Auger Observatory. I thank him for his kind advice, giving feedback and patient correcting of my mistakes.

I am very grateful to my collegues, especially to Jan Ebr and Petr Trávníček for their support, interesting discussions and for helping me almost anytime. I am very obliged to my wife Mirka for supporting me and family background, the essential base for any success. This thesis wouldn't have been finished without continuous and patient support of my parents. I am very grateful to them for encouraging me in difficult and stressful situations.

I declare that I have worked out this doctoral thesis independently, using only the literature stated. I agree with being it used for educational purposes.

I understand that my work relates to the rights and obligations under the Act No. 121/2000 Coll., the Copyright Act, as amended, in particular the fact that the Charles University in Prague has the right to conclude a license agreement on the use of this work as a school work pursuant to Section 60 paragraph 1 of the Copyright Act.

Prague, September 20th, 2014 Petr Nečesal

Název práce: *Studium interakcí částic kosmického záření při extrémně vysokých energiích*

Autor: *Petr Nečesal*

Ústav: *Fyzikální ústav AV ČR, v. v. i.*

Vedoucí doktorské práce: *prof. Jan Řídký, DrSc.; Fyzikální stav Akademie věd České republiky, Na Slovance 1999/2, 182 21 Praha 8*

Abstrakt: Dizertační práce je věnována studiu interakcí kosmického záření při extrémně vysokých energiích s využitím dat z Observatoře Pierre Auger, automatickému systému alarmů nazvaného Shift Guard a analýze korelací teplot a detektorové odezvy.

Observatoř Pierre Auger je největším experimentem určeným pro studium kosmického záření extrémních energiích. Předpokládaný vztah mezi teplotou a odevzdou detektorů je v této práci studovaný spolu s popisnou analýzou vlivu různých faktorů na teplotu v blízkosti fluorescenčních detektorů. Kalibrační korekční faktor je spočten na základě měřených kalibračních konstant a teploty a umožuje korekci odezvy detektorů v situacích, kdy klimatizace nezaručí stálé podmínky.

Shift Guard - systém alarmů je vytvořen pro ochranu fluorescenčního detektoru a zlepšení datové kvality. Představení a popis funkčnosti systému a jeho základních parametrů je doplněno implementační logikou. Shift Guard informuje měřící tým o důležitých událostech a situacích, které mohou ohrozit detektor nebo datovou kvalitu.

Rozdíl mezi měřeným počtem mionů v rovni pozemních detektorů ve srovnání se simulacemi z generátorů rozsáhlých atmosférických spršek je studován. Výsledky rozpadů hmotných temných fotonů jako možných zdrojů mionů jsou prezentovány spolu s analýzou vlivu zvýšené produkce těžších kvarků na množství mionů a chybějící energie.

Klíčová slova: Kosmické záření, Hadronové interakční modely, miony, Observatoř Pierre Auger, Alarm systém Shift Guard

Title: *Study of Interactions of Cosmic Rays at Ultra-high Energies*

Author: *Petr Nečesal*

Institute: Institute of Physics AS CR, v. v. i.

Supervisor of the doctoral thesis: *prof. Jan Řídký, DrSc.; Institute of Physics AS CR, v. v. i. , Na Slovance 1999/2, 182 21 Praha 8*

Abstract: This thesis is dedicated to study of interactions of utra-high energy cosmic rays using measured data from the Pierre Auger Observatory, automatic alarm system called Shift Guard and analysis of correlation of temperature and detector response.

The Pierre Auger Observatory is the largest experiment to study ultra-high

energy cosmic rays. The assumed relation between temperature and fluorescence detector response is studied together with descriptive temperature analysis, which shows that the air-conditioning system is not able to stabilize temperature enough. The temperature influence on camera response is investigated in order to measure the calibration correction factor.

Shift Guard - the alarm system dedicated to protect fluorescence detectors and data taking is introduced and its functionality is described. The alarm system informs shifters about some events and situations that can endanger detector or deteriorate data quality. The basic parameters and alarm system logic are described together with light and sound signals.

The discrepancy between measured and predicted number of muons at ground level calculated by EAS generators is showed and possible sources of this disagreement are studied. The result of massive dark photons decay in EAS as one of exotic muon source is presented. The analysis of increased heavy flavour particles production shows the influence on muon numbers and missing energy.

Keywords: Cosmic rays, hadronic interaction models, muons, Pierre Auger Observatory, Alarm system Shift Guard

Contents

Chapter 1

Introduction

It is almost one hundred years since the first evidence of the Cosmic Rays (CRs) has been discovered by Victor Hess [4]. Radiation measured in the atmosphere and its increase with altitude became important not only for Victor Hess and his Nobel Prize in 1936, but it laid basis of the upcoming scientific field in physics, *astroparticle physics*. After decades of considerable effort of generations of physicists still many unanswered questions remain unsolved.

The astroparticle physics joins together two branches of physics studying the nature at essentially different ranges and scales. The origin of CRs must be searched in astrophysical objects where astrophysics naturally plays its substantial role. Detailed knowledge of processes in galaxies, stars and other energetic objects can reveal the mystery of acceleration mechanisms of particles constituting the cosmic rays. Astrophysics searches for limit and conditions of the CR propagation through the space.

Particle physics stays on the other side of imaginary scale of physics, but it plays irreplaceable role in studies of the CRs. The whole experimental part of the astroparticle physics deals with particle interactions and particle detection methods being studied over last 70 years by the particle physics.

The energy range of the CRs spans many orders of magnitude. Even during the 1930's there were several observations that indicated a new phenomenon - air showers - induced in the Earth's atmosphere by particle with extreme energy. Subsequent measurements confirmed this observation and allowed to estimate the primary energy of the order 10^{15} eV. The CRs with energies above 10^{18} eV are denoted as Ultra-High Energy Cosmic Rays (UHECRs) and they became the research subject of many large experiments as the most interesting part of the whole CRs spectrum because they bring the information about their origin. The steeply falling differential flux of UHECRs makes their observation difficult and that is the reason why many of their aspects are not yet understood. According to today's knowledge UHECRs are charged particles with energies that can exceed 10^{20} eV. The observation of particles of such energy requires extreme collecting power because of their extremely low arrival rate of about 1 particle per square kilometer per century.

Several experiments were established during tens of years in the last century

without answering questions on UHECRs origin. Scientists faced a challenge in the 1990's to build a new experiment expanding the boundaries of knowledge. The largest astrophysics facility - the southern part of the Pierre Auger Observatory - designed for the study of UHECRs has been collecting data since early 2004 and was completed in June 2008. For its vast detection area it can be called 'a new window to the Universe'. The measurement precision and geometrical acceptance are far beyond of those of its forerunners. It fulfills all the original requirements to reveal the CR mystery.

1.1 Thesis overview

This thesis is dedicated to study of interactions of ultra high energy cosmic rays using measured data from the Pierre Auger Observatory.

The first chapter introduces readers into the problematics that this thesis concerns itself with. The thesis overview is included.

The second chapter describes briefly up-to-date knowledge of the cosmic rays aspects starting with the history of the cosmic ray discovery. Some basic characteristics of the cosmic ray phenomena are summarized including the spectrum and possible sources. This is followed by presentation of extensive air showers induced in Earth's atmosphere and simple model describing cascade interaction development. Detection methods of the cosmic rays conclude the section 2.6.

Chapter three presents a powerful instrument for the highest energy cosmic ray studies, the Pierre Auger Observatory. Used types of detectors giving the advantages of simultaneous CR measurements represent the most important improvement of the detection technique. Several sections of the chapter 3 deal with the measurement problematic comprising energy calibration procedure and atmospheric monitoring.

The fourth chapter is dedicated to the fluorescence detector alarm system. It describes the overall design and functionality of the device that helps to protect fluorescence detectors from dangerous situations and informs about important events that potentially may influence data taking and quality. The basic logic of the system behaviour and guide how to operate the alarm system can be found in this chapter.

Muon production study is the main subject of the fifth chapter. Number of muons in the extensive air showers is the fundamental variable used for the energy calibration of very inclined showers. On the other hand its measurement brings information about hadronic interactions and muon production mechanisms. The discrepancy between predicted and measured number of muons at ground was indicated one decade ago and some possible sources that could mitigate the discrepancy are discussed and examined in the fifth chapter.

Conclusions can be found in the sixth chapter. My contribution to particular subjects is summarized there with the most important results.

Appendices A to G contain supplementary tables, figures and technical details about calibration constants, muon production results, connection and communica-

tion schemas of the alarm system and its settings and distribution of reaction times on alarms.

Chapter 2

Cosmic Rays

The Earth is permanently exposed to a flux of cosmic rays, mostly charged particles coming from outside of the Solar System. More than 100 years have passed since the first evidence of CRs was discovered and still many issues remain unsolved. Nevertheless, considerable progress has been made during several last years, also thanks to the Pierre Auger Observatory.

CRs exploration includes astrophysical study of acceleration mechanisms to reach energies up to 10^{20} eV, much far away from the energy region achievable at the largest terrestrial accelerators. Charged particles traversing the Universe are bent in chaotic magnetic fields smearing the arrival directions and making the CRs isotropic in the most of the energy range. Observing the most energetic part of the CR spectrum helps to reveal mysteries of our Universe.

Scarcity of the most energetic particles doesn't allow to observe them directly and brings the opportunity to study a phenomenon called Extensive Air Showers (EAS) first observed in 1930s. Many large experiments have been established to explore the interesting upper end of the CR spectrum possibly carrying the information about CR origin and its propagation in the space.

2.1 History of cosmic ray research

It took many years to discover extraterrestrial origin of highly penetrating radiation from first suggestions and observations of this phenomenon. It was preceded by fundamental discoveries in the field of particle physics, starting in 1870's. Eugen Goldstein named special radiation as cathode rays observed in vacuum tubes. The phenomenon was first seen by Johann Hittorf in 1869. Several theories existed trying to explain cathode rays before the experiment carried out by J. J. Thompson in 1897 (winning the Nobel prize in 1906 for his work). He showed that the observed radiation is made of particles with ratio of mass and charge less than that of the hydrogen atom. Unquestionable progress was made also by inventions of W. Crookes and his tubes in which Röntgen discovered X-rays in 1895.

The discovery of unstable elements and natural radioactivity by Henri Becquerel in 1896 brought generally accepted explanation of electroscope discharging. It was observed that radioactive materials cause spontaneous loosing of charge of

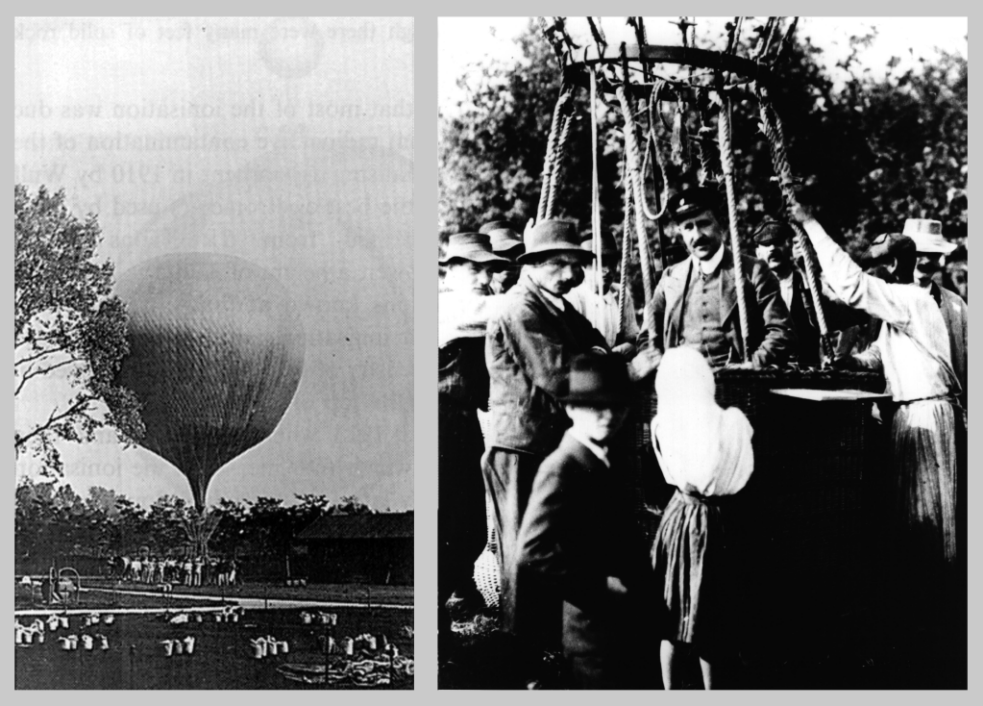

Figure 2.1: Left: Hess's balloon. Right: V. Hess surrounded by his staff after one of his ascensions during which he observed the radiation intensity increasing with altitude.

electroscopes and that's why it was believed they are responsible for air ionization. α and β components of radiation were distinguished by E. Rutheford by identifying their penetrability. It was showed that electrons observed in cathode rays just correspond to β component of radiation. γ rays completed the picture during studies of radiation from radium by Paul U. Villard in 1900.

Electroscopes were used as a standard device to measure the radiation level in the first decade of the twentieth century. Pioneer observations of electroscope discharging even without the presence of radioactive materials were imputed to omnipresent contamination by unstable isotopes. McLennan and Burton in 1903 and Rutheford and Cooke in 1903 investigated electroscope discharging in air-tight metal vessel which was shielded. They observed a charge leakage reduction by 30%. Though penetrating cosmic rays caused discharging, it was explained as contaminative effect.

An electrometer developed by Theodor Wulf in 1909 played important role in uncovering cosmic ray mysteries. Its inventor used it to measure the radiation level at the top of the Eiffel Tower (330 m above the ground level) and at its base. Surprisingly, measured 3.5 ions/cm^3 at the top corresponded to about half of the level measured on the ground and it was much higher then expected value [1]. γ rays, the most penetrating radiation according to that time knowledge, would attenuate rapidly to almost negligible level at height of 330 m above the ground. Italian physicist D. Pacini used an electroscope while observing simultaneous variations of

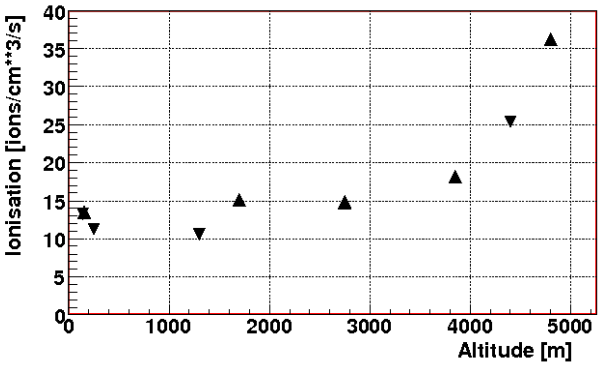

Figure 2.2: Hess's measurements of air ionization in 1912. There are average values from two detectors depicted. Ascent and decent measurements are distinguished by up and down triangles.

the rate of ionization over a lake, over the sea, and at a depth of 3 meters from the surface in 1911. He suggested other origin of certain part of the ionization than the radioactivity of the Earth from the decrease of measured values underwater [2]. In 1910 and 1911 A. Gockel made several balloon ascents to altitudes between 2500 m and 4000 m and he found out that the radiation did not disappear and even started to grow [3]. Austrian physicist Victor Hess flew in a balloon to investigate radiation behaviour with increasing altitude between 1911 and 1913. During his flights he went up to 5400 m using advanced airtight electroscopes and observed an increasing level of radiation. He even suggested the explanation of the phenomenon as a highly penetrating radiation entering the atmosphere from above [4]. Victor Hess performed the highest flight in balloon called Bohemia starting on August 7, 1912 from Ústí nad Labem (see Fig. 2.1). Thus, the year 1912 is considered as the year of cosmic ray discovery and Hess received the Nobel Prize in 1936. Victor Hess also ruled out the Sun as the radiation source. Values of air ionization measured by Hess are depicted in Fig. 2.2. Between 1913 and 1914 Werner Kolhörster followed the Hess's work and he confirmed his results by measuring at the altitude around 9 km above the ground [5]. The radiation observed by Hess and Kolhörster were known as *penetrating radiation*. Analysis of experiments showed that the penetrating power of such radiation was about 10 times the power of gamma rays. The term *cosmic rays* was established by Robert Millikan years later (in 1925) as some suggestions such as release of radioactive sources from the ground into atmosphere was not conclusively excluded. Millikan was able to perform measurements by means of unmanned balloon equipped by a special electroscope recording values on a film. The absence of staff in his balloon allowed to reach higher layers of the atmosphere where he discovered decrease of radiation level. Ironically, Millikan aimed at disapproving the Hess's and Kolörster's results, nevertheless, he proceeded in measurements with improved detection technique and instruments that were lowered in mountain lakes. Finally, Millikan realized that

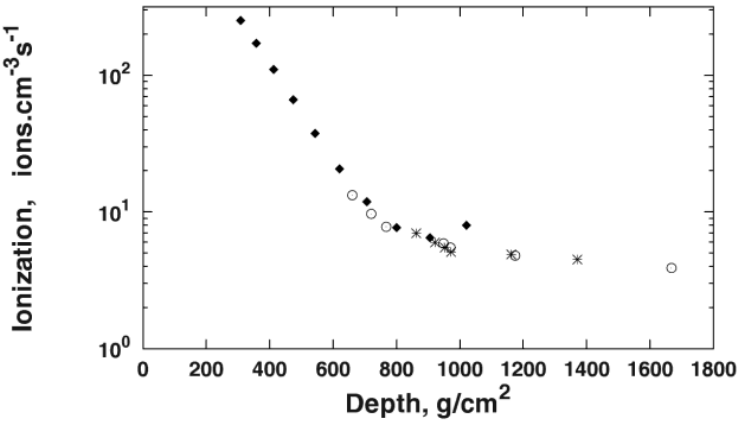

Figure 2.3: Ionization versus atmospheric depth from various types of experiments. The diamonds show values measured by Kohlhörster in balloon, while the asterisks and circles originate from Millikan's underwater measurements (taken from [7]).

the radiation must come from above after measurements with submerged electroscope in a lake in 1926 [6]. Millikan tried to determine the absorption length of the penetrating radiation with higher precision in comparison with atmospheric measurements since only 10 m of water corresponds to the total thickness of the atmosphere. Balloon measurements coincides with underwater results for the corresponding depth which is strong argument for radiation coming from above. The experimental results (showed in Fig. 2.3) indicate two different absorption lengths. From today's point of view this result is clear, since it corresponds to different air shower components - the electromagnetic component measured in the air and muons deeply penetrating into the water.

Cosmic rays were still supposed to be composed of gamma rays until some published experimental results suggested deflection in the Earth magnetic field. Thus, there must be charged particles in cosmic rays. A. H. Compton studied radiation level caused by cosmic rays at different latitudes. The measured variation could be explained as an effect of geomagnetic field that deflects charged particles (see Fig. 2.4) [8]. Even few years before (1927) [9] J. Clay published results that also show latitude variation of cosmic ray intensity. This was indication that the primary cosmic rays are deflected by the geomagnetic field and could not be composed of photons only, but also charged particles. Presented results are in accordance with presumption that the radiation is stronger at poles and weaker at the equator if primary cosmic rays are (at least partly) composed of charged particles. This observation was in contradiction with Millikan's idea of primary gamma rays producing electrons as they pass through the atmosphere (Bothe and Kolhrster also observed charged cosmic ray particles penetrating gold plate of 4.1 cm thickness, this indicates that such energetic particles could not be produced by photons). Latitude effect indisputably proved charged particles component in the primary radiation and this was indicated by wide variety of experimental investigation. Carl Störmer calculated trajectories of charged particles in geomagnetic

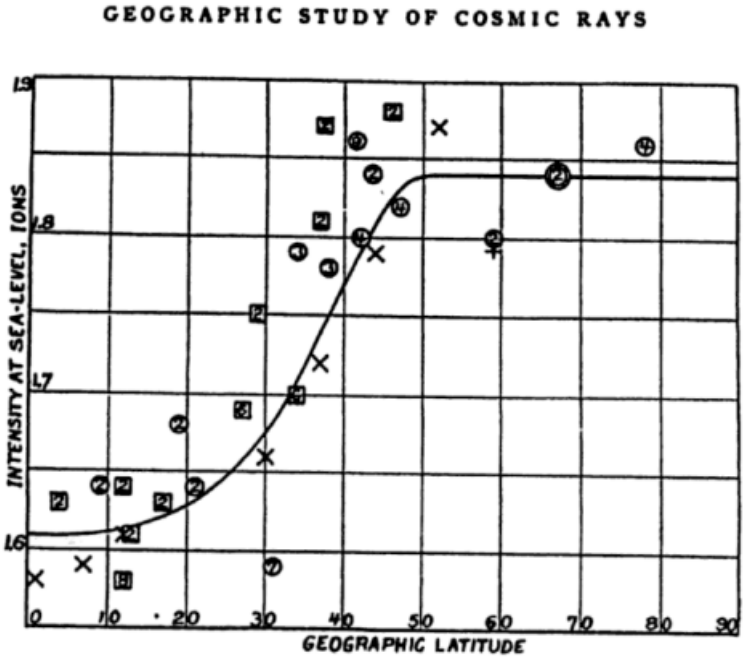

Figure 2.4: Dependence of measured radiation intensity versus geomagnetic latitude (by Compton [8]). Squares represent measurements from southern hemisphere and circles denote values measured in the northern hemisphere. Data of J. Clay are included for comparison.

field and explained phenomena called Aurora Borealis [10] as indirect confirmation of hypothesis of primary charged particles striking the Earth's surface.

The invention of new detection techniques brought new opportunities to studies of cosmic rays. Cloud chamber invented by Wilson in 1911 and Geiger-Müller counter constructed in 1929 played important roles in particle physics in many following years. In contrast to old electrometers Geiger-Müller counter was capable to detect individual particles. The theoretical knowledge made also the progress by the development of the quantum electrodynamics and the theory of electromagnetic cascade. It was preceded by the discovery of air showers induced by cosmic rays in 1929 by Skobeltsyn. He observed directly shower tracks in cloud chambers. He found out that tracks hardly bent in a magnetic field, probably observing muons unknown at that time he misinterpreted them as electrons.

W. Kolhörster and W. Bothe exploited the possibility of coincidence measurement by virtue of using two counters. They found many coincidences when they placed one counter above another even with strong gold absorber between detectors. They performed also experiment with 3 detectors which excluded accidental coincidences and also the explanation that signal is caused by Compton scattering. Gold plate between detectors would absorb energetic electron kicked off by gamma ray capable to trigger both counters. However, coincidences were still observed [11].

Italian physicist Bruno Rossi followed coincidence experiments with Geiger-Müller counters placed in a triangle. He observed coincidences even with lead

shielding [12]. In 1933 Rossi measured intensity of radiation below a lead plate with various thickness. He plotted intensity against the thickness. As a result he obtained a curves called *Rossi curves*. He reported that the intensity first rises to a maximum which is a proof of cosmic ray interaction with medium.

The phenomenon of coincidence was observed also by Pierre V. Auger and R. Maze and investigated in more detail through the experiment performed in Swiss Alps (at 3500 m.a.s.l.) in 1938. They separated detectors - cloud chambers and Geiger-Müller counters by distances more than 200 m one from another and they recorded simultaneous particles. They concluded that signal detected at wide distances apart must be caused by secondary particles produced in atmospheric interactions. They realized that coincidences can be associated to a single event, an extensive particle shower generated by high-energy primary cosmic ray particle. Its interaction initiates a cascade of successive interactions yielding a particle shower that reaches ground level [13]. Pierre Auger's calculation of the primary particle energy to induce such showers lead to the value of 10^{15} eV.

Cosmic rays played essential role in the field of particle physics as the natural source of high energy particles for tens of years. Cloud chamber pictures of air shower secondaries revealed new particles and processes. Dirac's theory of quantum mechanic and his prediction of electron anti-particle existence in 1928 was acknowledged by discovery of positron in 1931 by Carl Anderson [14]. 5 years later, in 1936, a particle with approximate mass of 200 times the mass of an electron was seen by Carl D. Anderson and Seth Neddermeyer. Initially it was called mesotron, however, todays term - muon was introduced in 1947. Cosmic rays were as well employed in the discovery of $\pi^{\pm}$ and π^0 particles in nuclear emulsions in 1947. Exposed to cosmic rays, layers of nuclear emulsions were mounted together to view charged particle tracks. Strange particles, originally identified as 'V' tracks, were firstly observed in cloud chambers exposed to cosmic rays by G. Rochester and C. Butler. It lead to the discovery of kaons and Λ particles. The progress of accelerators made in 1950's caused that cosmic rays lost their attraction. The intense beams of known particles produced by accelerators brought new opportunities in particle physics. However, cosmic rays still can offer wide range of phenomena of the uncovered part of the nature. Hyperon Ξ was observed in emulsion chambers by Manchester group in 1952 and one year later this was followed by Σ discovery. Photographic emulsions carried into the stratosphere in a balloon uncovered the existence of another unstable particles in 1971, later identified as D mesons.

2.1.1 Brief history and present of cosmic ray experiments

Characteristics of extensive air showers induced by cosmic rays became a subject of studies after coincidence discovery. Detector arrays were installed using Geiger-Müller counters since mid 1940s. Precise time resolution was needed to infer extensive air shower properties and those of the corresponding primary particle. Scintillation counters using photomultipliers and Čerenkov detectors fulfill such requirements and were used in extensive air shower detectors. The origin of cosmic rays, possible sources, energy spectrum and chemical composition were the open

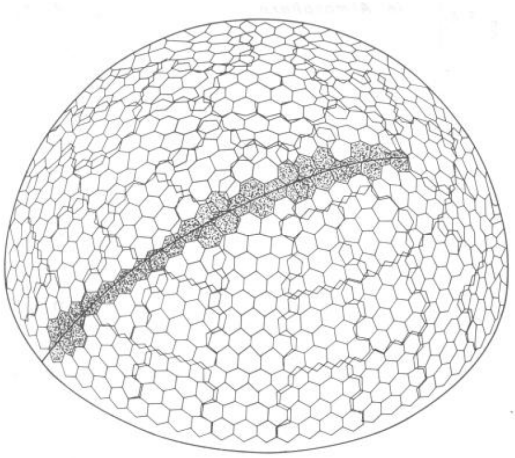

Figure 2.5: Full sky coverage of the Fly's Eye was provided by geometrical arrangement of individual detectors.

Figure 2.6: 67 detectors containing 880 photomultipliers in total at Little Granite Mountain. Barrels are set to positions which ensure full sky coverage of all modules.

questions (and still are not sufficiently answered). The investigation of cosmic ray energy spectrum shows that it follows the power law $dN/dE \propto E^{\gamma}$. Nevertheless, a distinctive bend in spectrum around energy of several PeV - nowadays called the 'knee' - was discovered by German Kulikov and George Khristiansen in 1958. Such characteristic feature opened debate about the origin of this structure and people believe that it is connected to the origin of cosmic rays, this view still prevails.

Cosmic ray research attracted more interest in 1960s when an event with estimated energy of 10^{20} eV was recorded at the Volcano Ranch Array in 1962 [15]. Such energy is far beyond potential capabilities of man-made accelerators. Volcano Ranch was an experiment to detect extensive air showers in New Mexico operating between 1959 and 1963 [16]. Total number of 20 scintillation detectors covered the area of 12 km^2. Each of 19 scintillator counters had detecting surface of 3.3 m^2 and was viewed by 5-inch photomultiplier. The last 20^{th} counter served as muon detector.

Array of scintillation detectors called The Sydney University Giant ARay (SUGAR) was placed in Australia and it started operation in 1968 [17]. For long time it was the only experiment built in the southern hemisphere. 54 detector stations were buried 1.7 m under the surface and they were spread with spacing 1610 m covering the area of 54 km^2.

Haverah Park [18] was the first experiment using water Čerenkov water tanks as surface detectors. It was operating between 1968 and 1987 originally with four detectors followed by several subarrays and infill array with different spacing.

Yakutsk [19] experiment which has sophisticated set up of scintillators and muon detectors was developed in Russia in 1970 and it is operating till now. The first stage of experiment started in 1971 and was composed of 43 scintillator stations, Cherenkov light detectors and detectors of muons. 4 years later the area of array was increased to 17 km^2 to study the energies around 10^{19} eV. Three nested arrays of different types of detectors and spacing increase the detector dynamic range.

Large area muon detector and infill array of 18 stations define the second stage of this experiment and it started operation in 1991.

Akeno Giant Air Shower Array (AGASA) [20] was the experiment located in Japan operating from 1990 up to 2004. AGASA covered an area of about $100\,\mathrm{km}^2$ and consisted of 111 scintillator detectors of $2.2\,\mathrm{m}^2$ each on the ground (surface detectors) and 27 detectors under absorbers (muon detectors). Each surface detector was placed with a separation of about 1 km. Muon detectors were deployed at chosen surface detector sites and their surface ranged from $2.4\,\mathrm{m}^2$ to $10\,\mathrm{m}^2$.

A completely new detection technique was developed and used at the experiment named Fly's Eye [21] located in Utah in USA. It was based on the direct observation of the longitudinal shower development in the atmosphere by means of fluorescence light emitted along the charged particles passage. In the first stage of the experiment (1981 - 1986) 67 detector modules, each of them contained mirror 1.5 m in diameter, were installed at Little Granite Mountain. Each module was equipped with 12 or 14 photomultipliers of hexagonal shape in focal surfaces of mirrors. Detector modules were oriented so that pixels overlaid the whole sky (see Fig. 2.5 and Fig. 2.6). The second part of the detector referred to as Fly's Eye II was composed of 36 mirrors and completed in 1986. Two sites 3.4 km apart were oriented towards each other allowing stereoscopic observation. The highest energy event ever recorded is assigned to the shower detected by Fly's Eye in November 1991. The energy of the shower was set to $3.2 \times 10^{20}\,\mathrm{eV}$ (51 J).

The High Resolution Fly's Eye (HiRes) followed the success of its predecessor starting operation in 1997. Similarly, two parts separated by 12.6 km utilized mirrors and photomultipliers detecting fluorescence light. First site, called HiRes-I, consisted of 22 mirrors and 256 pixels overviewing a sky band between 3 and 17 degrees in elevation. The second set of detectors known as HiRes-II comprised of 42 mirrors and it observed a cone ranging from 3 to 31 degrees in elevation. Such setup ensured $1^\circ \times 1^\circ$ segmentation of the sky with duty cycle $\sim 10\%$.

Measurement results of the two latest experiments, AGASA and HiRes, didn't fit well in the highest energy region of the spectrum (see Fig. 2.7). AGASA results suggested no suppression of flux beyond $10^{19.4}\,\mathrm{eV}$ while HiRes indicated clear cut-off as expected according to GZK cut-off theory. The disagreement of results at the end of the spectrum became a motivation to develop a new detector capable to measure this substantial region of cosmic ray energy spectrum. It required a very large active area and precise measurement methods to reduce uncertainties. The largest cosmic ray experiment, the Pierre Auger Observatory meets such demands. Section 3 is dedicated to the detailed description of the Pierre Auger Observatory with its essential feature - the hybrid detection technique. The nature of its measurement method is employment of two independent ways to detect and study high-energy cosmic rays. Surface detector array constituted by water filled tanks detects particles reaching ground level. The second detection technique tracks the development of air showers by observing ultraviolet light emitted in the Earth's atmosphere.

The Telescope Array located in the Millard County in Utah is another experiment combining two types of extensive air shower detection and nowadays the

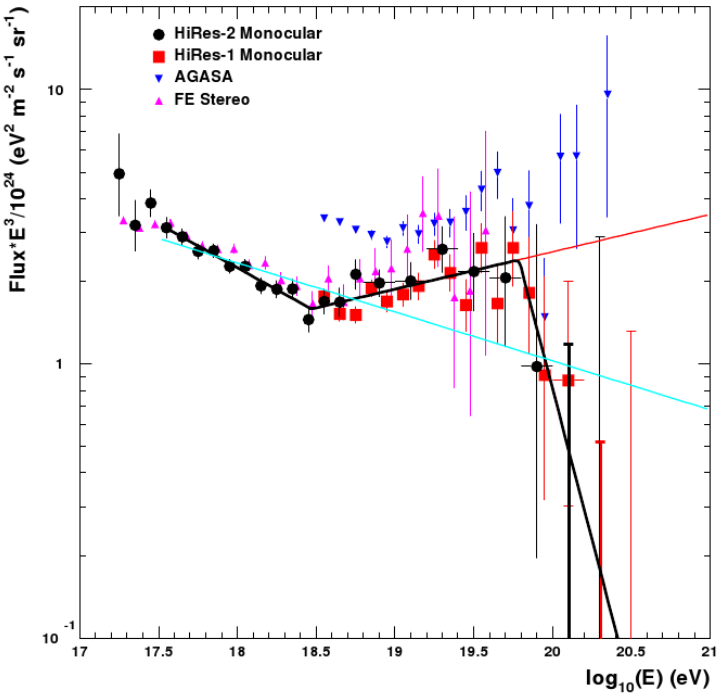

Figure 2.7: Energy spectrum of HiRes-I (red squares), HiRes-II (black circles), AGASA (blue triangles) and Fly's Eye (magenta triangles) experiments [22]. Flux measured by AGASA doesn't indicate any suppression beyond the energy of $10^{19.4}$ eV.

largest cosmic ray experiment that was build in the northern hemisphere [23]. 507 scintillation detectors measuring charged particle distribution on the Earth's ground are overviewed by three fluorescence detectors (see Fig. 2.10). Scintillators are deployed over the area of 762 km^2 with spacing 1.2 km between units. Each fluorescence detector is instrumented with 12 - 14 telescopes providing detection of a sky band from 3 to 31 degrees in elevation. An image viewed by a single telescope is segmented by 256 photomultipliers. The Telescope Array experiment involves also atmospheric monitoring and low energy extension.

There are several other experiments dedicated to cosmic ray research in the proposal or development stage. The All-sky Survey High Resolution Air-shower Detector (Ashra) is one of them, just under construction in Hawaii [25]. Very wide field images of 12 highly sensitive telescopes will cover approximately 77% of the whole sky using CMOS sensors and amplifiers. Planned resolution of a few arcmin is ensured by almost 80 megapixels images.

KArlsruhe Shower Core and Array DEtector (KASCADE) was German experiment studying properties of cosmic rays with energies between $10^{14} - 10^{17}$ eV [26]. The array of 252 stations covered the area 200 m $\times$ 200 m. Each station was composed of four gamma/electron detectors together with one muon detector. Later extension called KASCADE-Grande expanded the energy range up to 10^{18} eV (see Fig. 2.8) [27]. The original detector array was supplemented by 37 scintillators to

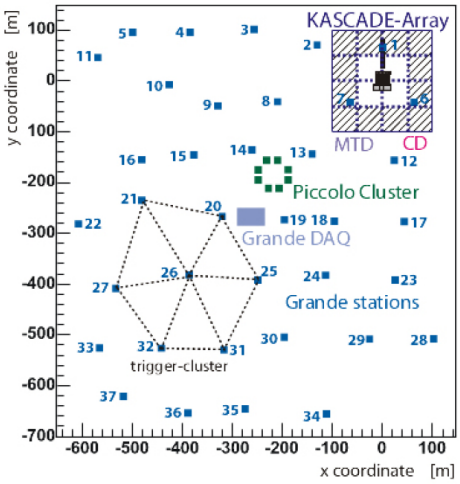

Figure 2.8: KASCADE-Grande array layout with position of the original KASCADE array on the top right corner.

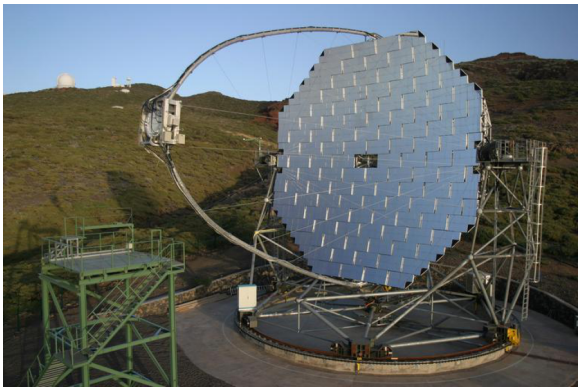

Figure 2.9: One of MAGIC telescopes collecting Čerenkov light emitted by charged particles. The diameter of the reflector is 17 m with total collecting area of 236 m^2. The active mirror surface is made of 974 square elements 49.5 × 49.5 cm.

the total area of 800 m × 700 m. By measuring electromagnetic and muon component, KASCADE was able to estimate primary cosmic ray composition. The average logarithm of primary mass $\langle ln(A) \rangle$ was derived from electron N_e and muon N_μ shower sizes detected on the ground. KASCADE collaboration is also known due to the project that is called Cosmic Ray Simulations for Kascade (CORSIKA) [28]. This is a Monte Carlo code developed for extensive air shower simulations. Nowadays this program is the most common tool used by many collaborations. Detailed information can be found in section 5.

Major Atmospheric Gamma-ray Imaging Cherenkov Telescope (MAGIC) is ground based experiment located in one of the Canary Islands detecting gamma rays [29]. Since 2009 2 telescopes (of the same characteristics) are operating at a distance of 85 m from each other (see Fig. 2.9). These instruments, both with collecting area of 240 m^2, are sensitive to gamma rays with energy above 30 GeV. The main scope of investigation is related to astrophysical questions by observing supernova remnants, pulsars or binary systems. The MAGIC telescopes have been also used to observe extragalactic objects, especially Active Galactic Nuclei (AGNs) and it has capability to follow Gamma Ray Bursts.

System of Imaging Atmospheric Cherenkov Telescopes (IACT) is a device focused on studying very high energy gamma-ray astrophysics. Beside MAGIC described above there are another major experiments of IACT type detecting gamma photons. High Energy Stereoscopic System (H.E.S.S.) located in Namibia allows to explore gamma-ray sources in the energy range tens of GeV to tens of TeV [30]. Phase I of the H.E.S.S. project was completed in 2003 when four telescopes arranged in form of a square of 120 m side length were fully operational. H.E.S.S. II has included additional fifth telescope with area of 614 m^2 since 2012.

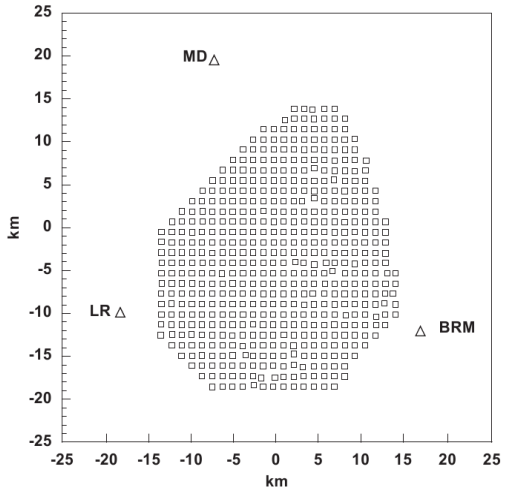

Figure 2.10: Telescope Array detectors arrangement: squares represent surface detectors that are overviewed by three fluorescence telescope stations depicted by triangles [24].

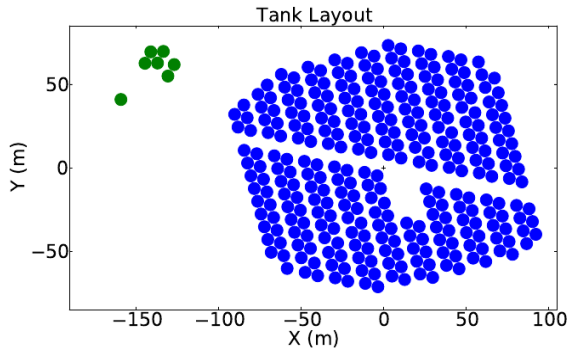

Figure 2.11: HAWC water čerenkov tank layout (blue points). Seven green points at the top left corner are test array [32]. Relativistic particles going through tanks produce Čerenkov radiation that are detected by photomultiplier tubes.

Array of four optical reflectors called Very Energetic Radiation Imaging Telescope Array System (VERITAS) is experiment of IACT type located in southern Arizona, USA. Completed array of 4 telescopes array has been operated since 2007. Each telescope reflector is composed of 350 individual mirrors collecting light for 499 pixel camera. The highest sensitivity energy band ranges from 50 GeV to 50 TeV.

The new generation of very high energy gamma-ray telescope instruments is currently under design. The Cherenkov Telescope Array (CTA) will extend reach of IACT predecessors. Both Southern and Northern hemisphere sites should be completed and fully operational in 2020 (partial operation of the array is planned to start after 2017). A factor of 10 improvement in sensitivity in the domain of about 100 GeV to some 10 TeV is expected (it is currently the main energy range for gamma ray observations). Two sites of CTA are planned to be build, one in the southern and the other in the northern hemisphere. Three types of telescopes will extend the accessible energy range from well below 100 GeV to 100 TeV.

Milagro was a water Čerenkov detector taking data between 2001 and 2008 and situated in the Jemez Mountains in New Mexico [31]. A large pool filled with water was instrumented with 723 photomultipliers. Milagro was primarily dedicated to gamma ray detection. Its successor, The High Altitude Water Cherenkov (HAWC) telescopes is supposed to comprise 300 detectors (see Fig. 2.11) to observe TeV gamma rays with continuous working time with an aperture covering more than 15% of the sky. High altitude of 4100 m a.s.l. at the Sierra Negra volcano near Puebla, Mexico, will provide a high-sensitivity survey of the sky at energy range between 100 GeV and 100 TeV.

Experiment	Location	Area [km^2]	Altitude [m]	Detector type	Operation
Volcano Ranch	New Mexico	8	1770	scintillators	1959 — 1963
SUGAR	Australia	60	250	scintillators	1968 — 1979
Haverah Park	United Kingdom	12	200	water Čerenkov	1968 — 1987
Yakutsk	Siberia	18(10)	105	scintillators	1969 —
AGASA	Japan	100	900	scintillators	1990 — 2004
Fly's Eye	Utah	—	1597	fluor. telescopes	1981 — 1992
KASCADE	Germany	0.04 (0.49)	110	scintillators	1996 — 2009
HiRes	Utah	—	1597	fluor. telescopes	1999 — 2005
Auger South	Argentina	3000	1450	hybrid	2004 —
Telescope Array	Utah	762	1400	scintillators	2007 —
ASHRA	Hawaii Island	—	3300	CMOS sensors	2008 —
MAGIC	Canary Islands	—	2200	Čer. telescopes	2004 —
H.E.S.S.	Namibia	—	1800	Čer. telescopes	2002 —
VERITAS	Arizona	—	1270	Čer. telescopes	2007 —

Table 2.1: Large ground-based cosmic ray experiments.

Cosmic ray experiments were not only placed on the ground, but the possibility of using detectors mounted on balloons led to a great precision of the knowledge of the chemical composition of cosmic rays in lower energy regions. There is also collection of experiments mounted on satellites at Earth orbit outside the atmosphere. These experiments require unusual condition to reach specific measurement precision or sensitivity that is disturbed or unattainable in ground-based condition.

Balloon-borne Experiment with Superconducting Spectrometer (BESS) denotes a series of experiments started in 1993 [33]. The main part of the detector was a magnetic spectrometer allowing to identify charged particles. The system is operating at high altitudes and therefore able to measure the amount of antimatter striking the Earth.

Alpha Magnetic Spectrometer (AMS-02) is external experiment module mounted on the International Space Station. It was installed in 2011 to study the origin of the Universe by measuring the composition and flux of cosmic rays. It performs precision measurement of the abundance of antimatter and searches of dark matter evidence.

There are also proposals of cosmic ray detection from satellite orbits. Ambitious experiment Extreme Universe Space Observatory JEM-EUSO plans to use Japanese Experiment Module (JEM) on the International Space Station [34]. Its aim is to observe fluorescence flashes in the atmosphere from the altitude of about 400 km.

One of working satellite experiment is Payload for Antimatter Matter Exploration and Light-nuclei Astrophysics (PAMELA) launched in 2006 [35]. PAMELA is focused on antimatter exploration by detection of antiprotons and positrons. Monitoring of long-term modulation of solar particle flux or search for dark matter

evidence belong also to objectives of this experiment.

Tab. 2.1 contains list of large ground-based air shower detectors, their location, period of operation, detector type, active area and altitude.

2.2 Cosmic ray flux and energy spectrum

The Earth is permanently exposed to a flux of ionizing radiation composed of various atomic nuclei (and neutral particles) at different energies. Abundance of CRs very strongly depends on their energy that can be observed in a wide range from a few MeV up to at least $\sim 10^{20}$ eV.

The overall CR flux at the top of the Earth's atmosphere[1] is several $\sim$ 1000 $\mathrm{m^{-2}sr^{-1}s^{-1}}$ (mostly protons) and such particles are called primaries. Particle flux at ground is dominated by electromagnetic particles and muons originating from EAS initiated by a primary CR and therefore they are called secondaries as products of consecutive interactions (see Sec. 2.5).

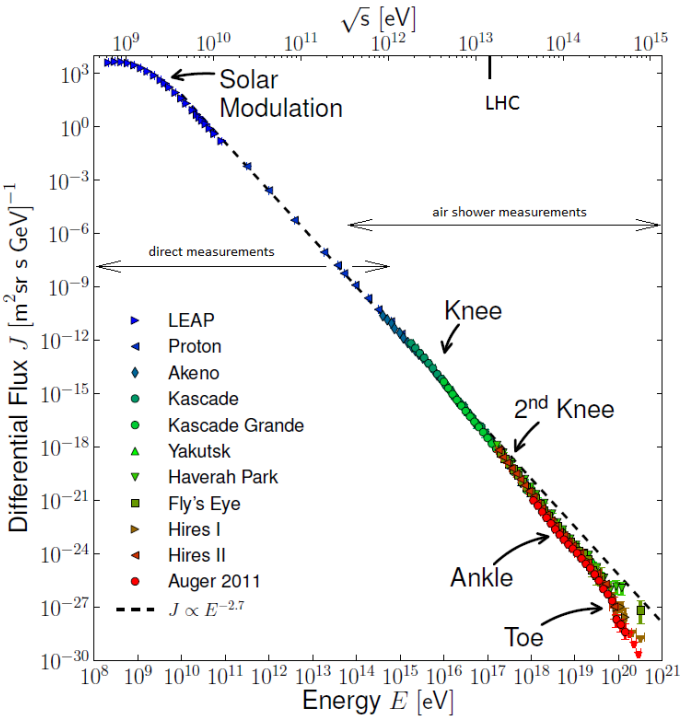

Figure 2.12: Cosmic ray energy spectrum with results from direct measurement experiments (at low energies, namely the primary proton flux) as well as from those using indirect methods (adopted from [36]). The laboratory energy of proton-proton collision is transformed into CMS energy and depicted on the upper axis. For comparison the flux below the *knee* is fitted by a curve $J \propto E^{-2.7}$.

[1]CORSIKA program applied to EAS simulations in this thesis uses several models all of them define the boundary of the atmosphere at $h = 112.83\,\mathrm{km}$ for Pierre Auger Observatory site – Malargüe in Argentina.

The CR flux J is commonly expressed as number of particles N_{inc} with energy E hitting the area S from the solid angle Ω per time unit t:

$$J = \frac{d^4 N_{inc}}{dE\, dS\, d\Omega\, dt} \tag{2.1}$$

Various experimental results both based on direct or indirect measurement methods lead to overall differential flux depicted in Fig. 2.12 that covers twelve orders of magnitude in energy scale. In addition, the scale of flux is even more broad and it changes by 27 orders from the smallest energies to the hardest part of the spectrum. Lowest energy region particles ($10^8 - 10^{10}$) eV come from the Sun and even 11-year cycle of solar flux variation can be observed[2]. While the lower part of the spectrum can be studied directly and the composition of primary particles is quite well known, because they are studied by means of balloon detectors up to TeV region, the strong decrease of flux poses difficulties of the studies of the rest of the spectrum. The shape of the energy spectrum in Fig. 2.12 shows rapid decrease of the cosmic ray flux with energy. CR with energies greater then $\sim 10^{11}$ eV can be observed with frequency of one particle per m^2 per second, while only one particle per m^2 per year can be detected with energy $\sim 10^{16}$ eV. Particles from the end of energy spectrum ($E > 10^{20}$ eV) are so rare that only one particle per century is statistically expected to hit the area of one km^2.

The differential flux of UHECRs seems to be quite simple without eminent characteristics on the first sight. While monotonous and steeply falling with energy, it can be described by a power law

$$J(E) \propto E^{-\gamma} \tag{2.2}$$

with spectral index γ between 2.6 and 3.2.

Detailed study can reveal two significant features in the energy spectrum – at $\sim 4 \times 10^{15}$ eV the so called *knee* where γ changes from 2.7 to 3.1 [37]. The flux below the *knee* decreases by a factor of 500 per decade of energy, whereas above the *knee* this factor is about 100. The second important feature is called *ankle* at 4×10^{18} eV with another change of spectral index from 3.3 to 2.6 [38]. Processes and mechanisms of achieving ultra-high energies are still unknown. Hence the main questions which people want to answer concern composition, energy spectrum and sources of UHECRs.

Collision energies reachable by largest ground accelerators (the maximum should be 14 TeV in proton-proton collisions at LHC) are compared to CR spectrum in Fig. 2.12. In spite of their rarity, the most energetic CR particles carry energies by a factor at least of 10^5 larger then particles artificially accelerated by man and factor of 10^2 in CMS of the collisions.

Above the energy of 5×10^{19}eV the strong suppression of CR flux is observed interpreted as propagation effect known as Greisen-Zatsepin-Kuzmin (GZK) effect (see section 2.4.2).

[2]Flux of charged particles coming from Sun generates additional magnetic field that creates barrier to low energy cosmic rays and anticorrelation with Solar activity and low energy cosmic ray flux can be observed

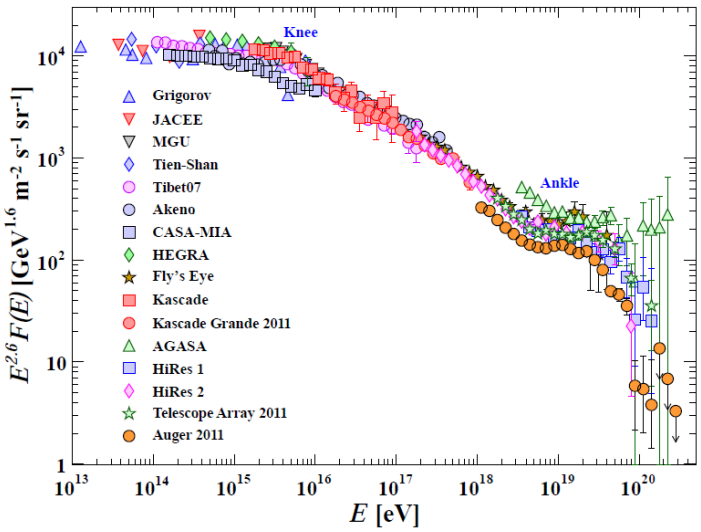

Figure 2.13: CR energy spectrum for energies above 10^{14} eV as measured from air shower experiments [39].

Spectrum of CR as measured by various air shower experiments is depicted in Fig. 2.13 ([39]). For clarity the differential energy spectrum is multiplied by a factor of $E^{2.6}$ to display all fine characteristics of spectrum.

There are several interpretations of the *knee* as significant feature of cosmic ray spectrum. Mechanisms of the formation of such cosmic ray flux break is discussed in literature, see [37, 40]. Particles of energy around *knee* are considered to be of galactic origin with possible acceleration mechanisms that are outlined in section 2.4. There are indications that spectral index change in the region of the *knee* is caused by spectrum break in light elements resulting in increase of the average primary particle mass. There are two main ways how to describe the energy spectrum structure. Proposals from the first group explain the *knee* by maximum energy attainable by sources and the second one by leakage of cosmic ray particles from the Galaxy.

Acceleration in strong supernova shock fronts is characterized by maximum energies that are dependent on the primary mass as $E_{max} \approx Z\,(0.1 - 5)\,\mathrm{PeV}$ [37]. Spectral index for an element from such cosmic ray source changes above 1 PeV. Individual spectra of elements exhibits breaks above maximum energy reachable by the acceleration process. Obviously, the position of spectral break is charge dependent. The *knee* seen in the all-particle spectrum is therefore explained as the consequence of element dependence of the maximum energy reachable by this acceleration mechanism as showed e.g. in [40].

The propagation of cosmic rays in our Galaxy is influenced by its magnetic field. Particles below some energy threshold are bounded in the Galaxy, while particles above this cut-off energy can escape from the magnetic trap. The Larmor radius for proton of energy 10^{18} eV is about 360 pc and that is comparable to galactic disc thickness. Nuclei with higher proton number and the same energy are more

strongly confined to the Galaxy.

The energy spectrum beyond the *knee* steepens, while at the region around the *ankle* the spectrum becomes more flat again which attracts physicists' attention. Widely accepted astrophysical interpretation of the *ankle* is the transition from galactic to extragalactic sources that likely occurs at energies between 10^{17} eV and $10^{18.5}$ eV. There are several models describing possible scenarios of the shape of ankle formation. The three main transition models as described in [42] are so called *ankle*, *dip* and *mixed composition* models. *Ankle* model assumes proton extragalactic component. The spectrum region at the beginning of the *ankle* corresponds to flux where extragalactic component starts to prevail. *Ankle* model assumes modification of galactic component with heavy nuclei contribution. Current results of Pierre Auger Observatory measurements are in contradiction with the light mass composition assumption above 1 EeV.

Dip model assumes prevailing galactic irons below some energy limits and extragalactic protons above that. Transition between two components and electron-positron pair production due caused by proton interactions with microwave background can explain some spectrum features. Proton extragalactic component can have only small mixture of nuclei $\lesssim 20\%$. The transition from galactic to extragalactic component occurs between energies 0.5 EeV and 1 EeV, that is in lower energy in comparison with the *ankle* scenario. The transition from galactic to extragalactic component is completed at ≈ 1 EeV where the spectrum feature *second knee* is observed. The interactions of protons with CMBs and consequent pair productions automatically lead to the prediction of energy and position of the *ankle*. Dip model predicts proton composition of CRs above ≈ 1 EeV and iron composition below that energy limit. The prediction of mass composition is not in agreement with Pierre Auger measurements as it will be described in the next section Pierre Auger predicts heavier mass composition at highest energies ([42, 43]).

Mixed composition model is based on assumption that there is an iron galactic component above 0.1 EeV and mixed composition of extragalactic particles. The mass composition becomes lighter for energies above $E > 10$ EeV. The comparison of pure proton extragalactic model with model assuming mixed composition is drawn in Fig. 2.14.

2.3 Cosmic ray composition

CRs at low energies are dominated by protons ($\sim 90\%$) and He ($\sim 9\%$), the remaining fraction could include heavier nuclei and neutral particles (photons, neutrinos and neutrons)[3]. Neutral particles are not deflected by magnetic fields and therefore some of them, especially γ rays, can be associated with some point sources (e.g. active galactic nuclei, pulsars, quasars).

[3]Particle abundances are measured in the flux of those particles that penetrated the geomagnetic field. One can identify also small part of antiparticles in the flux near the Earth (positrons and antiprotons) that are produced in interactions of CRs with interstellar matter. The extent of deflection caused by magnetic field is defined by *magnetic rigidity* $R = p/(z|e|)$, where p is the momentum of particle with charge $z|e|$

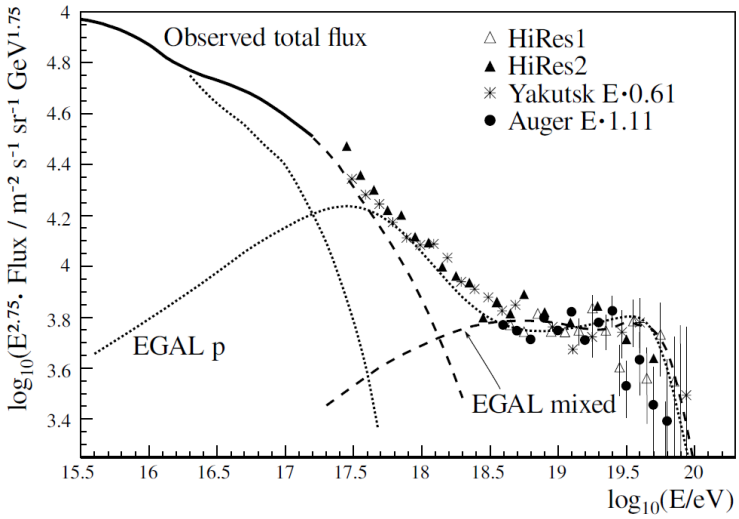

Figure 2.14: Breakdown in cosmic ray spectrum according to pure-proton galactic component models and mixed-model scenario (adopted from [41]).

Atmospheric Čerenkov telescopes measure these γ rays and contribute very intensively to the list of known γ rays point sources, e.g. Crab Nebula, Centaurus A, Sagittarius A and many others, but also a neutrino signal detected by The Kamiokande detector in 1987 was identified as neutrino burst from supernova *SN1987a* explosion in Large Magellanic Cloud.

Chemical composition of CR shown in Fig. 2.15 indicates conspicuous similarity with solar system abundances. Shape of both lines indicates excess of even-even nuclei as they are the most strongly bounded. The majority of elements have very similar relative abundances including C, O, Ne, Mg, Si, Fe, Ni. On the other hand, there are groups of elements that are overabundant in cosmic rays by several orders of magnitude. Indisputable discrepancies between spectra, most evident for Li, Be, B, Sc, Ti and V nuclei, can be explained by spallation processes[4]. Spallation is a natural process of nuclear fission. Cosmic rays heavier than helium suffer from interactions as they traverse the interstellar matter with nuclear composition transformation. Overabundant elements Li, Be and B in cosmic rays are products of carbon, nitrogen and oxygen fragmentation. Similarly, Sc, Ti and V in CRs are products of spallation process of Fe and Ni.

Overabundance of elements that are produced in spallation processes determines the average interstellar matter density that cosmic rays traverse (assuming knowledge of spallation cross sections and average matter density). A typical cosmic ray propagates through the space for $3 - 6 \times 10^6$ years[5].

[4]Li, Be and B are relatively rare elements in stars because of their weak Coulomb barrier. They easily enter stellar nuclear reactions and they are quickly burned in the core.

[5]This is a result of simple calculation of the so called *leaky box* model. Particles moved in three-dimensional volume with certain probability of escape. The average matter density ρ in the volume, lifetime of cosmic rays τ and mean amount of matter λ traversed by cosmic rays are related as $\lambda = \beta c \tau \rho$. Interstellar matter density ρ is about 1 proton m^{-2}. Cosmic rays density

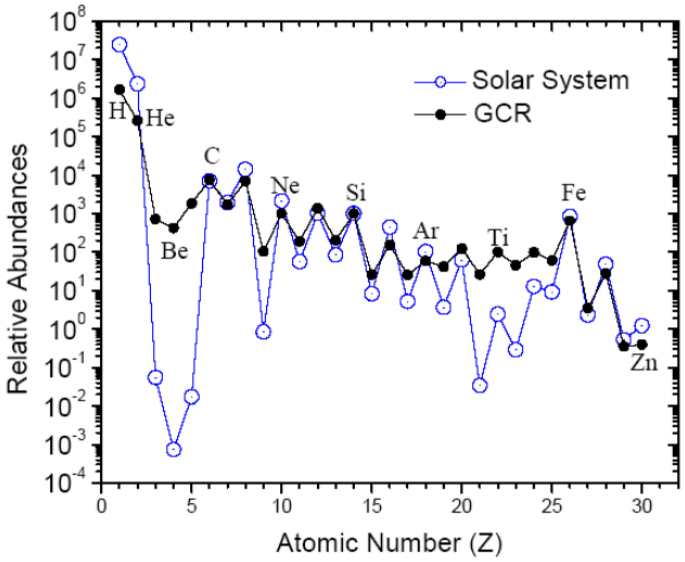

Figure 2.15: Composition of primary galactic cosmic rays (referred to as GCR), shown by black line, compared with solar system abundances, shown as a blue line and points. The figure is taken from [44] and cosmic ray abundances are gathered from various direct measurements (ACE, CRIS, BESS, GSFC), while solar system chemical composition was derived from [45].

The presented cosmic ray composition is measured directly by balloon-borne experiments or detectors flown on satellites. Scintillation counters and spectrometers have been employed to measure charge (proton number) of nuclei. At energies higher than 10^2 TeV direct measurement methods are not efficient due to low flux. Indirect methods are based on detection of fluorescence emission in the atmosphere or arrays of detectors that sample particles reaching the ground level (see 2.6.2 and 2.6.1). Fluorescence detectors can directly measure X_{max} – the depth at which the longitudinal development of a shower reaches its maximum. On its basis the average values $\langle X_{max} \rangle$ and fluctuations $RMS(X_{max})$ can be derived as they are sensitive to the cosmic ray chemical composition.

It is shown in the section 2.5.1 that the average of a shower maximum $\langle X_{max} \rangle$ of primary masses A at given energy E can be expected with simplified assumptions in the superposition model as follows:

$$\langle X_{max} \rangle = \alpha(ln(E) - \langle ln(A) \rangle) + \beta, \tag{2.3}$$

where α and β are factors related to hadron interaction properties such as elasticity, multiplicity and cross sections with air. In the simplified air shower description α and β coefficients are energy independent. Commonly used variable D_{10} called

and spallation cross sections give typical amount of material of 5 to 10 g cm^{-2} that is propagated by cosmic rays. From equation $\lambda = \rho c \tau \approx 5 - 10$ g cm^{-2} one can estimate $\tau \approx 3 - 6 \times 10^6$ years

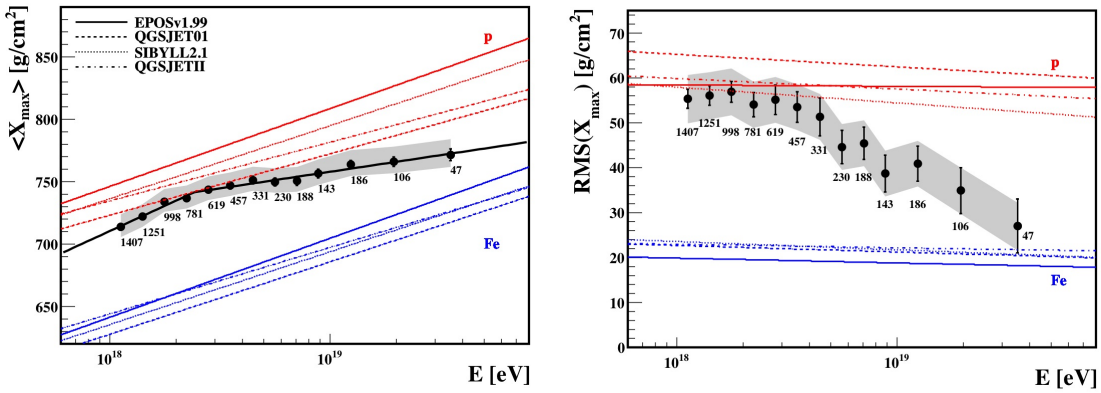

Figure 2.16: $\langle X_{max} \rangle$ (left plot) and $RMS(X_{max})$ (right plot) results measured by Pierre Auger Observatory compared with simulations [46].

elongation rate describes the change of $\langle X_{max} \rangle$ per decade energy:

$$D_{10} = \frac{d\langle X_{max} \rangle}{d\, log_{10}(E)} \approx \alpha \left(1 - \frac{d\ln(A)}{d\, ln(E)}\right) \ln(10) \tag{2.4}$$

and it is therefore sensitive to mass composition changes with energy. $\langle X_{max} \rangle$ measurement by Pierre Auger Observatory with simulations is depicted in Fig. 2.16. Elongation rate change of more than $80\,\mathrm{g/cm^2}$/decade is observed at energy $10^{18.24\pm0.05}\,\mathrm{eV}$ [43]. As seen from the plot the expected values as resulted from simulations between proton and iron differ by $\approx 100\,\mathrm{g\,cm^{-2}}$ (typical resolution of Čerenkov or fluorescence detectors used for X_{max} measurement is much smaller, it is at at the $20\,\mathrm{g/cm^2}$ for energies $E > 1\,\mathrm{EeV}$ for instruments installed at Pierre Auger Observatory [43]).

Another composition-sensitive variable $RMS(X_{max})$ decreases with primary mass A. In Fig. 2.16 results including simulations are shown with manifest decrease of fluctuations from 55 to $26\,\mathrm{g\,cm^{-2}}$. Complementary measurements of $RMS(X_{max})$ and $\langle X_{max} \rangle$ shown in Fig. 2.16 indicate increasing primary mass at energies beyond $10^{18}\,\mathrm{eV}$.

While Fig. 2.15 contains precise measurement results, the exact interpretation of $\langle X_{max} \rangle$ and $RMS(X_{max})$ in Fig. 2.16 is very difficult as it is dependent on simulations[6]. This apparent problem is typical for EAS measurement based on indirect secondaries measurement. It is very difficult to state precise numbers due to uncertainties between different simulation models.

[6]Other experiment results such as HiRes or Telescope Array are not in agreement with Pierre Auger Observatory conclusion that energy spectrum beyond $10^{18.5}\,\mathrm{eV}$ shows increase of primary mass.

2.4 Possible sources and acceleration mechanisms

A century since the discovery of cosmic rays, sources and acceleration mechanisms remain unknown except for the Sun emitting charged particles at energies up to $\sim 10\,\mathrm{GeV}$, within the region which can be identified according to the day-night variation. Nevertheless, there are several theories of astronomical objects and processes accelerating particles to energies above $10^{20}\,\mathrm{eV}$.

Sources cannot be identified simply by primary particle measurement due to propagation through magnetic fields. An estimate of such fields in galaxies in intergalactic regions turns out to be essential to cosmic ray source exploration. On the other hand, the end of the cosmic ray spectrum provides promising data sample to reveal origin of the most energetic ($> 10^{19}\,\mathrm{eV}$) CRs and this poses a great experimental challenge. However, many gamma ray sources at TeV energies have been discovered by dedicated experiments, some of them were described in the section 2.1.1.

There are two different groups of scenarios of UHECR generation being referred to as *bottom-up* and *top-down* models. Bottom-up models describe acceleration mechanism of particles with relatively low energy before beginning of the process. Particles are injected into some system which boots their energy. Conversely, top-down models assume superheavy X objects left over from the Big Bang. Quasi-stable long-lived X particles with mass M_x of the orders $10^{13}\,\mathrm{GeV}$–$10^{16}\,\mathrm{GeV}$ and lifetime $\tau_x \geq 10^{10}\,\mathrm{years}$ solve the problem of few celestial objects with favorable parameters to accelerate particles up to and beyond $10^{20}\,\mathrm{eV}$ (top-down models where UHECRs originate from massive particle decay are discussed in [47]). One of the models will be discussed in the next section 2.4.1. Difficulties and restrictions in possible source identification caused by propagation of CR will be analyzed in the section 2.4.2.

2.4.1 Acceleration mechanisms

It is important to notice a relation between breaks in energy spectrum and dominant origins of such energy regions. It is believed that any change in the spectral index of energy spectrum indicates change of acceleration mechanism or it is related to propagation processes or change in interaction cross section. Acceleration principles of UHECRs are subjects of particular interests of physicists trying to find an effective mechanisms how to gain subnuclear particle energies up to macroscopic values.

Any charged particle emitted into the interstellar space propagating through the galaxy (or even out of galaxy) is deflected by randomly oriented magnetic fields. If the momentum of a particle is not high enough it is entrapped. Larmor radius is defined as follows:

$$r_L = \frac{v_\perp m}{qB} \quad \longrightarrow \quad r_L[\mathrm{pc}] \simeq 1.08\,\frac{E\,[\mathrm{PeV}]}{Z \cdot B\,[\mu\mathrm{G}]} \tag{2.5}$$

where $v_\perp$ is component of particle velocity perpendicular to a magnetic field B, m and q are its mass and charge and Z is the charge of accelerated particle in units of elementary charge e. Particles also suffer from Coulomb scattering and interactions with instellar matter.

Larmor radius of a proton with energy around $\sim 10^{17}\,\mathrm{eV}$ (or an iron nuclei with energy around $10^{18.5}\,\mathrm{eV}$) in the Galaxy with typical value of the magnetic field of the order of several μG is almost 1 kpc. Such particles cannot be confined by magnetic field because of the thickness of the Galaxy and they probably escape. Hence, cosmic rays at energies above $10^{18}\,\mathrm{eV}$ are considered to be of extragalactic origin[7]. The above described process plays important role especially for bottom-up scenarios in which it modifies energy spectrum as well as composition.

Although prevailing majority of CRs come from the Sun and it is not surprising that their acceleration mechanism is known, principles of UHECRs origin are still subject of discussions and research. Two main principles can be considered - direct acceleration (inductive mechanisms) by strong electric field or diffusive mechanisms. Direct acceleration hardly produces power-law energy spectrum.

Astrophysical objects capable to accelerate particles up to the end of cosmic ray spectrum (according to the current knowledge $\sim 10^{20}\,\mathrm{eV}$) must be extremely large and, of course, must emit tremendous large amount of energy (brief estimation can be found e.g. in [48, 7]).

Particles with energies below the approximate limit of $10^{17} - 10^{18}\,\mathrm{eV}$ can be produced by supernovae as one of the assumed cosmic accelerators. There are still discussions about the maximum energy reachable by processes caused by supernova remnants (SNR) which will be described later in this chapter. However, supernova shock waves are likely the most possible accelerator site for galactic cosmic rays. The more general principle of diffusive shock acceleration including also SNR acceleration mechanism will be described in the following section.

Stochastic acceleration mechanism of charged particles encountering interstellar cloud with turbulent magnetic field moving in a specific direction was originally proposed by Enrico Fermi [49]. Let us assume that mass of the cloud is much bigger than the one of the particle moving towards the velocity of the cloud v_c (see Fig. 2.17). Particle enters the cloud with opposite direction of cloud velocity v_c in the laboratory frame. Multiple scatterings in the cloud are elastic and the magnetic cloud deflects original particle in the reversed direction gaining the energy (assuming velocity vectors before and after scatterings to have the same direction as v_c)[8]:

$$\frac{\Delta E}{E} = \frac{E_1 - E_0}{E_0} = \gamma_c^2(1 + \beta_c^2) - 1, \tag{2.6}$$

where E_0 and E_1 are energies of particle in the laboratory system before and after interactions with magnetic cloud and β_c is the cloud velocity in the units

[7]The radius of curvature r of a proton with energy $10^{20}\,\mathrm{eV}$ for a galactic magnetic field of $3 \times 10^{-10}\,\mathrm{T} = 3\,\mu\mathrm{G}$ is $r = 10^{21}\,\mathrm{m} = 36\,\mathrm{kpc}$. Taking into account typical thickness 0.3 kpc of galactic disc, one can conclude the the magnetic deflection of such proton would be only $\sim 0.5°$.

[8]There are also configurations in which particle gains no energy or losses some energy

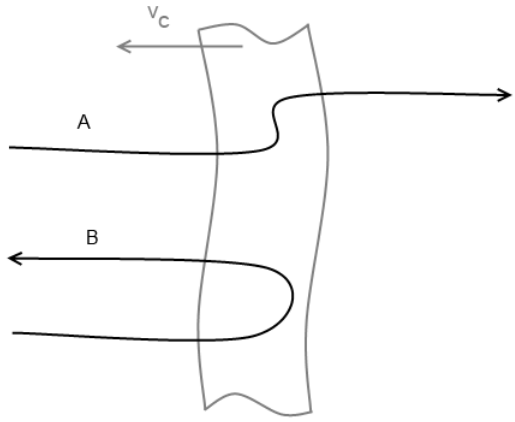

Figure 2.17: Schematic figure of Fermi's acceleration mechanism. Particle moving towards the magnetic cloud cannot be accelerated in the scenario A, but elastic collisions can change the initial direction to the opposite and collinear to v_c gaining particle energy (B).

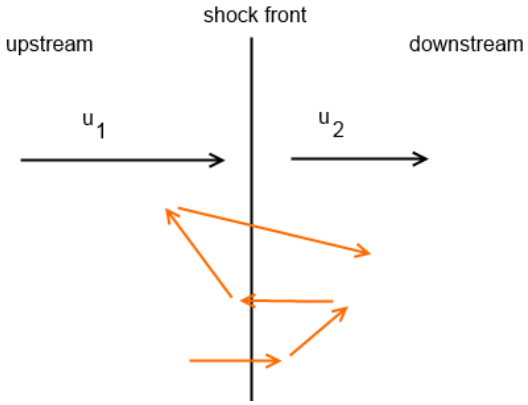

Figure 2.18: Acceleration mechanism in shock wave based on the repeated moving of a particle from upstream to downstream (red lines) gaining the energy that is proportional to difference $u_1 - u_2$, that is to the first order or relative velocity of plasma flow.

of c. The real energy gain depends very strongly on the angle between vectors of entering velocity and the exit velocity[9], therefore it is called the second-order Fermi acceleration.

This process ensures constant fractional energy gain per magnetic cloud encounter. However the β_c^2 dependence and sparse occurrence of magnetic clouds makes this acceleration very slow. Nevertheless, the probability that particle escapes the region of magnetic cloud before multiple scattering leads to power law energy spectrum. Maximum energy attainable by diffusive mechanism is commonly set between 10^{17} and 10^{18} eV.

The more efficient mechanism of particle acceleration is very similar and relies also on magnetized plasma and shock waves that are conditions in most astrophysical environments (e.g. expanding supernova remnants). Diffusive mechanism of acceleration of charged particles occurs in relatively widespread shock waves resulting in first-order Fermi acceleration. Stochastic process (described e.g. in [50]) is based on repeated scattering of fast particles around shock front in magnetic irregularities. This process also (as well as the previous one) results in power law energy spectrum in a natural way. The schematic picture of the acceleration mechanisms is in Fig. 2.18 seen from the shock frame. The shock runs ahead with velocity u_1 and this is also the velocity of which upstream (unshocked) matter flows into the shock in its frame. Downstream matter always move from the shock with velocity u_2. Particle that enters the shock front from the upstream side flows cross the shock

[9]Taking into account isotropic multiple scattering one can calculate that the average energy gain follows $\Delta E/E \approx 4/3\,\beta_c^2$

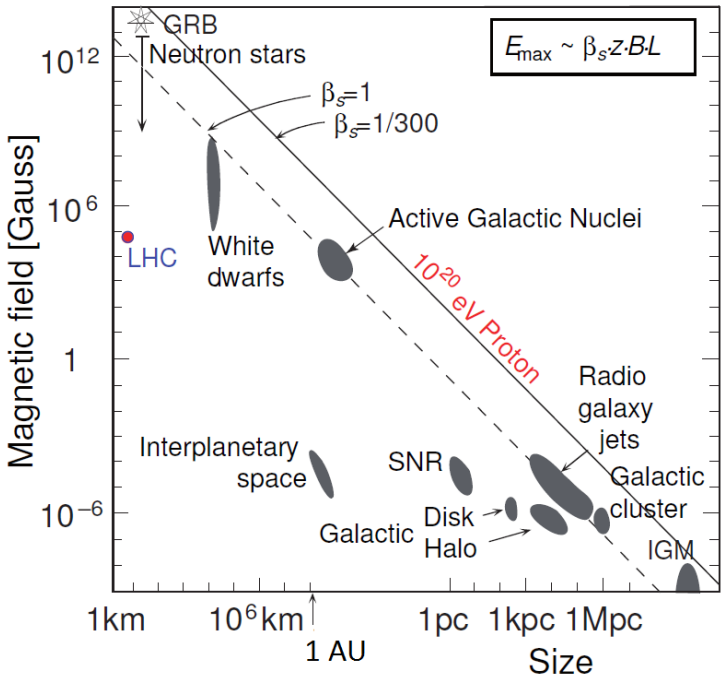

Figure 2.19: Hillas plot showing possible astrophysical accelerators from the point of view of relation between accelerator size and magnetic field. Solid line indicates limits for acceleration of proton at 10^{20} eV for non-relativistic shock front. Dashed line represents the same limit for a relativistic accelerator (adopted from [41]). Objects below lines cannot be candidates for UHECR particle sources.

front and it moves downstream. This particle can be elastically scattered back to upstream (the downstream particles are isotropized). This process can be repeated until the particle escapes the shock region, otherwise it can continue during the whole lifetime of the shock front. Energy gain per one transition is proportional to first order of relative plasma velocity $\beta_s = u_1 - u_2$. This makes the process much faster and obviously more efficient than stochastic second-order Fermi acceleration process.

The maximum energy attainable by the source with magnetic field B and of linear dimension R follows:

$$E_{max} \sim \beta Z \, B[\mu\mathrm{G}] \, R[\mathrm{kpc}] \;\; \mathrm{EeV}. \tag{2.7}$$

Widely known Hillas plot of astrophysical objects showing their size and magnetic field is depicted in Fig. 2.19 indicating capability of their acceleration. Solid line corresponds to the size-magnetic strength limit of acceleration source needed to boost proton to 10^{20} eV for non-relativistic objects. Some of possible galactic or even extragalactic accelerators are listed briefly in the following paragraphs:

- **SNR** is considered as the most likely galactic cosmic ray accelerator working on the described above principle of diffusive shock wave mechanisms. It can be shown that several supernovae explosions per century produce enough

energy to replenish cosmic rays in the Galaxy. Let's assume that the average age of particle in the Galaxy before leakage is 5×10^6 years (as derived in the previous section 2.3). 30 Supernovae of 10 solar masses[10] expanding with velocity 5×10^6 m s^{-2} can keep the cosmic ray density $\rho_E \approx 0,5\,\mathrm{eV/cm^3}$. Such SNRs would produce 3×10^{42} erg/s which is enough assuming acceleration efficiency of about 1%.

- **Neutron stars and pulsars** are UHECR galactic accelerator candidates. They are characterized by extremely high magnetic fields. Acceleration mechanisms involved in these objects are not stochastic, but rather magnetohydrodynamics or direct acceleration by strong electrostatic field is involved in these objects. Young neutron stars rotate with fraction of second period which forms conditions to boost particle to ultrahigh energies.

- **Active galactic nuclei** (AGN) are active objects in the core of some galaxies. Supermassive black hole in its center with accretion disc of matter rotating around the center powers the AGN. There are two jets emitting particles in the opposite directions. The central region with magnetic field that can reach values of 5 G is capable to contain particle up to 10^{20} eV, however energy losses can make it difficult to escape this region.

- **Radio galaxies**, especially so called *hot spots* of giant radio galaxies are remarkable objects that are hot candidates for UHECR sources. They are characterized by two jets of particle emission and a gigantic shock wave coming from the central part of the galaxy (therefore *hot spots* term is used) which is able to accelerate protons to energies up to $\approx 10^{21}$ eV.

- **Gamma-ray bursts** (GRBs) are ones of the most extreme energetic phenomena observable in the Universe. They are detected by outbursts of gamma-ray in $\mathrm{MeV} - \mathrm{GeV}$ energy region lasting from fraction of seconds to hundreds of seconds. Current measurements of GRBs cosmological distances raised doubts about possible source of UHECRs. Average redshift of GRBs is $z = 1$ which suggests that GRBs are so distant that they cannot contribute to UHERCs with energy above 10^{19} eV [7].

2.4.2 Propagation of cosmic rays

Acceleration mechanisms described in the previous section naturally lead to specific energy spectrum of particles at sources. In spite of that, spectrum of cosmic rays detected on the Earth can be influenced by processes that occur on the way from sources to detectors.

Particles traveling through galaxies and intergalactic space can interact with interstellar matter or photons or they can be deflected by magnetic field.

[10] it corresponds to supernova explosion rate in our Galaxy

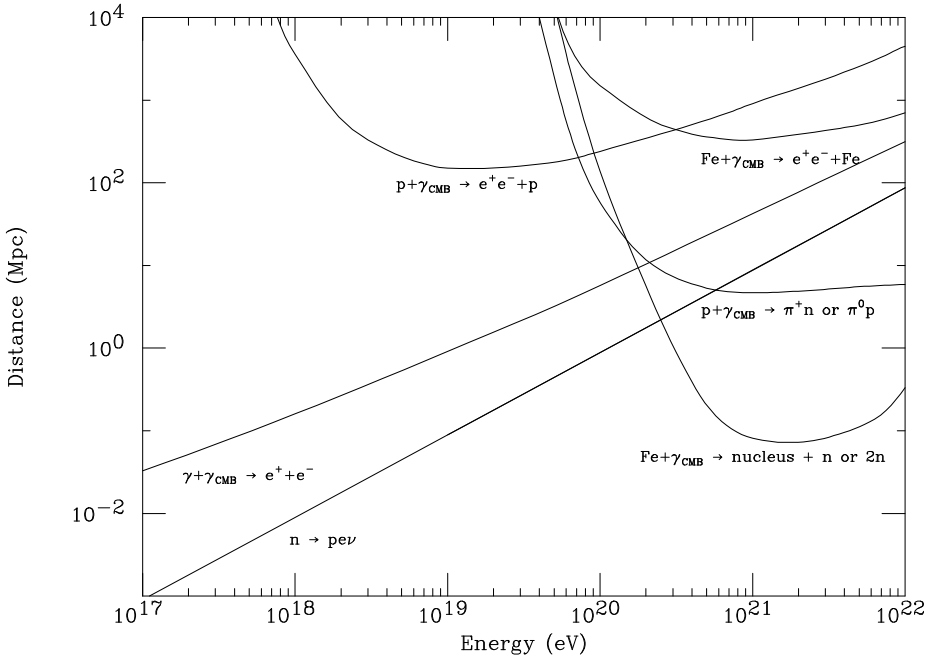

Figure 2.20: Mean free paths for particular interactions of CRs (protons, iron nuclei and photons) with CMB photons. There is also depicted a mean decay length for neutrons. The figure is adopted from [53].

Neutrinos as particles that suffer from only weak interaction[11] and bring no charge naturally point to their sources. To the contrary, flux of protons, nuclei and even photons is attenuated by various interactions.

Particles with energies below a limit (depending on the charge and mass) $\sim 10^{17} - 10^{18}\,\mathrm{eV}$ are confined by magnetic field in the Galaxy and can suffer from interactions with e.g. interstellar matter. Such assumption can be confirmed by direct measurement of cosmic ray composition at $\sim$ GeV energies. At this energy range cosmic ray composition is comparable to the abundance of elements in the solar system (see section 2.3 and Fig. 2.15). This signifies that only particles with enough energy $E \gg 10^{18}\,\mathrm{eV}$ can carry relevant direction information.

While interactions of CRs with interstellar matter has the highest probability in galaxies, energy losses of cosmic rays due to electromagnetic interactions, in particular with cosmic microwave background (CMB) radiation, infra-red or radio background radiation become important along the whole way from sources to the Earth since radiation fills the whole Universe. In 1966 it had not passed much time

[11]The probability of interaction is extremely small.

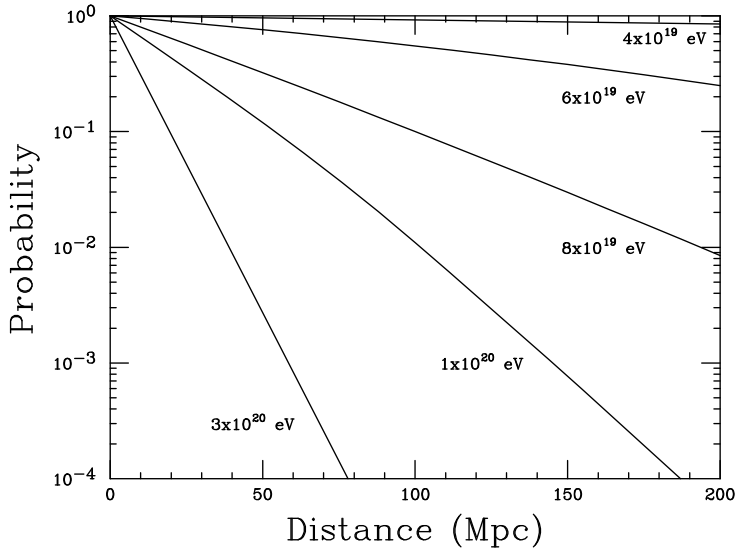

Figure 2.21: Probability of protons that they originate from source at distance greater or equal to that distance on x-axis. Values are calculated under assumption of source spectrum proportional to $E^{2.5}$. Adopted from [53].

from the discovery of CMB by Pensias and Wilson when it was predicted that the Universe becomes opaque for protons above energies of about several $10^{19}\,\mathrm{eV}$ by Greisen [51], Zatsepin and Kuzmin [52] due to photo-pion production. Interactions of CRs with CMB should cause fall-off in the energy spectrum known as GZK cu-off which is indicated also in data (see e.g. Fig. 2.7 where one can observe turn beyond $6 \times 10^{19}\,\mathrm{eV}$). CMB has blackbody thermal energy spectrum characterized by an average temperature of $T = 2.725\,\mathrm{K}$ and total photon density $\rho \sim 400\,\mathrm{cm}^{-3}$.

Protons lose energy by photo-pion production reactions that proceed through a $\Delta^+(1232)$ resonance:

$$p + \gamma_{CMB} \longrightarrow \Delta^+(1232) \begin{cases} \longrightarrow \Delta^+ \longrightarrow n + \pi^+ \\ \longrightarrow \Delta^+ \longrightarrow p + \pi^0 \end{cases} \tag{2.8}$$

with threshold energy $E^{th}_{p+\gamma_{CMB}}$ that corresponds to the minimal energy of proton beyond that the center of mass system of proton and γ_{CMB} has energy greater than the sum of proton and pion masses. Gamma-proton center of mass energy is therefore dependent on the incident angle θ:

$$s = m_p^2 + 2E_p\,E_\gamma(1 - \cos\,\theta). \tag{2.9}$$

Threshold energy can be estimated with typical energy of $\gamma_{CMB} \sim 6 \times 10^{-4}\,\mathrm{eV}$

that corresponds to head-on collision that results in threshold energy as follows:

$$E^{th}_{p+\gamma_{CMB}} \approx 10^{20}\,\mathrm{eV}. \tag{2.10}$$

The real threshold for reactions 2.8 is slightly less ($E^{th}_{p+\gamma_{CMB}} = 4 \times 10^{19}\,\mathrm{eV}$) due to tail of CMB energy spectrum. Proton-photon interaction cross section $\sigma_{p-ph} = 2 \times 10^{-28}\,\mathrm{cm}^2$ at the threshold energy gives mean free path for protons $\lambda = 1/\sigma n \sim 4\,\mathrm{Mpc}$, where $n = 400\,\mathrm{cm}^{-3}$ is CMB density. Typical energy loss is at the level of 20% per interaction [48] which implies that a proton's energy decrease by a factor of ten after 5 interaction lengths. It gives few tens of Mpc which is quite small compared with extragalactic distances.

There is also a pair production process with threshold energy about $10^{18}\,\mathrm{eV}$:

$$p + \gamma_{CMB} \longrightarrow p + e^+ + e^-. \tag{2.11}$$

The mean free path for the above stated interaction (2.11) is $\sim 1\,\mathrm{Mpc}$. Typicall energy loss is only $\sim 0.1\%$ and therefore it becomes less significant in comparison with the interactions 2.8.

Protons can lose their energy also by inverse Compton scattering which has no significant influence as the given cross section is proportional to the inverse value of center-of-mass energy.

Pair creation is important in the case of cosmic gamma rays interaction (of course, they are not deflected by magnetic field) with CMB above threshold energy of $4 \times 10^{14}\,\mathrm{eV}$:

$$\gamma + \gamma_{CMB} \longrightarrow e^+ + e^-. \tag{2.12}$$

Analogically to interactions 2.8 and 2.11 heavy nuclei of mass A will suffer from CMB interaction that produces $e^+ + e^-$ pairs and nucleons (photodisintegration):

$$A + \gamma_{CMB} \begin{cases} \longrightarrow (A-1) + N \\ \longrightarrow (A-2) + 2N \\ \longrightarrow A + e^+ + e^- \end{cases} \tag{2.13}$$

Mean free paths for specific interactions (and mean decay length for neutrons) are depicted in Fig. 2.20. Statistically UHECR loses $1/e$ of its energy when it travels one mean free path and simultaneously it is the mean value of distances between two interactions. Assuming specific energy spectrum (in this case $E^{2.5}$) one can calculate the probability that a particle of energy E comes from the distance greater than a given value. This plot for proton and several energies is depicted in Fig. 2.21.

Interactions of proton with CMB decrease its energy as was described above. Energy development of proton with diverse primary energies depending on traveled distance is shown in Fig. 2.22. There are three lines corresponding to three initial energies of $10^{20}, 10^{21}, 10^{22}\,\mathrm{eV}$. After traveling of about more than 100 Mpc energies of all three protons fall to the same value.

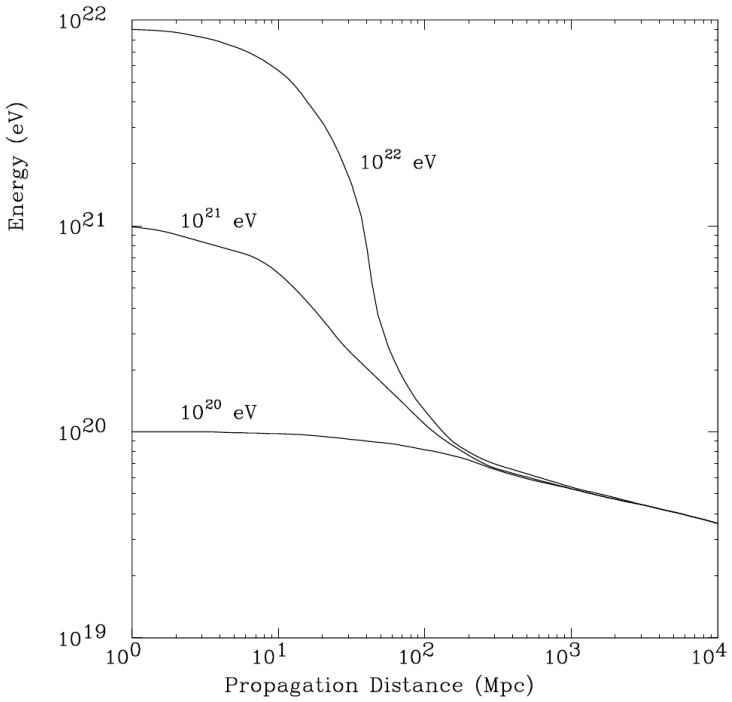

Figure 2.22: Energy decrease of a proton due to interactions with CMB for various primary energies. Adopted from [54].

2.5 Extensive air showers

Cosmic rays as high energy projectiles interact with air nuclei in the atmosphere. Collisions lead to fragmentation of the target nuclei with high energy remnants and new secondary particles. Subsequent processes follow resulting in cascade of interactions called Extensive Air Shower (EAS). The typical first interaction appears at the altitude $20 - 30\,\mathrm{km}$ and it is statistically determined by the interaction cross section[12]. Number of secondary particles increases very rapidly as the EAS develops and average energy of particles decreases. There are large number of charged particles that ionize air and excite nitrogen molecules. De-excitation process is accompanied by light emission that is observable by fluorescence detectors. When the energy of produced particles (or fragments) drops below some threshold and their energy is not sufficient to produce new particles, number of secondary particles is maximal. The position of that significant point, X_{max}, is commonly measured by fluorescence detectors in $\mathrm{g\,cm^{-2}}$. X denotes atmospheric depth, that is the integral density above the observation level at altitude h

$$X(h) = \int_h^\infty \rho(z)dz, \tag{2.14}$$

[12]The primary particle energy and its type are the main decisive factors for particle-air cross section.

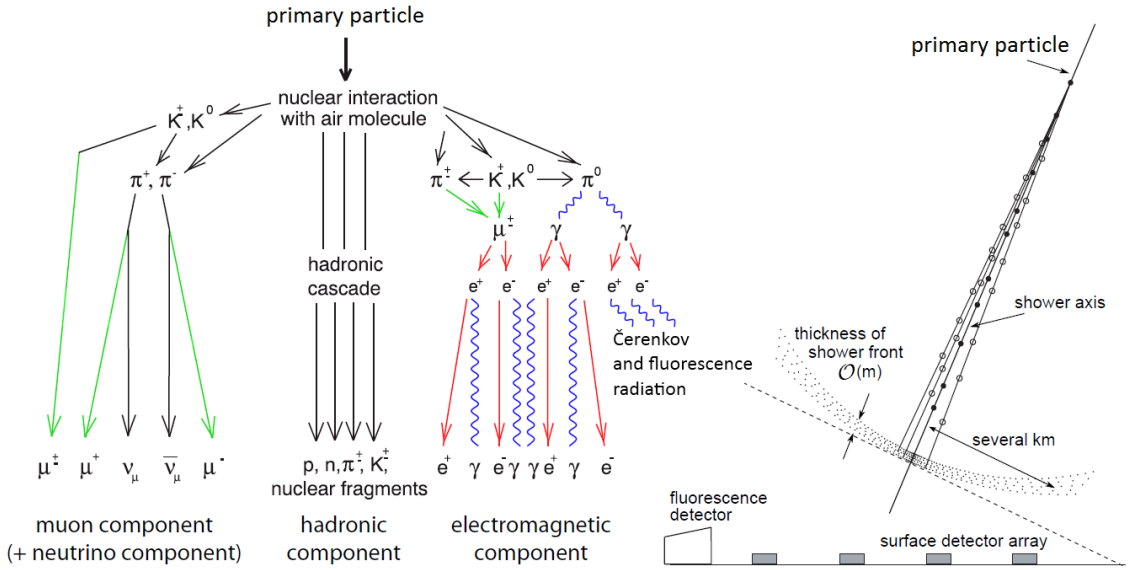

Figure 2.23: Main processes of primary cosmic ray interactions are shown in left figure. Muonic, hadronic and electromagnetic components are formed in EAS. Air shower is sketched on the right with curvature of the shower front, shower axis coincides with the primary particle direction. Adopted from [36] and [55].

in other words it expresses the amount of matter above the observation level h. It represents the crucial parameter for elementary interactions as well as cross section. The vertical integral density of atmosphere is approximately $1000\,\mathrm{g\,cm^{-2}}$. Primaries that enter into the atmosphere with zenith angle θ (see the right part of Fig. 2.23) measured from the vertical direction induce inclined showers. The thickness that particles traverse in these showers increases as $1/cos\,\theta$ for flat atmosphere approximation that is assumed for $\theta < 60°$. For larger θ one has to take into account atmosphere curvature. In the most extreme case of horizontal shower particles can traverse as large of amount of matter as $36\,000\,\mathrm{g\,cm^{-2}}$

The amount of matter that particle traverses through determines interaction probability and therefore a ratio of decays and interactions can be derived. Since the density of the atmosphere varies with the altitude, temperature and pressure, the knowledge of $\rho(h)$ at the moment of measurement is essential. The atmospheric depth variation with altitude is usually fitted by equation (e.g. in CORSIKA simulation program [28]):

$$X(h) = a_i + b_i e^{-h/c_i}, \tag{2.15}$$

where parameters a_i, b_i and c_i are fitted for several layers[13].

The shower front is slightly curved (see the right Fig. 2.23) and one can observe non-zero thickness of the shower envelope. Hardly interacting muons on shower front move at speed of light, while electrons are slightly lagged and they are part of electromagnetic hallo of typical thickness of the order of 1 m. The delay of

[13]There are usually 4 layers treated in described way, while the last (the highest - at the top of the atmosphere) fifth layer is modeled according to the equation $X(h) = a_5 - b_5 h/c_5$

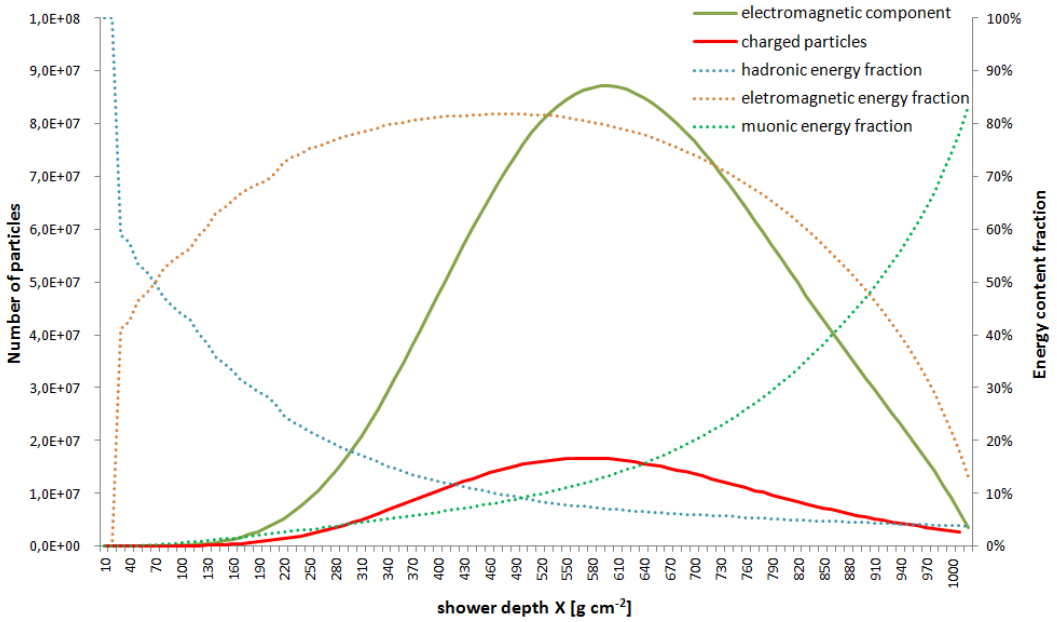

Figure 2.24: Number of particles (left axis) in proton induced of primary energy 10^{19} eV air shower as simulated by CORSIKA program is depicted by full lines. Muons and hadrons are omitted due to their small number in comparison with electromagnetic component. Energy content fraction (right axis) in particle groups is illustrated by dotted lines.

electromagnetic particles is caused by multiple scattering.

Secondaries of EAS are classified by particle type and their interactions. In left part of the Fig. 2.23 the extensive air shower components are illustrated. Interaction cascade distributes energy into four groups - hadronic, electromagnetic, muonic and neutrino component. Moreover, the energy flows significantly from hadronic component into the three others. Hadron primaries cause hadronic interactions. More than half of the energy of incident hadron is transformed into new particles generation. Production of mesons and baryons is followed by subsequent interactions or decays. The most frequent mesons are pions that decay into muons, electrons, photons and neutrinos. About 1/3 of all produced pions are π^0 that decay into 2 photons with probability of 0.988. Even the second decay mode leads to photon and electron-positron pair $\pi^0 \longrightarrow \gamma + e^- + e^+$. π^0 production causes that large fraction of energy is quickly transferred into electromagnetic component. Pions are most frequent mesons (about 90 %) and therefore hadronic component loses approximately 1/3 of energy in each step. An example of longitudinal development of number of particles in EAS differentiated according to particle type is depicted in Fig. 2.24. The illustration of particle tracks for an inclined shower is shown in Fig. 2.25.

The electromagnetic component comprising gammas, electrons and positrons are the most populated. Gammas produced by π^0 feed the electromagnetic cascade. High energy photons predominantly interact via $e^+ + e^-$ pair production and electrons and positrons via bremsstrahlung radiation. *Interaction length* λ and *ra-*

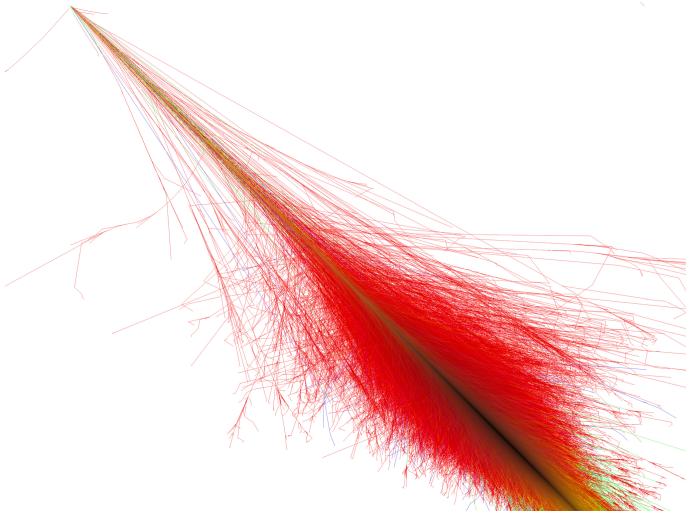

Figure 2.25: CORSIKA simulation of proton shower development with primary energy of 10^{19} eV. Electrons, positrons and photons are depicted by red color, muons and hadrons are green and blue, respectively [56].

diation length X_0 parametrizes mentioned processes. Radiation length of electrons in air has value of $X_0 = 36.7\mathrm{g\,cm^{-2}}$ [14]. Radiation length for electrons is the mean atmospheric depth after which it losses $1/e$ of its energy by bremmstrahlung. The energy loss of high energy electrons are described by equation

$$E(X) = E_0\, e^{-X/X_0}, \tag{2.16}$$

where E_0 is the initial electron energy. As mentioned above, electrons lose their energy by bremsstrahlung and ionization which is dominant below so called *critical energy* that is equal to $E_c = 85\,\mathrm{MeV}$ for air. The critical energy is defined as energy at which ionization and bremsstrahlung loss rates are equal.

Interaction that dominates for high energy photons is pair production. The mean free path for pair production λ_{pair} is related to radiation length X_0: $\lambda_{pair} = 9/7\, X_0$. Photon intensity I after passage of material depth X with initial values of I_0 and mean free path (or attenuation length) λ is calculated as $I = I_0\, e^{-X/\lambda}$.

The thickness of the atmosphere can be expressed in radiation length for photons and electrons in air which is about $\approx 27\, X_0$. Proton interaction length λ_p in air is approximately $90\,\mathrm{g\,cm^{-2}}$ [15] which means that the atmospheric column density corresponds to ≈ 11 nuclear interaction lengths.

Muons are highly penetrating and hardly interacting (in comparison with electrons and photons) particles. They are indisputably very important part of the air showers as their fluctuations are smaller and they can penetrate hundreds of

[14] For material of atomic number A and proton number Z the radiation length X_0 can be approximately calculated as follows $X_0 = \frac{716.4\, A}{Z(Z+1)\, ln(287/\sqrt{Z})}\,\mathrm{g\,cm^{-2}}$.

[15] Mean free path λ is defined as the mean distance between two interactions. It can be calculated as inverse value of product of number of nuclei with mass A per 1 gram of the matter the particle traverses through and the interaction cross section, i.e. $\lambda = A/(N_A\, \sigma)$.

meters of rock under the ground. Section 5 is dedicated to muonic component of air shower.

Beside air shower components that were described above there are also UV photons and Čerenkov photons. Relativistic particles of velocity βc larger than velocity of light in the medium (i.e. air in case of EAS) emit coherent Čerenkov light. The light is radiated in forward direction, the angle θ between particle direction and light emission depends on particle velocity:

$$cos\,\theta = \frac{1}{\beta n}, \tag{2.17}$$

where n is the refractive index of medium. The threshold for Čerenkov radiation (and thus for equation 2.17) is given by condition $\beta > 1/n$, this corresponds to energy $E_e = 21\,\mathrm{MeV}$ for electrons and positrons and $E_\mu = 4.3\,\mathrm{GeV}$[16]. There are special types of devices IACT that were described above based on Čerenkov light detection. The amount of light that is typically in the region between blue and ultraviolet wavelengths is proportional to the number of electrons. Charged particles traversing through air also deposit their energy into the atmosphere by molecule excitation. Part of this energy is promptly re-emitted in the form of fluorescence light by nitrogen molecules which is seen by fluorescence detectors and the longitudinal shower profile can be directly measured.

There are also neutrino particles and high energy muons that belong to the 'invisible' part of the shower. Some fraction of the primary particle energy is dumped into particles in various processes and they do not significantly dissipate energy into atmosphere as electrons and positrons do. Therefore this fraction of energy is called *missing*.

Most common particles in the EAS are pions $\pi^\pm$, π^0, electrons and positrons $e^\pm$, protons p, kaons $K^\pm$, K^0_L, K^0_S, muons $\mu^\pm$ and neutrons n which are characterized by different decay lengths. For such relativistic particles with velocity βc the decay length increases according to $\lambda_{dec} = \gamma\beta c\tau$. Comparison of decay length λ_{dec} and interaction length λ_{int} determines if the particle interacts and produces sub-shower or decays.

2.5.1 Heitler model of the particle cascade

A simplified, but very illustrative model of particle cascade that can describe its basic characteristics was developed by W. Heitler [57]. First model considered electromagnetic particles, nevertheless basic principles can be adopted in an analogous manner to hadronic part. The next section explains original Heitler's model of electromagnetic cascade which is followed by analogous hadronic shower model both exhibiting good predictions for various EAS parameters.

[16] Air ground level refractive index $n = 0.0003$ is assumed.

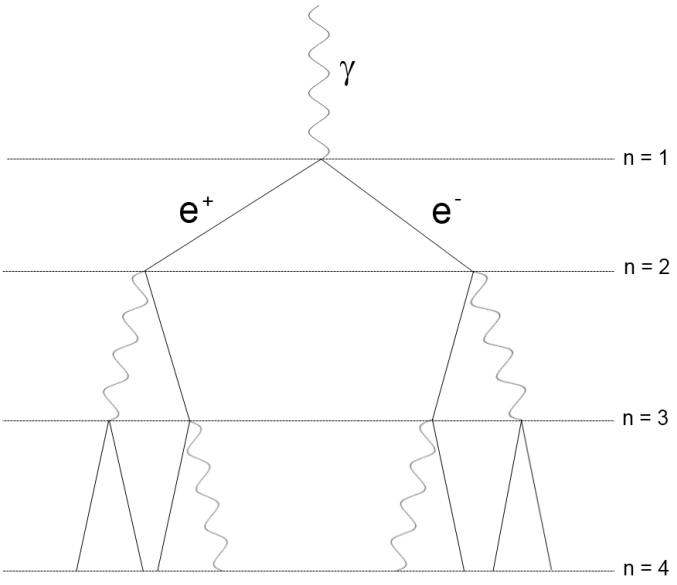

Figure 2.26: Electromagnetic cascade in Heiler model's approximation. In each step n photons produce $e^{\pm}$ pairs after they traversed mean free path and electrons and positrons dilute their energy by bremsstrahlung.

Electromagnetic cascade

In Fig. 2.26 Heitler's approximation of electromagnetic cascade is depicted. It assumes photon or electron (electrons denote in this section both electrons and positrons) initiated shower developing via pair production and bremsstrahlung processes[17]. Shower develops in regular steps when particles travel distance $\lambda_{em} = \ln 2\, X_0$. Each particle splits into two daughter ones each of them has half of the mother particle energy. In the n-th step of the shower the total number of particles is 2^n and each of these particle has energy $E_0/2^n$, where E_0 is the primary particle energy. Number of particles in atmospheric depth X can be expressed as $N(X) = 2^{\frac{X}{\lambda_{em}}}$. Shower development stops when the particle energy is smaller then the critical energy ξ_c^e when the ionization becomes dominant and particles start to be absorbed in the atmosphere. It gives automatically maximum number of particles

$$N_{max} = \frac{E_0}{\xi_c^e} \tag{2.18}$$

and the depth of the shower maximum

$$X_{max} = \lambda_{em}\, \log_2 \left(\frac{E_0}{\xi_c^e} \right). \tag{2.19}$$

Two last equations represent the most significant features of Heitler's model, i.e. number of particles N_{max} at shower maximum X_{max} is proportional to the primary particle energy E_0, while X_{max} increases logarithmically with energy E_0.

[17]Electron energy loss can be described as $\frac{dE}{dX} = -a(E) - \frac{E}{\lambda_{rad}}$, where the first term logarithmically increases with energy and the second one is the radiation term.

Assuming the relation between λ_{em} and X_0 the shower maximum is given by $X_{max} = X_0 \ln(E_0/\xi_c^e)$. Taking into account particle energy distribution the equation is modified to $X_{max} \approx (ln(E_0/\xi_c^e) + 1/2)$ [37]. The elongation rate D_{10} can be derived from the equation 2.19:

$$D_{10} = \ln(10)\, X_0 \approx 85\,\mathrm{g\,cm^{-2}} \tag{2.20}$$

While Heitler's model predicts fairly well the position of the shower maxium X_{max}, it overestimates total number of electrons in comparison to the number of photons. Moreover, electromagnetic size N_{max} predicted by Heitler's model differs from the measured data. Instead the ratio of electrons to total electromagnetic size $N_e/N_{max} \approx 2/3$ as the model predicts, number of electrons is approximately by a factor of 10 times smaller than N_{max} predicted by Heitler model, therefore a factor $g \approx 10$ is introduced for quantifying number of electrons:

$$N_e = \frac{N_{max}}{g}. \tag{2.21}$$

Hadronic cascade

Hadronic primary particle induces hadronic shower which can be described by a similar model to the one introduced in the previous paragraphs. The model is based on the assumption that particles interact in steps of scale interaction length λ_{int}, which is mean free path for inelastic nuclear interaction. As stated in [58] the value of λ_{int}^{π} for pions is in a fairly good approximation constant in the energy range $10 - 1000\,\mathrm{GeV}$ as follows: $\lambda_{int}^{\pi} \approx 120\,\mathrm{g\,cm^{-2}}$. Analogically to Heitler model, particle splitting occurs after the length of $\ln 2\lambda_{int}^{\pi} \approx 83\,\mathrm{g\,cm^{-2}}$. Hadronic showers contain significant number of highly penetrating muons, while muons in electromagnetic showers are very rare. Characteristics of hadronic interactions and the $\lambda_{int} > X_0$ are reasons that shower-to-shower fluctuations[18] are larger than for electromagnetic part of the shower.

The description of hadronic cascade follows in the rest of this section [59]. It is assumed that primary particle with energy E_0 undergoes successive hadronic interactions after each n_π number of pions are produced. One third of n_π is neutral pions that immediately decay into two photons and in that way this energy fraction is transfered into electromagnetic shower. Two thirds of all produced pions are charged ones, $(2/3\, n_\pi \equiv n_{ch})$, that undergo next hadronic interactions. Each of particles that is born in the interaction has the same energy, that is $E_0/(n_\pi)^n$ in the n-th step. Interaction process continues till the step when energy of charged pions falls below critical energy ξ_c^π after that pions decay into muons and (anti)neutrinos. Shower reaches therefore the maximum in n_{max}-th step for which one gets

$$n_{max} = \frac{1}{\ln(n_\pi)} \ln\left(\frac{E_0}{\xi_c^\pi}\right). \tag{2.22}$$

[18] EAS characteristics vary from shower to shower even when all other parameters are kept fixed - arrival direction, primary energy and particle type.

In each splitting step a fraction of energy is gone from pions (hadronic shower) and therefore after n step the total energy in hadronic shower E_{had} is

$$E_{had} = \left(\frac{2}{3}\right)^n E_0 \tag{2.23}$$

and the average charged pion energy E_π in the n-th step of the shower follows:

$$E_{\pi,n} = \frac{E_0}{(3/2\, n_{ch})^n} \tag{2.24}$$

After pions reach the critical energy ξ_c^π they begin to decay into muons and pion production ceases. The number of muons is supposed to be the same as the maximum number of pions:

$$\ln n_\mu = \ln(n_{ch})^{n_{max}} = n_{max}\, \ln\left(n_{ch}\right). \tag{2.25}$$

By using equation 2.22 one gets:

$$n_\mu = \left(\frac{E_0}{\xi_c^\pi}\right)^\alpha \tag{2.26}$$

with $\alpha = \ln\left(n_{ch}\right) / \ln\left(3/2\, n_{ch}\right) \approx 0.9$ [37]. Multiplicity n_{ch} of charged particles (π-nucleon collisions multiplicity) is comparable to that one of pp or $p\bar{p}$ [19]. Therefore the value of 10 can be adopted as stated in *A Heitler model of extensive air showers* [59]. This value is in appropriate accuracy in the pion energy regions from 1 GeV to 10 TeV. The pion critical energy ξ_c^π for the condition of shower initiated by proton with $E = 10^{15}$ eV can be approximated by 20 GeV and electron critical energy $\xi_c^e = 85$ MeV [59].

Incorporating results from electromagnetic shower model a primary energy can be expressed by means of number of electromagnetic particles N_{max} and number of muons n_μ. The energy is distributed into two components and in analogy to equation 2.18 and taking into account 2.21 [59]:

$$E_0 = \xi_c^e\, N_{max} + \xi_c^\pi\, n_\mu = g\, \xi_c^e \left(N_e + \frac{\xi_c^\pi}{g \xi_c^e}\right) \approx 0.85\,\text{GeV}\ \left(N_e + 24\, n_\mu\right). \tag{2.27}$$

The relations above suggest the primary energy can be calculated from measured number of electrons and muons. On the other hand, the relation between primary energy and number of muons is not linear (this is caused because part of shower energy is transfered continuously between hadronic and electromagnetic components) as follows from the equation 2.26:

$$n_\mu \approx 10^4 \left(\frac{E_0}{1\,\text{PeV}}\right)^{0.85}. \tag{2.28}$$

Nuclear primaries can be incorporated into the above stated considerations by means of the superposition model. It assumes that a nucleus of mass A with total energy E_0 can be viewed as superposition of A individual nucleon showers. The substitution $E_0 \to E_0/A$ can be used. Also a leading particle effect can be introduced in the model as in [59].

[19] pp collision multiplicity increases very slowly as $E^{1/5}$.

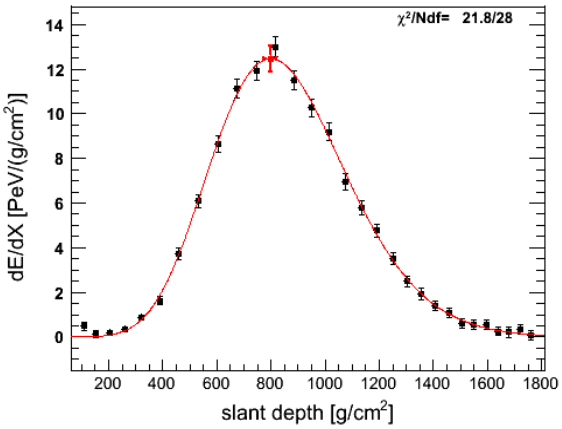

Figure 2.27: Observed shower profile as measured by fluorescence detector of the Pierre Auger Observatory. Solid line is the Gaisser-Hillas function fit. The energy of the shower was $(8.57 \pm 0.29 \pm 0.13) \times 10^{18}$ eV.

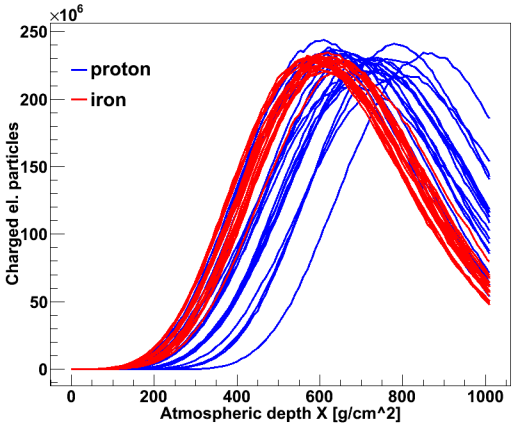

Figure 2.28: Shower profile developments as simulated by CORSIKA program. There are 20 proton primary showers with energy $E = 10^{19}$ eV (blue line) and 20 showers with iron primaries of the same energy (red line).

2.5.2 Longitudinal shower profile

Number of particles changes as the shower develops in the atmosphere. In the previous section there is a simple air shower model that predicts how particles are created until the critical energy of particles is reached at X_{max}. Longitudinal shower profile describes number of particles as a function of atmospheric depth X. Sometimes the term 'shower size' is used meaning total number of charged particles integrated over all energy. The shower size can be effectively identified with number of electrons.

Simulation of longitudinal shower profile (number of charged particles) by CORSIKA program can be seen in Fig. 2.28. There are 20 iron showers (red lines) with primary energy of $E = 10^{19}$ eV and 20 proton showers (blue lines) with the same energy. Proton showers are characterized by large fluctuations in penetrating through the atmosphere. X_{max} fluctuations are quite small for iron and it becomes larger as the primary mass A decreases. $RMS(X_{max})$ describing X_{max} fluctuations is a sensitive parameter for composition measure. Nevertheless, the mixture of cosmic ray primaries makes interpretation of $RMS(X_{max})$ difficult.

Longitudinal shower profile can be measured by experimental instruments - such as photomultipliers collecting light in specific wavelength ranges. Charged particles traversing the atmosphere excite nitrogen molecules that subsequently radiate isotropically fluorescence light in the ultraviolet spectrum. The amount of light is proportional to the energy deposited in the air. The measurement principle will be described in more details in the section 2.6.2. In the Fig. 2.27 the longitudinal shower profile is depicted as measured by Pierre Auger Observatory.

Parametrization of the number of charged particles (longitudinal shower profile)

has been derived by Greisen [60] (this can be also found in [61]) as follows:

$$N_e(E_0, t) = \frac{0.31}{\sqrt{y}} \exp\left[t\left(1 - \frac{3}{2}\ln(\chi)\right)\right], \tag{2.29}$$

where y stands for $y = \ln(E_0/\xi_c^e)$, t is atmospheric depth in units of radiation lengths $t = X/X_0$ and χ is phenomenological parameter called *shower age* that is defined as

$$\chi = \frac{3X}{X + 2X_{max}}. \tag{2.30}$$

The last parameter introduced in the section 2.30 is closely connected with 'shower universality' according to that all showers of hadronic primaries which have the same age χ have the same electron and photon energy spectra (and angular distributions) [61].

The following function proposed by Gaisser and Hillas [62] is commonly used to fit number of charged particles:

$$N_e(X) = N_{max}\left(\frac{X - X_0}{X_{max} - X_0}\right)^{\frac{X_{max}-X_0}{\lambda}} e^{\frac{X_{max}-X}{\lambda}}. \tag{2.31}$$

In the superposition approximation (mentioned at the end of the last subsection) the position of X_{max} can be derived as it is shown in [59]

$$X_{max} = X_{max}^p - \lambda_{em}\,\ln(A), \tag{2.32}$$

where X_{max}^p depends on the first interaction position X_0 and the primary energy E_0:

$$X_{max}^p = X_0 + \lambda_{em}\,\ln\left(\frac{E_0}{3\,n_{ch}\,\xi_c^e}\right). \tag{2.33}$$

Taking the two last equations into account one can expect the maximum of the shower induced by a primary particle of mass A to be expressed in the superposition model as follows:

$$X_{max} = c_1\,(\ln(E_0) - \ln(A)) + c_2, \tag{2.34}$$

where constants $c_1 = \lambda_{em}$ and $c_2 = X_0 - \lambda_{em}\ln(3\,n_{ch}\,\xi_c^e)$ define factors of linear relation between $(\ln(E_0) - \ln(A)) = \ln(E_0/A)$ and X_{max}.

2.5.3 Lateral shower profile

Density of charged particles as a function of distance from the shower core is described by lateral shower profile. Each hadronic interaction is characterized by transferred transversal momenta that are given to secondary particles. It causes together with Coulomb scattering the lateral spread of an extensive air shower. Charged particles traversing the atmosphere are scattered on nuclei.

Simulations of charged particles, muons and photons densities by CORSIKA program (with QGSJET and GHEISHA generators) for iron and proton primaries at energy $E = 10^{19}$ eV are shown in Fig. 2.30. Particle densities are depicted for the

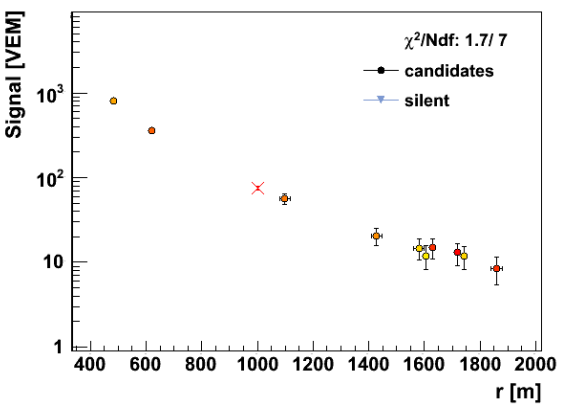

Figure 2.29: Measured lateral shower profile by surface detector at Pierre Auger Observatory in the Vertical Equivalent Muon units (VEM). Color of cirles indicates time of arrival (from yellow to red). The energy of the shower was $(1.61 \pm 0.08) \times 10^{19}$ eV.

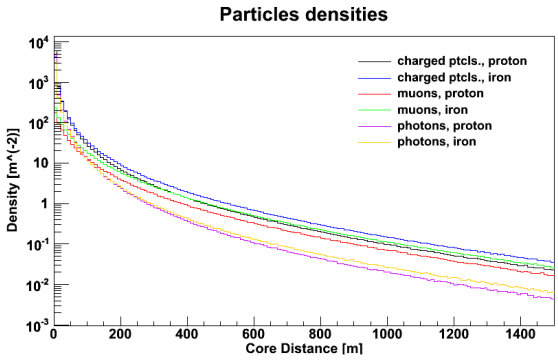

Figure 2.30: Simulation of charged particles densities at ground level for Pierre Auger Observatory conditions by CORSIKA program at primary energies $E = 10^{19}$ eV. Charged particles, muons and photons densities for proton primary are depicted by black, red and violet, respectively. Blue, green and orange lines depict charged particles, muons and photons densities for iron shower.

altitude above the sea level at Pierre Auger Observatory (1420 m a.s.l.). Energy cut-off used for hadrons and muons is 0.3 GeV, while energy cut-off 0.003 GeV was used for electrons and photons.

Lateral distribution of charged particles can be measured by surface detector, or rather it measures sample of charged particle density (see the next section 2.6.1). In the Fig. 2.29 there is a water Čerenkov surface detector measurement of charged particle density in units of vertical equivalent muons per m^2 as a function of a distance from the shower core.

Measured signal $S(r)$ at a distance r from the shower axis is commonly fitted by Nishimura-Kamata-Greisen distribution [63][20]:

$$S(r) = k \left(\frac{r}{r_0}\right)^{-\alpha} \left(1 + \frac{r}{r_0}\right)^{-(\eta-\alpha)} , \tag{2.35}$$

where r_0 is the Molière radius. In fact, the detector response $S(r)$ measures the density of charged particles $n(r)$ by means of the total number of particles N_{tot} proportional to the primary particle energy and calcuated as follows:

$$N_{tot} = \int n(r)\, dr \propto \int S(r)\, dr. \tag{2.36}$$

[20] Offline software used at Pierre Auger Observatory uses slightly modified NKG-like function $f_{NKG}(r) = k \left(\frac{r}{r_{opt}}\right)^{\beta} \left(\frac{r+r_{scale}}{r_{opt}+r_{scale}}\right)^{\beta+\gamma}$ with $f_{NKG}(r_{opt}) = 1$ and $r_{opt} = 1000$ m for standard array and $r_{opt} = 450$ m for the infill array (see section 3.5 for the explanation of the infill array). The value of r_{scale} was chosen to be 700 m for standard as well as the infill arrays.

2.6 Detection methods of ultra-high energy cosmic rays

Primary CRs hitting the Earth's atmosphere interact with air molecules and fragment at the top of the atmosphere. The secondary particles produced in such collision will undergo further hadronic and electromagnetic interactions, ultimately producing an extensive air shower cascade as was described in detail in previous sections. During many decades from discovery of extensive air showers various detection techniques were adopted and developed. All detection methods are based on interaction processes of charged particles or photons. There are interaction processes that predetermine possible detecors. Charged particles lose their energy mainly by ionization which is described by the following well-known Bethe-Bloch formula:

$$-\left\langle \frac{dE}{dx} \right\rangle = Kz^2 \frac{Z}{A} \frac{1}{\beta^2} \left[\frac{1}{2} ln \frac{2m_e c^2 \beta^2 \gamma^2 T_{max}}{I^2} - \beta^2 - \frac{\delta}{2} \right], \tag{2.37}$$

where $K = 4\pi N_A r_e^2 m_e c^2$ is among others product of Avogadro's number N_A, classical electron radius r_e and electron rest mass m_e. z, β is charge and velocity of incident particle, respectively and Z and A are charge and mass number of the target. T_{max} is maximum energy transfer to an electron, I is average ionization energy of the target and δ is correction. Ionization is an important process that is measured by gas detectors. Molecule excitation process is naturally connected to energy measurement of EAS using the atmosphere as the calorimeter. Čerenkov radiation is directly used in imaging air Čerenkov detectors and in water Čerenkov tanks.

There are two possible types of CR detection – direct and indirect methods. Direct methods can be performed by means of satellites and balloons catching primary particles, but cannot effectively measure CR at energies larger than 10^{14-15} eV because of small statistics (Eq. 2.2). On the other hand indirect methods require sufficient primary particle energy ($E \gtrsim 10^{15}$) eV to develop shower and large detector area is necessary. Indirect methods are based on the measurement of secondary particles that reach the ground in array of Čerenkov detectors, scintillators or muon detectors or on the collection of the isotropic fluorescence light emitted by excited nitrogen molecules.

There are currently two types of detection principles used to detect EAS (cartoon of air shower development and its detection is depicted in Fig. 2.31). First of them originated from Auger's idea of coincidence measurement by group of counters. This method is based on interactions of secondary particles in detectors deployed on the ground across a large area. Ground array counters sample secondary particles of EAS and significant parameters of primary cosmic ray can be inferred. Particles penetrating underground are of particular importance not only for EAS study, but also for neutrino astronomy. Layer of Earth or rock is used as shielding for muon counters (see Fig. 2.31). The other method collects light emitted by processes in the atmosphere caused by secondary particles. It includes fluorescence detectors which collect light emitted by excited nitrogen molecules and IACT (some

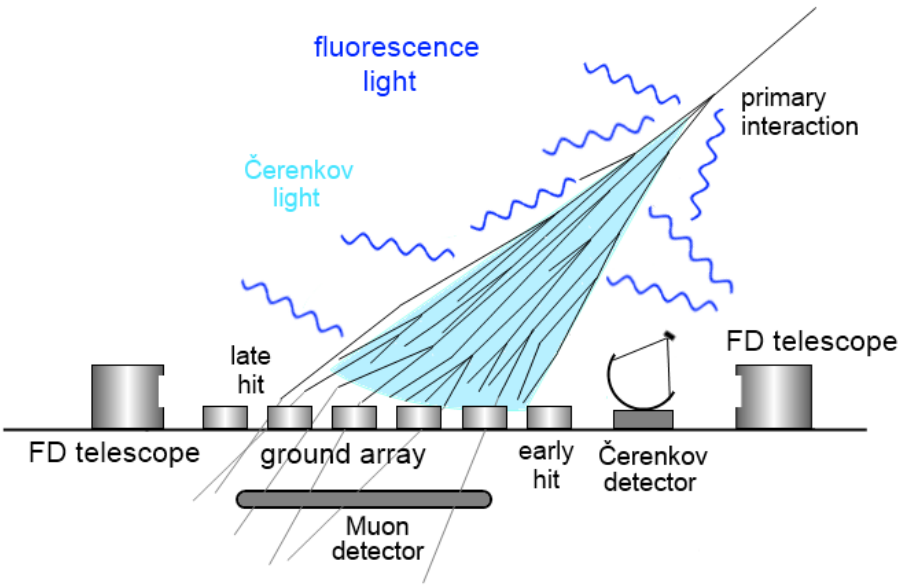

Figure 2.31: Measurement techniques used for EAS detection. Ground array of detectors samples lateral distribution of charged particles that reach the ground level. Fluorescence light is collected by telescopes overviewing the ground array which enables to detect longitudinal shower profile. Čerenkov light is collected by system of mirrors and photomultipliers. Underground detectors serve as muon counters.

of current experiments with IACT were mentioned in section 2.1.1 usually used for gamma-ray detection) collecting Čerenkov light produced by electrons. Čerenkov light is emitted in a narrow cone along to shower axis (hundreds of meters) which requires very close positions of IACTs to the shower axis.

A completely new approach is being developed during several recent years - radio detection technique that uses arrays of antennas sensitive to electron and positron synchrotron radiation emitted due to magnetic deflection in the atmosphere. Electrons and positrons are bent in the opposite directions by geomagnetic field as they propagate in EAS through the atmosphere. Synchrotron radiation at frequencies less than 100 MHz is emitted by electric dipole of electrons and positrons.

Combination of different detection techniques called *hybrid measurement* is used to achieve more accurate results.

Two types of EAS detection arrangements will be described in the following sections putting emphasis on the water Čerenkov arrays and fluorescence detectors.

2.6.1 Ground arrays

Secondary particles of EAS can reach the ground level and they are spread over substantial area. Array of ground detectors represents the most generic type of surface measurement device. Detectors are arranged in a regular structure. They are separated at a distance d typically of order hundreds of meters from each

other. They typically measure density of particles on which they are sensitive such as charged particles - electrons, hadrons, muons or photons.

Ground array measures signals from particular detectors in time sequence. Preferred altitude for surface detector arrays depends on the pursued energy range. It is convenient to locate ground array at altitude where the shower maximum occurs for studied energy in order to minimize relative shower fluctuations. EAS can spread over hundreds of m^2 to tens of km^2 at observation level. Therefore spacing between UHECR detectors is usually $\gtrsim 1\,\mathrm{km}$. Ground arrays are usually composed of scintillators that indicate charged particles or tanks filled with water working as Čerenkov counters. While scintillators are sensitive to all charged particles and they detect mainly electromagnetic component of EAS, Čerenkov counters obtain much stronger signal from muons and therefore they are more appropriate to detection of very inclined showers characterized by mostly muon signal at observation level. Each station detects the shower front arrival time (timing of the signal) and particle density (it corresponds to intensity of the signal).

Typically several stations with different timing data indicate real secondary particle interactions. Signal from at least three non-collinear stations in coincidence has to be detected so that the primary particle direction could be determined [21].

As indicated in Fig. 2.31 there are early and late hits in surface detector stations. Relative timing of detector signals is essential for directional reconstruction, but represents only one of several factors that determine accuracy level of shower geometry estimation. Besides others, higher number of hit stations increases reconstruction precision. Secondary particles of non-vertical showers at ground level can spread over much larger extent (approximately proportional to $1/(\cos\theta)$) compared to the area of vertical shower (see Fig. 2.31). Therefore, the reconstruction precision naturally relates to the detector area, as experiment of larger extent enables to register early arriving part of the shower. EAS forms a front wave of various thickness. Shower front is very thin near the shower axis and it increases axially (from a few nanoseconds to microseconds in time units). In first approximation it is assumed to have a planar geometry moving at the velocity of speed of light. After shower core is estimated realistic geometry of shower front wave is incorporated. Angular resolution of primary particle direction measured by giant surface detector array reaches $\sim 1^\circ$.

To estimate incident CR energy a signal at a given distance from shower core is measured (or estimated). It can be shown that due to fluctuations a density of shower particle component at larger distance ($\sim$ km represents more appropriate measure than at closer positions.

Surface detector arrays lose efficiency at larger zenith angles, on the other hand it can operate permanently in contrast to fluorescence detectors described in the following section.

[21] In fact the shower is assumed to be axially symmetric up to about 60°. Geometric reconstruction is based on shower axis determination which coincides with incoming primary particle direction.

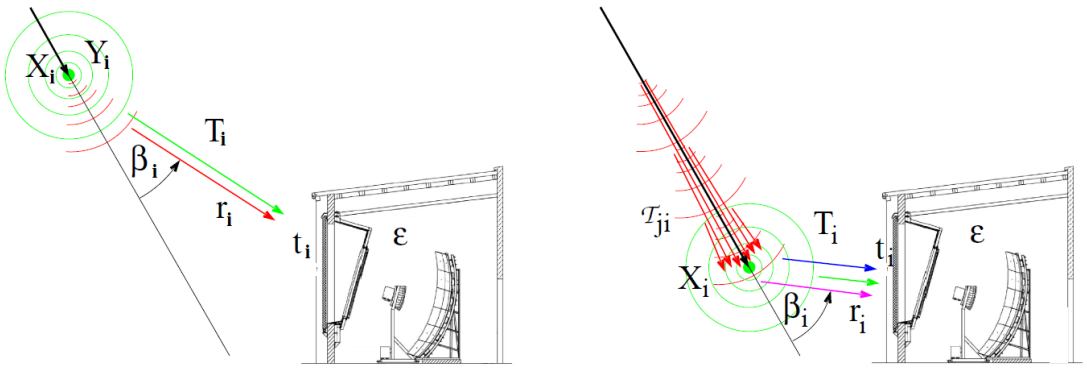

(a) *Direct light contribution.* (b) *Scattered light contribution.*

Figure 2.32: Light collection by fluorescence detectors (adopted from [64]). Isotropic fluorescence light is depicted by green color, red lines represent direct Čerenkov light, blue and magenta draw Rayleigh scattered and Mie scattered Čerenkov light.

2.6.2 Fluorescence detectors

Isotropic emission of ultraviolet fluorescence light stems from about 4 photons radiation per meter passed by a charged particle and it is detectable by means of photo-sensitive detectors at energies above $\simeq 10^{18}$ eV of the primary CR. The detector usually consists of mirror system with photomultipliers placed in a chamber with closable aperture and filter which enables to protect photomultipliers from background light and adverse weather conditions.

Only during clear moonless nights fluorescence telescopes can be operated which represents weakness of this technique - at convenient locations their duty cycle is roughly $\approx 13\%$.

Longitudinal shower development can be detected as emitted light is proportional to energy dissipated by charged particles in the atmosphere. As indicated in cartoon of detection techniques Fig. 2.31 EAS particles produce also Čerenkov light and therefore fluorescence telescope collect mixture of the two types of light (see Fig. 2.32).

Shower universality allows to write a relation between total energy deposit dE/dX at atmospheric depth X and number of electrons $N_e(X)$ [64]:

$$dE/dX = N_e(X)\,\alpha_X, \tag{2.38}$$

where α_X is the average energy deposit per electron at shower age χ defined in section 2.30 [22].

Fluorescence detectors are usually composed of photomultipliers playing role of particular pixels in the focal plane of the mirror. It enables to observe air shower

[22] α_X is calculated as energy integral over normalized electron energy distribution multiplied by energy loss of a single electron. However, fluorescence yield does not depend on the energy of exciting particle.

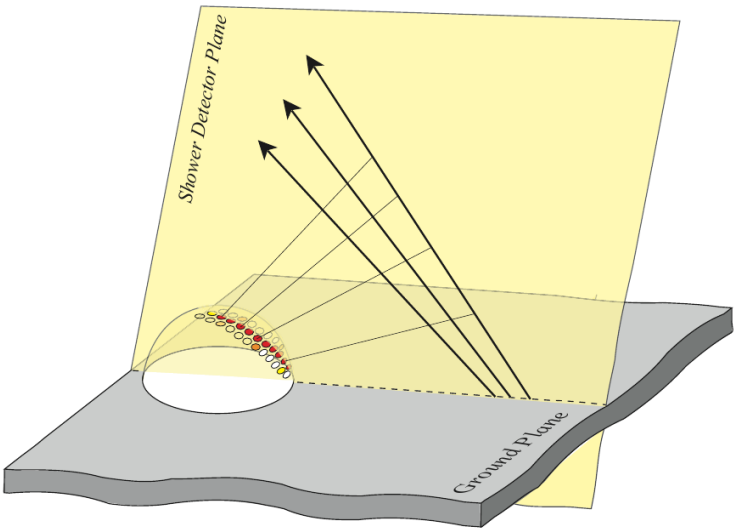

Figure 2.33: Shower detector plane and signal registered by FD telescope (adopted from [65]).

profile and to determine the shower detector plane. Together with relative timing measured by particular photomultiplier position, the shower axis can be determined as indicated in Fig. 2.33.

PMTs signal intensity corresponds to shower energy as described above (see e.g. Fig. 2.27). The following function proposed by Gaisser and Hillas [62] is commonly used to fit measured profiles by EAS reconstruction software such as Offline[23] [64, 66]:

$$f_{GH}(X) = \frac{dE}{dX_{max}} \left(\frac{X - X_0}{X_{max} - X_0} \right)^{\frac{X_{max}-X_0}{\lambda}} e^{\frac{X_{max}-X}{\lambda}} \tag{2.39}$$

From the integral over the energy deposit profile one can obtain the total energy deposited by air shower:

$$E_{cal} = \int_0^\infty f_{GH}(X)\, dX, \tag{2.40}$$

The primary energy (better to say *electromagnetic* energy) is determined as follows

$$E_{em} = 2.2\,\mathrm{MeV}/(\mathrm{g/cm}^2) \int_0^\infty N_e(X)\, dX, \tag{2.41}$$

which corresponds to the fraction of energy carried by particles causing fluorescence. In order to obtain the total energy of the arrival particle one has to add *missing energy* carried by muons and neutrinos. Depending on primary mass and interaction model the fraction of *missing energy* is about $\lesssim 10\%$.

[23] Offline is standard EAS reconstruction (and simulation) software used at Pierre Auger Observatory.

Fluorescence telescope measurement requires continuous atmospheric condition monitor since fluorescence yield and light propagation are dependent on humidity, pressure, temperature and overall weather conditions.

Reconstructed energy uncertainty is dominated by the absolute FD calibration it reaches $\sim 14\%$ at Pierre Auger Observatory experiment (a significant improvement has been made as the quoted energy uncertainty reached 22% until recently) [67]. Brief description of uncertainties that affect energy scale is listed in section 3.2.3.

Chapter 3

The Pierre Auger Observatory

The Pierre Auger Observatory [68] is a facility studying UHECRs operated by a large international collaboration. The original intention was to build two separated sites called *Auger South* and *Auger North* in both southern and northern hemispheres to cover the whole sky.

Auger South was completed in July 2008 and with its area of over 3000 km^2 it is the world's largest astrophysical instrument studying UHECRs. The observatory is located in province Mendoza in Argentina near the city Malargüe (69° W, 35° S, 1420 m a.s.l.) which allows among other things to observe the Galactic Center. The Pierre Auger collaboration includes 490 scientists from 18 countries and 100 institutions[1]. The Czech Republic significantly participates in the collaboration through following institutions: Institute of Physics of the AS CR, Faculty of Mathematics and Physics at Charles University from Prague and Palacký University in Olomouc.

The unique design of the observatory incorporates two detection techniques. It combines two independent and complementary detector types: Surface Detector (SD) which is composed of 1600 water Čerenkov stations and Fluorescence Detector (FD) which comprises 27 fluorescence telescopes. The ingenious approach allows to observe extensive air showers simultaneously by both type of detectors. This enables to cross-check measurements. It produces other benefits like improved angular resolution, specification of detector uncertainties, increase of measurement sensitivity, etc.. The most important advantage of such approach is the ability to carry out the energy calibration of the SD. The fluorescence telescopes observe the longitudinal shower profile by collecting the ultraviolet light emitted along the charged particles path. Such calorimetric measurement is almost model independent.

The layout of the southern site detectors is shown in Fig. 3.1. There is a picture of one SD station and an FD building in Fig. 3.2. SD stations are autonomous detectors with its own battery and GPS antena (for more details see Sec. 3.1) and they are deployed on a triangular grid with 1.5 km spacing. SD operation is almost unaffected by weather conditions and it has nearly 100% duty cycle (see Sec. 3.1). On the other hand the FD has duty cycle of $\approx 13\%$ [69] and its acceptance depends

[1] Current state in April 2013

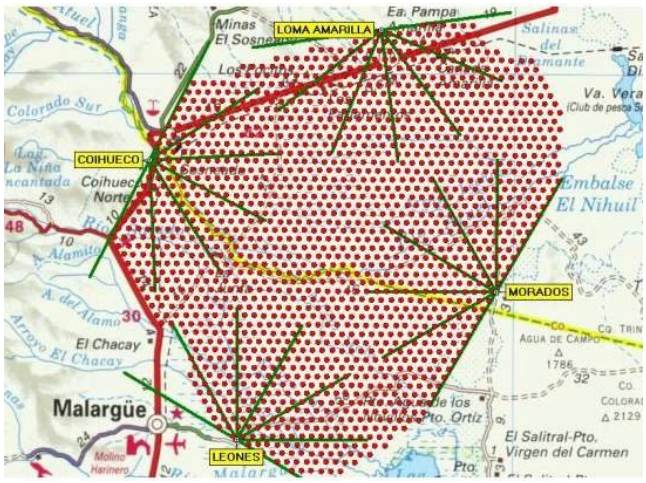

Figure 3.1: The detector layout of the Pierre Auger Observatory. Red dots indicate SD stations which are overviewed by 4 FD buildings. There are 6 fluorescence telescopes in each building. Green lines indicate field of view of each telescope.

Figure 3.2: A picture of an SD station and FD building. Each station has its own solar panel with battery and communication antenna. There is also the antenna close to the nearby the FD building.

on the atmospheric conditions (see Sec. 3.2).

The Pierre Auger Observatory was designed to measure UHECRs with energy above $\sim 10^{18}$ eV. However, there is also a low energy extension of SD stations based on additional surface detector deployment among original array with plastic scintillators beneath the tanks to detect muons (AMIGA [70]).

Therese is also extension of fluorescence detectors by set of 3 telescopes with high elevation called HEAT [70] (see Sec. 3.5). An extensive program of atmospheric monitoring is the essential part of the Observatory not only to control uncertainties concerning FD.

3.1 Surface Detector

The surface detector system (described in [71]) is an experimental device that consists of group of self-contained units. An array of currently more than 1600 water Čerenkov stations (the standard detector array of 1600 stations is depicted in Fig. 3.1, the section 3.5 refers to its enhancement) is characterized by almost 100% duty cycle. The array has roughly shape of a hexagon with another detectors and devices placed inside or on its edge (cf. figures Fig. 3.1 and Fig. 3.2). The schematic drawing of one station is shown in Fig. 3.3. The SD station [72] is a water Čerekov tank designed and constructed on the base of experiences obtained by previous experiment using similar type of detectors (Haverah Park Array [73]).

SD stations deployed into regular triangular grid with 1500 m spacing which forms a large ground detector array. Many secondary charged particles of a shower reach the ground level with enough energy to produce Čerekov light while moving

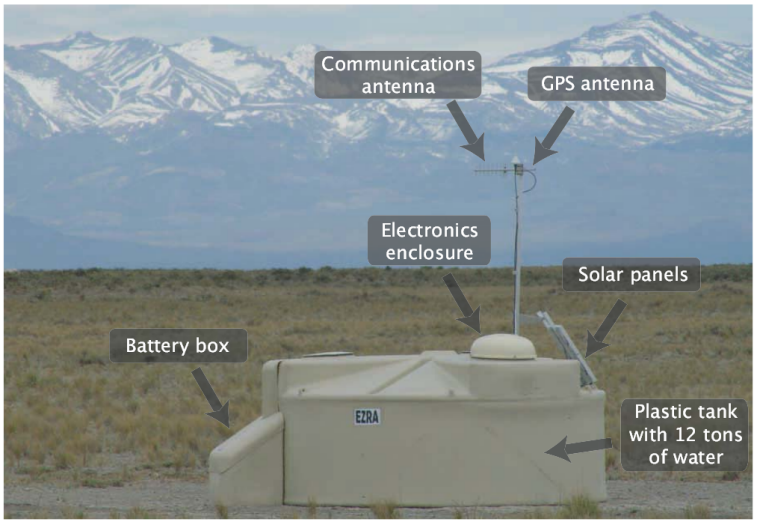

Figure 3.3: The SD water Čerenkov station drawing. Each tank is an autonomous detector with its own solar panel, battery, communication and GPS antennas. There are three photomultipliers inside the 12 m^3 of pure water (adapted from [65].

through water with refraction index of 1.33 (see Sec. 2.6.1). By measuring signals from surface detectors the lateral distribution function of charged particles can be derived that is the charged particle density. This is the starting and essential point of shower energy and core determination [2]. The array is designed to have full trigger efficiency for CR of energy above 3×10^{18} eV. Experiment altitude assures that surface array samples particle distribution close to shower maximum development at $\sim 10^{19}$ eV.

Lateral distribution of charged particles sampled by SD array is found to fit well the Nishimura-Kamata-Greisen function [63] describing particle density $S(r)$ at a distance r:

$$S(r) = k \left(\frac{r}{r_0}\right)^{-\alpha} \left(1 + \frac{r}{r_0}\right)^{-(\eta-\alpha)} , \tag{3.1}$$

where r_0 is the Molière radius which defines the region of 95% of shower energy, k is the scale factor and α and η are parameters determined from data.

The Offline reconstruction software employs the NGK-like function to fit SD signal according to the following function

$$S(r) = S_{1000}(E, A, \theta) \left(\frac{r}{r_{opt}}\right)^{\beta(\theta)} \left(\frac{r + r_{scale}}{r_{opt} + r_{scale}}\right)^{\beta(\theta)+\gamma} , \tag{3.2}$$

where $r_{opt} = 1000$ m and $r_{scale} = 700$ m and $S_{1000}(E, A, \theta)$ is SD energy estimator.

Each SD station [72] is a cylindrical plastic tank with radius of 1.8 m filled with 12 m^3 of purified water as a medium for Čerenkov light emission. Emitted photons inside the tank by going-through charged parcticles are reflected by inner

[2] In case only surface detector signal is available; shower energy and core can be also determined by only fluorescence telescope measurements.

Tyvek liner and collected by three 9-inch Photonis XP1805PA/1 photomultipliers (PMTs) (see Fig. 3.3). Autonomous operation of each SD station is ensured by two 12 V batteries and a solar panel that charges batteries during the day. The power consumption is quite constant at the value of 10 W.

HV module, which is protected from humidity determines the final gain that can be adjusted and it is of the order of 10^5. Signals from PMTs are read out from the anode and the last dynode, the latter is amplified by a factor of 32 [74]. Raw signal is filtered and digitized at 40 MHz by Flash Analog Digital Converters (FADCs) (2 per one PMT). Combined signal from both FADCs of one PMT provides the dynamical range from a few to 10^5 photoelectrons digitized into 10 bits. The wide measurement range allows to detect particle fluxes near the shower core ($\sim 1000\,\mu s^{-1}$) and in the region of marginal particle flux ($\sim\ 1\,\mu s^{-1}$). Therefore, a signal bin is of size of 25 ns and its value is referred to in units of channels ranging from 0 to 1023. Precise timing of each SD station is obtained by a Motorola GPS receiver that synchronizes the internal 100 MHz clock. GPS also verifies and gives accuracy to station positions. Calibration, communication, local data acquisition (monitoring) and trigger issues are provided by a micro-controller (80 MHz power PC).

In principle, electromagnetic and muonic component can be distinguished in the SD signal. In general, muons produce narrow and high-value peaks which are followed by large number of smaller pulses of electromagnetic particles coming a little bit later.

768 FADC bins are read out and stored when an event is triggered (see Subsec. 3.1.1). The data is temporarily stored in a memory block and available to be sent to the closest FD station and then to the Central Data Acquisition System (CDAS) in Malargüe by a wireless communication equipment. Measured monitoring data (battery voltage, water temperature,...) is send every 10 minutes in the same way to the CDAS. PMT linearity is also monitored by means of LED flasher placed in each SD station.

The majority of recorded EAS is detected by the SD array due to continuous operation and large detector area which provides the aperture of $7350\,\mathrm{km}^2\mathrm{sr}$ for zenith angles smaller than 60°. Atmospheric conditions (humidity, temperature and pressure) affect detector sensitivity. Fluctuations are measurable by event rates and modulations are at the level of 12% (2%) for seasonal (daily) scales [75, 76].

3.1.1 SD trigger system

Overall detected signals from SD stations cannot be recorded due to enormous data storage requirements. Signal traces of each SD station are temporarily stored in a short time buffer. Trigger system ensures rejection of background flux and noise seen as e.g. random coincidences. Trigger system of surface detector has three levels called T1, T2 and T3 [77]. Two first levels are implemented on the level of SD station. In case signal meets conditions of T1 and T2, so called *candidate* station ID and trigger time are send to CDAS. T3 is an array (central) trigger which combines T2 triggers from different stations at CDAS searching for compact

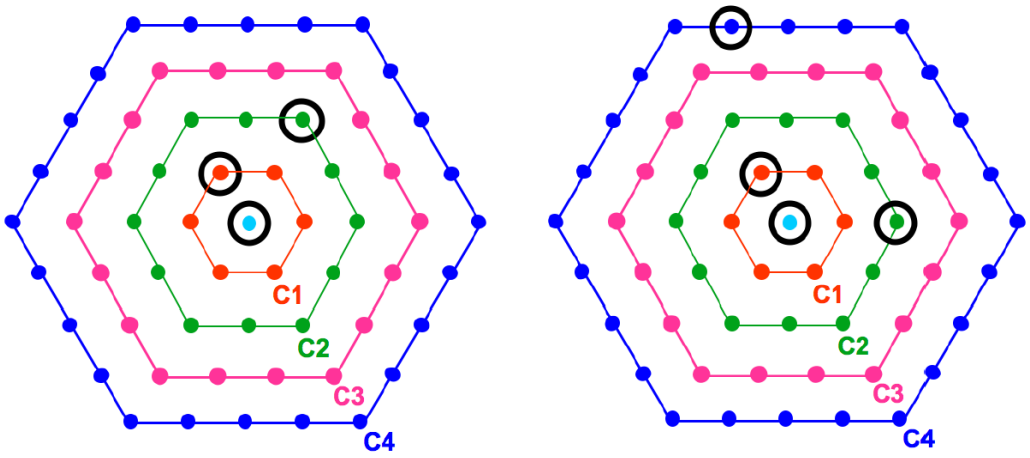

Figure 3.4: Example of central T3 triggers (adopted from [77]).

pattern in time coincidence. When correlated signal is recognized CDAS emits T3 trigger and signal traces are read out from SD stations. T1 and T2 trigger rates of stations are also monitored at CDAS to determine the SD exposure. Following items describe particular trigger levels in details:

- **T1** station level trigger selects strong enough signal at each station and T1 triggers are stored for 10 seconds. T1 works in two different modes detecting electromagnetic and muonic components of air showers. The *Threshold* mode (TH-T1) requires signal higher than 1.75 VEM from all PMTs in coincidence. Consequently TH-T1 should reduce signal rate from $\sim$ 3 kHz to $\sim$ 100 Hz. The second mode, so called *Time-over-Threshold* (ToT) trigger detects electromagnetic component of low energy nearby showers or signals very distant from shower core. It requires a higher signal than 0.2 VEM in 13 bins (corresponding to $>$ 325 ns) detected simultaneously in at least 2 PMTs in a sliding window of 3 μs.

  ToT-T1 trigger is automatically considered as T2 trigger, while TH-T1 trigger is tested to pass through T2 condition. ToT rate is about 2 Hz due to muon background.

- **T2** trigger is of *Threshold* type. TH-T2 triggers are those TH-T1s with signal exceeding threshold 3.2 VEM for all 3 PMTs [3]. TH-T2 results in signal rate reduction to about $\sim$ 20 Hz which allows T2 data to be continuously sent to CDAS where they are analyzed and coincidence pattern signal through detector array is searched for. TH-T2 varies only very slightly over the whole array when compared to ToT trigger which is very sensitive to the local detector characteristics (e.g. reflective liner).

- **T3** central trigger is implemented in CDAS. Compact T2 trigger configuration is searched in 50 μs sliding window. FADC signals are read out after T3

[3] For stations with only two (one) PMTs in operational mode thresholds are set to 2 VEM (2.8 VEM) for TH-T1 and to 3.8 VEM (4.5 VEM) for TH-T2.

trigger is raised for T2 triggered stations and also for T1 triggered stations within 30 μs with respect to T3. Two types of configurations are searched for. The first mode requires 3 ToT triggers in a compact spatial configuration (see left part of the Fig. 3.4). One triggered station has to be in the first hexagon from the central station and the second one has to lie in the second hexagon. Timing criteria are tested after ToT triggers that fulfill spatial conditions. Signal of each ToT trigger that is in n-th hexagon from the central station must be registered within $(6 + 5n)$ μs. This type of trigger is efficient for showers with zenith angle $\theta < 60^\circ$ and 90% of registered signals are real showers. The rate over full array is about 1600 events per day.

The other mode demands four T2 triggers. Two triggered stations have to be in the first two hexagons and the last triggered station has to be found withing first four hexagons (see right part of the Fig. 3.4). This trigger mode is efficient for horizontal showers and about 10% of such T3 triggers are real showers with overall day rate of 1200 triggers.

T3 triggers are generated on-line in the CDAS by a central computer software. Trigger system work ends at the time when data from T2-triggered stations are written into data storage. These data are analysed offline by software applying T4 and T5 triggers rejecting background muon coincidences and events close to border of the detector array.

3.1.2 Signal calibration

Individual conditions of each SD station including among others PMT optical coupling to water, PMT gain and Tyvek liner reflectivity require signal calibration to make measurement independent of such influence. Calibration procedure establishes PMT's high voltages to give an amplification of the last dynode, it sets the signal sizes of each SD station and makes it comparable among each other.

The SD calibration procedures are described in details in [74]. A signal generated by a charged particle going through the water volume has shape of a peak with an exponential fall (the upper right graph in Fig. 3.5). There are two most important quantities related to such pulse - the height of the pulse and the integral of the pulse. Both are proportional to the light generated by particle. The pulse height is equivalent to a current I at the anode and the pulse integral corresponds to the charge Q collected at the PMT anode. The Q turns out to be a more appropriate variable for SD calibration, whereas the trigger threshold is defined as the limit on the peak height I.

A basic quantity for the calibration procedure is a signal produced by a vertical muon going through the center of the tank (VCT). Such signal is denoted as VEM (Vertical Equivalent Muon). The equivalent values of integrated charge for VEM is Q_{VEM} and the equivalent value of the anode current (pulse height) is I_{VEM}. The aim of the calibration is to perform a conversion of 1 VEM signal to digital units (channels). During EAS measurement the signals recorded by tanks are

transformed into units of VEM. Also trigger threshold must be set in station-independent units. Consequently, signals from all tanks can be quantified in units of Q_{VEM}. Then reconstruction of the shower and setting the trigger thresholds is simplified to set properly the quantity I_{VEM}, same procedure for all stations.

Calibration method, i.e. the signal transformation to VEM can be done in two ways (on-line and off-line methods). The on-site computing power limitation and detector remoteness forces the on-line calibration to be as simple as possible. On the other hand the used on-line calibration method must be robust enough to take into account the possibility of PMT failures.

The off-line calibration method is based on the collection of background signal data which are sent every minute to the CDAS. The nature itself offers a lot of probes - atmospheric muons originating from air showers pass through the detectors at reasonable frequency. The rate of omnidirectional atmospheric muons is around $\sim$ 2500 Hz and gives a great opportunity to calibrate the detector. It is not possible to distinguish between vertical and inclined muons traversing the detector. However, the integrated signal from atmospheric muons produces a peak in the charge distribution giving the opportunity to extract VEM signal [78]. The total signal deposited in the tank is measured by the sum of all three PMT's signals, whereas the individual PMT can detect only a part of deposited light. The example of calibration measurement is shown in Fig. 3.5. The position of pulse height peak and charge peak are called I_{VEM}^{peak} and Q_{VEM}^{peak}. The experiment using scintillators placed on the top of a tank and underneath the station [79] shows that Q_{VEM}^{peak} corresponds to 1.09 ± 0.02 VEM for the sum of the signal of all PMT's and 1.03 ± 0.02 VEM for individual PMT measurement. Every minute the following histograms are sent to CDAS to determine the position of Q_{VEM}^{peak}: charge histograms of each individual PMT, charge histogram of the sum of signals from all 3 PMTs, pulse height histograms of each individual PMT, baseline histograms. The interval of 60 s of data collecting produces about 150 000 entries per each histogram. Each real event that is requested to be sent to CDAS is supplied to this set of histograms and therefore it has a high statistics of charge and pulse height distributions.

The off-line calibration estimates the value of I_{VEM}^{peak}, which cannot be determined on-line because that would increase the dead time of the SD above the unacceptable level. The aim of such procedure is to obtain the value I_{VEM}^{est} in electronics units (FADC channels). Therefore the I_{VEM}^{est} cannot be measured directly from histograms due to lack of computing power. The requirement of uniform trigger probability over the whole array is implemented to ensure that SD grid triggers uniformly.

This procedure has several steps. When the SD station is set up and the electronics is turned on for the first time, the gain of each PMTs is adjusted to have a rate of 100 Hz at 150 channels above the baseline. This process adjusts the trigger threshold roughly to $3I_{VEM}^{peak}$, in other words I_{VEM}^{peak} is calibrated to 50 digital channels. The differences of I_{VEM}^{peak} among PMTs decrease below 5 %. However, the influence of variation of conditions (temperature, pressure, water quality,...) causes drifts of the initial values. The on-line compensation via I_{VEM}^{est} determination ensures the trigger rate to be constant. Measurement of trigger rate in the

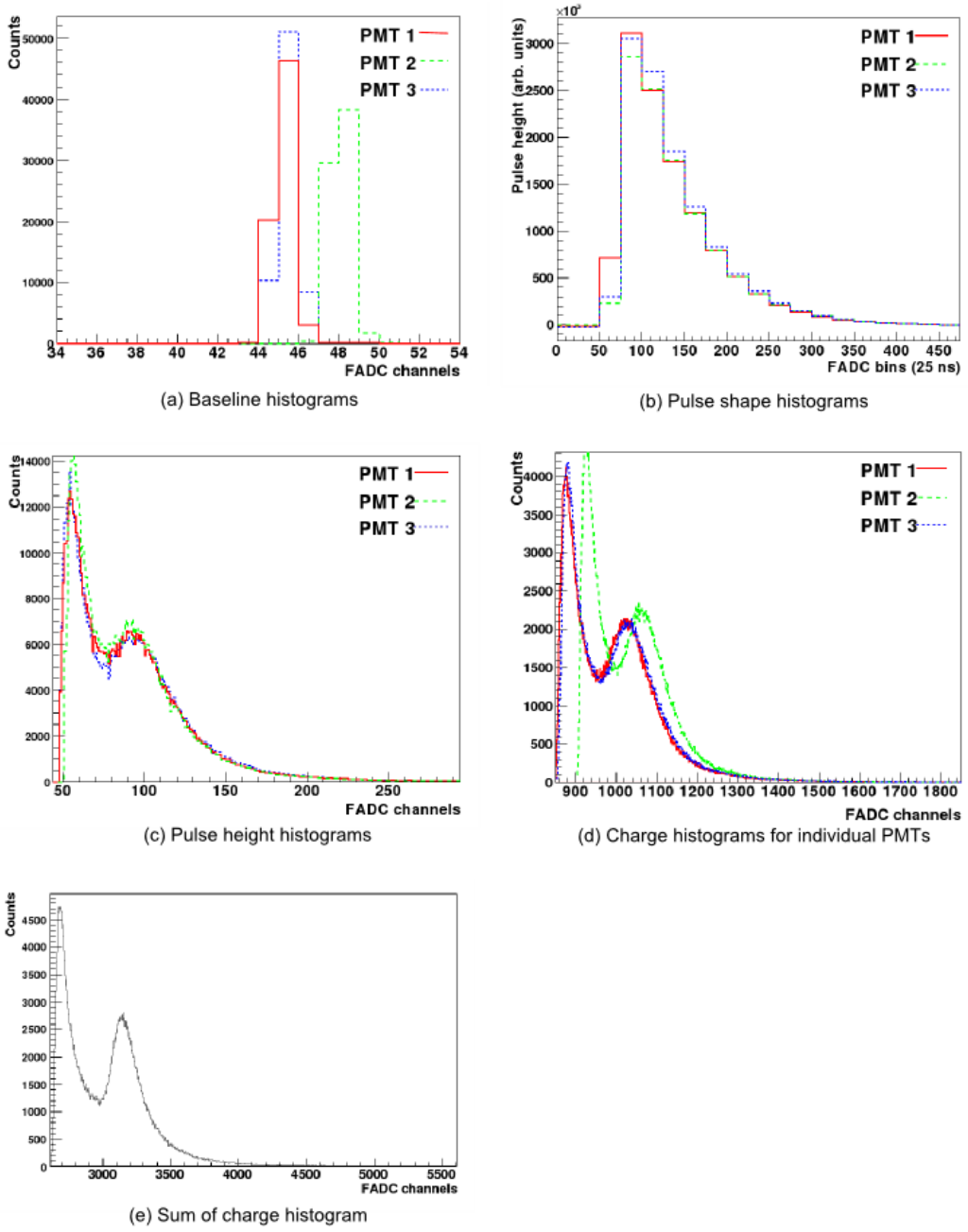

(a) Baseline histograms

(b) Pulse shape histograms

(c) Pulse height histograms

(d) Charge histograms for individual PMTs

(e) Sum of charge histogram

Figure 3.5: Calibration histograms with about 150 000 pulses produced by SD station to perform the calibration. Data are sent to CDAS through the closest FD building with each triggered event (adapted from [74]). There are baseline histograms (a), pulse height histograms, charge histograms (c) and (e) and shapes of the PMT's pulses.

reference tank resulted in the value of 70 Hz when the signal of the PMT is greater than 2.5 I^{est}_{VEM} and signal of all PMTs is greater than 1.75 I^{est}_{VEM}. A convergence algorithm is used to obtain this rate of triggers under the described conditions. 3-fold coincidence events with trigger set to the value of 3.2 I^{est}_{VEM} at all PMTs are looked for to obtain the rate and compare it to the reference value of 20 Hz as a test of success of the algorithm [4]. A direct measurement of I^{peak}_{VEM} from the pulse height histograms gives an opportunity to compare it with a converged value of I^{est}_{VEM}: $I^{est}_{VEM} = (0.94 \pm 0.06)\ I^{peak}_{VEM}$.

3.2 Fluorescence Detector

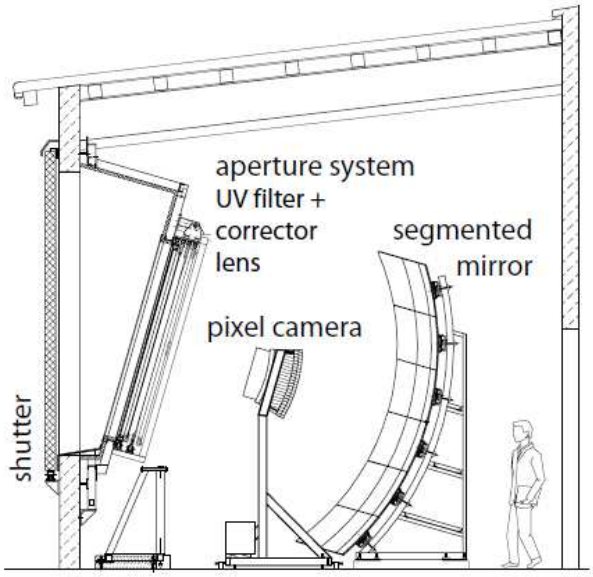

Figure 3.6: A scheme of telescope geometry. Light comes through the aperture, covered by a UV filter and a corrector ring, and it is reflected by a segmented mirror to the camera with 440 photomultipliers.

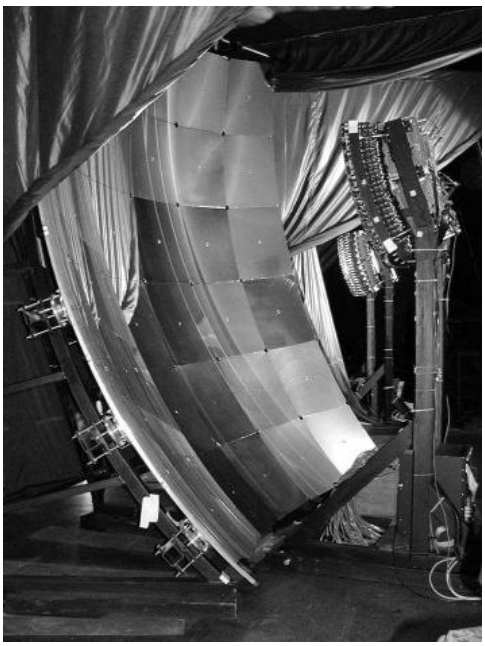

Figure 3.7: A photograph of the fluorescence detector camera and the segmented mirror. The other camera is seen in the background.

There are 4 buildings with 6 fluorescence telescopes each which overlook the area of SD stations (Fig. 3.1) as described in Sec. 3.1. Each telescope uses Schmidt optics and consists of a wide-angle, segmented spherical mirror, a spherical focal plane, an UV 300-410 nm passband filter, and a refractive corrector ring at the aperture of the telescope. The telescope field of view is 30° (in azimuth) x 28° (in elevation) so that each building has 180° range in azimuth (the 3 high-elevation telescopes observe from 30° to 60° in elevation). There are 440 photomultipliers in

[4]The rate of ~ 20 Hz is observed on the reference tank with all 3 PMTs set to the same I^{peak}_{VEM} value.

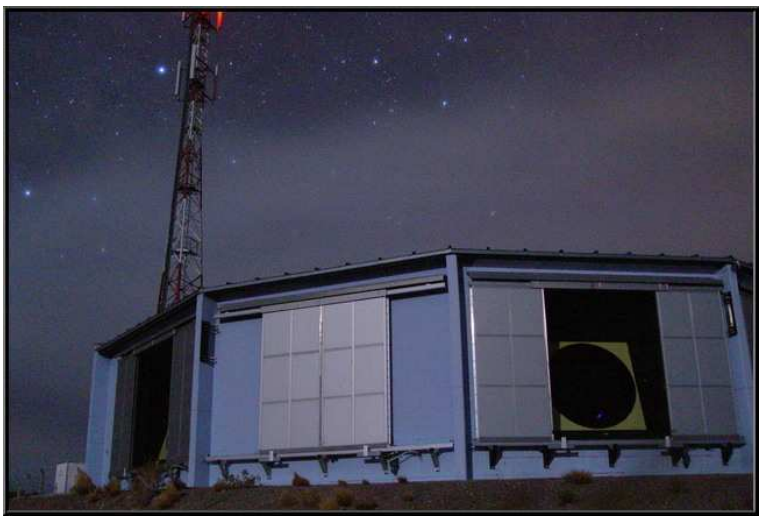

Figure 3.8: A photo of the FD building (Los Leones) on which 2 open shutters and a closed one can be seen. The communication antenna is behind the building [80].

each focal plane which collect reflected light. The longitudinal profile of a shower is thus measured as an image - a pattern of active PMT pixels along the shower axis. The layout of the FD geometry is shown in Fig. 3.6.

There are several trigger levels. The first level digitizes signals from an analog board in each pixel at 10 MHz. The second level trigger is also an internal trigger to search for track segments of at least five active pixels. Every 100 ns, a scan over the full camera is performed and the triggered pixels are searched for track-like patterns. The third level trigger is a software algorithm that rejects events caused by lightning, muons which impact the focal plane, or randomly trigged pixels.

FD telescopes are calibrated to find the proper conversion between digitized counts and the true light flux (in photons). This calibration is performed in several steps using absolute and relative methods. The absolute calibration uses a calibrated light source (known as a 'drum') mounted at the telescope aperture [69]. Using the drum, the light flux at each pixel is known and the response is measured. In addition to the drum calibration, vertical laser shots at wavelengths 337 and 355 nm [81, 82] are used as an independent calibration method. Between absolute calibrations (which occur several times per year), the relative response of each fluorescence camera is recorded using light pulses from LEDs and xenon flashers. The relative calibration occurs before and after each night of observations.

Photonis PMTs used for FD cameras have hexagonal shape. Despite the proper shape of PMT units which allows to assemble the camera, there are quite large insensitive area due to opto-mechanical design. The area of steel construction between adjacent pixels is covered by so called *Mercedes stars* covered by reflective aluminized foil. It increases the light collection efficiency approximately to 93% [69].

The circular aperture is physically limited by the circular diaphragm that is placed in the perpendicular plane to the optical axis. Incorporated Schmidt optics is characterized by coma aberration that is corrected by the so called corrector ring

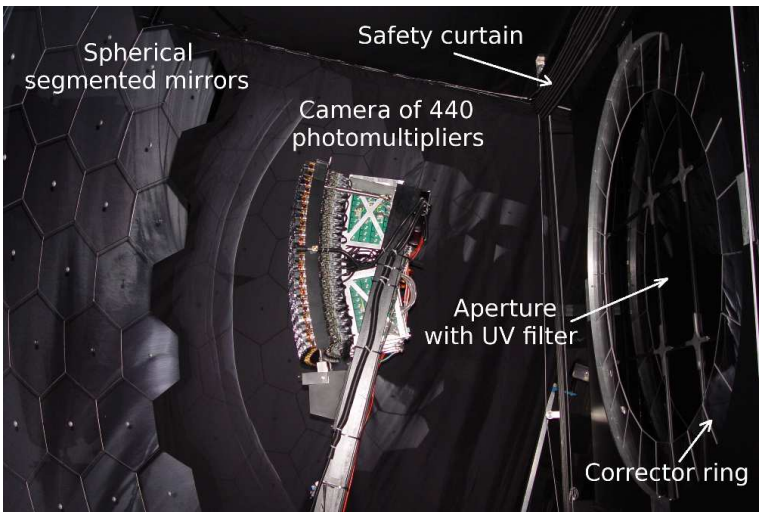

Figure 3.9: The camera with PMT array is mounted to the tough steel construction in order to hold stable position in respect to segmented mirror. There is a safety curtain in standby position that allows light to pass through aperture and corrector ring (adopted from [80]).

(see Fig. 3.9). Moreover, the corrector ring increased the aperture by a factor of ~ 2.

The area of mirrors is $\sim 13\,\mathrm{m}^2$ and therefore they are segmented for the sake of easier production and mounting. Two different configurations of mirrors are used for FD detectors. The first one consists of 60 hexagonal glass segments, whereas the second one employs 36 rectangular anodized aluminium mirror segments.

The FD is operated by the crew remotely from central campus in Malargüe by means of the Slow Control System (SCS) during nights when the moon fraction is below 60% [5]. SCS has web-browser interface to maintain low / high voltage on cameras, to close / open shutters, to operate curtains, etc. SCS monitors detector as well the weather and communication conditions. In case of a critical problem, SCS performs FD shutdown. There is also an alarm system which warns the crew about potentially dangerous situations (see 4).

Monitoring of conditions is provided by a specific tool using MySQL database filled by continuously measured data. Wind speed, temperature, cloud and light information or rain / snow flag can be checked by the crew via web-browser for all FD locations separately.

3.2.1 FD event reconstruction

Precise timing and pulse measurements of FD triggered pixels are essential factors for the air shower geometry reconstruction. Shower axis estimation defines prediction for signal arrival times that can be compared to measured ones and one can evaluate the estimation by χ^2 value. Event reconstruction algorithm finds that

[5] Observation time varies from 5 to 14 hours, on average 10 hours.

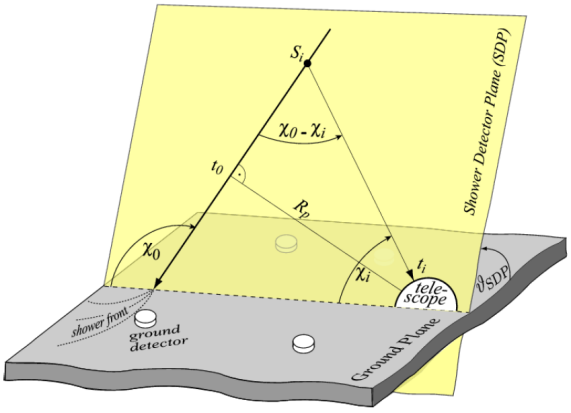

Figure 3.10: Shower detector plane sketch with reconstruction variables ([69]).

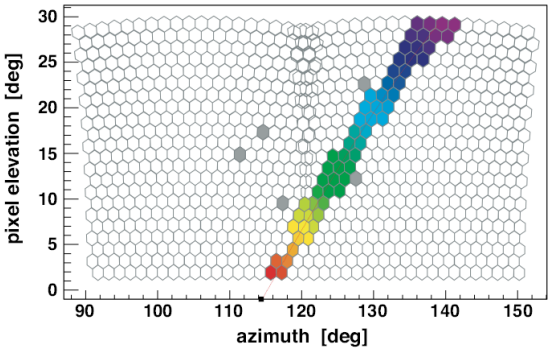

Figure 3.11: Los Morados camera signal of event # 3308259. Relative timing of pixel signal is depicted by colour ([65]).

configuration with minimum of χ^2 value.

In Fig. 3.11 there is an example of FD event seen by 2 cameras. Timing of pixels is depicted by color. Positions of at least two pixels are the crucial information to reconstruct *Shower Detector Plane* (SDP) defined by shower axis and FD detector. Event geometry sketch can be found in Fig. 3.10 with reconstruction variables. Shower detector plane intersects FD eye (see Fig. 3.11) and reconstruction uncertainty can be derived from event with known axis as it is in case of *Central Laser Facility* (CLF) pulses.

Shower axis lies in the shower detector plane and timing sequences from triggered pixels are used to find it. Geometry of FD event is depicted in Fig. 3.10. The angle between ground plane and shower axis measured in shower detector plane is χ_0, while perpendicular distance of shower axis to FD eye is R_p. In this configuration each pixel sees shower axis at angle χ_i measured from horizontal line in SDP. t_0 denotes time at which shower passes through the closest point of shower axis to the detector. Time of light arrival at i^{th} pixel delayed in comparison with t_0 as it follows

$$t_i - t_0 = \frac{R_p}{c\,\sin(\chi_0 - \chi_i)} - \frac{R_p}{c\,\tan(\chi_0 - \chi_i)} = \frac{R_p}{c}\tan\left(\frac{\chi_0 - \chi_i}{2}\right). \tag{3.3}$$

The effect of realistic speed of light was not accounted for, but it is elaborated e.g. in [83]. By fitting timing data from camera pixels to the equation 3.3 one can determine shower parameters - direction of arriving particle. Angular resolution strongly depends on time signal accuracy. PMT data are determined by fast electronics which samples signal at 10 MHz rate. The most critical case is a monocular event seen only by one camera. Shower axis angular reconstruction uncertainty of a monocular event depends on change of measured angular speed $d\chi/dt$ as it is described in section 3.3.

Energy estimation of the shower follows from integration of Gaisser-Hillas function (see 2.31) that is fitted to the measured data from PMTs. Before profile reconstruction the ratio of other than fluorescence light sources (e.g. direct and scattered Čerenkov light) must be estimated and subtracted from signal. The correction for missing energy has to be accounted for.

3.2.2 FD trigger system

Similarly to SD also FD trigger system has three levels ([69, 84, 85]) applied by firmware and software of the electronics - Field Programmable Gate Array (FPGA). It keeps constant noise rate over camera pixels and finds spatial and time structure in particularly triggered pixels which selects coincidence signals.

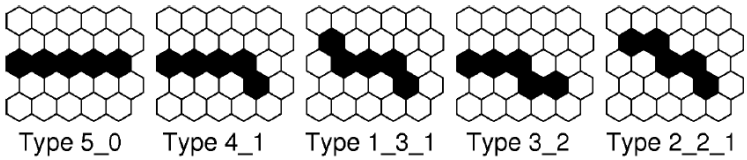

Figure 3.12: Basic examples of spatial configurations of tracks that are searched for by SLT (adopted from [69]).

- **First Level Trigger** (FLT) is implemented in front-end electronics and applies threshold cut on integrated pixel signal. Sliding window of FADC signal from last 10 time bins for each pixel is integrated and compared to a threshold of individual pixel. FLT is emitted if the sum of integrated signal exceeds the threshold which is adjusted for each pixel every few seconds in order to ensures constant pixel trigger rate at the level of 100 Hz.

- **Second Level Trigger** (SLT) is implemented at the camera hardware level in FPGA that searches for a geometrical pattern from bussed FLTs. Spatial configuration of neighbouring triggered pixels are searched for. The algorithm uses predefined fundamental patterns corresponding to a straight track (see Fig. 3.12). The trigger allows one pixel to be silent and therefore it requires 4 fired pixels that meet one of possible pattern configurations. Taking into account all possible rotations and mirror reflections of fundamental spatial configurations in Fig. 3.12 one can count 108 different four-fold patterns. SLT rate is about 0.1 Hz.

- **Third Level Trigger** (TLT) is implemented as a software algorithm rejecting noise events and working at the telescope level. It efficiently selects shower candidates and it is optimized to clean data of lightning events and random pixel triggers. TLT tests time correlation between triggered pixels stored in the previous step. The algorithm rejects 99% of lightnings, however only fraction of 0.7% of real showers are discarded. TLT camera rate is about 0.02 Hz.

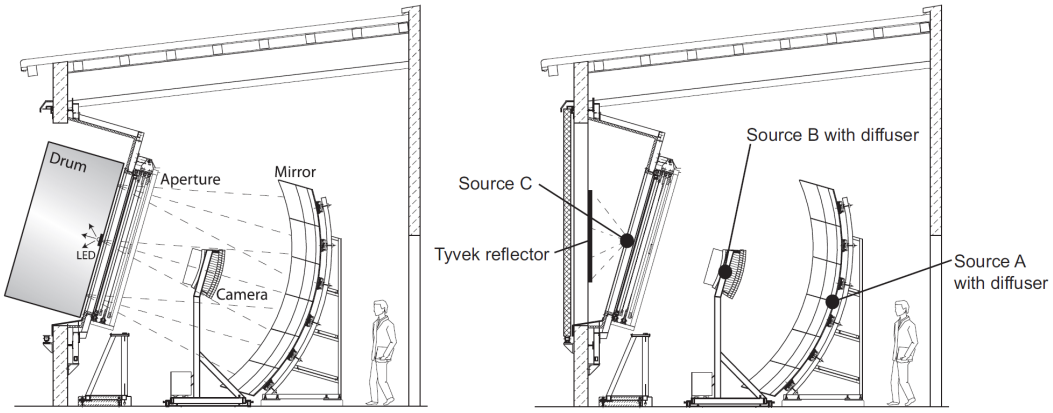

Figure 3.13: Schematic cartoon of *absolute* calibration method (left part) showing calibrated LED that emits light from drum mounted in aperture of the telescope. Positions of light sources used in *relative* calibration are depicted in the right figure (adopted from [69]).

Data passing TLT conditions are sent to so called *Eye-PC* that work on telescope level. Fast event reconstruction algorithm is working on *Eye-PC* which combines data from all mirrors. Directional and ground impact timing information are sent to CDAS and it works also as an external trigger for SD array readout [6].

3.2.3 FD calibration

Fluorescence detectors measure signal raised in PMTs in units of ADC counts, while absolute number of photons is needed in order to obtain total shower energy and to reconstruct shower longitudinal profile. The conversion of ADC signal received in each pixel into number of incident photons can be done due to calibration. It ensures pixel response transformation at given telescope aperture including among others optical filter properties, gain of PMTs, reflectivity of mirrors. These particular effects can be measured in different procedures, however signal calibration is done in two stages - *absolute* and *relative* calibration [69].

Absolute calibration

This type of calibration is also called *drum calibration* as very known cylinder-like diffuser of 2.5 m diameter is used. The diffuser provides the same light intensity at each pixel. NIST [7] calibrated LED light source [8] is enclosed in the drum mounted to the telescope aperture (see the left part of the figure Fig. 3.13. FD signal response

[6]The purpose of such external trigger is to select low energy hybrid events around 10^{18} eV with shower core close to FD telescope which trigger only small number of SD stations that do not satisfy standard SD trigger system.

[7]National Institute of Standards and Technology

[8]Pulsed UV LED (375 ± 12 nm) light uniformity of the drum is studied in the lab using CCD camera.

is measured and since the photon flux of LED is known, this method provides precise full calibration. The drum ensures that the photon flux is uniform over the whole camera. Absolute calibration is performed only every few years. Measured response of pixels is about 5 photons per one ADC count.

Relative calibration

Since absolute calibration is time consuming and cannot be performed automatically, there is another method for evaluating the camera response. Relative calibration is processed before and after each night of telescopes operation. It consists of three separated processes denoted as calibration A, B and C (see the right part of the figure Fig. 3.13).

Diffusive light sources are mounted to mirror (A), center of camera (B) and the third LED is mounted to aperture of the telescope (C). Light sources are the same for one FD-building and the light is distributed through optical fibers beyond light splitter.

Calibration A tracks camera pixels response via illumination of the camera face. The A fiber from 470 nm UV LED is mounted in the center of the mirror. LED works in 60 μs pulse mode. For calibration A, 470 nm were used until Nov 2011; around that time, all the LEDs were swapped for 375 nm.

Calibration B uses xenon flash lamp with fiber end at the sides of the pixel array illuminating the mirror. Therefore it can measure relative reflectivity of the mirror. B source uses a Johnson-U filter that covers the whole wavelength range of FD acceptance.

Calibration C includes camera aperture and light emitted outwards FD building. Inside part of the shutters are covered by Tyvek sheets that are used as reflectors which diffuse C light source towards the mirror and light passes through all optical components. It can test relative changes in aperture and mirror reflectivity. Calibration C uses several filters.

All relative calibration is controlled and commanded during night measurement from CDAS. Measured data are stored in CDAS in so called *Calibration PC*.

Systematic uncertainties on the reconstructed energy

Systematic uncertainties on the energy scale was updated and presented in [67] as the more precise measurement of the fluorescence yield together with improved estimation of missing energy was taken into account. In Tab. 3.1 the most important ingredients to the total systematic uncertainties are listed. The total systematic uncertainty (of 14%) is dominated by the absolute FD energy calibration.

3.2.4 Temperature measurement

PMT response plays essential role in the detector calibration which is of utmost importance for precise measurement of EAS energy. As described in the previous section the relative calibration of type A is performed each night during FD measurement period of each month (the period is called *shift*). While calibration A is

item	uncertainty
Absolute fluorescence yield	3.4%
Fluorescence spectrum and quenching param.	1.1%
Aerosol optical depth	$3\% - 6\%$
Atmospheric density profile	1%
Absolute FD calibration	9%
Optical efficiency	3.5%
Folding with point spread function	5%
Nightly relative calibration	2%
Invisible energy	$3\% - 1.5\%$
Total	14%

Table 3.1: The most significant and the total systematic uncertainties on the energy at Pierre Auger Observatory [67].

performed each night before and after measurement, i.e. two times per each shift night, calibration B and C data are taken nightly from June 2008 with various timing (before / after shift night) during FD shift periods.

Since the beginning of FD operation seasonal variation and even decrease of PMT response is observed. Several long and short-time studies were performed to know the impact of integral background light level to PMTs sensitivity (e.g. [86]), as well as the stability of camera response was studied (e.g. [87, 88]). The stability of calibration light sources is monitored by stable photodiodes in LED Control Units (LCU). LCU response of calibration A source shows also seasonal variations superimposed on the long term trend. The response of calibration A was corrected for those effects and analyzed (see Fig. 3.14). As described in [88] the decrease of response is measurable for all cameras, but with different slopes.

PMTs are very sensitive devices and their lifetime depends on integral as well as peak illumination. Too much light intensity can even damage PMT due to a change of the surface properties of the last dynodes. For that reason shift period proceeds when moon fraction is below 60%. Cameras with moon in the field of view are not operated during shifts and the corresponding bays are closed. This avoids direct exposure of cameras which is necessary but not sufficient in order to protect photomultipliers from prompt sensitivity losing. In addition to that current intensity background is measured and in case it exceeds some threshold the bay is closed automatically. Background light is induced by light scattering on aerosols or clouds, lightnings and artificial sources. The integral illumination decreases sensitivity of PTMs and it could be one of the reasons of overall response trend. Integral charge of PMTs at half-life is $Q_{1/2} \sim 500\,\mathrm{C}$.

Influence of different factors was discussed in [87] such as dark night exposure and high voltage variation applied to PMTs, but they did not explain response

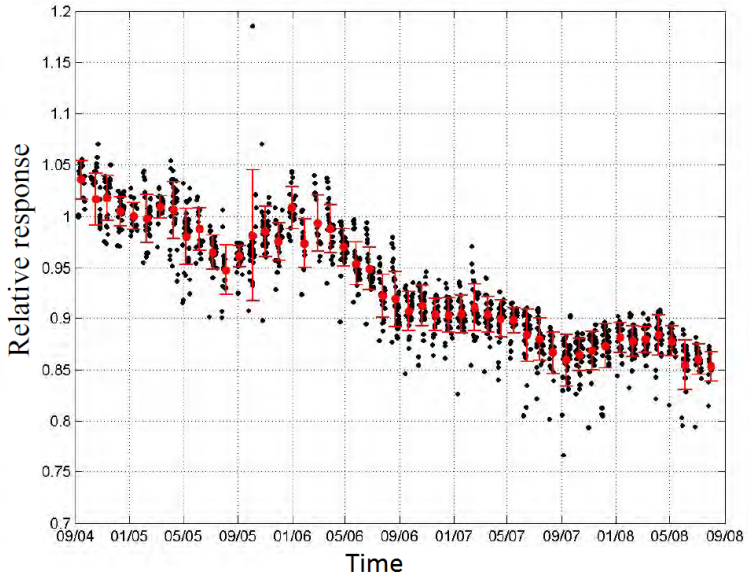

Figure 3.14: Calibration A constants measured at Coihueco bay#2 during period from September 2004 till September 2008 [88] corrected for intensity variations measured by monitor photodiode placed at light source in LED Control Unit. Data indicates cumulative effect of seasonal variations and decreased response trend. While black points represent particular calibration measurements, red points depict average values during dark periods.

behaviour and variations. Nevertheless, long-term response of cameras seems to be more stable after August 2006 when strict rule for closing shutters started to be applied. The mean yearly loss of PMT response was fitted and except for Los Leones bay#2 all cameras show more stable behaviour in period from November 2006. The recent period was characterized by average yearly loss of camera response at the level of 1.8%, whereas the yearly loss of previous period did not drop below 2.1%.

It was also shown that calibration run performed before and after night measurement shows systematically different values. In Fig. 3.15 *evening* (before run) and *morning* (after run) values of Coihueco bay#2 indicate difference of $\sim 2\%$.

Calibration constants of type A measured after the shift are used for absolute calibration calculation as follows [90]:

$$AbsCC_{corrected} = \frac{Q_{reference}}{Q_{cal\,A}}\, AbsCC_{drum}, \tag{3.4}$$

where $Q_{cal\,A}$ is calibration A measurement performed after the shift night, whereas $Q_{reference}$ is calibration A measured at the time of drum calibration when the absolute calibration $AbsCC_{drum}$ is taken. On that account it is of utmost importance to know reasons of response fluctuations for the sake of their possible reduction.

One of possible factors that affect current PMT response can be camera temperature. The air-conditioning system should guarantee stable temperature inside FD buildings. On the other hand temperature variations during seasons together

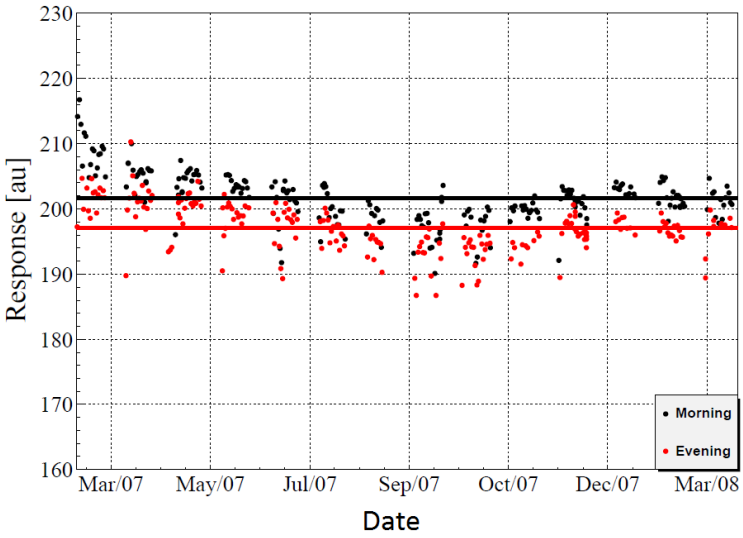

Figure 3.15: Comparison of average camera response (calibration A constants) for Coihueco bay#2 for measurement taken before and after shifts (referred to as *evening* and *morning*) (adopted from [89]). Data show systematic difference.

with open shutters could influence measurement conditions. Temperature fluctuations can affect not only light intensity produced LED, but also camera response, in particular PMT gain. The PMT's producer claims the temperature relative response change $-0.2\%/K$, while Pierre Auger Collaboration internal measurement showed slightly higher dependence at the level of $-0.3\%/K$ [91].

To monitor condition stability, temperature sensors of type *Dallas ds15B20* were installed in Coihueco building . 2 sensors were installed on each shutter (top and bottom), 2 on each camera (top and bottom), 5 sensors on each mirror (top, bottom, left, center and right) and 1 sensor was placed into calibration room in April 2009. Additional 4 sensors completed Coihueco site measurement array in October 2009 (see Fig. 3.16). Data are taken with 10 minutes frequency and they are stored in monitoring database.

In spite of the air conditioning system the temperature varies during shift nights and it depends also on voltage on cameras. When shutters are open, temperature decrease in bays is detectable even by camera sensors. Only the FD filter separates bays from the outside.

Long-term studies of seasonal calibration A modulation and its relation to the temperature were performed in [89]. FD response was compared to the bay temperature (see Fig. 3.17) and extremal values of both curves were found by fitting procedure. It was found that temperature profile does not correspond to the calibration A profile, but there is approximately constant delay of 90 days when the maximum response of calibration A occurred compared to the measured maximum of temperature.

Based on the above mentioned work and knowledge the temperature variation near cameras and in light source room has been analyzed in order to find if there

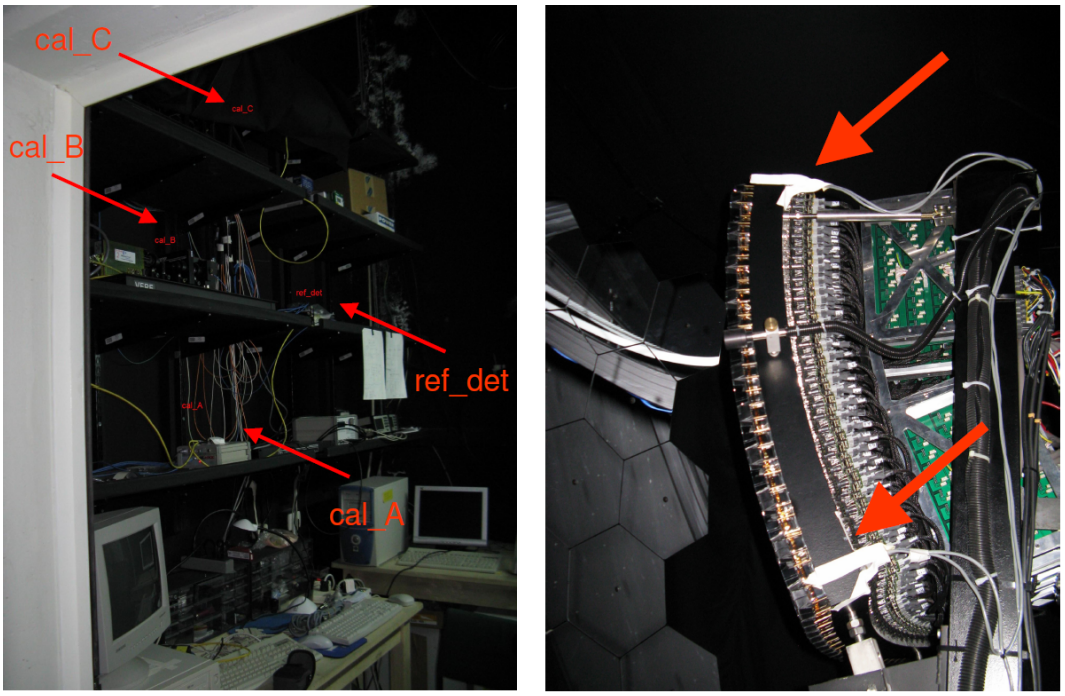

Figure 3.16: Position of temperature sensors at Coihueco's calibration room (left figure) - *cal_A*, *cal_B* and *cal_C* show the temperature sensors near light sources used for calibration. *ref_det* sensor is located near the light separator. Positions of temperature sensors mounted to the camera are showed in the right figure [92].

is some relation to measurement processes and if air conditioning system can keep temperature enough stable. The second part of the analysis focuses on the estimation of temperature variation impact and its possible elimination by correction factors.

The temperature stability in bays and near cameras was analyzed from long and short term point of view and the results are summarized in the next paragraphs. At first data measured from Coihueco sensors were plotted into graphs. As shown in Fig. 3.18 the temperature measured by sensor mounted to the camera (bay#1) fluctuates during shifts (depicted by arrows) as well as during seasons. Blue points represent particular measurements and the difference $\sim 16\,^{\circ}\mathrm{C}$ between long term minimum and maximum during April 2009 and November 2010 is shown.

The temperature variations in the Coihueco calibration room near calibration A light source are plotted in Fig. 3.19. Again, shift periods are indicated by green arrows. Data measured from October 2009 till November 2010 show that the temperature fluctuates so that the peak difference can exceed $\sim 10\,^{\circ}\mathrm{C}$.

The most extreme shift from the point of view of temperature variation was selected and it is shown in the Fig. 3.20. The temperature interval can range more than $5\,^{\circ}\mathrm{C}$ near calibration A light source during one shift.

Climate data for Malargüe show that the outside average temperature varies within the range of $\sim 30\,^{\circ}\mathrm{C}$. The warmest month is January when the average high temperature reaches almost $28\,^{\circ}\mathrm{C}$, while in July the average low temperatures drop

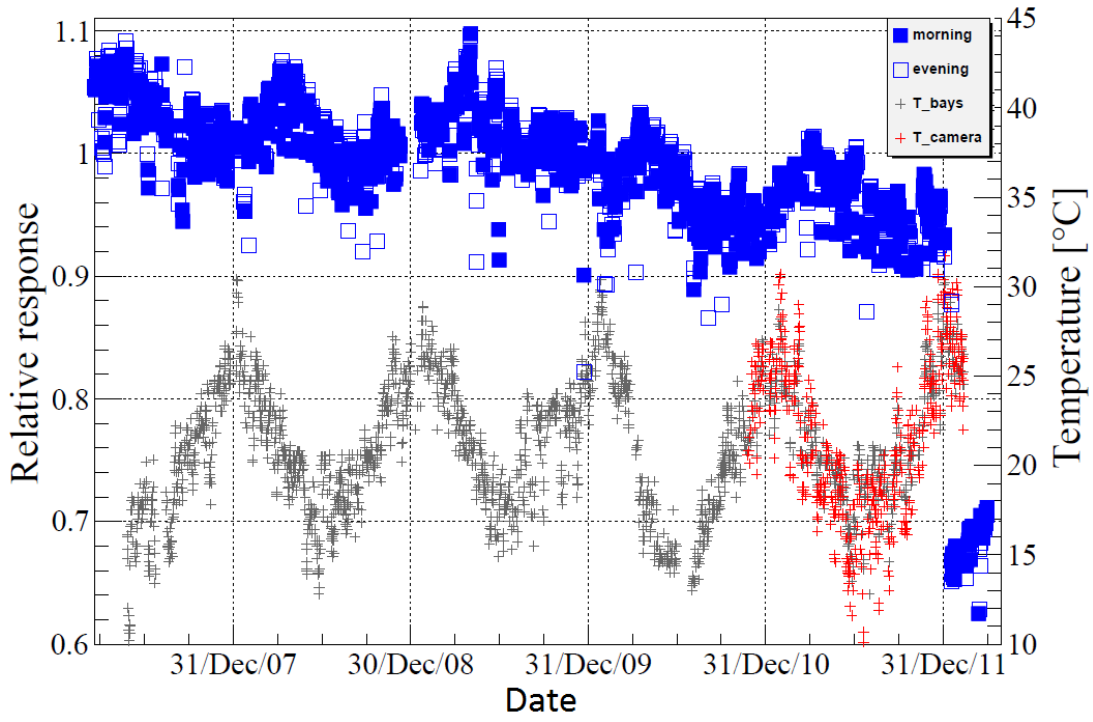

Figure 3.17: Calibration A response vs. temperature measured in bay#5 at Los Morados [89].

slightly below $-2\,^{\circ}\mathrm{C}$ [94]. The temperature variation inside FD buildings coincides with outside temperature profiles with respect to other effects, such as high voltage on camera as described later.

Temperature data are stored in standard Auger database table *SCDataPointTab* and they were enriched with Slow Control log table (*SCLogMessageTab*) in which Slow Control actions - logs are stored (e.g. timing of opening/closing shutters, applied high voltage,...). This enabled to identify significant operation actions during shift nights and map them into temperature development charts.

The short-term temperature variations in Coihueco bay#1 during April - May 2009 shift are depicted in Fig. 3.21. Additional information regarding bay#1 is plotted by means of arrows pointing downwards. The arrows pointing upwards indicate actions in bays #2 - #6. The top figure shows temperature variations measured by sensor mounted to the top of camera and the extrema values correlate with opening and closing the shutters. The bottom part of the figure includes also the outside temperature profile which tallies with camera temperature profile.

Camera temperature profile coincides with outside temperature development even in the case when all shutters remain closed as indicated in Fig. 3.21 for Coihueco bay#1 (confirmed by similar situations for other bays and dates). On the other hand, open shutters correspond to stronger temperature variation. The top section of the mentioned figure shows part of one shift period at the end of April and beginning of May 2009. Measured temperature profile at the top of the camera is depicted by blue crosses. The outside temperature profile is depicted by black

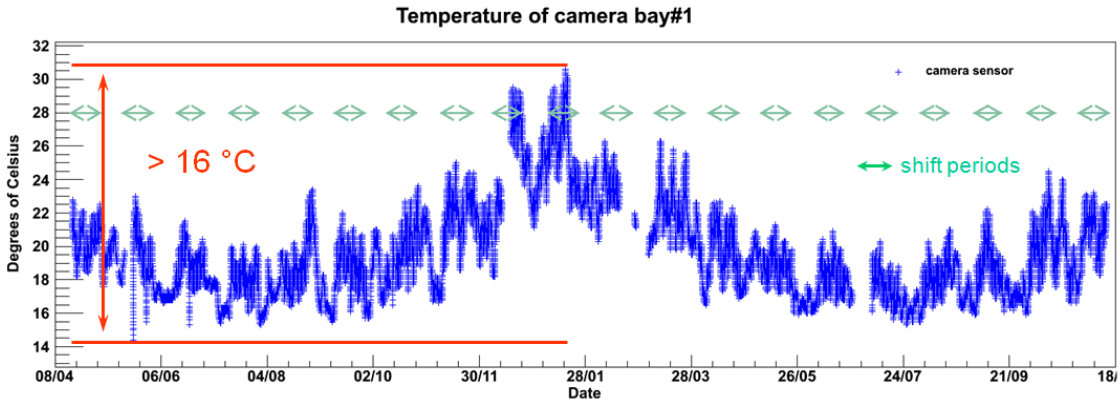

Figure 3.18: The long-term temperature variations measured on camera at Coihueco bay#1 during period from April 2009 till November 2010 [93]. The arrows depict shift periods. The overall variations exceed $\sim 16\,^{\circ}\mathrm{C}$.

crosses at the bottom part of forementioned figure. Although the air-conditioning system moderates the temperate variation it is not able to keep the temperature stable.

The top part of the figure Fig. 3.22 shows the same period of temperature profile from top part of Fig. 3.21, but with supplementary timing of high voltage applied on cameras. The logic of depicted timing information remains the same - arrows directing downwards correspond to the bay#1, whereas arrows aiming upwards concern the other bays (#2 - #6). The bottom part of Fig. 3.22 shows the detail development of temperature during two days with twilight and above mentioned Slow Control log messages. It naturally indicates that not only closing and opening the shutters influences camera temperature, but also high voltage implies additional variations. The bottom part of the Fig. 3.22 shows that the inside temperature starts to decrease after the end of twilight (this obviously coincides with decrease of the outside temperature). Nevertheless, high voltage warms the camera or it mitigates the decrease. When shutters close, the air-conditioning and high voltage as a heating are strong enough to stop the temperature decrease. Subsequently, the break can be observed when the high voltage on camera is turned off. This moment is a breakpoint after which the temperature starts to decrease again.

Typical winter temperature behaviour can be seen in Fig. 3.23. It confirms that the high voltage increases temperature and 'helps' air-conditioning system to stabilize conditions during low-temperature seasons. During winter the outside temperature is all the time below the values inside FD buildings, nevertheless temperature could be more stable during shift than in summer time as shown in Fig. 3.23 (even though it lies permanently below 20°C). The mentioned figure indicates that high voltage can influence the top of the camera temperature very significantly. When the high voltage is turned off after the shift, temperature drops by about almost $2\,^{\circ}\mathrm{C}$. This happens even when the shutters are closed and the outside temperature increases (in fact very mild increase is observed). Temperature increases once high voltage is turned on (see red and blue arrows in Fig. 3.23).

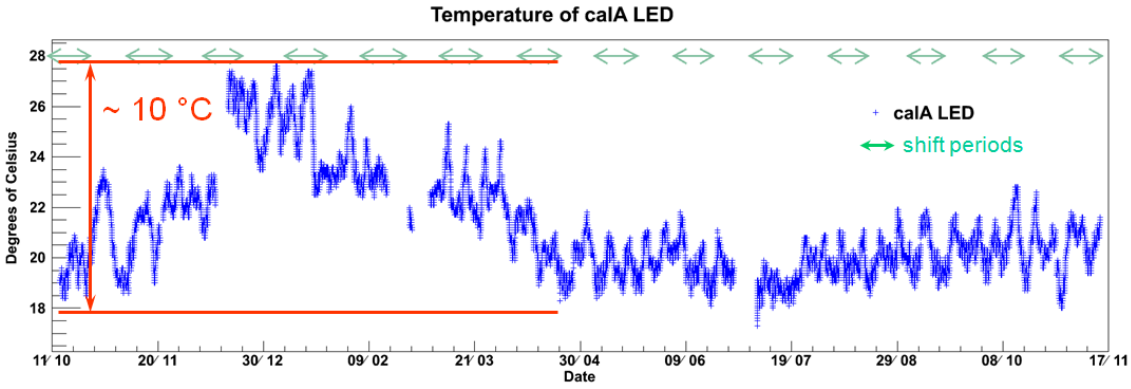

Figure 3.19: The long-term temperature variations measured near calibration A light source at Coihueco building during period from October 2009 till November 2010 [93]. The arrows depict shift periods. The overall variations exceed $\sim 10\,^{\circ}$C.

The air-conditioning system does not keep uniform temperature and various factors influence it during short and even long term periods. The typical temperature variation near the camera was found to be at the level of $\sim 3\,^{\circ}$C during shift night, whereas inside the calibration room the conditions seem to be more stable and only $\sim 1\,^{\circ}$C difference is commonly measured near calibration light sources during one shift night. Quite large variation of temperature (up to $\sim 8\,^{\circ}$C) can be seen near camera during one shift period. Thus, taking into account $\Delta_t = 8\,$K it could theoretically lead to the camera response variation in calibration A up to the level of [9]

$$\Delta_{cal_A} \approx -0.3\%/\mathrm{K} \times \Delta_t = -2.4\%. \tag{3.5}$$

As described in several studies (e.g. in [95]) the range of calibration constants variation during shift period exceeds 5%. The largest difference turns out to be between the first measurements and values obtained near the middle of shift period, but even short time variations during one shift night can be seen. Short-term temperature profile of camera that corresponds to its response was also demonstrated in [89].

Next paragraphs describe the correlation analysis performed on data from Coihueco with the aim to find the direct relation between temperature variation and camera response. Based on measured data the correction factor to the temperature could be found to get more stable camera response.

Absolute calibration constants covering period between January 2010 and January 2014 were used to analyze temperature correlation. Outlier values less than 1 that are obviously errors were discarded from the analysis sample. The average calibration value of topmost camera pixels are taken into account together with temperature measured at the top of the camera. In Fig. 3.24 calibration constants are depicted with linear fit that describes overall decreasing trend of the response.

[9] Provided that LED light intensity dependence on temperature can be neglected or that the temperature variation near the light source is negligible.

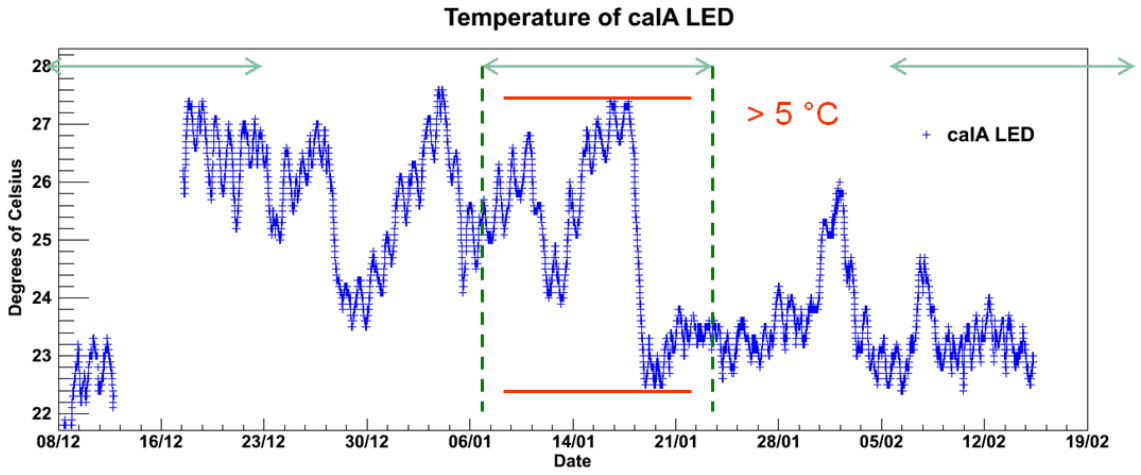

Figure 3.20: The short-term temperature variations of calibration light source A between December 2009 and February 2010 [93]. It is shown that during one shift period the temperature difference can exceed value of $\sim 5\,^{\circ}\mathrm{C}$. The temperature modulation during one shift period is evident (it corresponds to day-night variations and one shift night variations).

In order to find possible and expected temperature correlation with calibration constants the original constants were corrected so that the overall fit was constant function as one can assume that long time trend is not caused by current (or short time) temperature variation. Corrected calibration constant c_{corr,t_i} calculated from calibration constant measured at time t_i, it is obtained as follows:

$$c_{corr,t_i} = c_{t_i} + b \times (t_0 - t_i), \tag{3.6}$$

where $b \approx -1.072 \times 10^{-9}$ is the slope obtained from linear fit (see Fig. 3.24), c_{t_i} is the original calibration constant and t_0 is the time of the first measurement in the sample used in the fit (therefore this value was the only one without correction). The corrected absolute constants are drawn in Fig. 3.25. The correction resulted in stronger relation between temperature and calibration values as it will be shown further.

So far the monitoring of temperature was described and some important factors and events (e.g. opening and closing of shutters, switching of electronics, etc.) were identified. Following analysis studies relationship between calibration constants and temperature close to the camera and therefore it tries to find the temperature influence on the camera response. The result could serve as the temperature correction in case when the air-conditioning does not keep the temperature uniform.

For the analysis calibration constants with recorded precise time of performed calibration measurement were used. The average calibration constants from top row of the PMTs were calculated. Each value of averaged calibration constant was matched with camera temperature by means of algorithm that finds the minimum time difference between temperature and calibration measurements. The Pearson

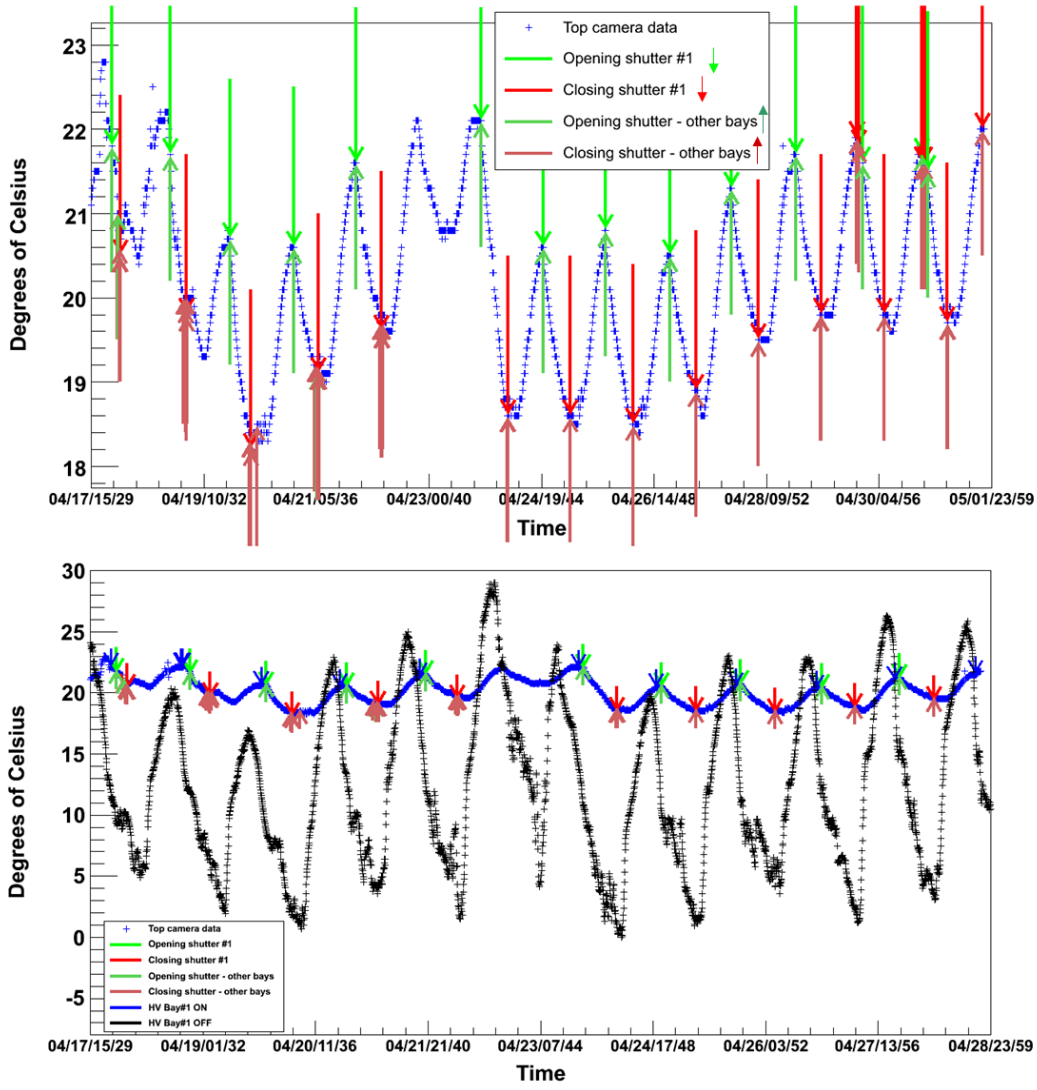

Figure 3.21: The top figure shows temperature of Coihueco camera bay#1. It is depicted by blue points [92]. Timing of opening shutter# 1 is depicted by green arrows pointing from top to bottom, whereas timing of other shutters is plotted by green arrows pointing bottom-up. Analogically closing of shutters is marked by red arrows. The bottom figure includes outside temperature plotted by black dots [93].

correlation coefficient for the case of original constants is -0.229 and -0.246 for corrected constants. This analysis measures the relation between camera response and immediate temperature. Since calibration constant measured at time t_c can be influenced by temperature of the camera at time t_T, where $t_T < t_c$ the relation of calibration values and temperature of the camera before the calibration measurement has been studied. Calibration constant can be influenced by temperature measured $\Delta_T = t_c - t_T$ before the calibration process. The value Δ_T is referred to as *offset*.

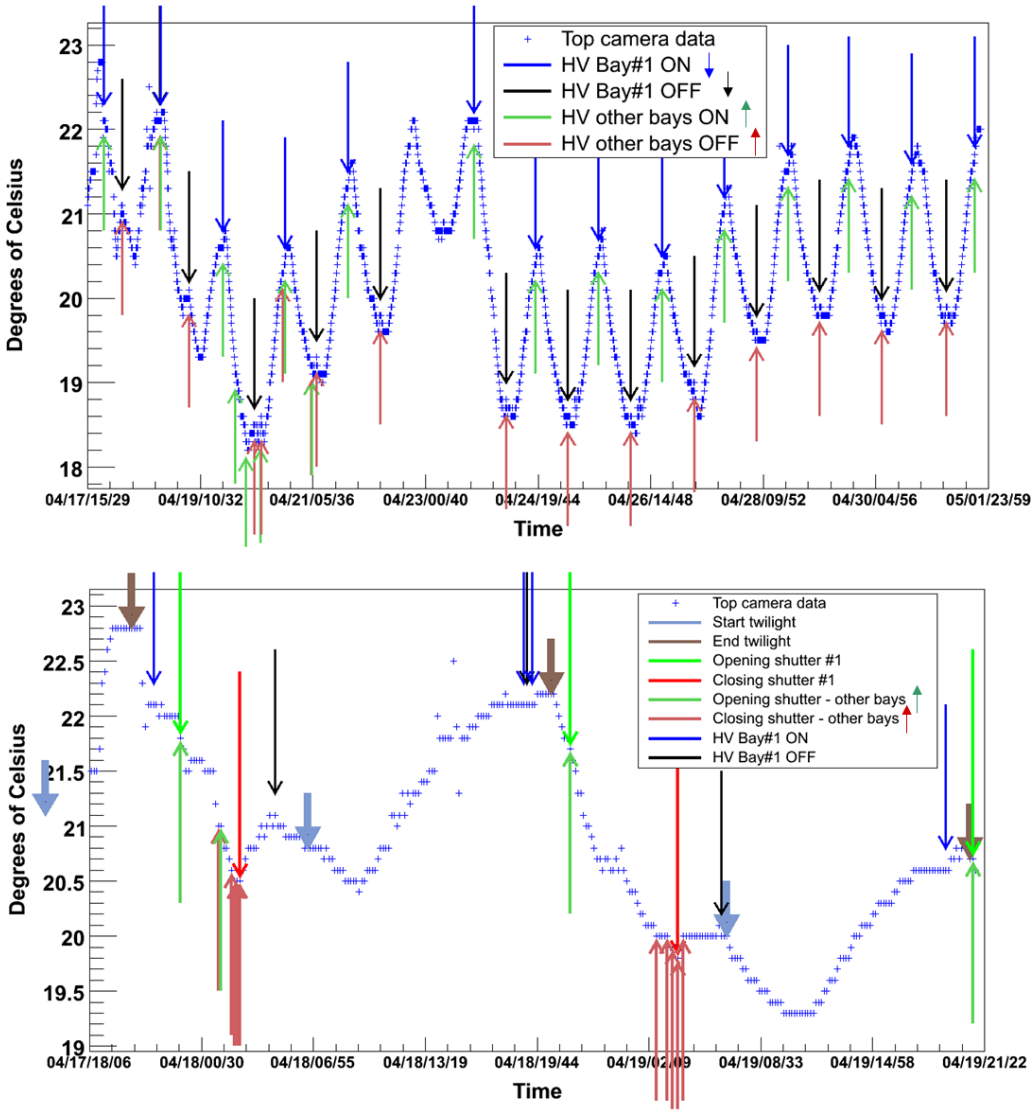

Figure 3.22: The top figure shows the short-term temperature variations measured at Coihueco bay#1 at the top of the camera during April and May 2009 [92, 93]. Arrows aiming downwards denote bay#1 and they mark time when high voltage is turned on and off. The arrows with opposite directions denote bays #2 - #6. The bottom figure shows temperature variations at the top of camera during one shift with additional timing information of opening/closing shutters, switching on/off high voltage and twilight.

For this correlation analysis the Pearson coefficient R_{Δ_T} was calculated for set of data with $\Delta_T = t_c - t_T$ with step of 1 hour. Results are depicted in Fig. 3.26. Correlation coefficients were calculated for non-corrected and for corrected constants. The relation between temperature variation and value of calibration constants is investigated in this analysis. There is certain decreasing trend in calibration constants in analyzed long time period (almost 4 years) which is not assumed to be

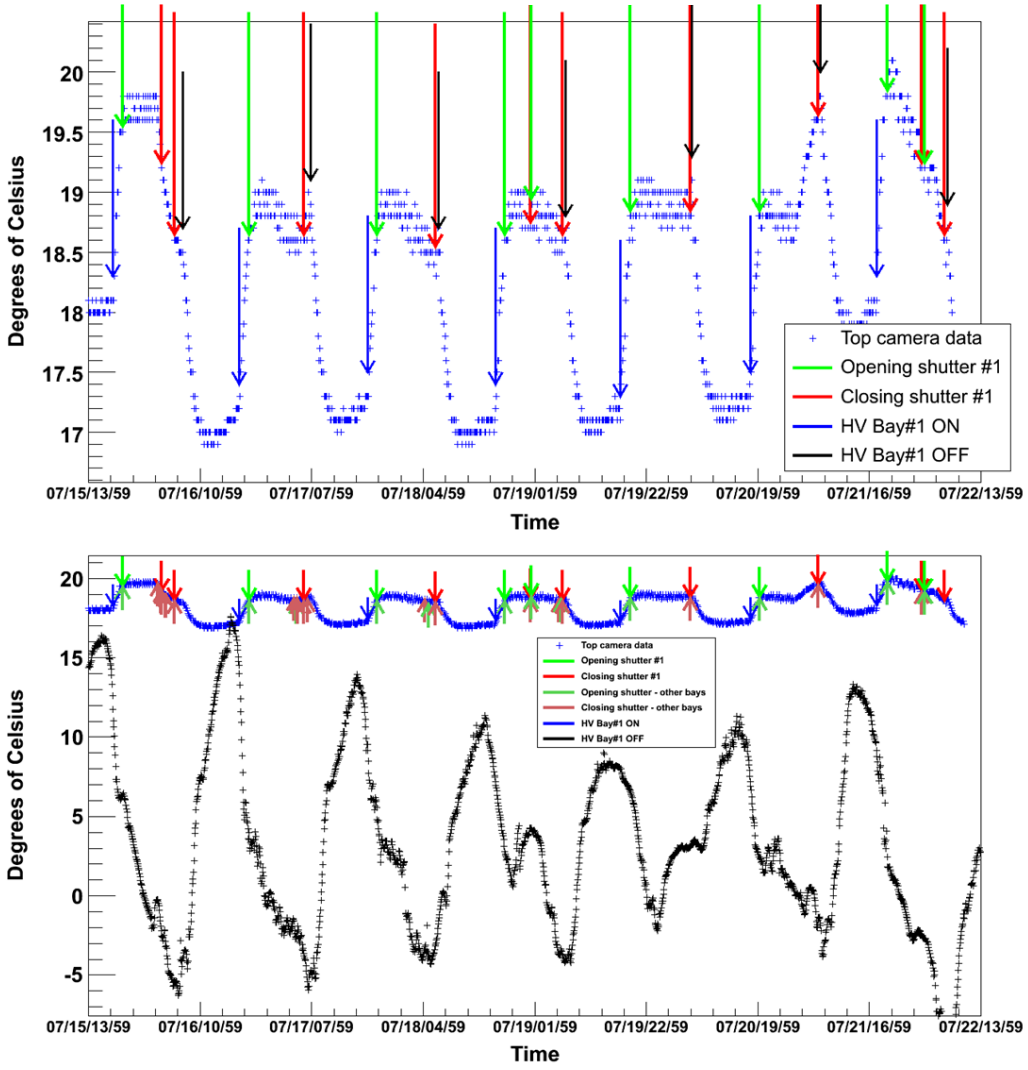

Figure 3.23: Typical winter temperature variations (measured at the top of Coihueco bay#1 camera) [92] are depicted in the top figure including opening/closing shutter information and switching high voltage. The outside temperature is plotted by black dots in the bottom figure [93].

caused by overall temperature shift. Therefore, this trend should be removed and one can expect stronger connection between temperature and calibration constants. In this case the absolute values of Pearson correlation coefficients should be greater for corrected constants than for non-corrected ones. Correlations were investigated in positive and also in negative *offset* regions. The relation between temperature and calibration constants is causal for values $\Delta_T > 0$, that is temperature influences the camera response. There is no physical reason to calculate correlations for negative offset Δ_T. On the other hand the development of correlations for $\Delta_T < 0$ gives some indications how correlations can look like in the non-causal region; with no meaningful interpretation. The development of correlations for positive *offset* can

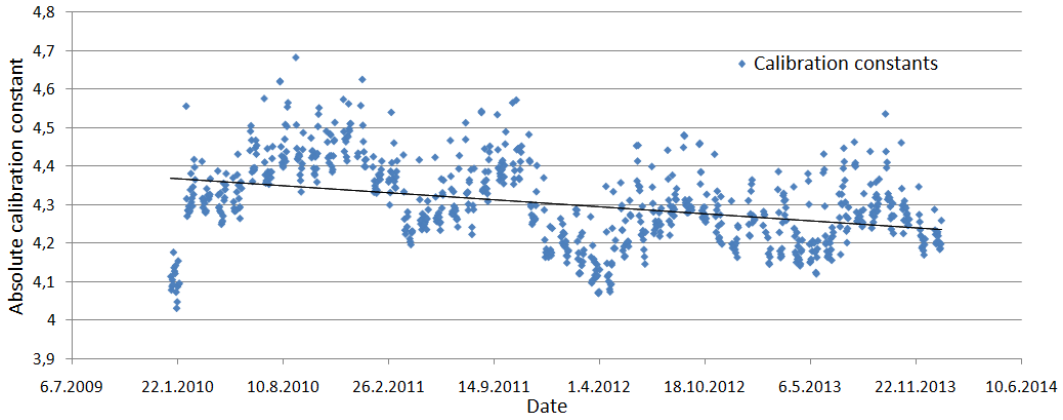

Figure 3.24: Absolute calibration constants used for correlation analysis with camera temperature (the official values used for shower reconstruction valid to April 2014. They cover period between January 2010 till January 2014). Data are fit by a linear function in order to extract decreasing trend of the response.

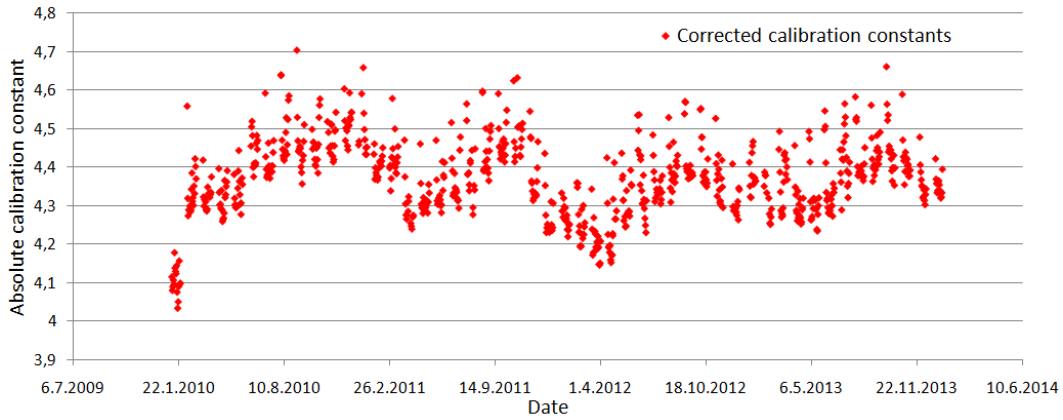

Figure 3.25: Corrected absolute calibration constants by means of the result from linear fit (see Fig. 3.24 and 3.6).

be compared to those calculated for $\Delta_T < 0$. As obvious from the figure Fig. 3.26 the corrected values (see the red curve) are systematically higher in absolute values than non-corrected calibration constants (the blue curve). Therefore, the relation between temperature and camera response is stronger for trend corrected values. It can be seen that for positive *offsets* Δ_T the correlation gets stronger till the first minimum. There are another three significant minimum values delayed by ≈ 28.5 days. After the correlation reaches the maximum the relation between calibration and temperature weakens as well as in the case of negative Δ_T which was assumed. Correlations R_Δ in negative region of Δ_T were calculated in order to show correlation behavior in non-causal region. On the other hand one can assume that similar correlation structure in positive region of Δ_T indicates that relation between temperature and calibration constants disappears or significantly weakens.

The regular structure of three periods in positive Δ_T is result of periodical

temperature variation and regular length of shift period. Beyond three periods the overall correlation is reduced. In other words, temperature probably behaves similarly during three months and after this period weather conditions start to change substantially. Simultaneously, periodic shape of correlation curve in positive R_Δ shows that calibration constant behavior during shift period has also regular structure.

In the region of the offset value $\Delta_T \gtrapprox 2500$ hours the correlation trend is similar to that one for $\Delta_T < 0$ h (see the figure Fig. 3.26). The threshold $\gtrapprox 2500$ hours has been estimated only from the correlation graph in forementioned figure. It is obvious that correlation behavior for large Δ_T values approximately greater than 2500 hours (around the third maximum) corresponds to the non-causal case and therefore the correlation disappears and becomes accidental.

In Tab. 3.2 fitted positions of four correlation curve minima are listed for offsets $0\,\mathrm{h} < \Delta_T < 2500\,\mathrm{h}$. 6-th order polynoms were used to get the minimum positions. Minima are counted starting from $\Delta_T = 0$ in positive *offset* Δ_T direction.

The fitted first minimum of the Pearson correlation curve in positive *offset* region drawn in Fig. 3.26 resulted in $\mathit{offset}_{min1} = (120.1 \pm 6.8)$ hours. Scatter plot of corrected calibration constants coupled with temperature corresponding to the offset 120.1 hours is depicted in Fig. 3.27. The Pearson correlation coefficient for corrected constants was found $R_{\Delta_T=120.1\,\mathrm{h}} = -0.376$ for the fist minimum [10]. The linear regression was applied on this data.

Minimum	**Offset mean [h]**	**Period length [d]**
1^{st}	120.1	–
2^{nd}	774.4	27.3
3^{rd}	1487.3	29.7
4^{th}	2173.3	28.6

Table 3.2: Fitted positions of correlation minima for corrected calibration constants and for offsets $0\,\mathrm{h} < \Delta_T < 2500\,\mathrm{h}$ (see Fig. 3.26). The length of period is calculated as difference between given and previous minima.

The linear fit gives the relation between corrected absolute calibration constants and the camera temperature

$$c_{corr,T} = 4.594 + (-0.011 \pm 0.001) \times T[^\circ C], \tag{3.7}$$

where statistical error is given. The slope -0.011 defines absolute change of calibration constant per $1\,^\circ C$. In order to be able to compare the result with PMT's producer data the relative change per $1\,^\circ C$ is derived taking into account the typical value (mean 4.30 and median 4.29) of calibration constant $\sim$ 4.3:

[10] The absolute minimum was found in the position of the second positive minimum $R_{\Delta_T=774.7\,\mathrm{h}} = -0.473$.

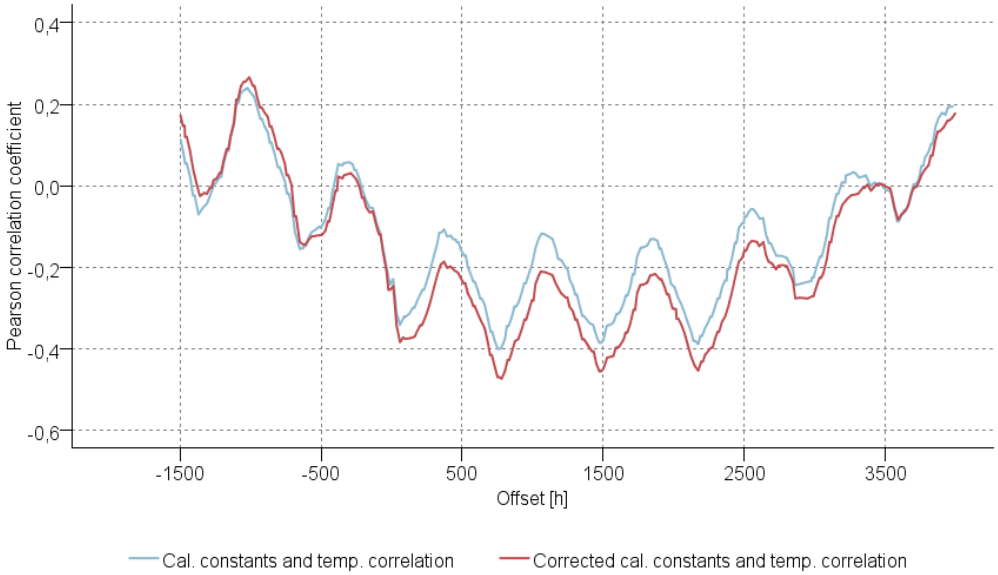

Figure 3.26: Pearson correlations between calibration constants and measured temperature shifted by offset value $\Delta_T = t_c - t_T$. Blue curve depicts correlation between original calibration constants and temperature, red curve represents correlation between temperature and corrected calibration constants. Results were obtained with 1 hour offset sampling, i.e. $\Delta_{step} = 3600\,\mathrm{s}$.

$\Delta_C \approx 0.011/4.3 \approx 0.26\%$, which is in agreement with internal Pierre Auger study [91].

The forementioned largest temperature fluctuations $\Delta_t \sim 8\,^{\circ}\mathrm{C}$ can therefore cause the change of calibration constant at the level of 2.1% (cf. value estimated in 3.5).

Calibration constants can be corrected based on slope parameter gained from 3.7. All calibration values were corrected to the temperature 21.5°C:

$$c_{corr,t_i,T_{t_i-120.1\mathrm{h}}} = c_{corr,t_i} + 0.011 \times (T[^{\circ}\mathrm{C}] - 21.5^{\circ}\mathrm{C}). \tag{3.8}$$

Standard deviations of corrected calibration values (the regression sample was used) before and after correction indicate that calibration constants distribution after trend correction gets obviously narrower:

$$\sigma_{c,trend\,corr.} = 0.099 \qquad \sigma_{c,trend\,and\,temp.\,corr.} = 0.092 \tag{3.9}$$

The temperature correction obviously removed the correlation between temperature and calibration constants (see Fig. 3.28) and made the distribution narrower (compare distribution of constants used for linear regression after the trend correction according to 3.6 in Fig. A.1 and distribution of constants after addition temperature correction according to 3.8 in Fig. A.2; both figures are in Appendix A.

In the Fig. 3.29 the long time development of pairs of corrected calibration constants for trend and temperature shifted by the first minimum offset value of

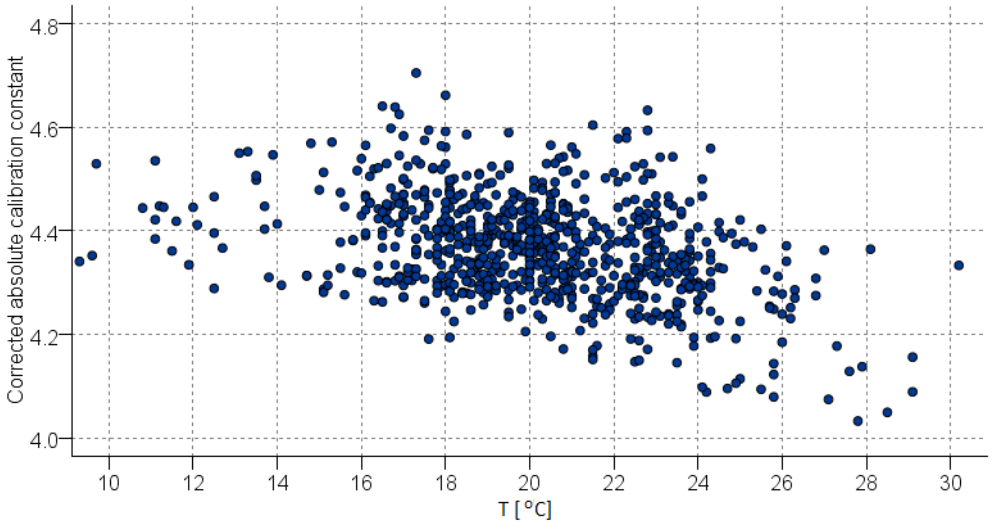

Figure 3.27: Scatter plot of corrected calibration constants and measured temperature shifted by 120.1 hours that corresponds to fitted first minimum of correlation curve for offset found at $\Delta_T = 120.1\,\mathrm{h}$ (see Fig. 3.26).

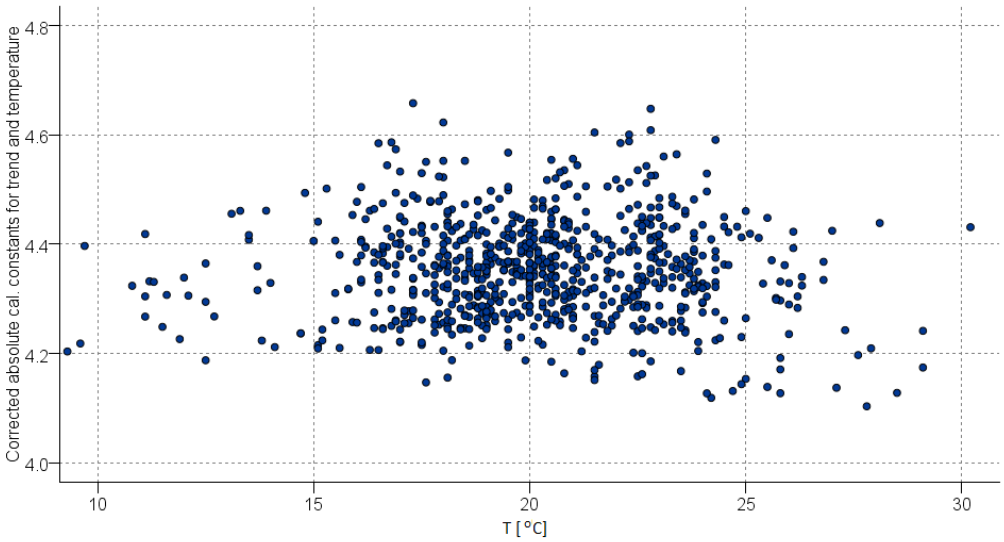

Figure 3.28: Scatter plot of corrected calibration constants for trend and temperature and measured temperature shifted by 120.1 hours that corresponds to fitted first minimum of correlation curve for offset found at $\Delta_T = 120.1\,\mathrm{h}$ (see Fig. 3.26).

$\Delta_T = 120.1\,\mathrm{h}$ is depicted. The short time development of selected period for the same offset is depicted in Fig. 3.30. Calibration constants vary during the shift period and the profile in forementioned figure has shape of 'U' letter. Figures indicate that the development of correlation in Fig. 3.26 can be result of long and

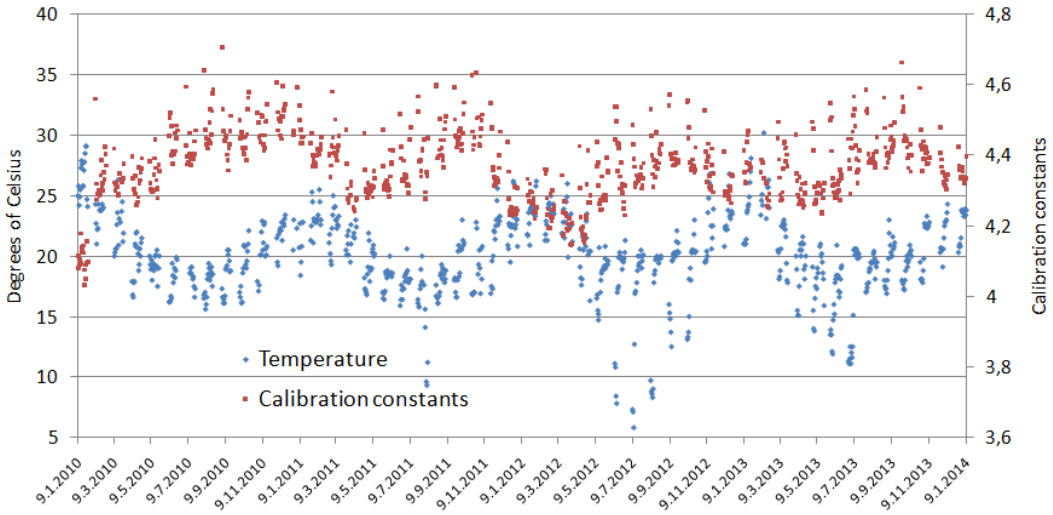

Figure 3.29: Temperature and trend-corrected calibration constant pairs for the offset value of $\Delta_T = 120.1\,\mathrm{h}$, long time period. The seasonal modulation and periodicity is clearly visible. Calibration constants are corrected for trend according to Eq. 3.6.

short time temperature development convolution. The period between correlation minima is obviously related to length of shift periods. For several months the temperature variation during day (day-to-day variation) is very similar so that there are several extremes at correlation development (it explains the periodicity of correlation curve for $\Delta_T > 0$ region for limited time period). After three months the long time anti-correlation weakens (the overall trend is relaxation). This effect is stronger than short time anti-correlation. The results of the analysis suggests that there is some effect of delayed influence of temperature.

3.3 Hybrid detection technique

The Pierre Auger Observatory is the pioneer experiment due to the combination of surface detector array with fluorescence telescopes referred to as a hybrid technique. In spite of the fact that FD uses fast electronics that ensures precise timing measurement and high accuracy of directional reconstruction, precision and accuracy can be increased by additional data measured by the SD array. On the other hand, the only SD data does not provide direct energy scale information and FD guarantees a calorimetric measurement almost independent of hadronic models. Therefore, this technique enables to calibrate signal of the SD array which has 100% duty cycle and to create converter between some SD observables and the primary energy. Except from energy spectrum also mass composition and anisotropy studies can profit from simultaneous measurements from different detectors. Schematic view of direction and hit SD stations of very rare triple event that are seen by three FDs is depicted in the figure Fig. 3.32.

The following paragraphs are dedicated to the main advantages of the hybrid

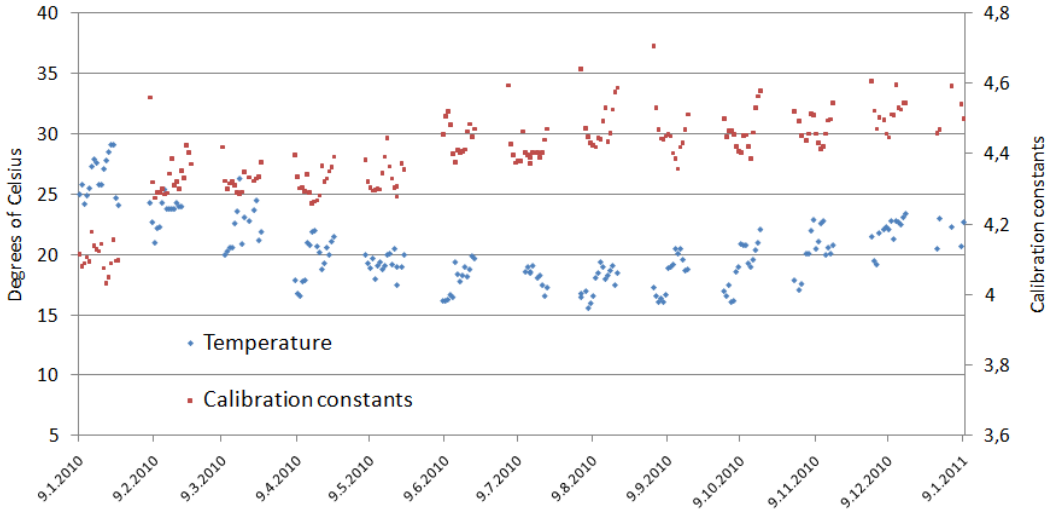

Figure 3.30: Pairs of temperature and calibration constants corrected for overall decreasing trend according to Eq. 3.6. Short time period is depicted. The offset value of $\Delta_T = 120.1\,\mathrm{h}$ is used to couple temperature and calibration data.

measurement technique. In order to stress the added value of hybrid detector measurement the description of geometry reconstruction process is explained by way of example of simple FD event. The monocular FD event reconstruction described earlier starts at finding the Shower Detector Plane (SDP), i.e. the shower plane intersecting the camera.

The SDP is fitted by means of χ^2_{SDP} minimization method taking into account signal w_i from i-th camera pixel used as a weight. In this way the algorithm prefers high PMT signal to noisy ones:

$$\chi^2_{SDP} = \sum_i w_i \left(\vec{n} \cdot \vec{d_i}\right)^2, \tag{3.10}$$

where $\vec{n}$ is the normal vector to the found SDP and $\vec{d_i}$ is the unit pointing direction vector of the i-th photomultiplier.

Once SDP is found the geometry reconstruction proceeds with shower axis finding reduced to two-dimensional problem. The shower direction within the SDP is determined using timing information from individual pixels i and minimization of χ^2_{pixel} function proportional to the sum of squares of difference between measured time of signal arrival $t_{measured}$ and expected time of arrival t_i:

$$\chi^2_{pixel} = \frac{\sum_i \left(t_i - t_{measured}\right)^2}{\sigma^2_{t_i}}. \tag{3.11}$$

where σ_{t_i} is the error of t_i pixel. The geometry reconstruction is improved in case when more than one FD camera detects the shower signal. Such events are called stereo ones and SDP can be defined as an intersection of several individually reconstructed SDPs from different eyes. The threshold for full efficiency of stereo observations by all 4 main FD telescopes is at about $\sim 2 \times 10^{19}\,\mathrm{eV}$.

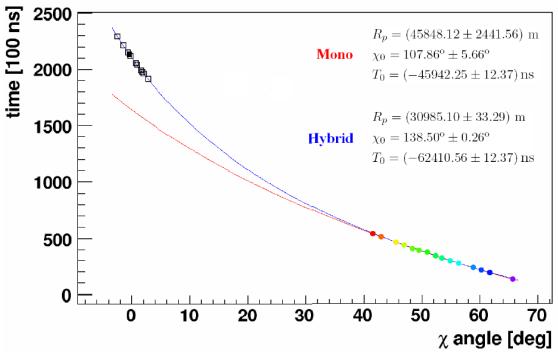

Figure 3.31: Measured arrival time from SD (black points) and FD detector (colored points) showing that for precise determination of primary particle direction SD information is necessary (adopted from [96]).

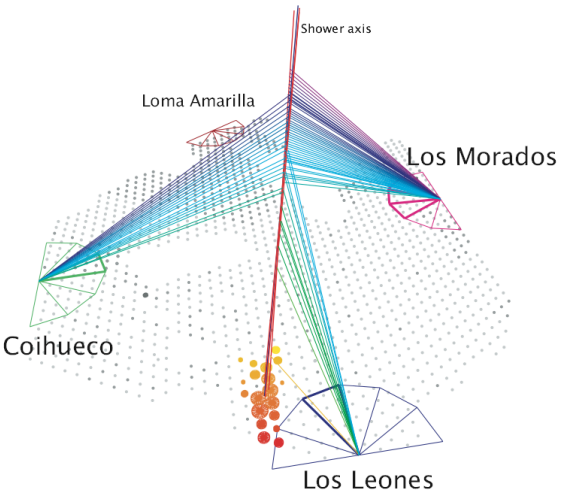

Figure 3.32: Illustration of event #3336808 geometry detected by three FD detectors - Los Leones, Los Morados and Coihueco (adopted from [65]).

Hybrid data bears fruit when the angular velocity $d\chi/dt$ of the shower is roughly constant. The angular velocity does not change very much for showers that are very close to FD or in the case of short signal track itself. For these cases the fit emerging from 3.11 minimization has quite large uncertainty. Solution of the time fit degenerates as predicted time of pixel signal arrival is calculated according to the equation 3.3. In case of constant angular velocity the relation between measured time t and angle χ on the basis of 3.3 is very close to linear. SD data remove the degeneration as indicated in the figure Fig. 3.31. Timing information from tanks is included in the time fit and the natural angular distance between FD and SD signals provides necessary additional data that lie away from straight line.

The χ^2_{pixel} function using timing information can be extended provided that one additional tank is used for geometry reconstruction:

$$\chi^2_{pixel} = \sum_i \frac{(t_i - t_{measured})^2}{\sigma^2_{t_i}} + \frac{(t_{SD} - t_{SD,measured})^2}{\sigma^2_{SD}}, \tag{3.12}$$

where t_{SD} is expected time of signal arrival from the SD tank and $t_{SD,measured}$ is measured value.

An example of the difference between FD reconstruction uncertainty and hybrid one is depicted in Fig. 3.31. Coloured points show measured FD signal and lie almost in straight lines. The degeneration results in large directional reconstruction uncertainty. The only FD data (denoted as *mono*) could lead to the solution shown by the red line. Additional SD data are represented by black points and fit by blue curve (*hybrid*) takes them into account and brakes the fit degeneracy. Reconstruction uncertainties of χ_0 and their values can be found in the legend of the figure.

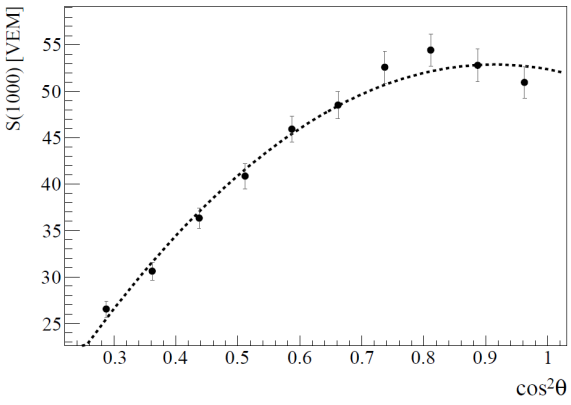

Figure 3.33: CIC attenuation curve with zenith angle θ dependence [99]. Data are fitted by a second degree polynomial in $x = \cos^2(\theta) - \cos^2(38°)$.

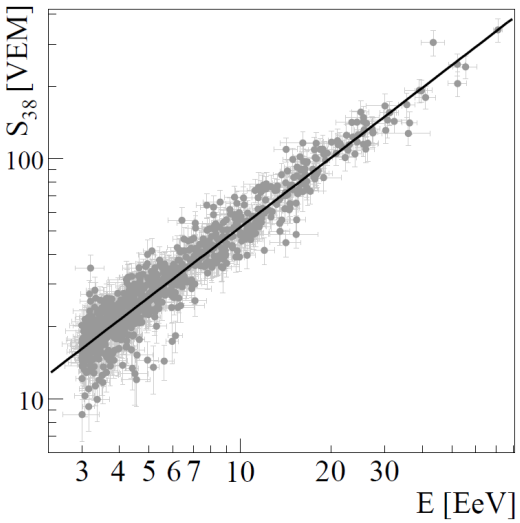

Figure 3.34: Dependence of S_{38} on energy measured by the FD from 839 reconstructed golden hybrid events [99].

FD provides the external trigger for SD array since it has lower energy threshold. On the other hand most of FD events are hybrid ones. Improvement of directional accuracy is not the only benefit of such measurement combination. Energy reconstruction enables model independent calibration of the SD as described in the next section. Shower profile reconstruction requires high quality FD measurement including X_{max} observed in the field of view (the uncertainty of X_{max} determination is $\sim 20\,\mathrm{g/cm^2}$). Number of photons at the aperture can be calculated from ADC counts measured by the camera and multiplied by the calibration constant. Emitted number of photons in atmospheric depth interval ΔX_i can be expressed by means the total energy released, fluorescence yield, atmospheric attenuation coefficient and geometric factor.

The angular resolution of SD data depends on the accuracy of the time measurement of shower front arrival. Number of hit stations naturally influences the precision of directional determination and it ranges from about 2.20 to 0.5 degrees. The angular resolution of hybrid events gets more precise with energy and it reaches resolution better than 0.5 degrees above $10^{19.5}\,\mathrm{eV}$. Nevertheless, there are many other factors like track length observed in cameras that influence the final resolution.

3.3.1 Surface detector energy calibration

Energy estimated only from SD signal depends on EAS simulations, whereas FD measures shower energy in a direct way (see 3.2). The unique design of the Pierre Auger Observatory enables to combine measurements from the two complementary detection techniques. SD array duty cycle is not restricted as opposed to FD measurement. Its duty cycle time of approximately 13% substantially decreases

integral exposure of the fluorescence detector, but it allows to measure relation between E_{FD} and some SD energy estimator in case of data recorded simultaneously by both detectors.

As mentioned in section 2.5.3 the signal measured at a fixed distance from shower core is correlated with primary energy. For this purpose 1000 m distance is the most appropriate and the corresponding SD signal is denoted as $S(1000)$ [97]. 1000 m turned out to be the optimum distance at Pierre Auger Observatory condition of SD array with 1500 m spacing in hexagonal array. At the distance of 1000 m the measured signal is robust against inaccuracies with respect to the assumed LDF [11]. After correction made due to attenuation in the atmosphere with respect to different zenith angles it is used as an energy estimator.

The signal $S(1000)$ decreases for a given primary particle with increase of zenith angle θ. This is caused by geometrical effects and increase of air mass thickness that EAS secondary particles pass through before they reach the ground level. Therefore the attenuation of $S(1000)$ is corrected for given θ by construction of so called Constant Intensity Cut (CIC) curve assuming isotropic CR flux [98] (see Fig. 3.33). Data of measured $S(1000)$ is fitted according to the following expression:

$$CIC(\theta) = 1 + ax + bx^2\,, \tag{3.13}$$

where $x = \cos^2(\theta) - \cos^2(38^\circ)$. Signal $S(1000)$ divided by $CIC(\theta)$ leads to zenith angle independent signal denoted as $S_{38} = S(1000)/CIC(\theta)$. The median zenith angle of CR arrival $\theta = 38^\circ$ is chosen as a reference angle and the equivalent signal at 38° is determined from $S(1000)$. S_{38} is the energy estimator used to calculate the primary energy by means of only SD observables. The relation between FD energy E_{FD} and S_{38} is found out by power law function regression (see Fig. 3.34).

Events used to SD energy calibration are called *golden hybrid events* which are the ones of high quality. Selection criteria are described in [67]; the data quality of each selected event enables SD data to be well reconstructed alone. 1475 events with $\theta < 60^\circ$ acquired during period between January 2004 and December 2012 with energy greater than 3×10^{18} eV were used in the analysis. The relation between energy and S_{38} can be well fitted by means of power law function:

$$E_{FD} = A\,S_{38}^{B}\,, \tag{3.14}$$

where parameters were found by the fit as follow: $A = (0.190\pm0.005)\times10^{18}$ eV and $B = 1.025\pm0.007$ [67]. The statistical energy uncertainty decreases with energy as the main deviation is dominated by low-energy showers. The uncertainties reached $\sim 18\%$ at energy below 3×10^{18} eV , which is similar to root-mean-square deviation of data sample.

[11] Expected signal was tested against assumed LDF function, the α slope parameter in the NKG formula (see Eq. 3.1). The most robustness of the expected signal was found at $r_{opt} = 1000$ m at which the signal variation was smallest.

3.4 Atmospheric monitoring

Monitoring of atmospheric parameters indisputably belongs to substantial processes of proper operation of fluorescence detectors to provide precise and reliable measurements. The production of fluorescent and Čerenkov photons as well as real amount of light transmitted to FD detector strongly depends on atmospheric conditions like humidity, pressure, temperature and aerosol concentration. Therefore, an extensive program that aims to characterize the atmosphere behaviour is operated at the Pierre Auger Observatory. It allows recording thorough information on the state of atmosphere as well as on Mie and Rayleigh scattering of UV light [100, 101, 102, 103].

Fluorescence yield depends among others on quenching of excited nitrogen molecules due to collisions with nitrogen and oxygen molecules and water vapour influenced mainly by temperature and humidity. On the other hand, Čerenkov photon production is easier to be expressed by means of temperature, humidity and vapour pressure factors.

Amount of light detected by FD telescope is affected by transmission conditions of the atmosphere. UV photons are absorbed and scattered and these both processes are usually described as light *extinction*. While absorption is negligible, UV light is scattered by molecules (Rayleigh scattering) and aerosol particles (Mie scattering). Isotropically emitted light of original intensity I_0 is attenuated during transmission so that the FD observing angle $\Delta\Omega$ at elevation ϕ can detect the intensity I as follows

$$I = I_0\, T_m\, T_a\, (1 + H.O.)\frac{\Delta\Omega}{4\pi} = I_0\, e^{-\tau(h,\lambda)/\sin\,\phi}\,(1 + H.O.)\frac{\Delta\Omega}{4\pi}, \tag{3.15}$$

where T_m and T_a represent transmission factors due to molecular and aerosol scattering. $H.O.$ is a higher-order correction that includes single and multiple scattering of photons. The right part of the equation 3.15 is the Beer-Lambert law with total vertical optical depth $\tau(h, \lambda)$ at altitude h for wavelength λ. Total vertical optical depth $\tau(h, \lambda)$ is expressed as simple sum of molecular and aerosol optical depths.

Molecular attenuation due to Rayleigh scattering has an analytical solution so that one can express vertical optical depth $\tau_m(h, \lambda)$

$$\tau_m(h, \lambda) = \int_{h_0}^{h} N(x)\, \sigma_R(x, \lambda)\, dx, \tag{3.16}$$

where $N(x)$ is density of scatterers at altitude x and $\sigma_R(x, \lambda)$ is the Rayleigh scattering cross section for light of wavelength λ which is in air approximately proportional to $1/\lambda^4$.

Aerosols are mostly produced near ground level and their density decreases vertically in the exponential way with a scale of about 1.5 km. The size of aerosol particles varies as they include bacteria, minerals, carbons and other solid particles. Aerosol optical depth does not have an analytical expression and it requires direct measurement. Nevertheless, the precise knowledge of aerosol optical depth

$\tau_a(h, \lambda_0)$ for wavelength λ_0 allows to express aerosol optical depth for other spectral wavelengths according to the following power law:

$$\tau_a(h, \lambda) = \tau_a(h, \lambda_0) \, (\lambda_0/\lambda)^\gamma \tag{3.17}$$

with Angström coefficient γ.

Monthly models of atmospheric state variables have been derived from meteorological radio-sondes mounted to helium balloons. Balloon program collected data of vertical profiles including density, temperature and humidity up to the altitude of 25 km from 331 flights between 2002 and December 2010 when it ended. Seasonal and daily variations have been studied to provide detailed model of atmospheric behaviour. The monthly models were called (new) Malargüe Monthly Models (nMMM) [104] and they were developed by averaging data from weather balloons. Besides that, the Global Data Assimilation System (GDAS) [105] has been implemented by the Auger Collaboration for air shower reconstruction. It is the meteorological model of the atmosphere developed at National Centers for Environmental Prediction (NCEP) of National Oceanic and Atmospheric Administration (NOAA). The fluctuations of the pressure, humidity and temperature on the day-to-day basis compared to GDAS model were studied by means of radio-sondes with the result of 1% uncertainty in the energy.

Each FD building is equipped with LIght Detection And Ranging (LIDAR) facilities to measure aerosol content by elastic backscatter signal from UV lasers. Backscattered light is detected by PMT with timing information that enables to reconstruct Vertical Aerosol Optical Depth (VAOD) $\tau(h)$. Two central lasers are installed in the surface detector array (see Fig. 3.35). The Central Laser Facility (CLF) produces 355 nm laser pulses which can be shot to any part of the sky with an accuracy of 0.2°. Laser pulses are detected by FD detectors. The second central laser, so called eXtreme Laser Facility (XLF) is located close the center of the SD array. Besides aerosol measurement two central laser facilities are used for the timing check, horizontal uniformity measurement and for energy and angular resolution measurements of the telescopes.

Horizontal Attenuation Monitors (HAM) are devices mounted to Los Leones FD and Coihueco buildings. They provide additional horizontal aerosol measurements. Two Aerosol Phase Function monitors (APF) are designed to determine aerosol differential cross section. InfraRed Cloud Camera (IRCC) and weather stations at each FD building are regularly monitoring sky to detect clouds and record weather conditions. This kind of information is stored in dedicated database.

Fotometric Robotic Atmospheric Monitor (FRAM) that was developed by Czech group of Auger Collaboration uses wide-field CCD camera for photometric measurements of standards (non-variable) stars that play the role of standard light sources. Photometric measurements in different filters are done to reduce wavelength dependence of studied parameters. Assuming that the magnitude of stars are known outside the atmosphere the extinction coefficient can be calculated for the whole air mass. Consequently it takes into account also the upper layers of the atmosphere above the first interaction of EAS.

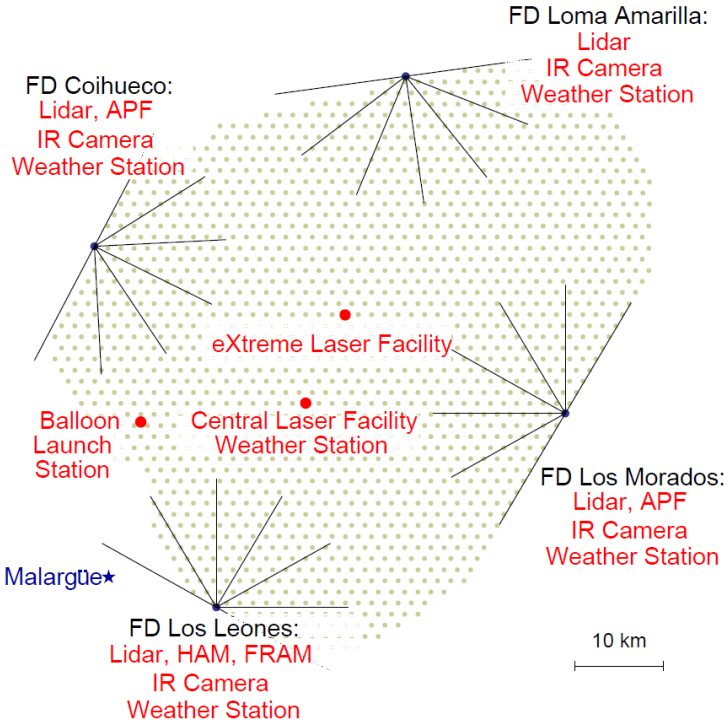

Figure 3.35: Cartoon of the Pierre Auger Observatory with location of atmosphere monitoring facilities [103].

Besides aerosols also clouds influence FD measurement very significantly because they attenuate UV light very well. This biases X_{max} measurement towards deep showers and total number of events decreases. About 30% of events are rejected due to high fraction of clouds for which the threshold 25% was set. Clouds are detected by LIDARs, CLF, XLF and IRCCs as outlined in the text above.

The quality of the atmosphere is checked also when a high-energy shower meeting some criteria is detected. LIDARs, balloons and FRAM perform rapid atmospheric measurements. FRAM checks the shower path of events close to Los Leones site by CCD camera. Up to 20 images per shower are taken to be automatically analyzed.

Shoot the Shower is performed by LIDARs triggered by high energy hybrid events. LIDARs (located at each FD building (see Fig. 3.35) as mentioned earlier) shoot around the direction obtained by fast reconstruction software to test the shower track quality. It can reveal local distorted sections in the atmosphere as well as small clouds.

Balloon the Shower was part of the atmospheric monitor program dedicated to measure pressure, humidity and temperature within three hours after an exceptional event. The program was operating between March 2009 and December 2010 and it covered more than 60 events.

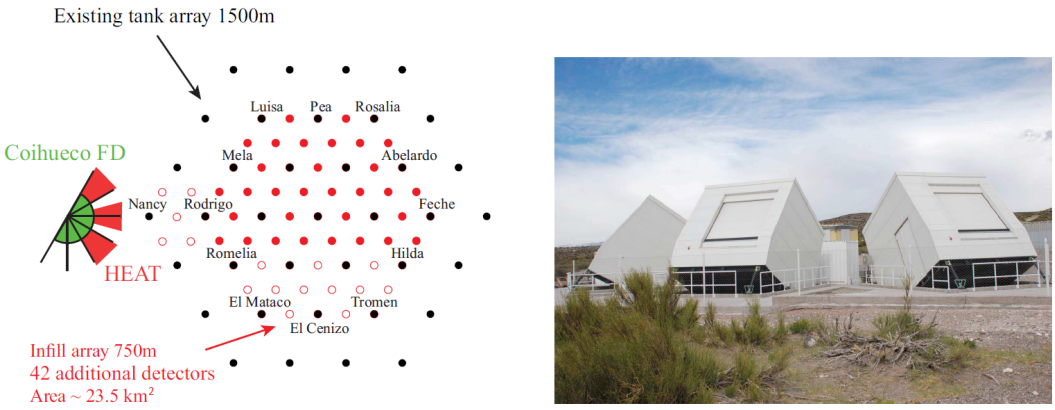

Figure 3.36: Cartoon of the AMIGA infill array and 3 additional telescopes of HEAT (left figure). A photograph of tilted HEAT fluorescence telescopes (right figure); (figures taken from [106]).

3.5 Extensions

Basic configuration of the Pierre Auger Observatory - the surface detector array overlooked by four fluorescence detectors, has been extended by new detector systems. The High Elevation Auger Telescopes (HEAT) are additional three FD detectors located at Coihueco site with field of view oriented above SD array that was infilled by additional surface detectors with muon counters called AMIGA (Auger Muons and Infill for the Ground Array) [70] (see Fig. 3.36).

HEAT lowers energy threshold to 10^{17} eV. While the original FD detectors are mounted to solid buildings, each of three HEAT fluorescence telescopes is mounted to a steel construction that enables to tilt. As can be seen from the right part of the Fig. 3.36 the operation field of view is elevated to see X_{max} of shallower showers. The field of view ranges from 30° to 58°. Except for the tilt possibility, the design of telescopes is very similar to the original FDs. Alignment of the system is adjusted in the horizontal position. Distance sensors are mounted to the camera monitor relative positions to keep the system stable.

Low energy extension of FD part is supplemented by complementary extension of SD array near HEAT at Coihueco (see the left part of the Fig. 3.36). The infill array of additional water Čerenkov stations is deployed on hexagonal grid with spacing 750 m and 433 m. Each of them is associated with muon scintillator counter of 30 m^2 area buried 2.3 m underground corresponding to equivalent atmospheric depth of 540 g/cm^2. The graded SD array allows to detect cosmic rays from energies 3×10^{17} eV and 10^{17} eV respectively.

Several devices have been developed to study radio signals of EAS. The Auger Engineering Radio Array (AERA) is a radiotelescope array composed of 21 stations with 150 m spacing deployed close to Coihueco site. Final stage of the experiment will cover nearly an area of 20 km^2 by means of 160 stations with different spacing [107]. Each radio detection station consists of an antenna with autonomous power system with readout and communication electronics. Detection of microwave

emission of ultra high energy particles in the atmosphere uses several systems. Air-shower Microwave Bremmstrahlung Experimental Radiometer (AMBER) is a large off-axis parabolic dish antenna with 30° field of view. AMBER is triggered by SD trigger T3. Its aim is to detect EAS with surface detector signal in coincidence.

Another system dedicated to detect microwave signal is MIDAS (Microwave Detection of Air Showers) with $20° \times 10°$ field of view which is provided by self-triggering 4.5 m parabolic reflector and 53 camera pixels. FDWave and EASIER (Extensive Air Shower Identification using Electron Radiometer) must be mentioned as prototypes of separated large dish antennae and antenna horns mounted to surface detectors.

Chapter 4

'Shift Guard'- the FD alarm system

The FD consists of cameras each of them is composed of 440 PMTs as it was described in Sec. 3.2. This device is very sensitive instrument requiring careful operation including precise timing. The staff that controls the FD operations are called *shifters* and during the shift night, i.e. the night when the FD is operated they need to check a lot of variables from the Monitoring System as well as the information from the Slow Control providing the interface to operate the FD [1]. Continuous checking of all systems and conditions is necessary to avoid dangerous situations. Therefore an automatic and reliable alarm system is the essential part of the whole detector to ensure its safe and stable long-term operation.

Shifters needed to check the FD system through browsing several web sites and screens without an alarm system. When the level of external conditions crossed the safe threshold, shifters did not have possibility to find out what happens without active checks. Also some failures of the internal system influenced data taking and they were indicated too late. Some situations or status of the FD requires immediate reaction in order not to lose data or in a worse case not to endanger the detector itself. E.g., light illumination of PMTs worsens its sensitivity, see Sec. 3.2. Therefore continuous measurement of the background light illumination is performed by means of the analysis of ADC (Analog to Digital Converter) counts [80]. The variance of ADC is proportional to the incoming photon flux and that is one of the observable that an automatic system must control.

A program named *Shift Guard* is a standalone C++ application to notify shifters in the Central Data Acquisition System room of some important situations or incidents. The Shift Guard serves as an automatic system to check devices and monitored values. It uses light and sound signals to inform the shifters of some alarms and therefore it solves possible situations mentioned above endangering detector and data-taking.

[1] Slow Control system enables to operate manually FD detectors; among other voltage on PMT control and it enables to open shutters before measurement from CDAS through web-page application.

4.1 FD Alarms

An FD alarm is an event raised at some situation that is very precisely described and should warn or force shifters to react according to defined instructions. Almost all information from different systems is being stored in a database system which is used as a basic data source for FD alarms. On the other hand, Shift Guard is designed to be able to get alarm signals from various communication channels.

A database system of the Pierre Auger Observatory is composed of several components. At each FD site there is one database running (hereinafter referred to as *FDLosLeones, FDLosMorados, FDLomaAmarilla, FDCoihueco, FDHeat*) that stores data regarding the given site. A replication system ensures sending all data to the main instance of the database (the monitoring database *AugerMonitor* is denominated in this text as *MonDB*) located in CDAS.

FD alarms are currently stored and written into the *AlarmTab* table of *AugerMonitor* database. They are generated by so called MySQL triggers (inside the main instance of the database checking values in *FDCoihueco, FDLosLeones, FDLomaAmarilla and FDLosMorados* databases) [2]. In other words, new entries in the database are checked immediately and if needed, an alarm is invoked and written into the *AlarmTab*. The definitions of alarms are described in the table *AlarmDefinitionTab* and one can find related threshold values in the table *AlarmLimitTab* (see Sec. 4.3.3).

An FD alarm has several attributes (from the alarm system's point of view), the most important are

- AlarmID
- AlarmDefinitionTabId
- Level (Warning, High, Critical) [3]
- FDSite (and TelescopeId if relevant)
- DateOccured
- DateAcknowledged
- Resolved (UnResolved, Self, System, Admin, uknown, Expert, SD shifter, FD shifter, Maintenance)
- DateResolved

AlarmID is the unique key for the alarm event. *AlarmDefinitionTabId* is the unique key for the alarm type. *FDSite* is a string variable with the name of site where an alarm occurred; *TelescopeId* is filled-in with number of the telescope, however

[2] Pierre Auger Database uses the Classic command based replication and this means that all commands are propagated to all other instances - mirrors.

[3] The level attribute of the alarm is implicitly contained in the unique alarm type identification, which is in the *AlarmDefinitionTabId*.

in case an alarm concerns the whole FD site (e.g. in case of some rain alarm) it contains '−1'. *DateAcknowledged*, *DateOccured* and *DateResolved* are timestamps, which means that they contain date and time information about the event associated with the alarm. The implicit boolean attribute *Acknowledged* is described further in the text and the value can be derived from the *DateAcknowledged* attribute whether it contains *NULL* or non-*NULL* value. When an alarm is invoked, the *DateAcknowledged* field contains *NULL* value, whilst the actual timestamp is filled-in when shifters acknowledge the alarm. In case the alarm is resolved the relevant field contains information how it was done otherwise it contains literal value *UnResolved*.

Shifter is notified of an alarm by means of sound and light signals. Each level of alarms has an unique and specific sound signal differentiated from each other also by the length and repetition. Colour of light signals depends on the alarm level and on the acknowledged attribute. The attribute *Level* contains one of three possible strings and the descriptions of alarm levels are as follows:

— **CRITICAL** - indicates a situation that seriously endangers the hardware and requires immediate reaction. Most probably the shifter has to call somebody to go out, or he might do something by hand because the automatic procedure failed. The change to this status causes an annoying and permanent sound alarm until it is resolved or acknowledged. Acknowledging the alarm stops the sound.

— **HIGH** - indicates that there is something wrong that surely effects the data-taking. The shifter is required to react fast, but not in a hurry. The change to this status gives a moderate but permanent sound alarm until it is resolved or acknowledged. Acknowledging the alarm stops the sound.

— **WARNING** - indicates that either some part of the FD is in a pre-stage of a high status, or that something under normal circumstances would effect the data-taking. Change to this status causes moderate sound alarm once and orange light turns on. Acknowledging this alarm causes switching light from orange to blue color in order to inform that situation can still worsen.

The logic of the alarm-system communication is depicted in Fig. 4.1. Shift Guard is running on a PC with instant access to the main database instance *MonDB* where all information about alarms is stored. Shift Guard turns on/off lights through *QUIDO* module which is an input/output system of relays that can communicate via Ethernet [4]. Alarms can be solved or acknowledged via the Auger Monitoring page interface (see Sec. 4.3). In case shifters react on the situation when an alarm is invoked they can send the signal through the web page interface saying they are aware of the alarm. The attribute *Acknowledged* is written into the database and Shift Guard indicates that.

[4]QUIDO module has in basic configuration 16 relay outputs and 1 input, it is possible to extend it by additional 16 outputs [108].

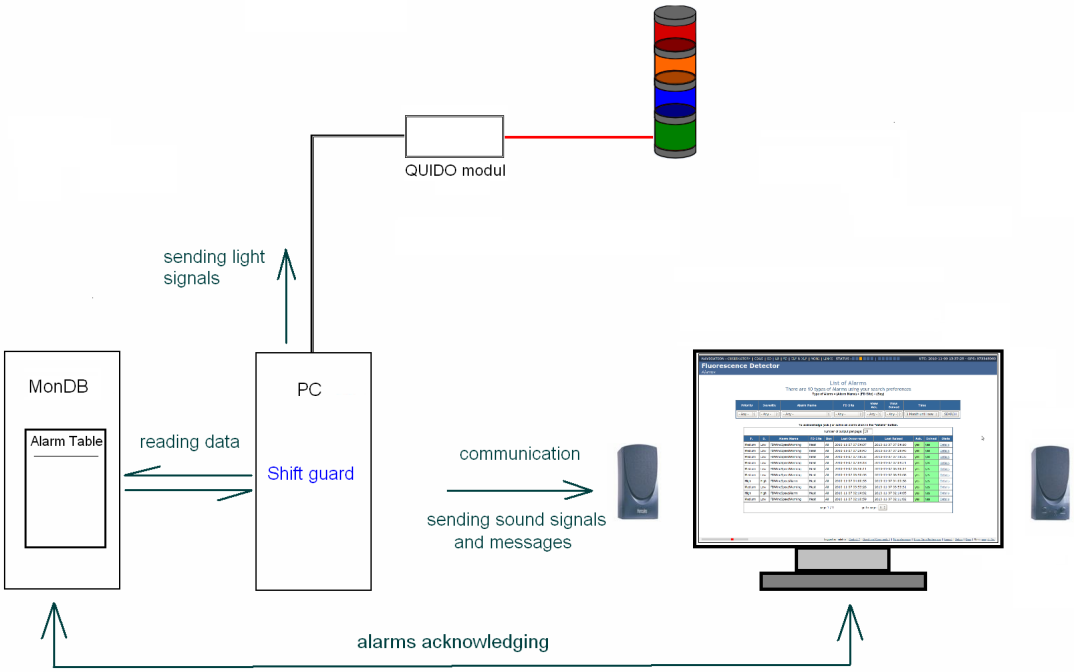

Figure 4.1: Alarm system communication logic. Shift Guard permanently reads information from *MonDB* where all alarms are inserted by triggers or external sources. There is the *QUIDO* module depicted that makes the connection between lights and the Shift Guard PC.

Figures included in Appendix D are showing schema of electric connection (see Fig. D.1) of the currently used lights and relays. There is a photo of plastic cover of the command system in Fig. D.2 that is composed of the QUIDO module and the power supply. The QUIDO module has an Ethernet plug to communicate with managing program Shift Guard (C++ application running on the steering PC). The light column is an extendable system of individual diode modules. The QUIDO module uses 24 V power supply which is itself powered by 230 V.

4.2 Functionality of Shift Guard

Shift Guard is primarily devoted to the FD alarms and it reacts to a change of *AlarmTab* which contains all types of alarms (originated from FD, SD, CDAS,...). It is implemented as an extendable multi-threaded C++ application to provide the opportunity to cover different part of FD and also SD detector or IT systems (it enables to monitor communication channels, responsiveness of systems, Lidar functioning). Communication interfaces and multi-thread approach allow to use different data sources of MySQL type or based on TCP/IP protocol.

Shift Guard application uses a list of associated alarms to manage a set of ac-

tivated alarms. It contains a basic description of alarms, their level and related sound (a special sound can be assigned to each alarm) in addition to other characteristics. By editing the list one can add or modify a set of active alarms (see Sec. 4.3.2). The current list and descriptions of these alarms are listed on the Auger wiki pages [109]. When *AlarmTab* changes Shift Guard tests if any of monitored active alarms was invoked (occurred) or changed.

The current host PC for Shift Guard is called *Ronja* and it is accessible only from CDAS. Shifters are supposed to check if the Shift Guard process is running before the start of the measurement each shift night. It is common practice to shut down the Shift Guard after the measurement and to start up the program at the beginning of the shift night [5]. The step-by-step description of the checking procedure can be found in [108].

The detailed view of the Shift Guard architecture is depicted in Fig. 4.2. New entries in five databases (*FDLosLeones, FDLosMorados, FDLomaAmarilla, FDCoihueco* and *FDHeat*) are checked by MySQL triggers and if they fulfill appropriate alarm condition, an alarm is invoked or its status is changed (e.g. to *'Resolved'*). Afterwards, if there is any change of *AlarmTab* table in the *MonDB* Shift Guard reads it and updates alarm status information. Sound and light manager of Shift Guard immediately reacts to data stored in *AlarmTab*.

Shift Guard uses its own logic of alarm management taking the attribute of alarm level into account. Multi-threaded implementation allows simultaneous alarm processing. Intrinsic code uses a queue of unresolved alarms which can be extended by a new alarm at any time or some alarm can be excluded when it is resolved. When the queue changes, the highest level alarm is found to play its melody. A melody of highest alarm is played at any time and after resolving or acknowledging the remaining alarms are processed. The lights can be turned on at the same time, but the logic of alarm sound is set to inform shifters about alarms with the highest level attribute.

The *Slow Control* system provides all hardware operations and conditions checking. This is a basic part of the whole fluorescence detector. The Slow Control measurements are of several types ('change', 'watch') depending on the information significance and they are logged in the database. It is intention to implement additional alarms raised by Slow Control that concerns e.g. unexpected closing of shutters (that can be recognized using known shutter schedule and the information who closes the shutter) and problems with air-conditioning. Some of checks can require the external data input as indicated in Fig. 4.2. A new background camera technology provides reliable cloud conditions that directly affect data quality. The Shift Guard implementation offers a way how to control and to document data quality, since defined changes can be evaluated and shifters can be notified.

Running of the Shift Guard must be continuously checked by a superior system to ensure permanent control of the detector system. It could be done either manually as described further in the text, but Shift Guard process can be repeatedly checked by *NAGIOS* that plays the role of the alarm system control raising

[5] Currently there is an intention of this thesis and the Alarm system author to develop automatic check of the Shift Guard running via NAGIOS system (see next sections).

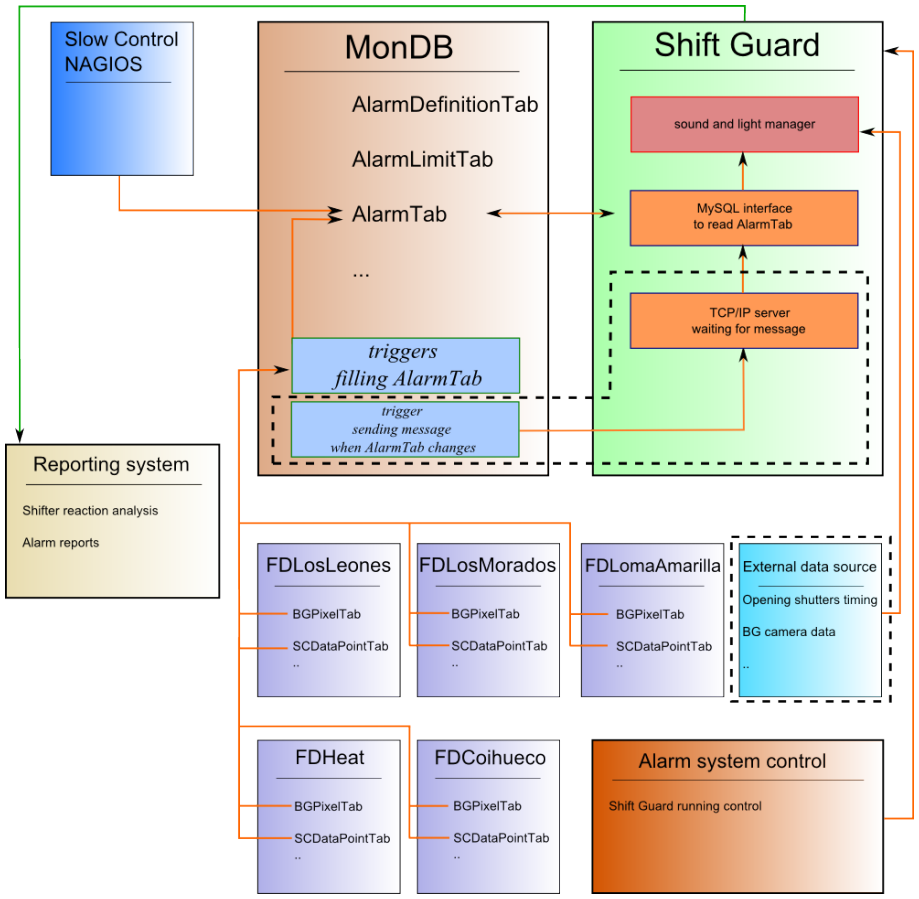

Figure 4.2: Detailed communication schema of the alarm system with the database alarm source and other sub-systems. All alarms are written into the *AlarmTab* database table which is read by Shift Guard. The Slow Control system and database instances *FDLosLeones, FDLosMorados, FDLomaAmarilla, FDCoihueco* and *FDHeat* are sources for MySQL triggers that invoke alarms. The dashed line depicts parts of the system that is still being under construction or patially installed.

its own alarm of type *Nagios_Extreme* on condition that it unexpectedly crashes. *NAGIOS* is the monitoring system that enables to identify and resolve IT infrastructure problems. The *NAGIOS* also periodically checks timing system and it is another source of alarms that writes occurred serious problems into the *AlarmTab* table. Therefore it ensures that Shift Guard reacts to that type of messages.

As a benefit, shifter's reactions on alarms and unexpected situations can be verified as time stamps are written into the database when an alarm is invoked, acknowledged or solved. The reporting system exploits information from *MonDB* and also from log files of the Shift Guard. The current solution of the Reporting system is implemented off-line (besides the monitoring website with the most recent alarms and filter described later in the text). On the standalone basis the stored data are analyzed (the analysis is performed in IBM SPSS Modeler software) and performance summary is described in Sec. 4.5 of this chapter.

Starting, stopping and getting status of Shift Guard application is provided by a script called **shiftGuard** [110] accessible from CDAS on the steering PC. The *FD Run Checklist* that helps shifters to check if everything needed was done contains also description of necessary operations with the FD Alarm System [111]. The checklist is used by shifters during FD operation. The Shift Guard is needed to be working during each night of the measurement period. In order to deactivate the application during the day when maintenance can produce fake alarms it is recommended to stop the Shift Guard and it disables the intrinsic alarm management system during the day or between two measurement periods. The lights are turned off.

The script **shiftGuard** to operate Shift Guard application is located on the steering PC and there are commands to start and stop the application. Moreover, a script to get status of the Shift Guard helps to check if the alarm system is active. There is also a command to stop playing all melodies in case of exceptional situations, however it is supposed to be used only after the Shift Guard is stopped and there are still sounds.

When the Shift Guard is being about to start the light column test is performed and sound signal confirms that all systems are ready. When the Shift Guard is stopped all sounding melodies which is or those just about to being played are also halted and lights are turned off.

4.3 Alarm logic

Programmed alarm logic describes envisaged treatment of alarms including automatic invoking and solving. It is designed in accordance with the idea of *minimal shifter intervention* making the system as much automatic as possible. The current list of the active FD alarms is listed in Tab. 4.1. The updated list of alarms used during the shift night is defined in the settings file `moniDB.alarms` stored in the steering PC (system of settings files is outlined in Appendix E). `moniDB.alarms` file is described in the end of this section. There are alarms that are associated to an FD site (LosLeones / LosMorados / LomaAmarilla / Coihueco / Heat) or more concretely to a bay. Logic of all alarms were proposed according to the two basic rules to help shifters to react promptly on important situations and to avoid to detract attention from considerable issues:

- The rule of *maximum autonomous system*
- The rule of *one active alarm* of each kind related to the same source site

A human intervention is needed only when it is really necessary. *One active alarm* ensures that there won't be successive or multiple warnings concerning the same alarm. That is - the same alarm type related to the same situation at the same site. When the wind speed exceeds the threshold value at e.g. Coihueco several times only one alarm will be invoked. On the other hand in case that wind speed breaks the limit at some different site simultaneously an additional

Alarm name	Level	Assigned to	Description
FDWindSpeedWarning	WARNING	FD site	**I**: Wind speed is greater than *MaxValue*; **R**: Wind speed is lower then *MinValue*.
FDWindSpeedAlarm	HIGH	FD site	**I**: Wind speed is greater than *MaxValue*; **R**: Shutters are closing and DAQ is stopped.
SinglePixelVarianceWarning	WARNING	bay	**I**: $N_{pixel}^{var>200\,\mathrm{ADC}^2} > MaxValue$; **R**: $N_{pixel}^{var>200\,\mathrm{ADC}^2} < MinValue$.
FDRainAlarm	HIGH	FD site	**I**: Rain is detected; **R**: Raining stops.
FDChktimeError	HIGH	FD site	**I**: A problem with the FE crate times detected; **R**: Problem is fixed, system resolves the alarm itself.

Table 4.1: List of the FD alarms. In the column 'Description' there is rule for invoking the alarm (**I**) and for automatic denoting as *Resolved* (**R**). Limits for invoking and automatic solving of alarms (*MinValue* and *MaxValue*) are defined in *AlarmLimitTab* in *MonDB* table. Each type of alarm has its own limits *MaxValue* and *minValue*.

FDWindSpeedWarning alarm is invoked. There is always only one 'UnResolved' alarm of each kind (assigned to specific site - an FD site or bay) in the *MonDB*. Shifter's reaction is demanded when there is a new alarm. Shifter acknowledges all new alarms (see Sec. 4.3.1) and takes all the necessary steps to avoid dangerous situations. Each alarm type has its specific limits *MaxValue* and *MinValue* that define when alarms are invoked and possibly automatically solved.

An illustrative wind speed measurement is depicted in Fig. 4.3 showing points where alarms are invoked and automatically solved. The limit for high level alarm *FDWindSpeedAlarm* is set to 50 km/h and warning limits are set to 20 km/h (*MinValue*) and 40 km/h (*MaxValue*). The 20 km/h difference between the low and high levels defines a hysteresis to avoid successive invoking and solving the alarm immediately after that and frequent recurrences. When the wind speed value reaches the higher warning level (40 km/h), an WARNING alarm is written into the *AlarmTab* to warn of possible disruption of the data taking. If the wind speed decreases below the lower warning level (20 km/h), the MySQL trigger (see Sec. 4.3.3) solves the alarm without necessity of shifter's reaction. The high level alarm *FDWindSpeedAlarm* has only one limit 50 km/h (*MaxValue*) when the data taking is stopped by automatic closing of shutters. Shifter needs to stop the DAQ when it occurs and after that, the MySQL trigger denotes the high level alarm as 'Resolved'. The rule of *one active alarm* of each kind is applied and if there

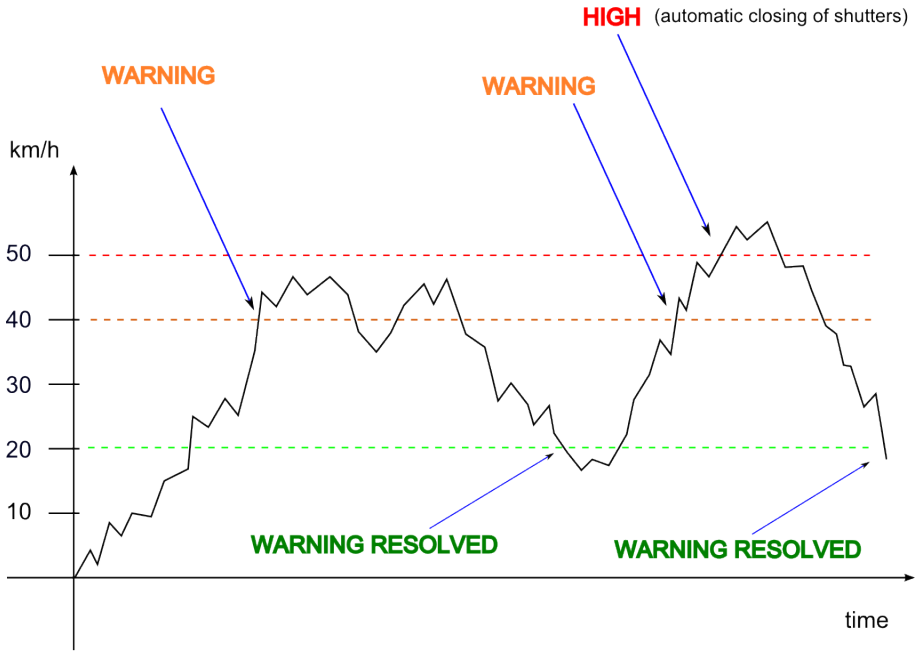

Figure 4.3: The wind speed alarm logic illustrates when the alarm is raised and automatically solved by MySQL triggers. When the winds peed exceeds the limit 40 km/h *FDWindSpeedWarning* is raised until the value decreases below the limit 20 km/h. If the value surpasses above the 50 km/h *FDWindSpeedAlarm* is invoked which is automatically solved after stopping DAQ in conjunction with closing shutters.

is 'UnResolved' alarm, let's say *FDWindSpeedWarning*, no other alarm is invoked even if the value of wind speed vary around the higher limit 40 km/h. Moreover, there is a minimal count of limit exceeding that must occur consecutively defined in the database table *AlarmLimitTab*). This minimal number (> 1) of successive breaking the threshold prevents from the situation of sudden increase of some monitored value. In the case when the minimal count of limit exceeding is set to be greater than 1 the alarm is not invoked when the monitored value breaks the limit only once and after that the value decreases to the normal level.

The logic of *SinglePixelVarianceWarning* alarm is similar to the previous warning level alarm regarding the hysteresis and automatic solving logic. MySQL trigger (see Sec. 4.3.3) performs the automatic checks of the camera pixel variances. Hot pixels that denote individual pixels with high variance values should be monitored as high variances can damage the camera sensitivity (see Sec. 3.2.4). There is no automatic procedure to close the shutters in case of several too hot pixels regardless of their variances. Schema of *SinglePixelVarianceWarning* alarm is showed in Fig. 4.4 with limits 10 (*MaxValue*) and 5 hot pixels (*MinValue*) (with variances higher than 200 ADC^2). When the number of hot pixels (with variances higher than 200 ADC^2) exceeds the higher limit (10), the alarm is invoked and according to the formerly described rules, it is automatically resolved when the number of pixels falls below the lower limit (5).

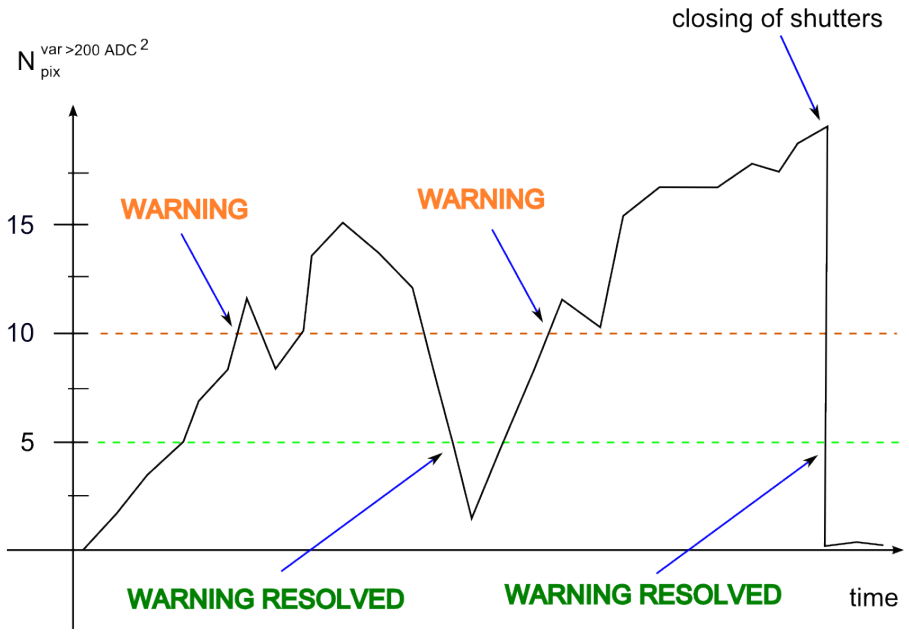

Figure 4.4: The logic of single pixel variance alarm which is sensitive to $N_{pixel}^{var>200\,\mathrm{ADC}^2}$ that counts the number of pixels on camera with variances higher than $200\,\mathrm{ADC}^2$. If $N_{pixel}^{var>200\,\mathrm{ADC}^2} > 10$, *SinglePixelVarianceWarning* is invoked until $N_{pixel}^{var>200\,\mathrm{ADC}^2}$ is less than 5.

The list and descriptions of alarms are accessible on the Auger Monitoring wiki pages hosted in Malargüe [109]. Current active alarms checked and processed by the Shift Guard application are enumerated in the settings file `/home/auger/alarms/settings/moniDB.alarms` stored in *Ronja* PC and contains the following information:

84 FDWindSpeedWarning FD-WE Medium Low 1 noSoundMessage
85 FDWindSpeedAlarm FD-WE High High 2 noSoundMessage
86 SinglePixelVarianceWarning FD-FE High Medium 2 noSoundMessage
87 FDRainAlarm FD-FE High High 2 noSoundMessage
90 FDchtimeError FD-FE High High 2 noSoundMessage

There is description of the meaning of individual fields by the following example:

84	FDWindSpeedWarning	FD-WE	Medium	Low	1	noSoundMessage

- *84* - The unique key of the alarm type referred to as `Id` in the *AlarmTab* database table called *AlarmDefinitionTabId*. This is the unique number assigned to each alarm type. Shift Guard searches for alarms according to this key.
- *FDWindSpeedWarning* - The unique name of the alarm.
- *FD-WE* - The system which is ultimately responsible for calling the alarm.

- *Medium* - Priority of the alarm.
- *Low* - Severity of the alarm.
- *1* - Level of the alarm. **1** means WARNING, **2** means HIGH, **3** means CRITICAL.
- *noSoundMessage* - Specific sound message associated to the alarm. *noSoundMessage* means that only predefined sound signal is played when the alarm is invoked until it is resolved or acknowledged. Predefined sound signals would enable to use specific sound message to each alarm in the next release of the alarm system.

4.3.1 Acknowledging and solving the alarms

Sound and light signals are initiated immediately after a new alarm is invoked. Nevertheless, the sound signal can be stopped by acknowledging the alarm. It is always done by a human intervention through the Monitoring web page [112]. There is a filter to allow shifter to find a specified alarms and below it one can find list of alarms ordered by time, the most recent is the first one (see Fig. 4.5). Each of found alarms can be denoted as 'Acknowledged' by clicking on 'Details' button in the alarm list. Acknowledging the alarm stops playing the sound and in case of warning alarm the light signal changes from orange to blue one. It makes Shift Guard possible to show another warning alarm via the orange light signal. Therefore acknowledgement must be the first shifter's action when an alarm occurs. In exceptional cases there is a way to solve the alarm 'by hand' via the alarm management, too. *AlarmTab* contains column 'Resolved' to identify who solved the alarm, except for 'UnResolved' entry there is an identification of person or system ('FD Shifter', 'Self', 'Admin', 'Expert',...).

Just after acknowledging or solving an alarm, the alarm management interface writes changes into the *AlarmTab* of *MonDB* and the Shift Guard immediately reacts on that. Time stamps of all such actions are stored in the database and provide the collaboration with the feedback through specific analysis.

Alarm Level	Not acknowledged	Acknowledged
warning	orange	blue
	a gong played once	no sound
high	red	red
	a permanent melody	no sound
critical	red	red
	a permanent melody	no sound

Table 4.2: Alarm level signal summary with respect to *Acknowledged* attribute.

The Tab. 4.2 summarizes light and sound signals of all three alarm levels regarding *Acknowledged* attribute. It describes behaviour of the alarm system in case

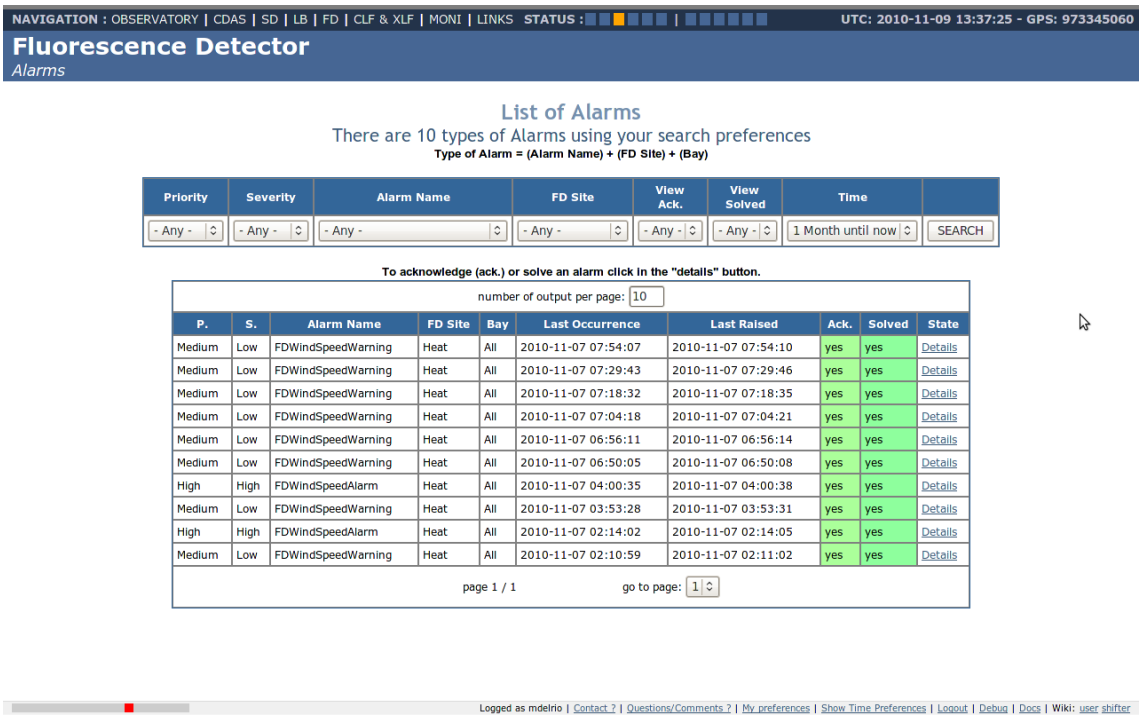

Figure 4.5: FD Alarm management from the monitoring web page allows shifters to acknowledge alarms and to solve them if needed. There is an alarm filter and list of found alarms below that.

of an alarm is acknowledged.

4.3.2 Necessary steps to manage a new alarm

When a new alarm is implemented via some intrinsic algorithm (e.g. a new trigger that fills the *AlarmTab* table, or external code that writes directly into the *AlarmTab*) there is a quite straightforward, but essential sequence needed to be done. To prepare the Shift Guard in order to react on a new alarm one has to change list of active alarms defined in the file `moniDB.alarms`. This settings file is read during the start of the Shift Guard. The analogical sequence can be used to deactivate the alarm - it avoids the Shift Guard to respond to a particular alarm:

1. Stop the Shift Guard.
2. Add/remove the alarm into `moniDB.alarms` settings file.
3. Start the Shift Guard.

In case of some failure (e.g. when the alarm is not properly defined in the settings file `moniDB.alarms`) the intrinsic exception is invoked that ends in written specific message to the current log file stored on the steering PC.

Trigger	Table	Related alarms
SCDataPointTabTrigger	SCDataPointTab	FDWindSpeedWarning FDWindSpeedAlarm FDRainAlarm
RunTabCleaner	RunTab	FDWindSpeedWarning FDWindSpeedAlarm FDRainAlarm
PixelVarianceTrigger	BGSampleTab	SinglePixelVarianceWarning

Table 4.3: MySQL triggers and their characteristics. Each trigger is running on definite table and can invoke or update several alarms.

4.3.3 MySQL triggers

There are automatic checks of all new values of specified variables performed by MySQL triggers. They are procedures associated with tables and they are activated when a particular event occurs in the table, e.g. after inserting or updating values. Triggers that are used for FD alarms are listed in Tab. 4.3 with associated tables and alarms. Whenever a new (or updated) value is written to the table, the trigger is executed. Trigger contains above described logic to create or update an alarm if the checked value exceeds limits that are read from the database when executed. When the trigger finds that some variables or situation meet the conditions for the new alarm it is checked whether the alarm of that type is already active in the table (not resolved). Only in the case that there is no such alarm the new item is inserted into the table.

Changing the limits requires only *AlarmLimitTab* database table update. Tab. 4.3 also shows alarms that can be raised by each of the trigger. Some triggers are implemented in each of the FD site databases and some triggers can run on the *MonDB* database. Beside triggers writing or updating alarm entries in *AlarmTab*, there is a new MySQL trigger called *AlarmTabTrigger* that sends a message to the Shift Guard in case the *AlarmTab* changes. At the time of finishing this thesis this trigger is not used as it requires new MySQL server installation. The *AlarmTab-Trigger* should decrease the MySQL load. On the other hand the current approach of permanent database table polling (3 times per a second) have an advantage of immediate information when the MySQL database is not available. These failures are logged and are evaluated off-line through the alarm reporting system (see the Sec. 4.5). In case the new trigger *AlarmTabTrigger* is implemented, the continuous checking of MySQL database connectivity will remain (with lower frequency than now). *AlarmTabTrigger* calls a simple C++ program that uses TCP/IP protocol that only sends the predefined message.

The database architecture distinguishes master database (*MonDB*) and slave database (*PaoMonDB*) (there is a replication process from FD site database (Eye)

database and *MonDB* and data are mirrored by means of another replication process *MonDB-PaoMonDB*). *PaoMonDB* is Auger database mirror located in Wuppertal in the Germany. Thus, the process of a trigger addition / removal has to be done carefully. The brief process how to drop / add MySQL triggers follows the sequence:

1. Connect via socket
2. (Stop slave)
3. Drop/create trigger(s)
4. (Start slave)

The above listed command sequence represents the conservative one. Stopping the slave is not necessary, however one should connect to the correct instance. Generally, the current database mirroring solution uses the statement-based replication (also called the classic command based replication) and therefore triggers executed on the master are replicated and executed on the mirror site. The effect of the triggers (filling into the *AlarmTab*) is not replicated and therefore it is necessary that the alarms are triggered on the mirror-sites. Thus, triggers work also on the mirrored MySQL database server (the slave), that is on *PaoMonDB*.

The replication process should be stopped when the trigger is (or is about to be) installed on *MonDB* not to make it break if the client fails with the command.

Although the current solution of reading the *AlarmTab* unnecessarily increases the workload of database processes, the additional load is reduced. The permanent process of *AlarmTab* check is controlled by an individual thread of the ShiftGuard that mediates communication interface to general MySQL database. The table pooling frequency is three times per second and the database select is optimized. Even then the Shift Guard should work only during the FD shift night.

AlarmLimitTab contains limits. After their exceeding an alarm is invoked. It can be defined by minimum value *MinValue*, maximum value *MaxValue* and maximum number of occurrences *MaxOccurances*. This enables to implement hysteresis - that is the different values for the situation when an alarm is invoked and when it is resolved. Moreover, *MaxOccurances* defines number of occurrences that must be exceeded successively to raise the alarm [6]. On the other hand *MaxOccurences* defines maximum number of tolerated limit breaches. The two last features ensure the stability of the alarm system announcements (see Fig. 4.3 where the hysteresis is described by the example.).

4.3.4 Alarm priorities and alarm information update

In general, more than one alarm can be raised and therefore they must be stored and processed. The list of managed alarms is dedicated to that purpose internally

[6] Defined number of last measurements of each variable is monitored in this way in the alarm triggers.

in the Shift Guard program. When a new alarm is pushed to (or removed from) the alarm list queue, it is checked whether some light should be turned on/off and whether a different sound (assigned to greater/lower level of alarms) should be played and lights and sound are adjusted. The same procedure is performed when some status of an alarm is changed.

The interface with MySQL database provides communication with *MonDB*, but it is prepared to be used for general database information exchange. MySQL interface checks alarms with *UnResolved* attribute when the Shift Guard starts and they are immediately processed. Then, in a closed cycle *MonDB* is checked if a new alarm was written in. Besides, all alarms stored by *AlarmManager* are checked if their status changed. The last check searches for unresolved alarms and they are sent to be processed. This is the control whether some alarms with *Resolved* attribute changed their status to *UnResolved*. The above described procedure that ensures the alarm checks by means of the table polling can be summarized in three steps:

- Check all *UnResolved* alarms with *AlarmID* greater than the last one: these are new alarms.
- Check the list of alarms stored by *AlarmManager* and control it in the *AlarmTab* if something has changed.
- Search for all unresolved alarms - this check brings new message in the case that some old and *Resolved* alarms changed status to *UnResolved*.

4.4 Technical implementation

The Shift Guard software description can be found in [113] and detailed documentation in *html* format is attached to the Shift Guard source code stored in internal collaboration software versioning and revision control system. The C++ application was implemented in the thread-safe way with three main threads (see Fig. F.1 in Appendix F):

QUIDO thread provides synchronized QUIDO module operation and implements list of tasks which is one of attributes of the *AlarmManager* that handles all alarms [7].

TCP/IP thread provides communication via TCP/IP protocol and enables to control functioning of various range of systems and to communicate with them. The current operation is limited and it permanently sends signal to check *MonDB* database table. After installation of new MySQL version the database trigger will communicate via TCP/IP when the table with alarms is changed instead of continuous reading. The *TCP/IP thread* can be used to ping the Shift Guard to check its functioning.

[7] QUIDO thread is ready to read input value that can be connected to e.g. emergency button in CDAS.

MySQL thread is independent separate thread that ensures database communication. It is used to read data from *AlarmTab* table where FD alarms are written. The general approach enables to add another database sources to be read (it could be another external data used for alarms evaluation or another separate alarm source). *MySQL thread* ensures check the *MonDB* connectivity via permanent table polling. In case the connectivity is broken it is logged in the standard log file and the Shift Guard tries to reconnect.

Besides these threads, there is an advanced thread-safe *Logger* implemented in the Shift Guard that enables to log messages of different seriousness for further analysis (the brief operation analysis report is included in the next section).

4.5 Operation summary

Operation data from the alarm system is analyzed off-line in the Reporting system (so far implemented in IBM SPSS Modeler software and as a standalone C++ application) and the summary follows in this section. The operation of the alarm system started in October 2010. Reporting system uses data from two sources - database *MonDB* and log files that directly document working of the Shift Guard and writes possible crashes, problems and errors and up-time of the application. All external commands to Shift Guard (e.g. stop and start the system) are logged. Number of

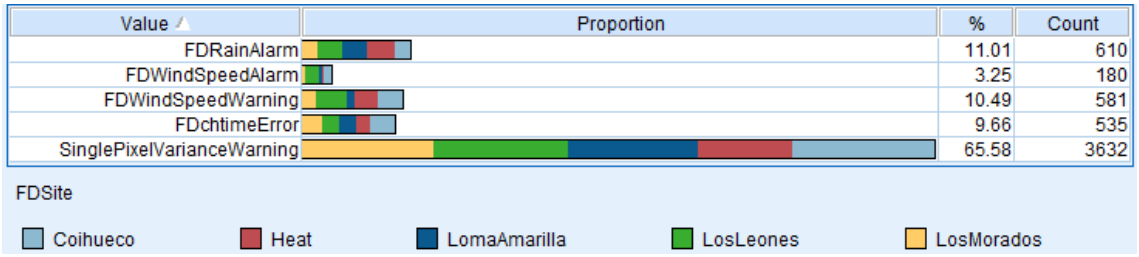

Figure 4.6: Statistics of raised alarms during period from October 2010 till February 2014 distinguished according to the alarm type and FD site at which alarms were invoked.

individual raised alarms from operation start in October 2010 till February 2014 is summarized in Fig. 4.6 segmented according to the FD site. Histogram with four types of alarms - all alarms that were raised during Shift Guard operation, shows that the prevailing alarm type is the variance related one (more than 65% of all alarms). There is also evidence that the overall number of variance alarm events is roughly the same for all Eyes (slightly smaller number of occurrences for Heat).

The time distribution of alarm types plotted for the last two years is in Fig. 4.7. The most frequented alarm type is *SinglePixelVarianceWarning* which is very often raised in January and February in the period of short nights.

Similar view on time distribution of raised alarms is drawn in Fig. 4.8 together with absolute numbers and percentage ratios calculated from all number of alarms (cf. Fig. 4.6).

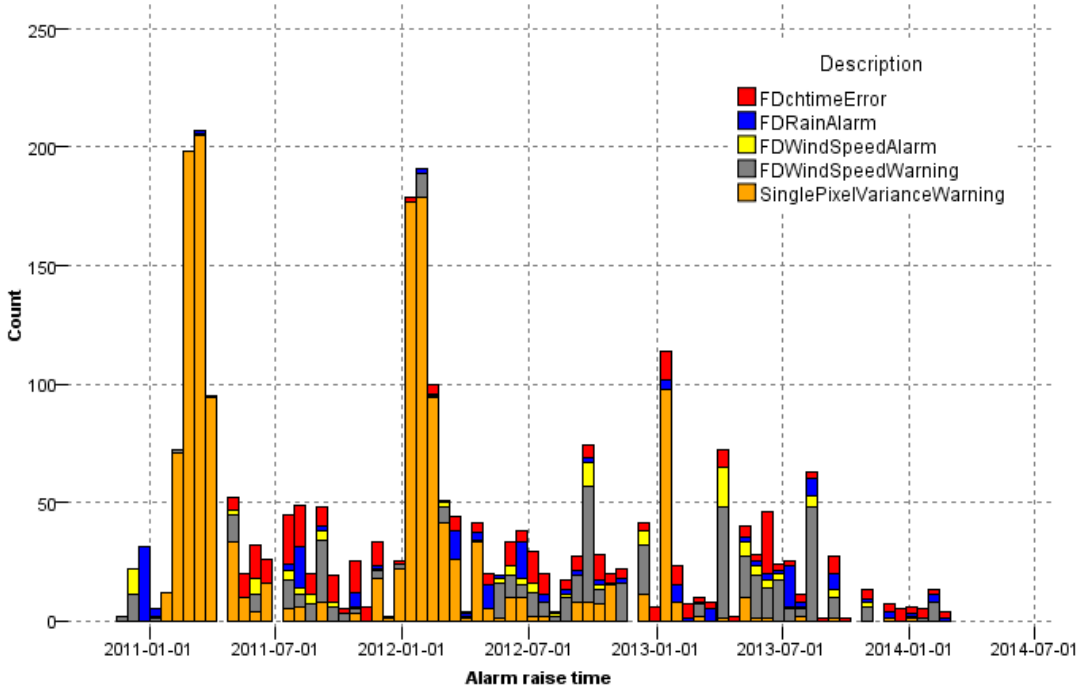

Figure 4.7: Distribution of raised alarms during operation period from October 2010 till February 2014 according to the alarm type.

Distribution of time needed to acknowledge the alarm is drawn in detailed view (short time range from 0 up to 300 seconds) in Fig. 4.9. This time difference between the moment when the alarm is raised and the moment when it is acknowledged can be considered as the reaction time since the manual input from shifter is needed.

Distribution of reaction time with x-axis range up to high values is depicted in Appendix G in Fig. G.1. The basic descriptive statistics can be found in Tab. 4.4. Only alarm observations with *Acknowledged* status were selected (there are alarms that were raised, not acknowledged, but resolved) [8]. 91 outlier values (time to acknowledge greater than 24 hours) were excluded from the sample.

Median values vary from slightly longer time than 2 minutes for wind alarm and pixel variance warning and approximately 3 minutes for the rain alarm and wind warning. There are few outliers. Some of them could be caused by situation when the Shift Guard runs even after the end of shift night, but some of them could indicate not sufficiently careful operation of shifters.

Distribution of time intervals needed to resolve alarms is drawn for short time range (from 0 up to 300 seconds) in Fig. 4.10. The same variable distribution with x-axis ranging up to high values is depicted in Appendix G in Fig. G.2. Descriptive statistics can be found in Tab. 4.5 [9].

[8] 69% of *FDRainAlarms* were directly solved by DAQ stop command instead of acknowledgement before that. Similarly 44% for *FDWindSpeedAlarm*, 33% for *FDchtimeError* and 17% for *FDWindSpeedWarning*. Absolute numbers can be found in Appendix G in Tab. G.1

[9] *SinglePixelVarianceWarning* alarm is omitted from statistics as resolved times were not stored

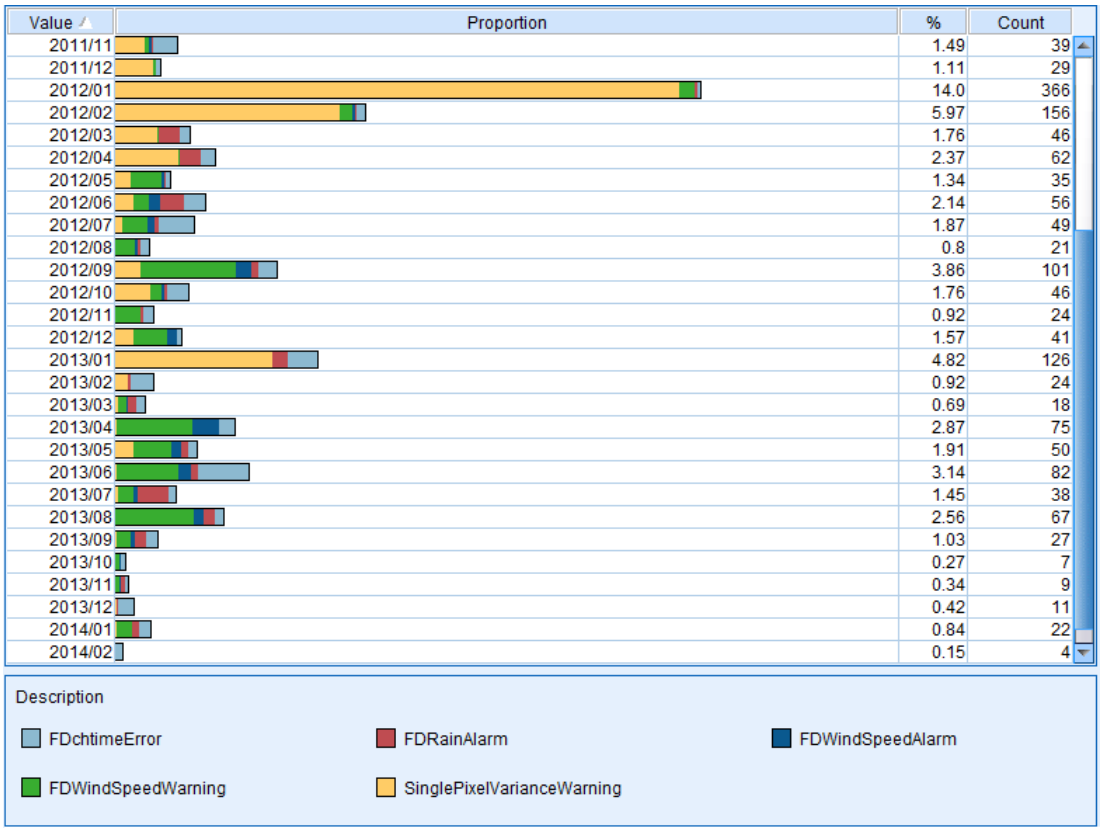

Figure 4.8: Number of raised alarms and their types during the most recent period. The absolute numbers of raised alarms and percentage rations are listed.

Alarm	mean [s]	median [s]	Q_1 [s]	Q_3 [s]
FDWindSpeedWarning	11417	164	41	585
FDWinSpeedAlarm	18723	68	28	369
SinglePixelVarianceWarning	6791	86	34	1134
FDRainAlarm	13122	192	44	7163
FDchtimeError	10822	2449	166	11426

Table 4.4: Summary of *Acknowledgement* reactions to individual type of alarms. Difference between the moment when an alarm was raised and acknowledged by a shifter is calculated in the reporting system and evaluated. Some alarms are not acknowledged, but raised and after that directly resolved. Q_x denotes $x-$th quartile.

Median values vary between approximately 1.5 minutes for wind and rain alarms and $\sim$ 5 minutes for wind warnings. The time when the latter type of alarm is

correctly.

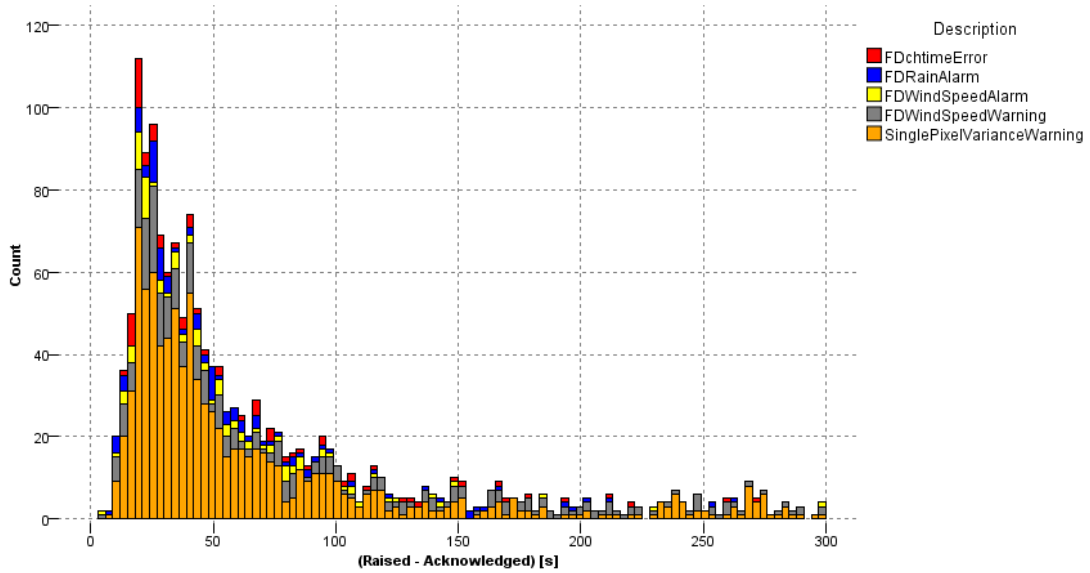

Figure 4.9: The stacked histogram of shifters reaction time - difference between the time of acknowledgement and the time when an alarm was raised.

Alarm	mean [s]	median [s]	Q_1 [s]	Q_3 [s]
FDWindSpeedWarning	8219	366	76	1168
FDWindSpeedAlarm	13593	90	42	379
FDRainAlarm	2978	88	42	216
FDchtimeError	25164	2700	600	12304

Table 4.5: Summary of *Resolved* reactions to selected types of alarms. Difference between the moment when an alarm was raised and resolved is calculated in the reporting system. Q_x denotes $x-$th quartile.

Resolved depends on weather condition or on closing shutters. Similarly to the previous case there are few outliers. Especially they occur in the case of wind and rain alarms; the time when they are resolved is fixed to the time when DAQ is stopped (it is done manually by shifters). This indicates that in some cases shifters reactions to such high priority alarms were too slow. According to third quartile 75% of wind or rain alarms (high level ones) are resolved within $4-6$ minutes. The largest values of third quartile reaction time can be seen for wind warnings (*FDWindSpeedWarning*) which is probably caused by the weather condition when DAQ can run in the 'warning zone'.

Log files of the Shift Guard C++ application are stored in the local directory of the steering PC *Ronja* and all commands that are sent by operator (e.g. shifter in CDAS) are logged together with errors, communication problems and exceptional conditions, which are indicated by the software. The title of each log file is named

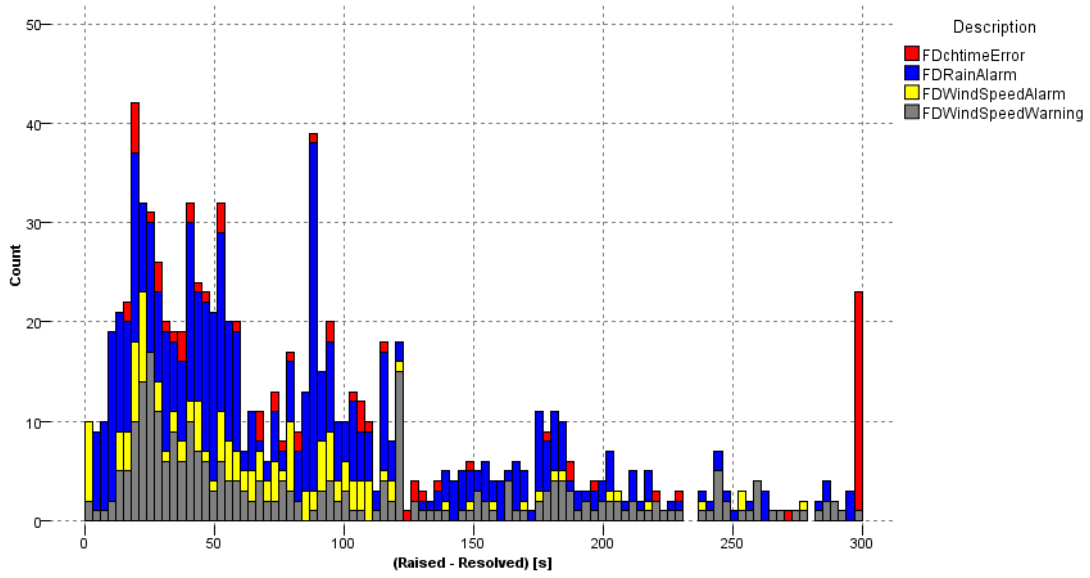

Figure 4.10: The stacked histogram of distribution of time between raised time and the time when an alarm is resolved for four types of alarms - FDChtimeError, FDRainAlarm, FDWindSpeedAlarm and FDWindSpeedWarning.

after date and time of its creation. Each logged message is preceded by the clock time started at application launch and therefore the time of the message and the related event is traceable.

Since the Shift Guard operation start almost one thousand log files were stored and analyzed (912). The Tab. 4.6 contains principal summary of the analysis. In vast majority of the Shift Guard launches, namely in 98.1 % the standard start process was recorded. There are only two types of error messages detected - communication problem with QUIDO and MySQL communication failure of various types. MySQL communication failure occurs during DAQ and MySQL interface implemented in the Shift Guard has to restore the communication. On the other hand all QUIDO communication problems occurred when the Shift Guard starts. Operation problems are elaborated in the details in the following paragraphs:

QUIDO communication incidents

8 cases of the QUIDO module connection failures occurred in October 2010 when it was not possible to establish communication and shifters tried to restart the Shift Guard several times. The problem was fixed after 20 minutes. The other 3 failures occurred in 2012 and 2013 and connection to QUIDO was created by the Shift Guard application restart. In summary, only during 3 nights the QUIDO connection problem was indicated and one can conclude that the Shift Guard operates smoothly and reliably.

MySQL communication incidents

The analysis of MySQL communication problems showed that almost half of all 70 failures to open communication channel to MySQL database occurred in November 2012, namely 34 occurrences. 8 notices were recorded both in 2011 and 2013. The rest 20 log files are dated in 2012. MySQL interface is implemented in order to reestablish the connection when it is possible (the Shift Guard tries to connect to MySQL in a cycle). On the other hand, when the MySQL connection is broken it is not able to check new alarms.

The detailed analysis revealed that there were only 34 shift nights when communication problem with MySQL database was indicated; 8 in 2011, 20 in 2012 (there were 3 problematic nights in November 2012) and 6 shift nights when notifications were recorded in 2013.

# starts	# incident-free starts	# MySQL errors	# QUIDO errors	# others
912	895	70	11	0
100.0 %	98.1 %	7.7 %	1.2 %	0.0 %

Table 4.6: Log files analysis summary - reliability analysis. Total number of Shift Guard starts is supplemented by the number of incident-free starts and two types of errors, which were found in log files. In some cases the Shift Guard was started several times per shift night.

Log files analysis summary shows that only during 37 shift nights (between October 2010 and February 2014) some kind of problem was detected and in most cases problems were successfully eliminated, most of them by repeated start of the Shift Guard. Therefore the Shift Guard is considered to be stable and reliable application.

Chapter 5

Muon production study

Primary cosmic rays striking the Earth's atmosphere induce extensive air showers. They start developing in the upper levels of the atmosphere (usually in depth of about tens of $\mathrm{g\,cm^{-2}}$). Its electromagnetic as well as hadronic component develop as was described in section 2.5. Only secondary particles reach the ground level. Among them the muons play an important role as they are highly penetrating and they can traverse from hundreds of meters to tens of kilometers (depending on their energy). For $10^{19}\,\mathrm{eV}$ shower the distance d_{max} between the shower maximum and the impact point on the ground varies from 100 m to $\sim 60\,\mathrm{km}$ depending on the zenith angle $10^\circ < \theta < 80^\circ$. The decay length of muons at the energy of 10 GeV is $\gamma\beta c\tau = 66\,\mathrm{km}$ which is even larger than the previously estimated d_{max} in the limit case.

Electromagnetic component of the shower is continuously absorbed in the atmosphere so that muonic component dominates in showers with zenith angles $\theta > 60^\circ$. Consequently, muons and electromagnetic particles originated from their decays are the only particles that reach ground level for very inclined showers. Simultaneously muons are probes of hadronic interactions that we simulate only with considerable uncertainties in contrast to the electromagnetic shower which is well described also analytically.

Muons are produced mainly in pion and kaon decays:

$$\begin{aligned} \pi^- &\longrightarrow \mu^- + \bar{\nu}_\mu, \qquad & \pi^+ &\longrightarrow \mu^+ + \nu_\mu \\ K^- &\longrightarrow \mu^- + \bar{\nu}_\mu, \qquad & K^+ &\longrightarrow \mu^+ + \nu_\mu, \end{aligned}$$

to lesser extent by direct production in nuclear reactions, pair productions, charmed and beauty and other strange particle decays. As it will be outlined in the following chapters there are indications that even more exotic production processes can be involved. Measured muon number discrepancy compared to its prediction is discussed and some possible sources are studied in order to mitigate the discrepancy.

As a consequence of weaker interactions of muons in comparison with electromagnetic particles they are less deflected by Compton scatterings. More straight tracks of muons cause that they form the front wave of the air shower accompanied by slower electromagnetic particles (halo) that are also provided by muons passing

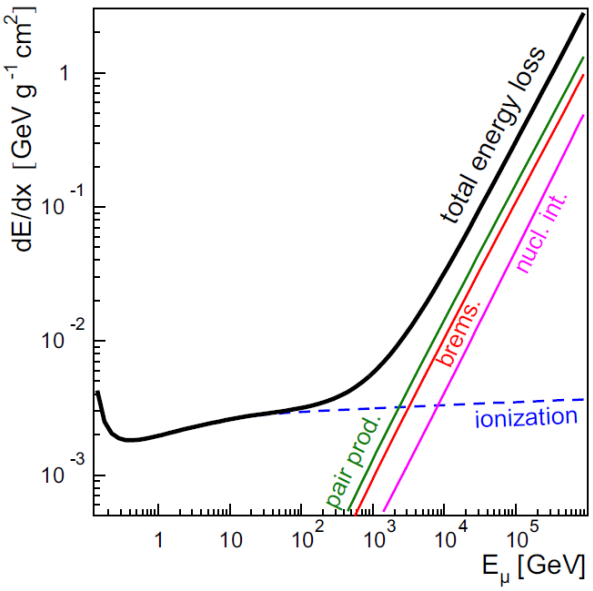

Figure 5.1: Total energy loss of muons as a function of energy in the air is shown by full black line together with particular contributions as calculated in CORSIKA [28]. Adopted from [55].

through the atmosphere. This is also the reason why electromagnetic halo has almost constant gap after the muon shower front wave.

In Fig. 5.1 the muon energy loss in the air is drawn for wide range of energies. For most of muons in the EAS the energy loss of about $3\,\mathrm{MeV/g\,cm^{-2}}$ occurs. Due to the energy of produced muons and energy dissipation processes the muon attenuation is quite negligible up to zenith angle $\theta \sim 80°$. Therefore muon study provides the possibility to reveal a window to study hadronic interactions for phase space regions and energies far away from those accessible at accelerator experiments.

5.1 Discrepancy in number of muons at ground level

Many studies have been done towards the analyses and comparisons of muon content in EAS for various interaction characteristics. Measured muon signal compared to that one predicted by spectrum of interaction models can be found in many works. Next paragraphs are devoted to recent analysis and measurement of the muon signal using the temporal and spectral structure of the signals in surface detectors of the Pierre Auger Observatory.

Even without special dedicated equipment to measure the muonic signal some methods have been developed using total surface detector signal by applying different filtering techniques to separate electromagnetic from muonic signal. Cherenkov photons produced by particles that pass the water tank can be the deciding factor to recognize their sources. Peaks above a smooth background indicate muonic signal

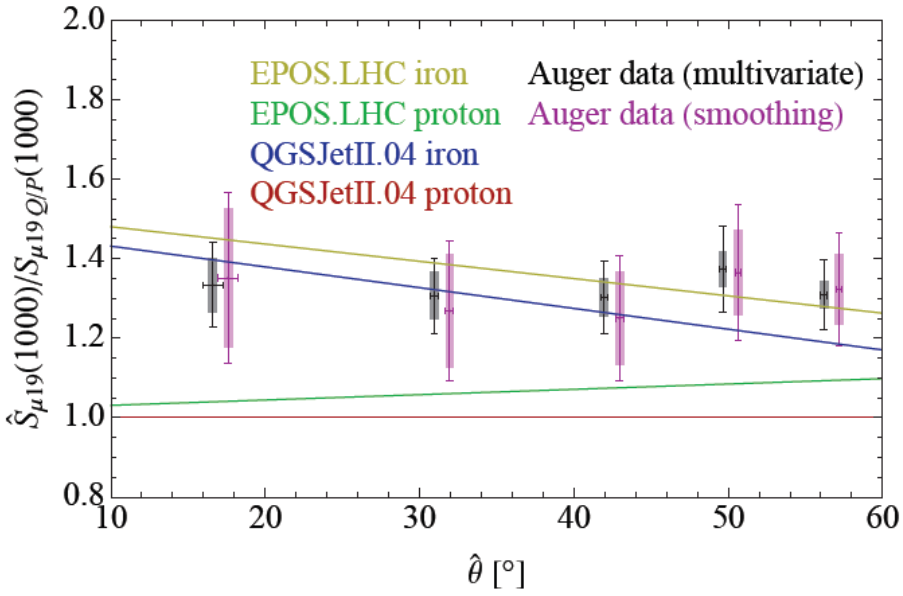

Figure 5.2: Measured muon fraction signal using two different methods - multivariate and smoothing for different zenith angles are compared to EPOS LHC and QGSJetII.04 proton and iron primaries simulations. Signal is rescaled to $E = 10\,\mathrm{EeV}$ with QGSJetII.04 proton as a baseline. Systematic and statistical uncertainties are represented by rectangles and the error bars respectively [67].

that surpasses lower energy deposition induced by electromagnetic components.

The fraction of muon signal is scaled to the energy of 10 EeV at a core distance of 1 km (with the goal to compare it with interaction model predictions). Muonic signal is derived from time profile and spectral characteristics of Cherenkov light signal measured by PMTs of the SD. The analog signal of each of three PMTs of one SD tank is converted by FADC to digital form and these three traces are averaged so that it forms time binned signal denoted as a set $x = (x_1, ..., x_N)$ for time bin 1 up to N. Let us assume that total signal S measured by SD is composed of electromagnetic part S_{em} and muonic part S_μ. The muon signal fraction f_μ is expressed as the following ratio:

$$f_\mu = \frac{S_\mu}{S}. \tag{5.1}$$

The total signal S stands for $S = \sum_{j=1}^{N} x_j$, where x_j is averaged detector signal for time bin j.

Individual particles produce almost the same time response profile and the observed sum of such profiles does not allow to separate electromagnetic and muon components. Number of electromagnetic particles is roughly of an order of magnitude larger than number of muons for analyzed energies and core distances. Though the mean signal of a single muon is 1 VEM and the amplitude distribution is close to a Gaussian (with tail caused by short muon track and delta rays), the mean signal of an electromagnetic particle is much smaller. As mentioned formerly muon

signal precedes the electromagnetic one. These two features - timing of muon signal and single particle amplitude characteristics are used in the following filter methods to estimate f_μ fraction.

- Multivariate method estimates muon fraction by means of the muon content sensitive parametrization [67, 114]:

$$\hat{f}_\mu = a + b\,\hat{\theta} + c f_{0.5}^2 + d\,\hat{\theta}\,P_0 + e\hat{r}, \tag{5.2}$$

  where parameters $f_{0.5}$ and P_0 are muon sensitive as short peaks and large fluctuations are reflected in these variables. $f_{0.5}$ is the fraction of the digitalized signal above 0.5 VEM from the total signal S. P_0 is calculated as ratio of the mean value of the signal $\langle x \rangle = S/N$ and its second moment $\langle x^2 \rangle$:

$$P_0 = \frac{\langle x \rangle^2}{\langle x^2 \rangle}. \tag{5.3}$$

  $\hat{r}$ is the reconstructed distance from shower axis to the detector.

- Smoothing method applies low-pass filter several times in order to separate low frequency electromagnetic component from muonic high frequency one. Measured signal is smoothed in 5 successive steps and for each bin $\hat{x}_j = \sum_{i=1}^{N} x_i p_{ij}$, where p_{ij} is non-zero only for defined tuned window $|i-j| \leq L$. The value of smoothing window L depends on the zenith angle. Only positive differences $x_j - \hat{x}_j > 0$ are summed into the final muon signal.

Simulations were used to estimate parameters of models. Tuned models were applied to real data and compared to set of four different simulation libraries to test them. The standard Auger SD reconstruction cuts were used for events with zenith angle $\hat{\theta} < 60^\circ$ and reconstructed energy $10^{18.98}\,\mathrm{eV} \leq \hat{E} \leq 10^{19.02}\,\mathrm{eV}$. Only detectors with distance $\hat{x}$ between 950 and 1050 meters from reconstructed shower axis were selected. The muon fraction $\hat{f}_\mu$ has been estimated according to both described methods and compared to simulation libraries using CORSIKA with hadronic models QGSJetII.04 [115] and EPOS LHC [116] for proton and iron primaries. Both methods were in very good agreement and systematic uncertainties roughly overlap the peripheral simulations for proton and iron-induced showers [67]. The simulated and measured muon fractions have been inserted into the following equation to obtain the muon signal at the distance 1000 meters from the shower core:

$$S_{\mu 19}(1000) = f_\mu\, S_{19}(1000) \tag{5.4}$$

by means of the total signal $S_{19}(1000)$ rescaled to the energy of $10^{19}\,\mathrm{eV}$ at 1000 m from the shower axis. In Fig. 5.2 the resulting muon signal is depicted divided by the muon signal of proton showers simulated by QGSJetII.04 for zenith angle range $\theta \in [0^\circ; 60^\circ]$. Compared to the signal of proton showers simulated by QGSJetII.04 the measured muon signal is greater by a factor of $1.33 \pm 0.02\,(\mathrm{stat.}) \pm 0.05\,(\mathrm{sys.})$ for multivariate and $1.31 \pm 0.02\,(\mathrm{stat.}) \pm 0.09\,(\mathrm{sys.})$ for smoothing method. As

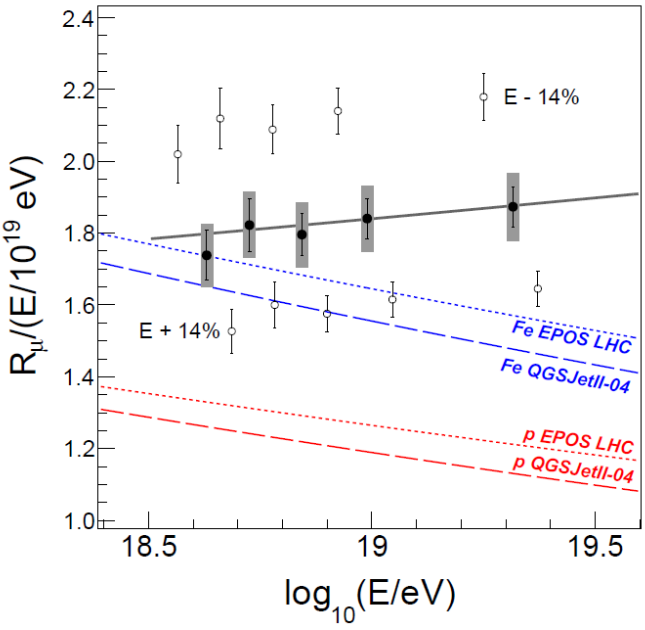

Figure 5.3: Distribution of measured $R_\mu/(E/10^{19}\,\mathrm{eV})$ for various primary energy (full circles) supplemented by hypothetical values in case of FD energy scale shifts (open circles) for inclined showers. Predictions for proton and iron-induced showers simulated by EPOS LHC and QGSJetII.04 are depicted by coloured lines [67].

apparent from Fig. 5.2 which combines muon fraction and total signal it is evident that the detector signal assigned to the muon component is similar to the angular dependence predicted by proton-induced simulations of QGSJetII.04. On the other hand, the overall level is rather closer to iron showers.

Taking into account X_{max} and $RMS(X_{max})$ distributions [117] around $10^{19}\,\mathrm{eV}$ the chemical composition does not correspond to iron primaries which leads to the conclusion that predicted muon signal is underestimated.

The independent study of muon content for zenith angles above 62° has been presented [67] with the use of special methods designed for inclined hybrid events. The main advantage of inclined shower study is the fact that it provides the direct measurement of muon signal due to the absorption of electromagnetic component as shower passes through vast atmospheric mass. Number of muons is mass sensitive observable, however it is dependent on the hadronic interaction properties.

The common decomposition of the muon density ρ_μ at ground level introduces size parameter N_{19}:

$$\rho_\mu = N_{19}(E, A)\,\rho_{\mu,19}(x, y, \theta, \phi), \tag{5.5}$$

where $\rho_{\mu,19}$ is reference profile density for proton shower of the energy of $10^{19}\,\mathrm{eV}$ simulated with CORSIKA, QGSJetII-03 and FLUKA. The above stated factorization of ρ_μ results from the fact that for given slant depth in atmosphere the shape of muon number density is independent of energy and mass composition. Total number of muons is simply $N_\mu = \int \rho_\mu$, analogically number of muons $N_{\mu,19}$ for

reference muon density can be calculated as integral of $\rho_{\mu,19}$. It follows that N_{19} can be expressed as the ratio $N_\mu/N_{\mu,19}$.

As described in [67] measured N_{19} can be corrected to the true number of muons using MC simulations and after that it is referred to as R_μ. Hybrid golden events allow to calibrate R_μ by means of measured calorimetric energy E_{FD} [67]:

$$R_\mu = A\,[E_{FD}/10^{19}\,\mathrm{eV}]^B, \tag{5.6}$$

with $A = 1.84 \pm 0.03 \pm 0.09\,(\mathrm{sys})$ and $B = 1.03 \pm 0.02 \pm 0.05\,(\mathrm{sys})$. R_μ has been measured in the energy range between $4 \times 10^{18}\,\mathrm{eV}$ and $2 \times 10^{19}\,\mathrm{eV}$ and compared to proton and iron-induced shower simulations with EPOS LHC and QGSJetII.04 (see Fig. 5.3). Auger data is partly comparable to iron simulations in case of FD energy scale shift (open circles). Taking into account the recent study [117] X_{max} and $RMS(X_{max})$ do not correspond to iron primary mass composition which means that the number of muon predicted by simulations is underestimated in accordance to conclusion of the study for zenith angles $\theta < 60°$.

The discrepancy of measured number of muons compared to simulations was already observed a decade before the above described analyses. In the work of Petr Trávníček [118] cosmic rays were measured by DELPHI detector (DEtector with Lepton Photon and Hadron Identification) that was situated 100 m underground. It ensures that vertical muons with energy more than roughly $\sim 50\,\mathrm{GeV}$ [1] could reach the Hadron Calorimeter (HCAL) used for muon track detection and shower direction reconstruction.

Petr Trávníček performed two set of simulations with CORSIKA and QGSJET model with proton and iron primaries [118]. The integral muon multiplicity compared to simulated ones are shown in Fig. 5.4. Each bin contains integral number of events with given measured or simulated muon multiplicity or higher. At low multiplicities data corresponds to pure proton scenario, while at the region with multiplicities $N_\mu > 20$ data reproduce pure iron component of primaries. At the highest multiplicities data exceeds even predictions coming from iron primary simulations. In comparison with iron simulations the fraction of observed events to measured events for $N_\mu \geq 70$ (resp. $N_\mu \geq 80$) was determined as 1.28 ± 0.18 (resp. 1.45 ± 0.23) [118].

5.2 Possible muon sources in air showers

Most of muons in EAS are produced in $\pi^\pm$ decays. Therefore, the average muon energy relates to pion critical energy introduced in the section 2.5, namely it is supposed to be of the order of $\xi_c^\pi \sim 10\,\mathrm{GeV}$. The most frequent two-body decay of a pion yields very light neutrino and muon. Because of incomparable masses of the decay products, most of the energy is carried away by the muon and it also roughly preserves the original pion movement direction. In the decay process Lorentz factor greater than approximately 100 is transferred to muons. They undergo Coulomb

[1] A small fraction of muons with energy lower than 50 GeV could be detected due to access shafts.

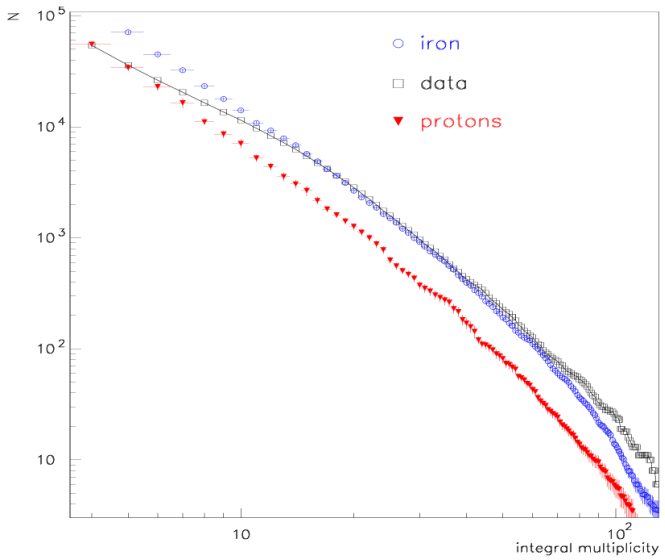

Figure 5.4: Distribution of integral muon multiplicity measured in HCAL at DELPHI experiment compared with iron and proton simulations [118].

scattering and geomagnetic deflections, but compared to electromagnetic particles they generally suffer much less scattering. For that account a muon beam in forward direction follows hadronic shower and can penetrate very thick atmospheric mass.

The following short sections briefly describe various possible sources of muons.

5.2.1 Soft sources

Soft type of muon sources is represented by $\pi^{\pm}$ of mass 139.6 MeV. There is a large amount of charged pions in EAS. In the two-body decay $\pi^{\pm} \longrightarrow \mu^{\pm} + \nu_{\mu}$ most of energy (up to $\sim 80\%$) is inherited by the muon which moves practically in the same direction as the parent particle. The pion mean life implies $c\tau_{\pi} = 7.80\,\mathrm{m}$. Taking into account interaction length (roughly equivalent of $\sim 100\,\mathrm{g.cm^{-2}}$) (see Fig. 5.5) it follows that high energy pions rather suffer from hadronic interactions than decay. Pions of $\sim$ TeV (or higher) energy have mean decay length $> 50\,\mathrm{km}$ and therefore they most probably undergo hadronic interaction (cf. Fig. 5.5). New particle production in each interaction (characterized by multiplicity ~ 10) leads to decrease of the average energy per pion. As a consequence the mean decay length shortens and if it gets below the mean interaction length decay into muons is more likely than hadronic interaction. For vertical showers at the altitude of $\sim 10\,\mathrm{km}$ number of charged particles rapidly increases and pions with $E_{\pi} > 60\,\mathrm{GeV}$ still more likely interact but below this threshold they decay and produce muons with energy around $\sim 50\,\mathrm{GeV}$. As most of the pions are produced at roughly below this altitude typical muon energy is of the order of $\sim$ GeV up to tens of GeV.

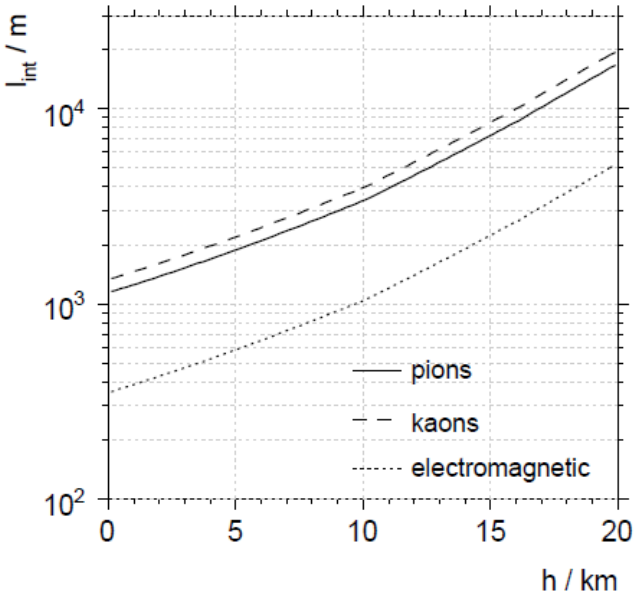

Figure 5.5: Interaction lengths for pions, kaons and electromagnetic particles versus altitude for energies between 10 GeV and 1000 GeV, taken from [55] and adjusted.

5.2.2 Hard sources

Another important sources of muons are strange and heavy flavour particles which in some channels decay to muons and pions.

The lightest of them are kaons. The curve of kaon interaction length lies above the pion curve (see Fig. 5.5) and, having mass almost five times higher than muons $m_{K^\pm} = 493.7\,\mathrm{MeV}$ ($c\tau_K = 3.71\,\mathrm{m}$), kaons produce muons of typically an order higher energy than pions. The analogical estimation of threshold kaon energy at the height around 10 km as derived for pions above gives $E_c^K \sim 600\,\mathrm{GeV}$.

For sufficiently energetic interactions which allow c quark production charmed particles appear as direct (and of course even indirect) sources of muons. $D^\pm$, the lightest charmed particles have $c\tau_{D^\pm} = 315\,\mu\mathrm{m}$ with mass $m_{D^\pm} = 1869.3\,\mathrm{MeV}$ decay almost immediately with respect to light mesons decay lengths. Neutral D mesons and resonances or higher spin states have even shorter mean decay length or greater resonance width Γ. The influence of charmed mesons in EAS on muon content and observable characteristics will be studied and discussed in section 5.3.5.

5.2.3 Exotic sources

The excessive number of muons doesn't have to be necessarily caused by known and described processes extrapolated or adjusted to UHECR energy region. The fact that muon number discrepancy is apparent at energies far from energy and phase space regions known from accelerator data leaves room for new physics. One of possible exotic theories considers dark sector consisting of weakly-coupled particles that can be potentially source of additional muons. Conditions can reach

	proton		iron	
Energy	mean value	central 68%	mean value	central 68%
10^{18} eV	0.39 ± 0.02	$0.30 - 0.45$	0.28 ± 0.03	$0.20 - 0.32$
10^{19} eV	1.05 ± 0.63	$0.60 - 1.34$	1.3 ± 0.2	$0.38 - 1.33$
10^{20} eV	5.9 ± 2.7	$2.5 - 7.4$	5.8 ± 1.2	$1.6 - 7.6$

Table 5.1: Number of dark photons with central 68% interval resulted from simulations using GHEISHA and QGSJETII for proton and iron primaries [124].

some threshold level for new physics dark sector particles creation at ultra-high energy interactions in EAS (review of dark matter models can be found in [158]). A particular study of exotic muon source described below is based on works [159, 121] that consider general cosmological observations and takes into account relatively light particle of mass $\sim 250\,\mathrm{MeV}$ with coupling to ordinary matter.

Results of contribution of massive photons

Measurements from satellite experiment such as PAMELA [122] showed excessive positron flux compared to cosmic ray electrons (beginning at energies above $10\,\mathrm{GeV}$) [2]. It stirs up dark matter models investigation, since dark matter annihilation could explain observed positron excess. Models that lead to lepton flux increase can also describe additional muon production and therefore they become important also for research of EAS.

Motivated by above cited measurements and mentioned dark matter model a contribution of massive photons from the dark sector on the muon content was studied by the author with cooperation with Jan Ebr [124]. The aim of the study was to answer whether some portion of extra muons can be explained as originating from dark matter decays or interactions. The dark photon production was estimated by means of cross sections ratio of derived formula for massive photon bremsstrahlung and well-know photon massless case. For each bremsstrahlung event the probability of dark photon production expressed by the forementioned ratio was accounted for in case of possible kinematics (that is the probability was zero in case that kinematics does not allow to produce a dark photon).

The upper limit for kinetic mixing factor $\epsilon^2 \sim 10^{-4}$ that couples ordinary matter to dark matter (and suppresses their interactions) has been incorporated on the basis of astrophysical constraints. The resulting muon production has been estimated and found unobservable. Dark photons can decay into a pair of charged leptons, that is into e^+e^- and $\mu^+\mu^-$ pairs with equal probabilities as opposed to pair production in the electromagnetic field. This holds for sufficiently massive dark photons and is valid also for the examined dark photon mass range $m_\gamma \in (212; 280)\,\mathrm{MeV}$.

[2] These results have been confirmed by other experiments, e.g. Fermi Gamma-Ray Telescope [123].

Interaction model	mean value	central 68%
GHEISHA + QGSJETII	1.05 ± 0.06	$0.60 - 1.34$
FLUKA + QGSJETII	1.40 ± 0.20	$0.64 - 1.68$
GHEISHA + SIBYLL	1.50 ± 0.23	$0.76 - 1.61$
GHEISHA + EPOS	1.06 ± 0.08	$0.59 - 1.47$

Table 5.2: Total number of dark photons as simulated for proton primary particle of energy 10^{19} eV for different interaction models [124]. 100 showers were simulated per each configuration.

In such mass region dark photons decay in most cases instead of pair production. This mass interval was chosen as the most probable dark photon mass for the purpose of the analysis [124]. The mean value of dark photons has been estimated to be less than 6 for proton as well as for iron primaries and the highest studied energy range that was 10^{20} eV. CORSIKA (version 6.900) was used with EGS4 routines for electromagnetic cascade including LPM [3] effect.

Results for proton and iron primaries using GHEISHA and QGSJETII interaction models can be found in Tab. 5.1 for three primary energies 10^{18} eV, 10^{19} eV and 10^{20} eV for the most common arrival zenith angle of $\theta = 38°$ and randomly generated azimuth. Conditions such as observation level and magnetic field corresponded to those of at the Pierre Auger Observatory. There are mean values of total dark photons count. Due to neither symmetric nor Gaussian distribution the central 68% values are included to have a picture of distributions. Produced number of dark photons depends on the primary energy in the first approximation in a linear way. Taking into account the mixing factor $\epsilon^2 = 10^{-4}$ even at highest energy of 10^{20} eV we predicted one muon of dark photon origin per 1000 showers [124] which is certainly negligible and one concludes that massive photon decays produced in EAS do not contribute to the muon content. To test the influence of individual interaction model FLUKA, SIBYLL and EPOS interaction models have been also tested at proton primary energy of 10^{19} eV to show that there is no significant differences and results remain the same as for QGSJETII with GHEISHA simulators (see Tab. 5.2). The table indicates comparable results as for GHEISHA and QGSJETII interaction models and one can conclude that unobservable effect on muon content is general and independent of interaction model choice.

[3] The Landau-Pomeranchuk-Migdal effect (LPM) is a suppression of the bremsstrahlung and pair production cross sections at high matter densities and high energies [125].

5.3 Hadronic interaction models and muon production

Nowadays interaction models are indisputably an essential part of cosmic ray as well as collider physics research. They make an inevitable contribution to the detailed knowledge of the detector response which helps to extract and understand measured data. On the other hand, interaction models serve as a link between measured data and theory. They enable to confront new ideas (even phenomenological ones) with real data.

As current UHECR detection approaches are based on indirect methods the inferred projectile properties from secondary particles signal strongly depend on simulations which predict relation between primary cosmic ray characteristics and measurable variables that relate to secondary particle attributes. Interaction models are based on different theoretical approaches but incorporate a wide range of phenomenological factors and assumptions. It requires tuning for known energy-phase space, that is for collider data followed by extrapolation to UHECR energies where the models are applied. The main purpose of interaction models is to describe observables rather than particular interactions. Thus, uncertainties that are introduced via artificial factors must be considered from that point of view.

Hadronic interaction models can be divided into two main groups according to the used approach. Full chain of cascade interactions is simulated using *Monte Carlo* (MC) simulators. Each particle is processed and its track is followed, however statistical sampling methods have to be used due to otherwise necessary excessive computing power above primary energies 10^{18} eV.

Second large group of interaction models - used in UHECR physics - treats air shower simulations via *cascade equations*. This approach could overcome difficulties outlined above (artificial fluctuations that emerge from statistical sampling and extreme computing power needed). Differential cascade equations describe flux development of specific particles along a shower axis (that is in one space dimension). The numerical solution gives number of particles $n_s(E, X)dE$ of species s at atmospheric slant depth X and in the energy interval $(E, E + dE)$. Models using cascade equations are tuned to reconstruct average fluxes of particles. Precise one-dimensional profile particle density allows to predict longitudinal fluorescence profile. Contrary to that, lateral distribution function required for surface detector response simulation is not reproduced.

There are also models which take advantages of forementioned simulator types. So called *hybrid models* combine both of above outlined approaches. Numerical solution of cascade equations cannot form fluctuations that are typical for probability based interactions and which are important mainly for several first interactions of EAS. This as well as particle lateral spread can be introduced by hybrid model that uses Monte Carlo approach for first interactions until some energy cut-off. Afterwards cascade equations are applied and last part of EAS is again calculated using Monte Carlo that results in lateral spread calculation.

The following paragraphs describe the most common MC high energy interac-

tion models used in cosmic ray physics incorporated into shower simulation packages that describe development of EAS. Before that the concepts of *soft* and *hard* interactions will be introduced. The distinction between them is made via the transverse momentum $p_\perp$. Large $p_\perp$ interactions are denoted as *hard* and they can be dealt with perturbative Quantum Chromodynamics (pQCD) contrary to the *soft* processes which are characterized by small transversal momentum $p_\perp$ and are usually described in a phenomenological way.

5.3.1 The Quark-Gluon String Model with Jets - QGSJET

QGSJET model [126] has been extensively used in UHECR field for many years with undoubted success that ended in general update of the model that will be described below.

The basis of the QGSJET is the Quark Gluon String Model (QGSM) [127] generalized to nucleus-nucleus interactions and extended by semihard processes incorporation. The basic framework is the Gribbov-Regge approach. It describes hadronic collision as a multiple scattering among incident and target hadrons. From microscopic perspective the interaction is mediated by parton (quark or gluon) cascades. The individual scattering contributions are phenomenologically described as Pomeron exchanges. Pomeron is a hypothetical colour and charge neutral particle used in Gribbov-Regge theory. On the left part of Fig. 5.6 the picture of high energy interaction is depicted - hadronic collision is treated via multi-Pomeron exchanges (violet vertical lines) where each of them represents parton cascades. Multiple scattering process, hadron-hadron collision can result in hadrons production (inelastic interaction) or elastic scattering without particle production. Partons mediate colour and momentum exchange and they fragment into secondary hadrons when the coherence of parton cascades is broken. Contrary to the latter in the elastic case the underlying cascade can be composed of multiple elastic scatterings and mediating partons recombine to the incident hadrons without conversion of partons into new particles.

QGSJET as other high energy interaction models used in UHECR physics deals not only with *hard* interactions, but also treats *semihard* ones. Thus, it incorporates high p_T regime described by pQCD with DGLAP formalism for $q^2 \geq Q_0^2$, where Q_0^2 is a virtual cutoff that represents artificial line between two regimes - *soft* and hard parton dynamics. Interactions for $q^2 < Q_0^2$ cannot be treated via precise pQCD theoretical formalism and therefore the phenomenological Pomeron exchange approach is adopted for this *soft* (non-perturbative) regime. It allows to consider hadron interactions at small transverse momenta which imply according to the uncertainty principle ($\Delta b^2 \sim 1/p_T^2$) large impact parameters. In fact most of the parton cascades proceed entirely or at least partially in the *soft* region. In the eikonal formalism one introduces function $\chi(b, s)$ for the impact parameter b and energy s that describes the elementary interaction between hadrons. The inelastic cross section can be then written in the eikonal form (derived by means of the

optical theorem) as follows:

$$\sigma_{total} = \int d^2b \left[1 - e^{-2\chi(b,s)}\right]. \tag{5.7}$$

Eikonal function $\chi(b,s)$ represents one elementary interaction - general Pomeron exchange - (one of violet vertical line on the left Fig. 5.6). It consists of two parts - pure non-perturbative *soft* parton cascade described by eikonal $\chi_s(b,s)$ and *semihard* cascade with eikonal $\chi_{sh}(b,s)$ which at least partly develops in the *hard* region (right part of Fig. 5.6). *Semihard* cascade is depicted as QCD parton ladder sandwiched between two soft Pomerons [128]. The total eikonal function corresponds to the sum of two contributions:

$$\chi(b,s) = \chi_{sh}(b,s) + \chi_s(b,s). \tag{5.8}$$

The form of the used eikonal function can be found in [126] and it consists of several parameters that are extracted from experimental data. QGSJET model (and generally QGSM) was generalized to treat hadron-nucleus and nucleus-nucleus interactions using Glauber approach [129]. QGSJET model is enriched by minijets in comparison to the original QGSM. The importance of semihard processes was evident from accelerator data and therefore also minijets implementation was essential. As a solution the *Quark-Gluon String model with JETs* (QGSJET) [130] was created.

In the paragraphs above the general strategy how to describe high energy interactions has been sketched apart from the final particle production. The hadron interaction process ends by the mechanism of hadronization. Hadronization (fragmentation) of strings is used in QGSM and QGSJET. Strings are fragmented with a procedure similar to the Lund model [131] (there are differences in treating of the momenta at the end of the string). Strings of color field are stretched between constituent partons of incident hadrons as far as the *soft* interaction is concerned. Production of partons in *semihard* processes results explicitly from QCD calculation using well-known Dokshitzer-Gribov-Lipatov-Altarelli-Parisi (DGLAP) evolution equation formalism [132, 133, 134, 135]. Thus, in *semihard* interactions strings are stretched between *hard* partons and *soft* constituents [126]. The basic fundamental property of the strong force causes that as interacting partons move apart the string stretched between them gains potential energy. Then, coloured strings can fragment into colour neutral objects. According to the constituent mass strings break up into either again strings or particles.

A lot of measured CR data by large experiments (for instance KASCADE and Pierre Auger Observatory) were reproduced by EAS generators with implemented QGSJET as the high energy interaction model. Thus, in the recent time it was found that QGSJET reproduces the experimental EAS data quite well, especially at the energy region of $10^{15} - 10^{19}$ eV. QGSJET predictions of the lateral distribution of muons and charged particles as well as the correlation between X_{max} and the primary energy compared to data demonstrated good agreement [126]. QGSJET fitted best the experimental data measured by KASCADE experiment [26] compared to several interaction models [136, 137]. However, at large muonic shower

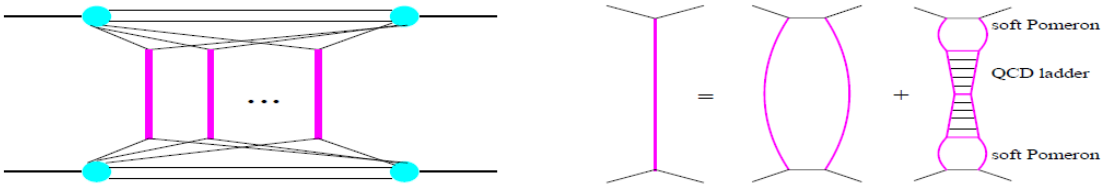

Figure 5.6: Multiple scattering process is phenomenologically described as a multi Pomeron exchange (vertical lines) (left). A general Pomeron exchange (right) is composed of *soft* (the first figure on the right) and *semihard* Pomerons (the second figure on the right) taken from [128].

sizes, which is clearly evident at energies above the *knee*, this model fails to reproduce certain observables, namely QGSJET predicts less muons than observed experimentally [137].

QGSJET is one of the high energy interaction simulators (for particles with energy $E > 80\,\mathrm{GeV}$) implemented in EAS generator CORSIKA [28]. The version of the first generation of QGSJET, which was used in some presented analysis, was denoted by the author of the generator as *QGSJET01c*. This version allows to generate also charmed particles. Nevertheless, only 20 types of particles are produced in high energy interactions treated by QGSJET: π^0, $\pi^\pm$, p, $\bar{p}$, n, $\bar{n}$, $K^\pm$, K^0_S, K^0_L, Λ, $\bar{\Lambda}$, $D^\pm$, D^0, $\bar{D}_0$, $\Lambda^\pm_C$, $\bar{\Lambda}_C$, η.

QGSJET01c enables to switch on production of charmed particles, probabilities of $c\bar{c}$ quark pairs creation (and quark-diquark) have to be set in the *QGSJET01c* code manually. The default setup for these parameters is 0 as CORSIKA did not explicitly treat charmed particles at the time the *QGSJET01c* was released. Some of further described simulations and analyses were performed with nonzero charmed particles production probabilities to analyse their influence on the muon content. The decay of charmed particles (as it was neither part of CORSIKA nor QGSJET codes in the time of the analysis) was implemented by the author of the thesis through separate routines according to known branching ratios as it is described in the section 5.3.5 further in the text and by means of the unpublished particle decay program written by Jan Řídký. It was adopted and extended to the purpose of charm and beauty particles decays (hereinafter referred to as *DecRoutine*). The special interface to CORSIKA was developed that enables to pass a mother particle to *DecRoutine*. Mentioned program carry out particle decay. Inclusive particle decays were incorporated into decay scheme of charm and beauty particles. As not all branching ratios and decay channels are known for such heavy flavours the inclusive particle decay has to fill up the gap.

DecRoutine was extended by $B^\pm$ decay channels using the same principle that preserves known inclusive branching ratios. The code of CORSIKA was adjusted in order to treat charm and beauty particles. As the interaction lengths are hardly known and mean life times are very short compared to EAS size immediate decays are performed.

5.3.2 QGSJET-II

Very successful high energy interaction model QGSJET has its successor denoted as QGSJET-II [128]. It is based on QGSJET with key improvement that seems to be crucial for reliable ultra-high energy interaction model. QGSJET-II incorporates non-linear interaction effects; *soft* and *hard* interference terms. Parton cascades treated by QGSJET are supposed to be independent of each other. The validity of such assumptions is limited to small number of elementary scattering processes. The condition of ultra high energy interactions combined with small impact parameters probably leads to a large number of scattering processes during the interaction and in these cases the necessity to account for parton cascades interaction strongly increases. High parton densities emerge at ultra high energies even at small impact parameters. Parton densities in the low virtuality region are saturated for the typical energy collisions studied by UHECR physics and fusion of other parton cascades compensates additional parton branchings. Unlike its predecessor, QGSJET-II accounts for Pomeron-Pomeron interactions. Individual parton cascades represented by Pomeron exchange are no longer independent and non-linear corrections are taken into account. The low virtuality scale $q^2 < Q_0^2$ is assumed for the latter processes. Thus, vertices of multi-Pomeron interactions include only *soft* Pomerons or *soft* part of *semihard* Pomerons (see Fig. 5.7). At highest energies sum of all Pomeron-Pomeron vertices has to be accounted for, however for lower energies only partial contribution of higher corrections is adequate enough. The proposed formalism used for multi-Pomeron vertices in QGSJET-II allows to calculate hadron-hadron cross sections and treats in a similar way hadron-nucleus and nucleus-nucleus interactions. The non-linear screening effects are naturally included by using this framework and are important for nucleus collisions. This makes differences compared to the basic linear superpositon model.

The above described improvement is supplied by realistic nuclear density parametrization for each nucleus in QGSJET-II, as well as two component low mass diffraction treatment. Enhanced Pomeron diagrams preserve high p_T jet spectra and QCD factorization scheme. Importance of Pomeron-Pomeron interactions has been presented for calculation of proton-proton cross sections and proton structure function $F_2(x, Q_0^2)$ [128]. Enhanced Pomeron diagrams allow to be in agreement with measured proton-proton cross section and proton structure functions.

Model parameters including the triple Pomeron coupling have been fitted and calibrated to wide set of currently known accelerator data (e.g. hard diffraction in deep inelastic scattering). Only 14 types of secondary particles are produced by QGSJET-II generator: π^0, $\pi^{\pm}$, p, $\bar{p}$, n, $\bar{n}$, $K^{\pm}$, K_L^0, K_S^0, η, Λ, $\bar{\Lambda}$. Due to the further analysis provided in this work it should be emphasized that QGSJET-II does not include with charmed particles contrary to its predecessor QGSJET.

Technically, all hadronic interaction models including QGSJET and QGSJET-II incorporated in EAS generator CORSIKA comprehend subroutines for particle decays. Hadronic interaction generators treat only the collision between particles and end their job at the point where products of such interactions are identified and passed for further development to original code of EAS simulator.

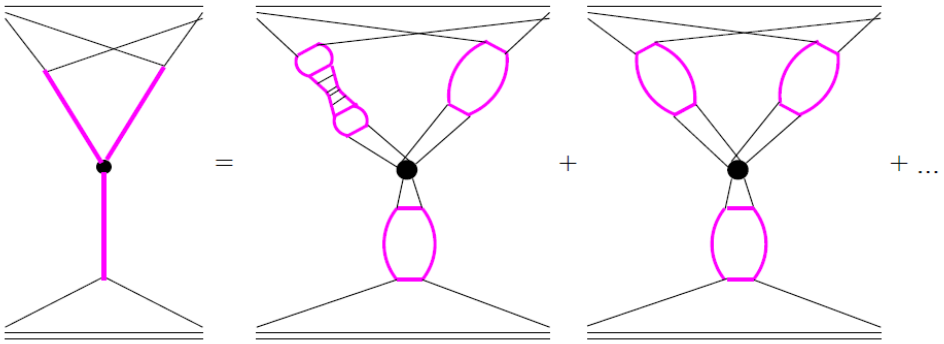

Figure 5.7: The amplitude of the general triple Pomeron interaction (l.h.s.) is sum of interactions of soft and semihard Pomerons, taken from [128].

5.3.3 EPOS

The new model generation is represented by EPOS[4] [138, 139, 140]. On the basis of results from heavy ion collisions enhanced (anti)baryon cross section has been implemented. Consequently, use of EPOS in EAS simulation leads to enhanced muon production compared to other hadronic interaction models. Muons are finally produced by pions, formerly classified as soft sources.

EPOS is a multiple parton scattering model based on phenomenological principles. That increases importance of high parton densities and collective effects. This seems to be very important especially for proton-nucleus and nucleus-nucleus collisions. The treatment of effective Pomeron-Pomeron interactions introduces implicitly screening and saturation effects. As a consequence, e.g. pp cross section predictions correspond to measured values as well as charged particle distributions measured in particle-nucleus collisions.

The parton picture of a hadron-hadron collisions is adopted. It assumes that the initial state before elementary parton scattering is preceded by parton emission. It results in so called parton ladder (see Fig. 5.8). Open ladders correspond to inelastic interactions, while the closed ones represent elastic scattering. Projectile and target remnants are supposed to be colourless objects, as well as the parton ladder. Partons from the parton ladder can also interact with other partons from the target (projectile) particle. This configuration called parton ladder splitting is depicted in Fig. 5.8. The latter is important effect in nucleus collisions. When two partons are close enough in terms of the impact parameter scale, a parton-parton scattering occurs and a ladder is created. Due to high parton density in the target (nucleus) there is probably another parton that is close enough to one of the partons from ladder and they may interact which splits the ladder. Moreover elastic splitting effect (see right part of Fig. 5.8) leads to the so called screening effect which suppresses amplitudes of parton collisions at low x. It agrees with the

[4] **E**nergy conserving quantum mechanical multiple scattering approach, based on **P**artons (parton ladders), **O**ff-shell remnants, and **S**plitting of parton ladders

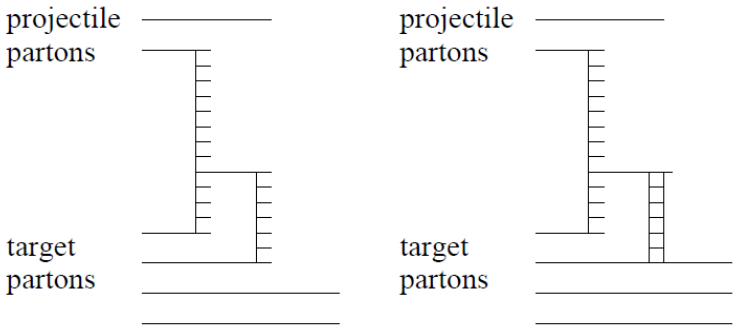

Figure 5.8: Parton-parton scattering is preceded by parton emissions (initial space-like state cascade) for which a symbol of so called *parton ladder* is used. A parton from the ladder can interact with other parton from the target particle referred to as *splitting* of a parton ladder. The inelastic and elastic splitting is depicted on the left, resp. right part of the figure [138].

concept of saturation [138].

Final transformation of partons into hadrons is treated via relativistic string model. Parton ladders correspond to colour field, these partons form strings which are fragmented into final hadron products. Additionally, for parton splitting a so called collective hadronization is adopted meaning that partons from parallel ladders undergo the hadronization process together.

As shown in [138] the effect of ladder splitting leads to the pp cross section reduction. As a consequence, energy dependence of pp cross section corresponds to measured data up to 3×10^4 GeV. EPOS simulation also reproduces data from deuteron-gold collisions, namely pseudorapidity spectra of charged particles from PHOBOS, STAR and BRAHMS experiments [138]. Screening effect results also in reduction of the multiplicity growth.

5.3.4 Missing energy

As already mentioned in the section 2.5 some fraction of the primary energy called *missing energy* is taken away into particles that almost do not dissipate energy as they pass through the atmosphere and therefore this energy is invisible for fluorescence detector. Most of the missing energy is carried by muons and neutrinos. Muons in EAS have mean energy loss rates close to the minimum, and are said to be minimum ionizing particles. They almost do not deposit their energy into air molecule by excitations and actually neutrinos do not lose their energy in the atmosphere at all. In following sections some decay channels of charmed and beauty particles will be identified which significantly contribute to this undetectable part of EAS. Among others, the missing energy fraction relates to the charm and beauty production in EAS. This will be investigated in the section 5.3.5.

Missing energy can be determined by means of MC simulations. Nevertheless, the dependence of the overall missing energy on hadronic interaction generators

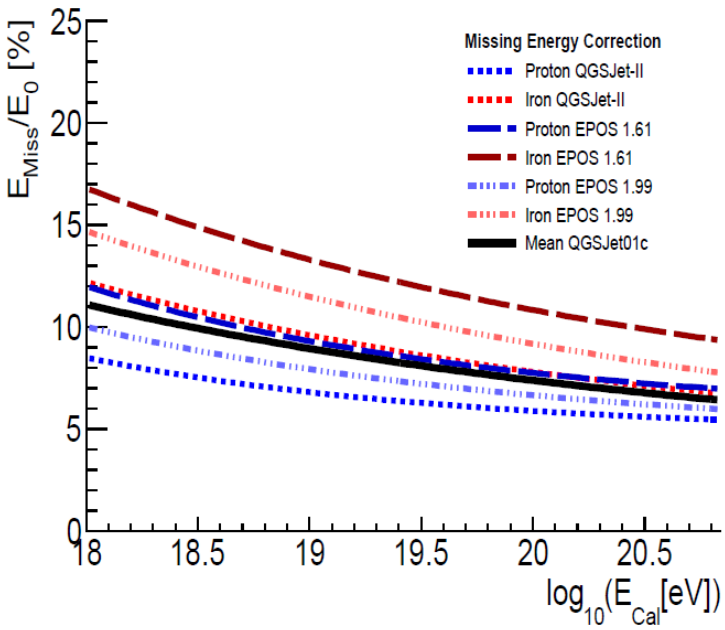

Figure 5.9: Missing energy E_{Miss} fraction as a function of the calorimetric energy E_{Cal} determined by different MC hadronic interaction models [141]. The primary energy E_0 is the sum of measured calorimetric energy E_{Cal} and missing energy E_{Miss}.

is up to level of $\pm 5\%$ as can be seen from Fig. 5.9. It is obvious from the figure that the lack of the knowledge on hadronic interactions leads to the uncertainty of the missing energy (as well as the overall energy scale). The primary mass also significantly influences the missing energy and as it is not possible to determine chemical composition event by event the average composition has to be taken into account.

According to the extended Heitler model the primary energy E_0 is distributed into electromagnetic and muonic component of the EAS so that $E_0 = \xi_c^\pi\, n_\mu + \xi_c^e\, N_{max}$ (see section 2.5.1) [59]. From this simplified model the energy E_μ of the muonic component of the shower is proportional to the number of muons[5] n_μ. Muons are produced in pion decays that occur when the pions energy drops below the critical energy ξ_c^π. Consequently, the missing energy can be identified with this muonic energy and estimated by (see eq. 2.26) [143]:

$$E_{Miss} \propto \xi_c^\pi\, n_\mu = \xi_c^\pi \left(\frac{E_0}{\xi_c^\pi}\right)^\alpha . \tag{5.9}$$

The pion critical energy ξ_c^π depends on the medium density, but it is well described

[5] In Trávníček's work [142] a missing energy correction has been investigated among other by means of the number of muons at the ground level. It has been shown even without explicit use of the Heitler model that missing energy calculated according to the number of muons reduces the dependence on the hadronic interaction models.

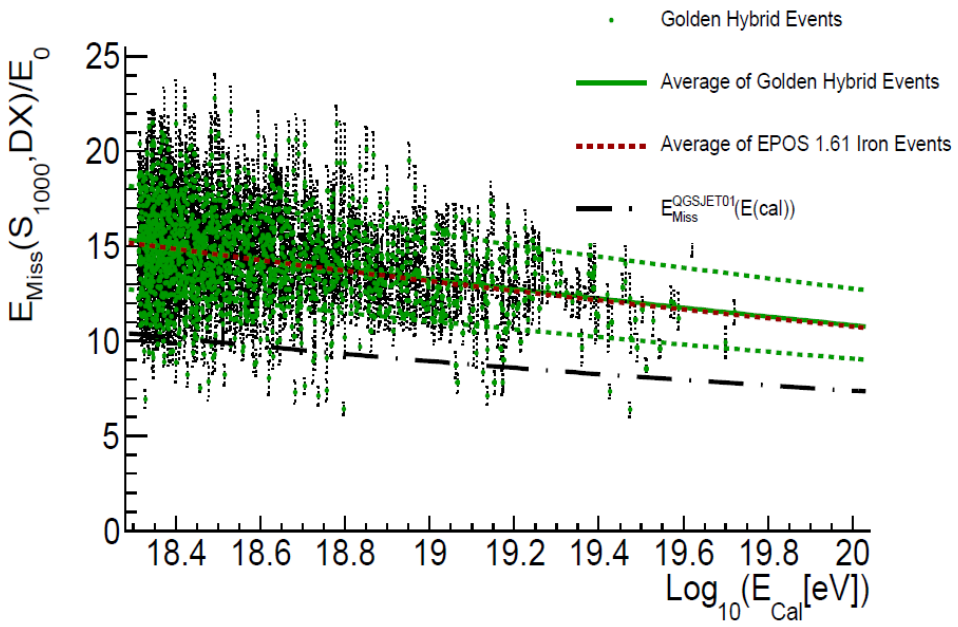

Figure 5.10: Missing energy $E_{Miss}(S_{1000}, DX)$ calculated according to the model for set of golden hybrid events [141] (green) together with prediction calculated by EPOS 1.61 with iron primaries. $E^{QGSJET01c}_{Missing}(E_{Cal})$ is the missing energy calculation used in the official Pierre Auger's reconstruction.

and known from other measurements and makes the muonic energy expression quite robust. The relationship of the total primary energy E_0 and the signal S_{1000} is a power law not only at a fixed zenith angle (as it is used for the energy estimator S_{38}) [99], but also for fixed atmospheric slant depth between shower maximum and ground level DX [141], i.e. $E_0 = \gamma_0(DX)\,[S_{1000}]^{\gamma}$. Based on previous equations, the model for the missing energy has been proposed [141, 143, 144]:

$$log(E_{Miss}[GeV]) = \log(\xi_c^{\pi}) + \log(\beta_0) + \beta\,\log\left(\frac{\gamma_0(DX)}{\xi_c^{\pi}}\right) + \beta\,\gamma\,\log(S_{1000}) \quad (5.10)$$

Logarithm of the missing energy is then parametrized as a function of S_{1000} and DX [141]:

$$log(E_{Miss}[GeV]) = A(DX) + B\,\log(S_{1000}[VEM]), \quad (5.11)$$

where parameters $A(DX) = (1-\beta)\,\log(\xi_c^{\pi}) + \log(\beta_0) + \beta\,\log(\gamma_0(DX))$ and $B = \gamma\beta$ are determined by means of MC simulations.

Free parameters were fitted using full MC simulations and hybrid events. Missing energy determined for the set of golden hybrid events is depicted on Fig. 5.10. The average value of missing energy determined by the above described model (green line) corresponds very well to missing energy calculated by EPOS 1.61 with iron primaries (red dashed line).

It is shown in Fig. 5.10 that the missing energy fraction decreases with increasing energy and the average value (average mass composition was assumed in the corresponding analysis) varies from about 15% at $10^{18.3}$ eV to 11% at 10^{20} eV.

The parametrization of the missing energy as a function of E_{Cal}, that is to determine missing energy event by event where no S_{1000} is known has been determined as follows [141]:

$$\frac{E_{Miss}}{E_0} = 0.1626 \left(\frac{E_{Cal}}{\mathrm{EeV}}\right)^{-0.088} \pm 0.02(\mathrm{syst.}) \pm 0.004(\mathrm{stat.}) \tag{5.12}$$

5.3.5 Implementation of charm and beauty into EAS simulations

As the current situation with discrepancy of predicted and observed muons was elaborated in the section 5.1 incorporation of charm and beauty particles production has been analyzed with results summarized in the following sections.

Charm

One of the possible source of muons could be charm particles and their decays or interactions as some hadronic interaction models did not include their production. Since more than one decade there was quite clear that predictions of muon number and its spectrum are not described properly by means of the current hadron interaction models integrated into most common EAS simulators [145, 146, 147, 148]. There were some indications and suspicions that charm particles missing in hadronic interaction models could mitigate part of this discrepancy [149].

Branching ratios of production of c quark and charm particles themselves are known with quite large uncertainties [6]. Charmed particles directly produce muons, kaons, pions and strange particles which subsequently decay into pions and muons.

There is an example of decay channels of D^0 meson (two semileptonic and one hadronic mode):

$$D^0 \longrightarrow \begin{cases} \longrightarrow K^- e^+ \nu_e & (3.55 \pm 0.04)\,\% \\ \longrightarrow K^- \mu^+ \nu_\mu & (3.30 \pm 0.13)\,\% \\ \longrightarrow K^- \pi^+ & (3.88 \pm 0.05)\,\% \\ \longrightarrow \ldots \end{cases} \tag{5.13}$$

in which μ^+ is produced directly from D^0 decay and other muons are produced via K and π mesons chain decays. Consequently, a non-negligible fraction of additional muons can be produced by introduction of charm particles into hadronic interaction models. Mean life time of charmed mesons is very short $\tau_{D^\pm} = 1.04 \times 10^{-12}$ s, or

[6] There are evidently large uncertainties regarding charm particle interactions and cross sections but this fact can be omitted in our consideration without losing possibility to answer the substantial question whether charm production can mitigate the muon number discrepancy.

$c\tau_{D^\pm} = 0.3\,\mathrm{mm}$ [150]. The mean life times of neutral charmed mesons and charmed baryons are even shorter. When charmed particles decay they give rise to formation of kaons, pions and other baryons, leptons and muons part of which are produced as prompt direct products and the rest are produced in cascade secondaries decays. Let us summarize main sets of $D^\pm$, D^0 and Λ_C particles inclusive decay channels from the point of muon production [150] (branching ratios are rounded and listed without errors due to lucidity):

$$
\begin{array}{lllllll}
D^- & \xrightarrow{18\,\%} & \mu^- \ldots & & & & \\
 & \xrightarrow{52\,\%} & \bar{K^0} \ldots + K^0 \ldots & ; K^0_L & \xrightarrow{27\,\%} & \mu^\pm \ldots & \\
 & \xrightarrow{28\,\%} & K^\pm \ldots & ; K^\pm & \xrightarrow{64\,\%} & \mu^\pm \ldots & \\
 & & & & & & \\
D^0 & \xrightarrow{6.7\,\%} & \mu^+ \ldots & & & & \\
 & \xrightarrow{47\,\%} & \bar{K^0} \ldots + K^0 \ldots & ; K^0_L & \xrightarrow{27\,\%} & \mu^\pm \ldots & \\
 & \xrightarrow{53\,\%} & K^\pm \ldots & ; K^\pm & \xrightarrow{64\,\%} & \mu^\pm \ldots & \\
 & & & & & & \\
\Lambda_C & \xrightarrow{2\,\%} & \mu^+ \ldots & & & & \\
 & \xrightarrow{33\,\%} & \Lambda \ldots & & \xrightarrow{64\,\%} & p\,\pi^- & ; \pi^- \xrightarrow{\sim 100\,\%} \mu^- \ldots \\
 & \xrightarrow{10\,\%} & \Sigma^\pm \ldots & & \xrightarrow{48\,\%} & n\,\pi^\pm & ; \pi^\pm \xrightarrow{\sim 100\,\%} \mu^\pm \ldots
\end{array}
\tag{5.14}
$$

The directly produced muons highlighted by blue color in the above stated decay schema have statistically more energy than muons produced by pions or secondary kaons. The chain decay 5.14 illustrates the complexity of implementation of charmed mesons and baryons decay chains. They lead to very energetic prompt muons and neutrinos (they are not included in the decay schema 5.14 for brevity).

QGSJET01c enables production of charm quarks and antiquarks [151]. Despite the fact that the original QGSJET code was tuned in the way that observables agree with measured values without the introduced fourth charm quark, it is not necessary to re-tune all model parameters to explore c quark production influence on the muon content in EAS with other consequences. As described in one of the previous chapters, charmed particle production is represented by 6 mesons and baryons in QGSJET01c: $D^\pm$, D^0, $\bar{D}_0$, $\Lambda_C^\pm$, lightest from all possible particles that contain c quark. Due to very short life time of charmed hadrons they mainly decay after passing corresponding distance. $\pi^\pm$ and nucleon cross-sections with air were used to approximate these parameters for charmed mesons and baryons to take into account particle interactions.

As decays and treatment of charmed particles were not implemented into the CORSIKA that missing part was coded as a separate program and interfaced to CORSIKA. Decays were carried out by means of currently known branching ratios and particle production [152]. Charm particles decays were programed by the thesis author with permission and using unpublished program of Jan Řídký's program that was extended and adjusted to this analysis.

Beauty

Besides charm quark c that was incorporated into hadron interaction model QGSJET01c and consequently into EAS, also b quark production and its inclusion into air showers was elaborated in a very simple way. Due to the fact that none of the QGSJET versions produce particles with b quark the solution follows from the existing QGSJET01c generator with implemented charm particles decay chain supplied by beauty particle decays. The charm particle creation is turned on and used to subsume b-particles into the shower. The implementation includes two b-hadrons to test its impact on muon content and spectrum. Beauty particles are represented by two lightest particles $B^{\pm}$. Their production was implemented as artificial transformation of $D^{\pm}$ particles when they are produced and stacked as secondary particles in the following way: $D^{+} \longrightarrow B^{+}$ and $D^{-} \longrightarrow B^{-}$ with probability of 10%. Thus, such solution decreases number of primary charm particles, but on the other hand it replaces them by b-hadrons. Interactions of b-hadrons can be neglected taking into account their lifetime $\tau_{B^{\pm}} = 1.641 \pm 0.008 \times 10^{-12}\,\mathrm{s}$ [150] so only decays of beauty particles were taken into account.

In the following table the basic inclusive decay chains are pointed out (branching ratios are rounded and listed without errors due to lucidity reasons). Decay sequence ends when it leads to D mesons. Their decay cascade was outlined in the previous section in 5.14 [150]:

$$
\begin{array}{lllllll}
B^{+} & \xrightarrow{11\,\%} & \mu^{+} \ldots & & & & \\
 & \xrightarrow{79\,\%} & \bar{D}^{0} \ldots & ; \bar{D}^{0} & \rightarrow & \ldots & \\
 & \xrightarrow{9\,\%} & D^{0} \ldots & ; D^{0} & \rightarrow & \ldots & \\
 & \xrightarrow{12\,\%} & D^{\pm} \ldots & ; D^{\pm} & \rightarrow & \ldots & \\
 & \xrightarrow{9\,\%} & D_{S}^{\pm} \ldots & ; D_{S}^{\pm} & \xrightarrow{36\,\%} & K^{0;\pm} \ldots & \\
 & \xrightarrow{5\,\%} & \Lambda_{C}^{\pm} \ldots & ; \Lambda_{C}^{\pm} & \rightarrow & \ldots &
\end{array}
\tag{5.15}
$$

Besides the above outlined decay products (D-mesons and muons) numbers of kaons and their excited forms K^{*}, pions as well as neutrinos are produced. From decay branching ratios one can suppose that relatively large fraction of energy would be transfered directly to muons and neutrinos (similarly to the charm case also in this decay scheme neutrinos were not listed in 5.15 in order to keep lucidity). In case of enhanced production of beauty particles (in our case the production is restricted only to $B^{\pm}$), large fraction of primary energy flows into them. In the second step, they decay within very short time into muons and neutrinos with branching ratio 10.99%.

Results

The effect of heavy flavours on muon numbers and other characteristics of EAS has been studied by means of implementation of charm and beauty production into EAS simulations as described above. *CORSIKA version 6.900* with low energy interaction generator *GHEISHA* has been used in its original release without

$\theta = 0°$

Variable	**Original**	**5x charm**	**10x charm**	**100x charm**
$n^{rel}_{\mu,TOTAL}[\%]$	100.00 ± 1.47	99.50 ± 2.07	97.98 ± 2.05	94.87 ± 2.02
$n^{rel}_{\mu,E>50\,\mathrm{GeV}}[\%]$	100.00 ± 1.97	99.41 ± 2.77	103.85 ± 2.84	111.47 ± 2.95
$\bar{E}_\mu[\mathrm{GeV}]$	8.00 ± 0.07	9.15 ± 0.32	9.81 ± 0.23	19.37 ± 1.09
$E_{Miss}/E_0[\%]$	8.66 ± 0.18	9.47 ± 0.20	10.12 ± 0.32	14.22 ± 0.56

$\theta = 60°$

Variable	**Original**	**5x charm**	**10x charm**	**100x charm**
$n^{rel}_{\mu,TOTAL}[\%]$	100.00 ± 1.50	95.78 ± 2.07	94.24 ± 2.06	89.86 ± 2.01
$n^{rel}_{\mu,E>50\,\mathrm{GeV}}[\%]$	100.00 ± 1.63	96.59 ± 2.27	98.40 ± 2.29	98.55 ± 2.29
$\bar{E}_\mu[\mathrm{GeV}]$	18.65 ± 0.18	20.55 ± 0.58	22.16 ± 0.43	40.51 ± 1.13
$E_{Miss}/E_0[\%]$	8.52 ± 0.19	9.14 ± 0.29	10.19 ± 0.68	13.89 ± 0.46

Table 5.3: Average muon energy $\bar{E}_\mu$ and relative number of muons to original CORSIKA with QGSJET01c without charm for different level of charm production; $n^{rel}_{\mu,TOTAL}$ denotes relative number of all muons, $n^{rel}_{\mu,E>50\,\mathrm{GeV}}$ is relative number of muons with energy greater than 50 GeV. Two sets for different zenith angles $\theta = [0°; 60°]$ were simulated. Original QGSJET01c (**Original**) results are taken as a reference for number of muons and given zenith angle set. Relative number of muons are listed for charm production increased by a factor of 5, 10 and 100. The missing energy given in percentage of the primary energy is given. For each of type and configuration 100 events were simulated with proton primary of energy of $E = 5 \times 10^{18}$ GeV. Only statistical errors are given.

charm production (denoted as **Original** in tables and figures). The effect of charm and beauty production on muon numbers turns out to be very mild. The use of predefined official level of charm production in QGSJET01c does not bring any observable changes from muon production point of view. Therefore, the level of charm production must be increased. In order to see and to quantify the effect of charm particles its production has been turned on and increased by factor of 5, 10 and 100. The unrealistic charm production was chosen in order to find and identify a trend of missing energy development and number of hard and all muons. The primary energy was set to 5×10^{18} GeV in order to find compromise between studied effects, data storage and CPU time demands. The following variables are estimated from 100 events per each configuration (which is sufficient statistics to make conclusions). Thinning version of CORSIKA was used.

Among others the overall number of muons (with $E > E_{\mu,cut} = 0.3\,\mathrm{GeV}$) [7] at ground level and number of muons with energy more than 50 GeV have been counted to find out whether heavy flavours production could be the source of discrepancy between predicted and measured number of muons with $E \gtrapprox$

[7] The energy cut for muons was set in the shower generator to $E_{\mu,cut} = 0.3\,\mathrm{GeV}$.

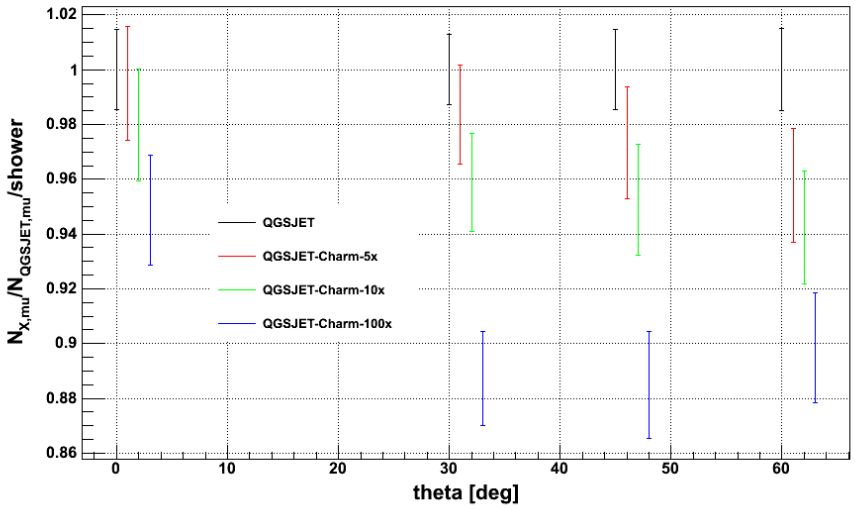

Figure 5.11: Ratio of muon numbers to original QGSJET01c without charm production. 100 proton showers were simulated to calculate presented average values with primary energy of $E = 5 \times 10^{18}$ GeV. Original QGSJET01c with CORSIKA without charm, 5 times more charm production, 10 times and 100 times are shown. For lucidity reasons results for different charm production are slightly shifted (each one by 1°) along x-axis, however only events for zenith angles $\theta = [0°; 30°; 45°; 60°]$ were simulated. Statistical errors are given.

50 GeV [118]. In the Tab. 5.3 these basic muon characteristics are listed as simulated for different charm production configuration of CORSIKA and QGSJET01c. Relative number of total muons $n^{rel}_{\mu,TOTAL}$ to original QGSJET01c settings without charm are calculated for several excessive charm production rates. Moreover, relative number of muons with energy greater than 50 GeV is shown together with average muon energy. The missing energy E_{Miss} in percentage of the primary energy E_0 is given. E_{Miss}/E_0 increases with charm production level up to the value of greater than 1.63 times of non-charm original value. One can estimate from the Fig. 5.9 that the most intensive c quark production in proton showers in this analysis leads to the missing energy at the level 1.35 times greater compared to QGSJET-II with iron primaries at this energy. Results in Tab. 5.3 are calculated based on 100 proton showers with primary energy of $E = 5 \times 10^{18}$ GeV. Two sets of shower configuration were chosen, namely vertical showers ($\theta = 0°$) and inclined showers with zenith angle $\theta = 60°$. The complete table of results for simulation with zenith angles $\theta = [0°; 30°; 45°; 60°]$ is included in Appendix B in Tab. B.1.

From presented results one can conclude that only for charm production increased 100 times compared to the original settings of charm production in QGSJET01c and for vertical showers number of muons with $E > 50$ GeV is statistically greater then that produced by original QGSJET. On the other hand, the

total number of muons decreases in this case. For inclined showers (in our case for $\theta = 60°$) number of muons with $E > 50\,\mathrm{GeV}$ is comparable for all types of charm levels. This is an implication of the fact that excessive charm production changes energy distribution of $\mu^{\pm}$ and longitudinal profile of particles. Muons produced as decay product from charm particles have much larger energy than 50 GeV and they are produced in early stages of EAS. On the other hand large fraction of energy is transfered into high energy muons (and neutrinos) and therefore, as evident from particle profiles presented further in this section, there are less electromagnetic particles and also smaller number of hadrons compared to the original QGSJET without charm. The primary energy $E = 5 \times 10^{18}\,\mathrm{eV}$ is chosen so that for the inclined showers with $\theta = 60°$ the X_{max} is close to the ground level and still significant number of hadrons are not decayed. The situation changes for inclined showers ($\theta = 60°$) where all hadrons are decayed when particles reach the ground level. This causes that for inclined showers additional muons with $E > 50\,\mathrm{GeV}$ are produced from non-charmed sources and this effect is more intensive for the showers that contain more hadrons. Therefore, for inclined showers number of high energy muons with $E > 50\,\mathrm{GeV}$ is comparable for all types of configurations.

It is evident that the average muon energy rises together with charm production level as was assumed in the previous part of this chapter. High energy muons are produced in early stages of EAS as direct (or indirect) products of charm particle decays. The average energy of muons detectable at the ground level also rises with zenith angle. This is obviously caused by the effect of the lowest energy muon decay (see Tab. B.1 in Appendix B).

The relative number of total and high energy muons (with $E > 50\,\mathrm{GeV}$) is depicted in the figures Fig. 5.11 and Fig. 5.12. Table of results with statistical errors can be found in Appendix B in Tab. B.1. As evident from figures the total number of muons decreases with growing zenith angle for given level of charm production compared to non-charm version of CORSIKA with QGSJET01c. The same conclusions stand for high energy muons with energy greater than 50 GeV. Total number of muons also decreases with increase of the charm production level at given zenith angle. From Fig. 5.12 one comes to the opposite conclusion for muons with $E > 50\,\mathrm{GeV}$. The higher charm level production the higher number of high energy muons compared to QGSJET01c without charm.

Tracks of muons distinguished by their ancestors are displayed in Fig. 5.13. Depicted tracks are supposed to be linear and the lateral origins are put on the shower axis for illustration purposes. Those muons that have one of their predecessors charmed particle are denoted as charm-originated. There are both direct decay products as well as muons that were produced from particle decay after several steps, but in both cases muons originate from charmed particle(s). One can estimate from Fig. 5.13 that charm-originated muons are produced in average in earlier stages of EAS compared to other muons. The average height of muon production differs by more than $\sim 1000\,\mathrm{m}$ measured for vertical proton shower of primary energy $E = 5 \times 10^{18}\,\mathrm{eV}$.

The fact that charmed particles are produced in the early stages of EAS development also leads to the change of muon lateral distribution at ground level.

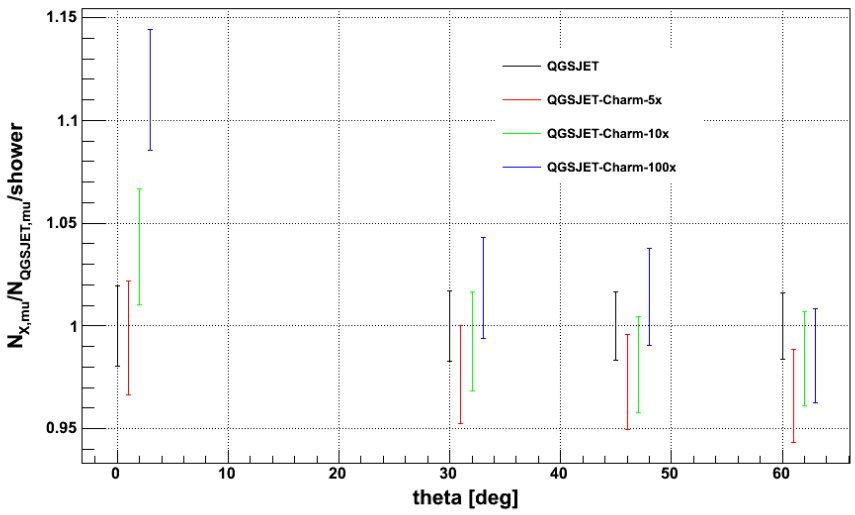

Figure 5.12: Relative number of muons with energy $E > 50\,\mathrm{GeV}$ compared to original QGSJET01c without charm production. 100 proton showers were simulated and averaged with primary energy of $E = 5 \times 10^{18}\,\mathrm{GeV}$. Original QGSJET01c with CORSIKA without charm, 5 times more charm production, 10 times and 100 times are shown. For lucidity reasons results for different charm production are slightly shifted (each one by 1°) along x-axis, however only events for zenith angles $\theta = [0°; 30°; 45°; 60°]$ were simulated. Statistical errors are given.

Lateral distributions of muons at ground level displayed according to their origins (the principle of division is the same as described in the previous paragraph) are depicted in Fig. 5.14. Muons that originate from charm particles are more concentrated around the shower axis at the ground level than other muons. This also relates to the fact that muons originating from the charm have in average more energy and are produced in earlier stages - before the hadronic shower maximum. Charm particle sources have rather large energy and their direction is close to the shower axis. High energy muons are only slightly deflected as they pass through the atmosphere.

To show the effect of charm production in inclined showers 50 proton showers with proton primary energy of $E = 7 \times 10^{18}\,\mathrm{eV}$ for different zenith angles were simulated. In Fig. 5.15 muon energy spectra are shown for original QGSJET01c code without charm (red color) and with charm production increased by a factor of 100 (blue color). For the latter case the energy distribution of muons with charm origin is given separately (green color) as well as non-charm muon energy distribution (black color). Muons originated from charm particles are obviously hard. Up to roughly $E_\mu \sim 3.7\,\mathrm{TeV}$ there are more muons originated from non-charm particles. As a consequence, up to $E_\mu \sim 330\,\mathrm{GeV}$ there is higher number of muons from original QGSJET01c without charm option compared to simulations

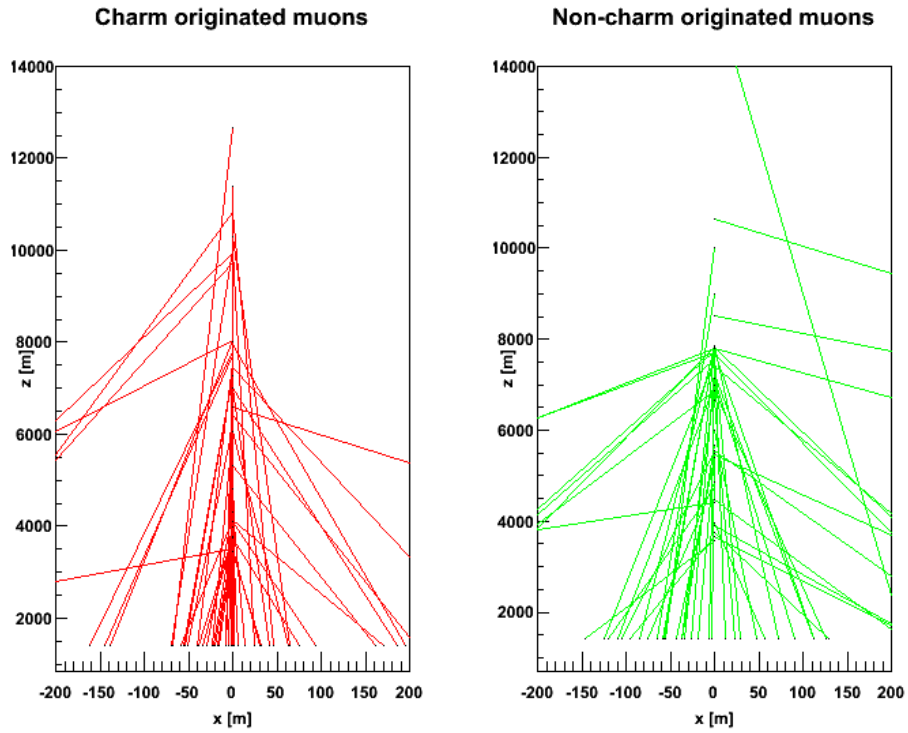

Figure 5.13: Illustration of muon tracks simulated with charm production in QGSJET with CORSIKA. Muons originated from charmed particles are depicted in red on the left figure. Tracks of other muons that come from non-charmed particles are depicted by green line on the right figure. Origins of tracks are put to the axis for illustration purposes and tracks are supposed to be straight without deflections. Depicted muons originate from vertical proton shower with primary energy of $E = 5 \times 10^{18}$ eV.

with charm option turned on.

Longitudinal profile of hadrons, muons and electrons from original CORSIKA with QGSJET01c without charm production is shown in Fig. 5.16 compared to modified CORSIKA with increased charm production by a factor of 100. Events with excessive charm production are characterized by smaller number of muons along the whole shower profile as was already indicated in the previous part of this chapter. Moreover, due to large energy fraction carried to hadronic part of the shower, less electrons as well as hadrons are produced in comparison with non-charm QGSJET configuration. As a consequence, it leads to increased fraction of missing energy despite the fact that number of muons decreases. In the previous section it was shown that missing energy can be parametrized by number of muons detected on ground level (see 5.3.4). In this situation missing energy increases because of increase of average energy of muons and neutrinos. Increase of missing

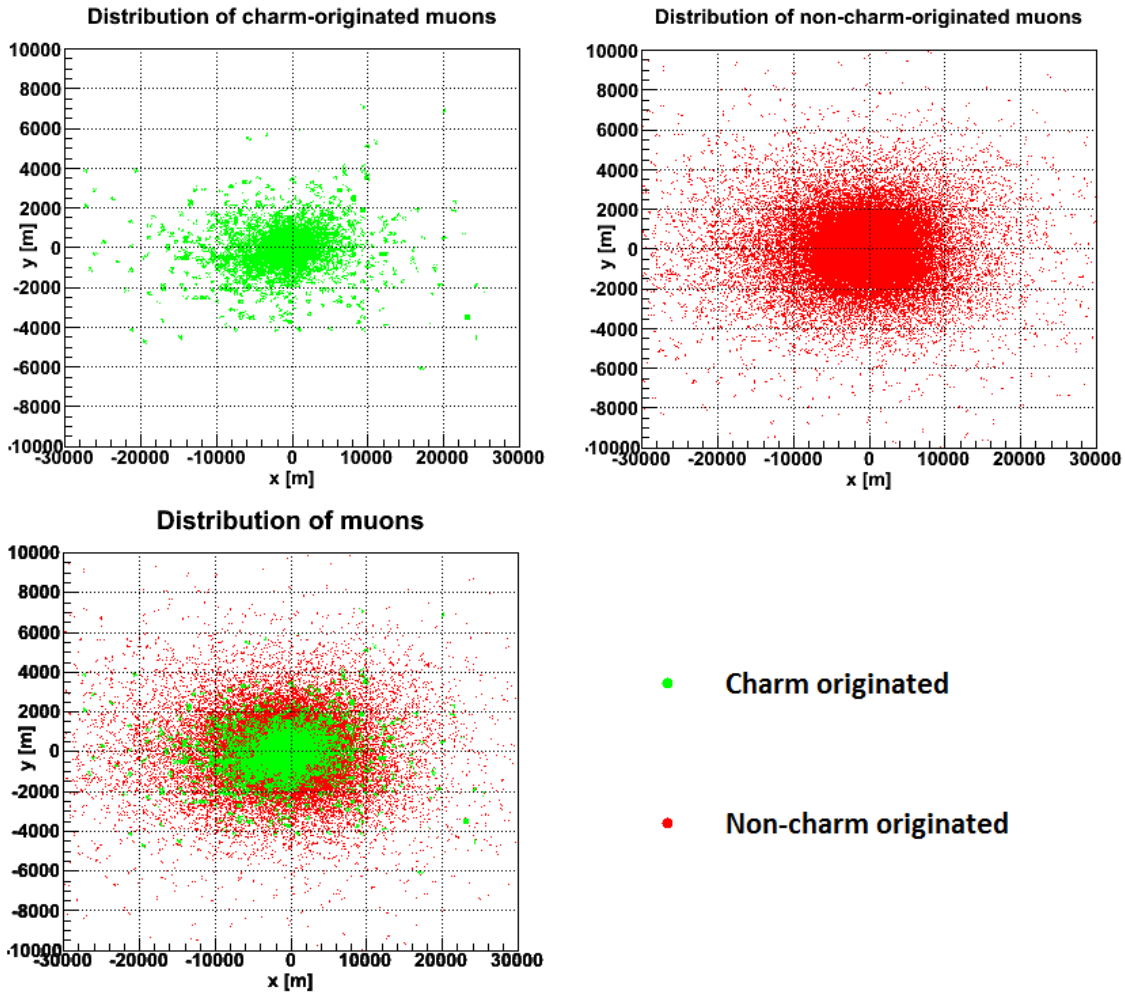

Figure 5.14: Lateral muon distributions according to the muon origin. Charm-originated muons are depicted by green color, while other muons are depicted by red color. Those muons that have in their decay chain a charm particle predecessor are denoted as charm-originated. Muons that come from charmed particle are more concentrated around the shower axis. The simulated shower energy was 7×10^{18} eV with $\theta = 80$ deg and proton as a primary particle.

energy could be still within an acceptable range as indicated in Fig. 5.10, but excessive charm production results in decrease of number of muons which is the opposite effect as it would be desired. Small number of total hadrons as excessive charm production in showers relates also to the number of high energy muons. As it was shown above whilst exorbitant charm production leads to larger number of high energy muons in vertical showers, in inclined showers the deviation disappears compared to non-charm simulations. This can be explained by the fact that showers that do not contain charm particles have more hadrons that produce secondary pions decaying into muons (see Fig. 5.16).

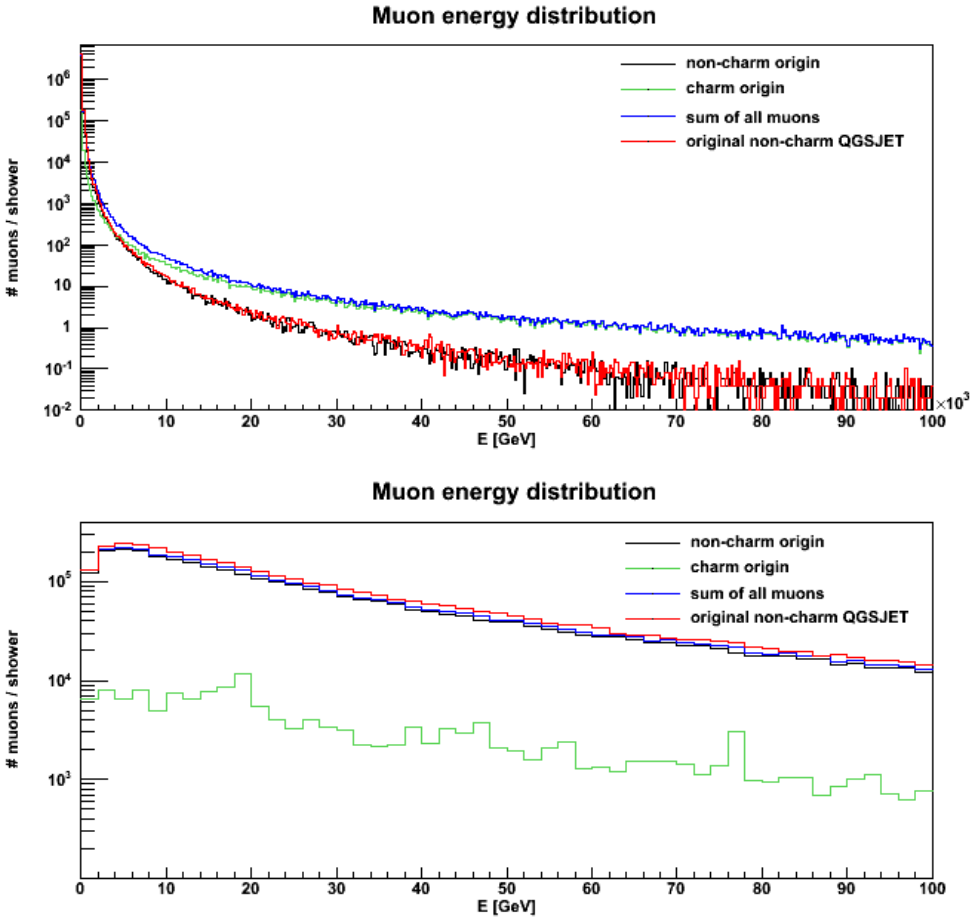

Figure 5.15: Muon energy distributions according to the muon origin. Original CORSIKA with QGSJET without charm option is depicted as benchmark by red color. Energy distribution is averaged over 50 events of protons shower with primary energy of $E = 7 \times 10^{18}$ eV and $\theta = 80°$. QGSJET with charm option (charm production probability is increased by a factor of 100) is drawn by blue color and it is also divided into two components - charm originated muons (green color) and non-charm originated muons (black color).

In the Tab. 5.4 the increase of missing energy with increasing charm production for several sets of simulations is shown. For each configuration 200 proton showers were simulated in total (100 events per each zenith angle; $\theta = [0°; 60°]$). There are four different energies in order to see the behaviour with respect to primary energy. The missing energy was calculated from CORSIKA longitudinal energy profile outputs according to estimated contributions of different particle types described in [153].

Decrease of missing energy ratio with primary energy for different level of charm production from Tab. 5.4 is depicted in Fig. 5.17. When comparing with other primaries and hadronic interaction models in the Fig. 5.9 it is obvious that the

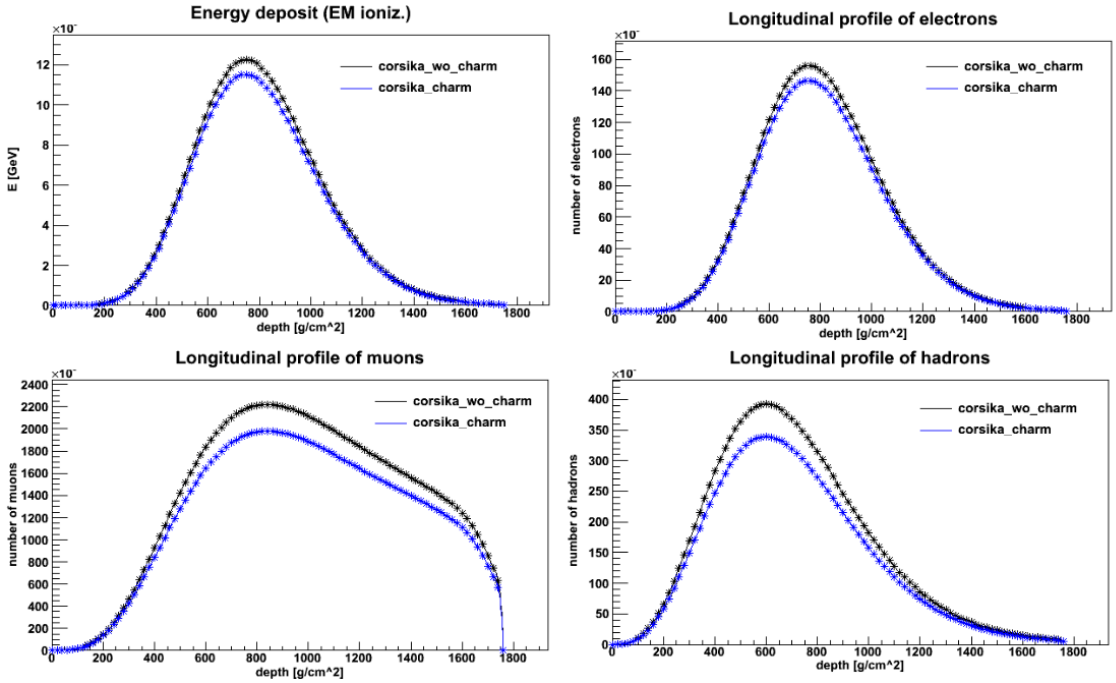

Figure 5.16: Longitudinal profile of electrons hadrons, muons and longitudinal energy deposit averaged over 100 events for original CORSIKA with QGSJET01c without charm production (black curves) and modified CORSIKA / QGSJET01c with charm production increased 100 times (blue curves). Proton showers were simulated with primary energy $E = 5 \times 10^{18}$ eV and $\theta = 60°$.

missing energy for highest charm level production reaches higher values than those given by other generators for iron primaries except for EPOS 1.61 for energies below 5×10^{19} eV. The increase of charm production by the factor of 100 causes that the missing energy increases by tens of percents compared to non-charm proton simulations. The ratio $r_{Miss,100x} = E_{Miss,100x}/E_{Miss,Original}$ represents the increase of the missing energy for highest charm production level compared to the non-charm simulations. $r_{Miss,100x}$ increases with primary energy by factor 1.52 for the primary energy $E_0 = 1 \times 10^{18}$ eV to factor 1.74 for the energy $E_0 = 5 \times 10^{19}$ eV.

As shown earlier the number of muons does not increase at the ground level with charm production. On the other hand the missing energy does significantly increase. In case that from some energy level the charm production is getting significantly stronger the conclusion from the work [142] that the missing energy correction can be expressed simply according to the number of muons at the ground level would not be valid.

In order to assess the effect of b quark, production of beauty particles was implemented in a simple way. With probability of 10% $D^{\pm}$ particles were in program converted to $B^{\pm}$. The relative number of all muons $n^{rel}_{\mu,TOTAL}$, muons with energy greater than 50 GeV $n^{rel}_{\mu,E>50\,\mathrm{GeV}}$ and the average muon energy $\bar{E}_{\mu}$ are statistically comparable to presented results for charm only particle production (see Tab. 5.3).

E_0[eV]	E_{Miss}/E_0 [%]			
	Original	**5x charm**	**10x charm**	**100x charm**
$E_0 = 1 \times 10^{18}$	9.77 ± 0.10	10.31 ± 0.15	11.00 ± 0.23	14.85 ± 0.32
$E_0 = 5 \times 10^{18}$	8.54 ± 0.09	9.12 ± 0.17	9.96 ± 0.22	14.12 ± 0.31
$E_0 = 1 \times 10^{19}$	8.15 ± 0.07	8.57 ± 0.14	9.13 ± 0.19	13.62 ± 0.32
$E_0 = 5 \times 10^{19}$	7.10 ± 0.05	7.62 ± 0.13	8.19 ± 0.14	12.36 ± 0.29

Table 5.4: Missing energy ratio to the primary particle energy E_0 for original CORSIKA without charm production (denoted as **Original**) compared to different levels of charm production. 100 proton events were simulated for each shower type and for 4 different zenith angles $\theta = [0°; 30°; 45°; 60°]$, i.e. for each energy and charm production level 400 showers were generated (azimuth angle was generated randomly).

Results for vertical and inclined showers with zenith angle $\theta = 60°$ were compared to those with charm increased production and no significant differences were found.

As obvious from presented results for different charm production levels heavy flavour generation does not lead to increased muon number production without substantial increase of missing energy. Heavy flavours production can not solve the muon discrepancy observed and described by Petr Trávníček in his thesis mentioned in the section 5.1 [118].

Total number of muons does not increase as a consequence of very high energy charm and beauty particles creation in EAS. In the early stages of EAS development, large fraction of energy is carried away by charmed (or beauty) particles. As outlined in previous sections charm particles decay either directly to muons and neutrinos or indirectly via kaons or pions in later EAS stages. Even in the latter case muons and neutrinos carry away significant fraction of energy. There are two consequences of such phenomena. First of all, energy that could be transferred into further development of hadronic shower is taken away early and therefore lower energy fraction is transformed into muons via pion (kaon) channel. Therefore, also less electrons, but also hadrons are produced along shower development compared to the non-charm case. This causes that for vertical showers and for some energies larger number of high energy muons can be seen ($E > 50\,\mathrm{GeV}$), but for inclined showers small number of produced hadrons outweighs this phenomenon and number of high energy muons is again statistically close to the case of non-charm showers. Simultaneously the average muon energy increases which leads to missing energy increase.

Results from D0 and LHCb experiments from Tevatron and LHC accelerators respectively do not indicate excessive charm production. The $c\bar{c}$ cross section necessary to reproduce charmed hadron production at center-of-mass of 7 TeV in the

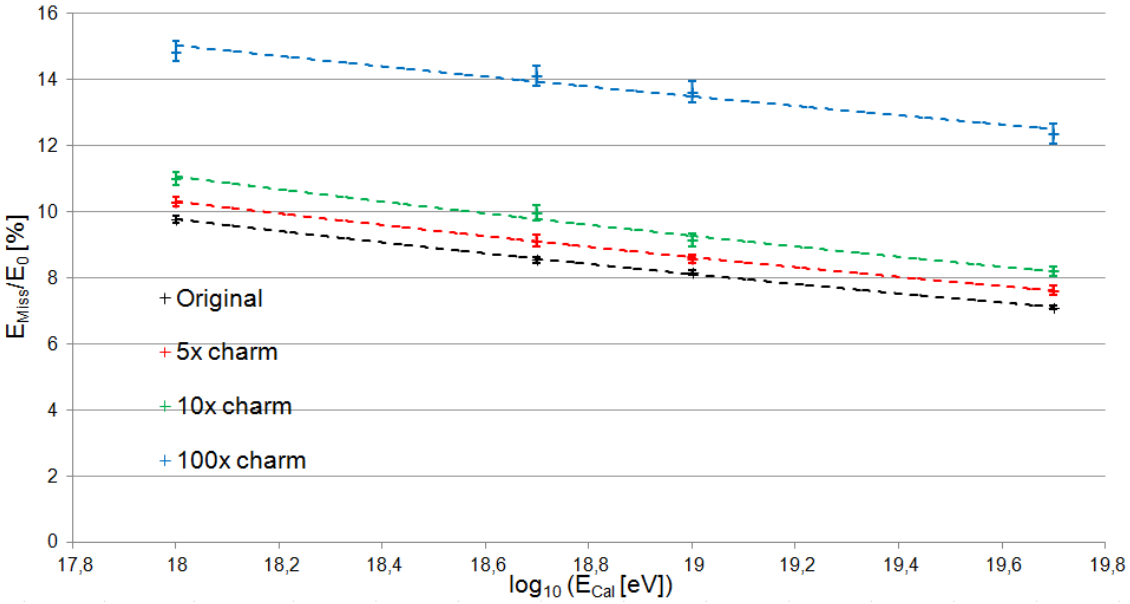

Figure 5.17: Missing energy ratio to the primary energy for proton showers of different charm production and energies from Tab. 5.4. The exponential fit is included for each type of simulation to see decrease of the ratio with primary energy.

kinematic range $0 < p_T < 8\,\mathrm{GeV}$ has been found as follows [154][8]:

$$\sigma(c\bar{c})_{p_T<8\,\mathrm{GeV}} = 1419 \pm 12\,(\mathrm{stat}) \pm 116\,(\mathrm{syst}) \pm 65\,(\mathrm{frag})\,\mu b. \qquad (5.16)$$

The official charm particle production implemented in CORSIKA is performed mainly via creation of $c\bar{c}$-pair. The cross section of such processes is energy dependent and originally in CORSIKA it is set at in the range of $\sigma = 39\,\mu\mathrm{b}$ at $E_{lab} = 200\,\mathrm{GeV}$ and of $\sigma = 24\,\mathrm{mb}$ at $E_{lab} = 10^{10}\,\mathrm{GeV}$ for pp collisions [155]. In the work [156] the charm cross section in CORSIKA has been tested and at center-of-mass of 7 TeV it was found at the level of more than 2 mb which is higher than above stated measured value 5.16.

All the presented results indicate that heavy flavour quark production does not explain either the muon number with $E > 50\,\mathrm{GeV}$ discrepancy observed by Petr Trávníček nor total number muon discrepancy observed also from Pierre Auger Observatory data. As a conclusion there is no indication that either charm production or even heavier quark production such as b could explain the observed muon number discrepancy.

[8] Differential cross section of neutral and charged mesons D^0, $\bar{D}^0$, $D^{\pm}$, $D^{*\pm}$, $D_S^{\pm}$ together with $\Lambda_C^{\pm}$ has been studied and taken into account.

Chapter 6

Conclusions

The materials dealt with in the submitted dissertation arisen during my work at the Pierre Auger Observatory. This comprised participation in the hardware development, data taking and data analysis.

Concerning the hardware I have designed, delivered and implemented the alarm system for FD shifters. The necessity of this system become obvious during the period when supervisor of this dissertation acted as FD task coordinator.

Also my study of PMT calibration dependence on the ambient temperature during operation stems from the long term participation of the Czech group in FD operation.

The data analysis and Monte Carlo studies deal with the muon production with the aim to find possible sources of muons in the secondary particle spectrum of EAS and to propose some ways how to mitigate the observed discrepancy between predicted and measured numbers of muons at ground level. This study started in time when no results of heavy flavour production were known from LHC data and therefore their possible contribution and influence were investigated. Obtained results consecutively lead to an assessment of heavy flavour influence on muon content. Finally, it leads to the conclusion that the discrepancy of the number of muons should be explained rather by standard soft sources (pions, kaons) and that eventual production of hard muons would significantly change the relation between the missing energy and muon content of EAS.

Temperature measurement study

Temperature sensors have been installed in FD buildings to monitor thermal stability as the temperature influences sensitivity of photomultipliers in FD cameras. The analysis of data measured at Coihueco site showed that long term temperature near the camera can vary in the range up to $\sim 16\,^{\circ}\mathrm{C}$. Temperature varies also in the calibration room and the difference between long term maximum and minimum can exceed $\sim 10\,^{\circ}\mathrm{C}$.

The air-conditioning system does not keep perfectly uniform temperature and various factors have been identified that correlate with temperature such as opening of shutters, switching of electronics, twilight. The typical temperature variation

near the camera was found to be at the level of $\sim 3\,^{\circ}\mathrm{C}$ during one shift night. Inside the calibration room the temperature is more stable and only $\sim 1\,^{\circ}\mathrm{C}$ difference is commonly measured near calibration light sources during one shift night. Up to $\sim 8\,^{\circ}\mathrm{C}$ temperature difference can be seen near the camera during one shift period. Therefore, taking into account $\Delta_t = 8\,\mathrm{K}$ it could theoretically lead to the camera response variation in calibration A up to the level of

$$\Delta_{cal_A} \approx -0.3\%/\mathrm{K} \times \Delta_t = 2.4\%, \tag{6.1}$$

provided that LED light intensity dependence on temperature can be neglected.

The correlation between temperature measured in immediate proximity of camera pixels (at the top of the camera) and calibration constants has been studied and the anti-correlation was confirmed. Long time camera response trend was eliminated and it was shown that correlation between instantaneous temperature measured at the time of calibration measurement is $R_{\Delta_T=0} = -0.246$. The correlation gets higher in absolute value when it is calculated for temperature shifted by Δ_T before calibration is performed. The first minimum of correlation (the highest anti-correlation) was found for $\Delta_T = 120.1\,\mathrm{h}$ as $R_{\Delta_T=120.1\,\mathrm{h}} = -0.376$ and the correlation varies with other 3 minima for higher Δ_T values with average delay of $\approx 28.5\,\mathrm{days}$. For $\Delta_T > 2173.3\,\mathrm{h}$ the correlation weakens.

The linear fit for offset value $\Delta_T = 120.1\,\mathrm{h}$ gives the relation between corrected absolute calibration constants and the camera temperature

$$c_{corr,T} = 4.594 + (-0.011 \pm 0.001) \times T[^{\circ}C],$$

the statistical error is given. The slope -0.011 defines relative deviation per $1\,^{\circ}C$ change taking into account typical value (mean 4.30 and median 4.29) of calibration constant ~ 4.3: $\Delta_C \approx 0.011/4.3 \approx 0.26\%$, which is in agreement with Pierre Auger experiment internal measurement $-0.3\%/K$.

The main result of the correlation analysis is the correction that can be applied to calibration constants in case the temperature deviates from target value of air-conditioning (21.5°C):

$$c_{corr,t_i,T_{t_i-120.1\mathrm{h}}} = c_{corr,t_i} + 0.011 \times (T[^{\circ}\mathrm{C}] - 21.5^{\circ}\mathrm{C}).$$

The regular time structure of three periods in the correlation between camera temperature and calibration constants is result of periodical temperature variation and regular length of shift period. Beyond three periods the overall correlation is reduced. In other words, temperature behaves similarly during three months and after this period weather conditions start to change substantially. Simultaneously, periodic shape of correlation curve in positive R_Δ shows that calibration constant behavior during shift period has also regular structure. After three periods the correlation disappears and becomes accidental.

Shift Guard - FD Alarm system

The FD alarm system with control C++ program called *Shift Guard* has been proposed and developed and installed by me to monitor operation and to inform

shifters about serious or dangerous situations in order to protect FD detectors. It is an automatic system that checks weather condition, light condition, Internet communication, database connectivity and other aspects of measurement and data taking which can influence data quality and possibly endanger fluorescence detectors.

Shift Guard uses the light column with 4 different lights that is able to signalize different levels of alarms, namely *warning*, *high* and *critical*. Alarms are supported by specific sounds for each level of the message. FD shifters can acknowledge or resolve alarms via web site interface, but they are primarily informed about specific situations and in some cases it is necessary to perform specific defined actions. The Shift Guard not only helps to protect detectors, but it also increases in an indirect way up-time of the FD. The up-to-date version of the Shift Guard ensures monitoring of the following weather conditions and connections:

- wind speed
- camera pixel variances
- MySQL connectivity
- rain
- internal GPS timing.

The use of the Shift Guard is described and available on the web site and checklist used by shifters during shift night as a guide and in detail in the internal paper together with procedure how to extend and to add a new alarm. The alarm system is designed in order to be easily extensible. The standard code documentation is supplemented with overall code architecture of the Shift Guard.

The alarm system is a flexible tool that offers to monitor wide range of physical variables, conditions, statuses of detectors and connections. Shift Guard was installed in October 2010 and since then it is operating smoothly and reliably.

All alarms and actions as well as important internal messages and statuses are stored. Off-line reporting has been designed and implemented to show reaction times to acknowledgement or solution of the alarms. Besides these tasks, there is a website to select most recently raised alarms with detailed information.

Muon production study

The influence of heavy flavours has been studied by charm and beauty particles incorporation into EAS development. The effect of charmed and beauty particles produced in EAS on muon characteristics is not significant at the level of expected c and b quark production. Significant charm production would lead to smaller total number of muons, whilst number of muons with energy above 50 GeV would be higher than in normal case. As heavy flavour particles are created in early stages of EAS, number of high energy muons can be higher than in case of showers with negligible heavy flavour production. Nevertheless, this effect is outweighed by smaller number of hadrons which decay into muons.

The most recent measurements from LHCb experiment and D0 from Tevatron do no indicate increased or excessive charm production compared with original charm settings in QGSJET01c generator.

Exotic muon source from the dark sector described by various models [158] has been studied. Instead of considering the whole set of different dark matter models, rather general idea was adopted [159]. According to this approach one can expect besides dark matter of TeV-scale mass relatively ligh particles with mass around 250 MeV and weak coupling constant to ordinary matter. Massive dark photons as a possible additional source of muons can be produced in EAS and its number has been estimated via massive photon Bremsstrahlung formula expression in a simplified way incorporated in the EAS simulations using CORSIKA. With some astrophysical constraints on mixing factor the number of muons of dark photon origin is approximately not greater then two per 1000 proton showers at primary energies of 10^{19} eV. Similar results have been obtained for four sets of interaction models (and for proton and iron primaries). Thus the effect is unobservable.

It has been shown in Trávníček's work [142] that a missing energy correction depends on the number of total muons on the ground level. The analysis of charm and beauty production suggests that the relation between missing energy and number of muons on the ground level would be broken in case of significant increase of charm production at UHECR collisions. The average muon energy increases with the charm production. Simultaneously, number of muons at ground level decreases while the missing energy grows up with charm production level. Consequently, the significant increase of charm production at some energy would change the relation between missing energy and number of observed muons at ground level. On the other hand the missing energy dependence on the muon numbers at ground level implicitly carries information about heavy flavour production.

The missing energy rapidly increases with significant charm or beauty production due to high energy muons and neutrinos production. The level of missing energy is substantially higher than expected values.

Appendix A

Calibration constants distributions

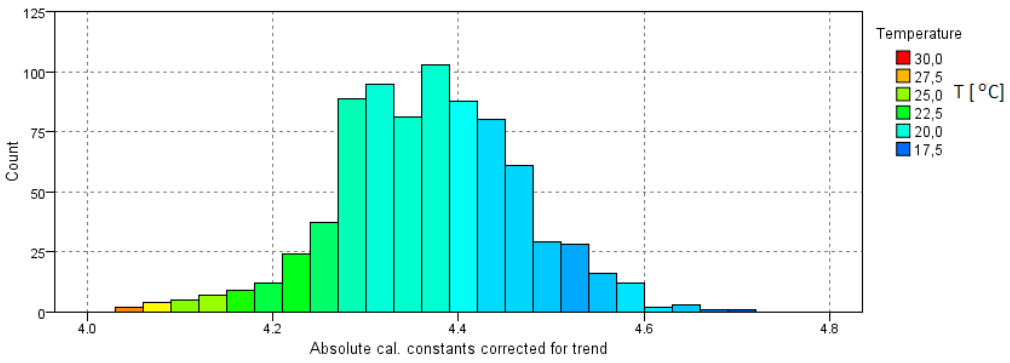

Figure A.1: Distribution of calibration constants corrected for trend used for linear regression with temperature. Standard deviation is $\sigma_{c,trend\,corr.} = 0.099$.

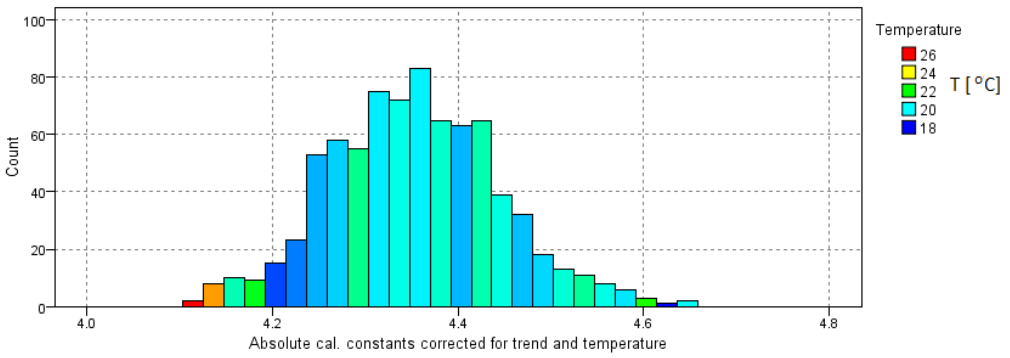

Figure A.2: Distribution of calibration constants corrected for overall trend and temperature to 21.5°C. Standard deviation is $\sigma_{c,trend\,and\,temp.\,corr.} = 0.092$.

Appendix B

Muon production results

$\theta = 0°$

Variable	**Original**	**5x charm**	**10x charm**	**100x charm**
$n^{rel}_{\mu,TOTAL}$	100.00 ± 1.47	99.50 ± 2.07	97.98 ± 2.05	94.87 ± 2.02
$n^{rel}_{\mu,E>50\,\mathrm{GeV}}$	100.00 ± 1.97	99.41 ± 2.77	103.85 ± 2.84	111.47 ± 2.95
$\bar{E}_\mu$[GeV]	8.00 ± 0.07	9.15 ± 0.32	9.81 ± 0.23	19.37 ± 1.09
E_{Miss}/E_0[%]	8.66 ± 0.18	9.47 ± 0.20	10.12 ± 0.32	14.22 ± 0.56

$\theta = 30°$

Variable	**Original**	**5x charm**	**10x charm**	**100x charm**
$n^{rel}_{\mu,TOTAL}$	100.00 ± 1.29	98.37 ± 1.80	95.88 ± 1.78	88.73 ± 1.72
$n^{rel}_{\mu,E>50\,\mathrm{GeV}}$	100.00 ± 1.72	97.63 ± 2.40	99.26 ± 2.42	101.85 ± 2.45
$\bar{E}_\mu$[GeV]	9.18 ± 0.08	9.93 ± 0.13	11.07 ± 0.76	22.40 ± 1.21
E_{Miss}/E_0[%]	8.66 ± 0.15	8.96 ± 0.58	9.79 ± 0.40	14.52 ± 0.90

$\theta = 45°$

Variable	**Original**	**5x charm**	**10x charm**	**100x charm**
$n^{rel}_{\mu,TOTAL}$	100.00 ± 1.46	97.32 ± 2.04	95.26 ± 2.02	88.50 ± 1.96
$n^{rel}_{\mu,E>50\,\mathrm{GeV}}$	100.00 ± 1.17	97.29 ± 2.32	98.13 ± 2.33	101.42 ± 2.37
$\bar{E}_\mu$[GeV]	11.93 ± 0.09	13.62 ± 1.15	13.93 ± 0.29	28.41 ± 1.73
E_{Miss}/E_0[%]	8.33 ± 0.19	8.92 ± 0.17	9.72 ± 0.18	13.83 ± 0.51

$\theta = 60°$

Variable	**Original**	**5x charm**	**10x charm**	**100x charm**
$n^{rel}_{\mu,TOTAL}$	100.00 ± 1.50	95.78 ± 2.07	94.24 ± 2.06	89.86 ± 2.01
$n^{rel}_{\mu,E>50\,\mathrm{GeV}}$	100.00 ± 1.63	96.59 ± 2.27	98.40 ± 2.29	98.55 ± 2.29
$\bar{E}_\mu$[GeV]	18.65 ± 0.18	20.55 ± 0.58	22.16 ± 0.43	40.51 ± 1.13
E_{Miss}/E_0[%]	8.52 ± 0.19	9.14 ± 0.29	10.19 ± 0.68	13.89 ± 0.46

Table B.1: Average muon energy $\bar{E}_\mu$, ratio of muon numbers $n^{rel}_{\mu,TOTAL}$ and ratio of number of muons with $E > 50\,\mathrm{GeV}$ $n^{rel}_{\mu,E>50\,\mathrm{GeV}}$ to original CORSIKA with QGSJET01c without charm. QGSJET01c is compared to simulations with increased charm production by a factor of 5, 10 and 100. The missing energy E_{Miss} in percentage of the primary energy is given. 100 proton events per case were simulated with $E = 5 \times 10^{18}\,\mathrm{GeV}$ for zenith angles $\theta = [0°; 30°; 45°; 60°]$.

Appendix C

Muon production results for charm and beauty particles implementation

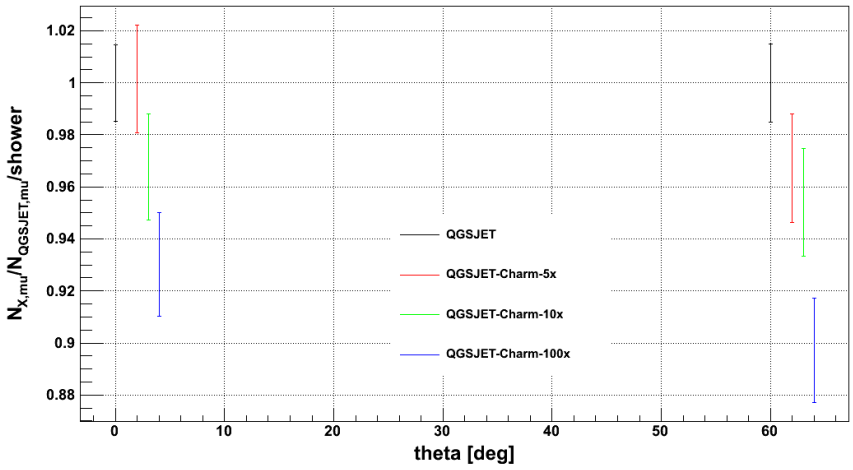

Figure C.1: Relative number of muons that reach the ground level; original QGSJET01c without charm production represents 100% for each zenith angle set. Beauty production is implemeted together with charm production. 100 proton showers were simulated and averaged with primary energy of $E = 5 \times 10^{18}$ GeV for zenith angles $\theta = [0°; 60°]$. Original QGSJET01c with CORSIKA without charm, 5 times more charm production, 10 times and 100 times are shown. For lucidity reasons results are slightly shifted along x-axis even though only for two zenith angles simulations were performed. Statistical errors are shown.

Figures Fig. C.1 and Fig. C.2 show relative number of muons at the ground level and high energy muons (with $E > 50$ GeV) for different levels of charm production

(5 times more charm production, 10 times and 100 times). When a charmed particle is produced we assign a probability 10% that this particle is transformed into $B^{\pm}$. Results for vertical inclined showers $\theta = 60°$ are shown, but for lucidity reasons particular results are slightly shifted along x-axis.

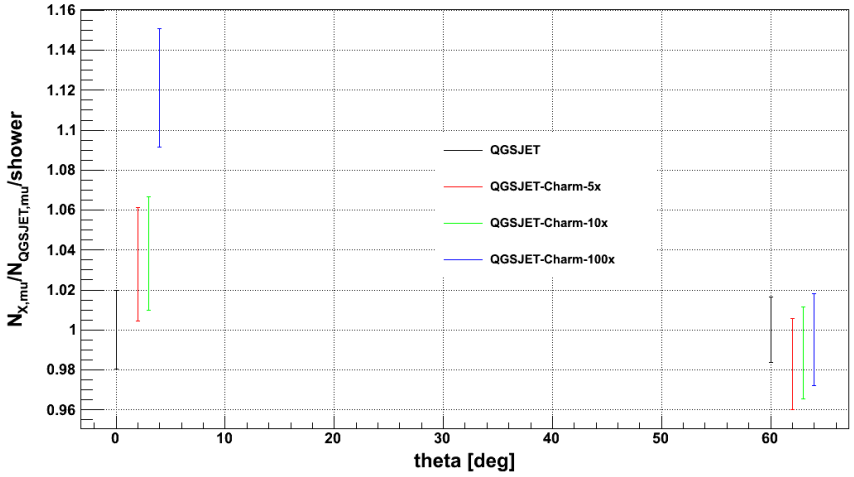

Figure C.2: Relative number of muons with energy $E > 50\,\mathrm{GeV}$; original QGSJET01c without charm production represents 100% for each zenith angle. Beauty production is implemented into charm production. 100 proton showers were simulated and averaged with primary energy of $E = 5 \times 10^{18}\,\mathrm{GeV}$. Original QGSJET01c with CORSIKA without charm, 5 times more charm production, 10 times and 100 times are shown for zenith angles $\theta = [0°; 60°]$. For lucidity reasons results are slightly shifted along x-axis even though only for two zenith angles simulations were performed. Statistical errors are shown.

Appendix D

QUIDO module and light connection schema of the Shift Guard

The QUIDO base module of relays is composed of 16 individual relays that can be operated via specific protocol that can be send via Ethernet to QUIDO. There are 3 contacts on each relay - **NOx**, **Cx**, **NCx**, where **x** means the relay ID. Contacts **Cx** should be connected to the positive power supply input. Labels **NOx** and **NCx** mean **normally open** and **normally closed**. Contacts **Cx** and **NOx** are interconnected if the signal with specific command to turn on the relay number **x** is sent to QUIDO. The electric circuit scheme can be found in Fig. D.1. Each relay operates one light (diode). Additional module that can be connected to the basic system of 16 relays extends number of relays up to total number of 32.

The base modul of relays with the power supply is mounted together in the white plastic box (see Fig. D.2). Relays used to operate lights are labeled by color corresponding to color of the connected light.

The light column of the *Shift Guard* alarm system is composed of several plastic single light-modules. They form a flexible and extensible tower of lights with plastic base including conectors and electric supply. Light modules can be separated from the black plastic holder. Fig. D.1 illustrates the electric connection of the currently used relays and lights.

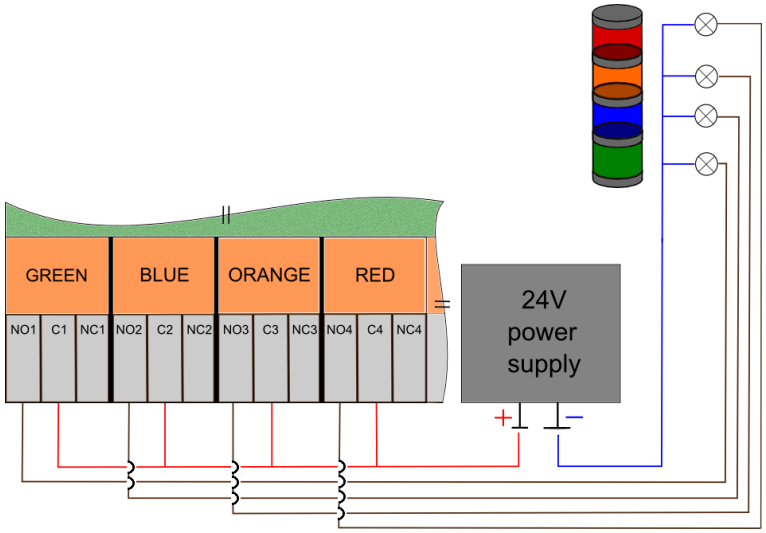

Figure D.1: A connection schema of the alarm-system electronic circuit. Only currently connected part of the QUIDO relays is shown.

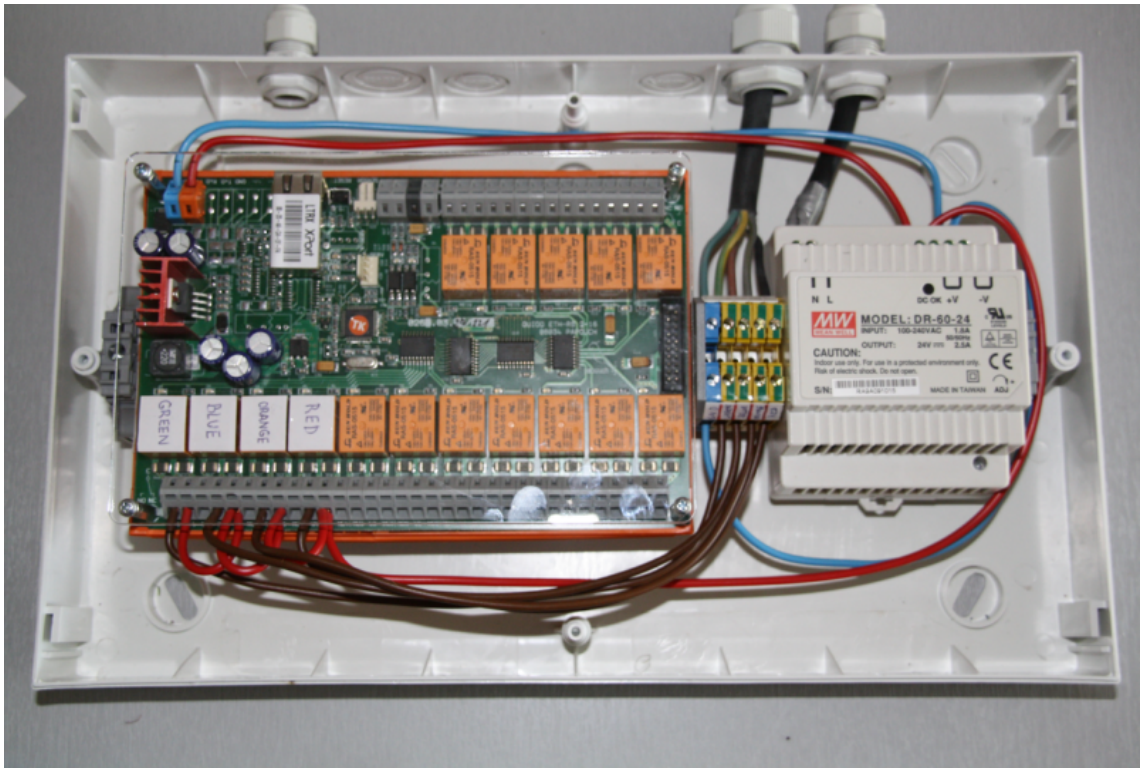

Figure D.2: A photo of QUIDO module monted into the cover plastic box. The power supply (mounted on the right side to the plastic box) ensures stability and sufficient energy for the whole module.

Appendix E

Settings and communication of the Shift Guard

The Shift Guard settings can be changed only by the administrator, but it offers wide options to configurate and adjust alarm system in case of necessity. It covers flexible and immediate addition of new alarms, change of alarms priority (alarm level), lights, sounds, and other attributes. There are 3 main setting files in the directory `/home/auger/alarms/settings` on *Ronja* PC:

settings file	**Information contained**
`settings.dat`	General settings of the Shift Guard (communication with the QUIDO module, sounds settings, TCP/IP communication settings).
`moniDB.dat`	Login information and other settings of communication with *MoniDB*.
`moniDB.alarms`	Current list of active alarms

Table E.1: Main setting files for Shift Guard alarm system

The most important settings (from files `settings.dat` and `moniDB.dat`) for the Shift Guard application are listed in the table E.2, E.3.

item	description
quidoIP=192.168.2.237	The IP address of the QUIDO module.
quidoPort=10001	The port of the QUIDO module.
timeout=1000	Milliseconds timeout for comm. with the QUIDO module.
GREEN=1	Number of the relay connected to the green light.
BLUE=2	Number of the relay connected to the blue light.
ORANGE=3	Number of the relay connected to the orange light.
RED=4	Number of the relay connected to the red light.
emergencyInput=1	Number of the relay used for input reading (envisaged for an emergency button in the future).
soundAlarmDirectory=/home/auger/alarms/sounds/	Directory that contains sounds used for alarms.
warningLevelSound=warningAlarm.mp3	The sound file used as warning level sound alarm.
highLevelSound=highAlarm.mp3	The sound file used as high level sound alarm.
criticalLevelSound=tornadoSiren.mp3	The sound file used as critical level sound alarm.
tcpCommunicationPortNumber=19050	The port number for TCP/IP communication between *Ronja* and *Moni* PCs for envisaged *AlarmTabTrigger*.

Table E.2: The most significant items in the *settings.dat* file.

item	description
serverAddress=moni.auger.org.ar	Database server address
databaseUser=...	Username
userPassword=...	Password
databaseName=AugerMonitor	Database name where alarms are stored.
tableName=AlarmTab	Name of the table with alarms.

Table E.3: The most significant items in the settings file *moniDB.dat*.

Appendix F

Technical core implementation

The description of the core implementation is outlined in Fig. F.1. Three threads perform QUIDO module operation, reading and sending messages via TCP/IP protocol and reading data from MySQL database.

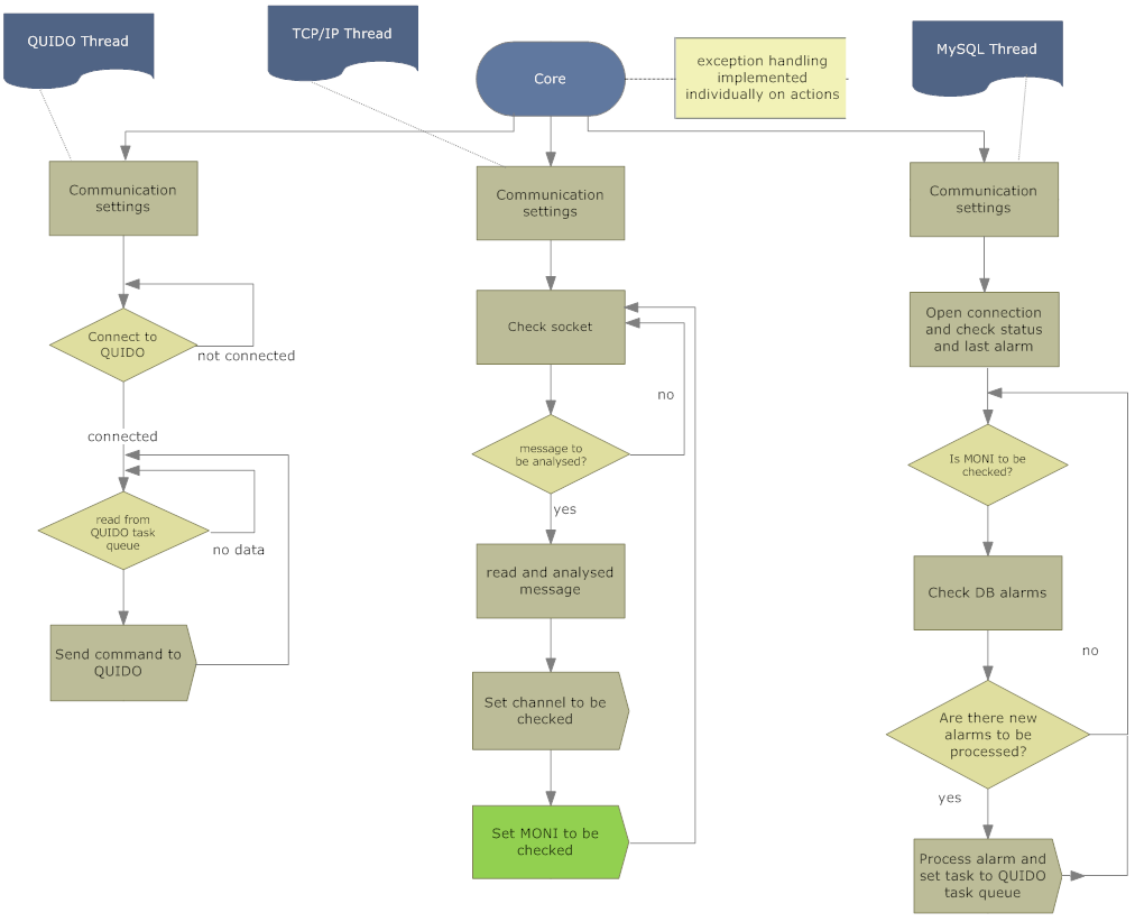

Figure F.1: Technical implementation of the Shift Guard core. It consists of three main threads - *QUIDO Thread*, *TCP/IP Thread* and *MySQL Thread*.

Appendix G

Distribution of reaction times on alarms

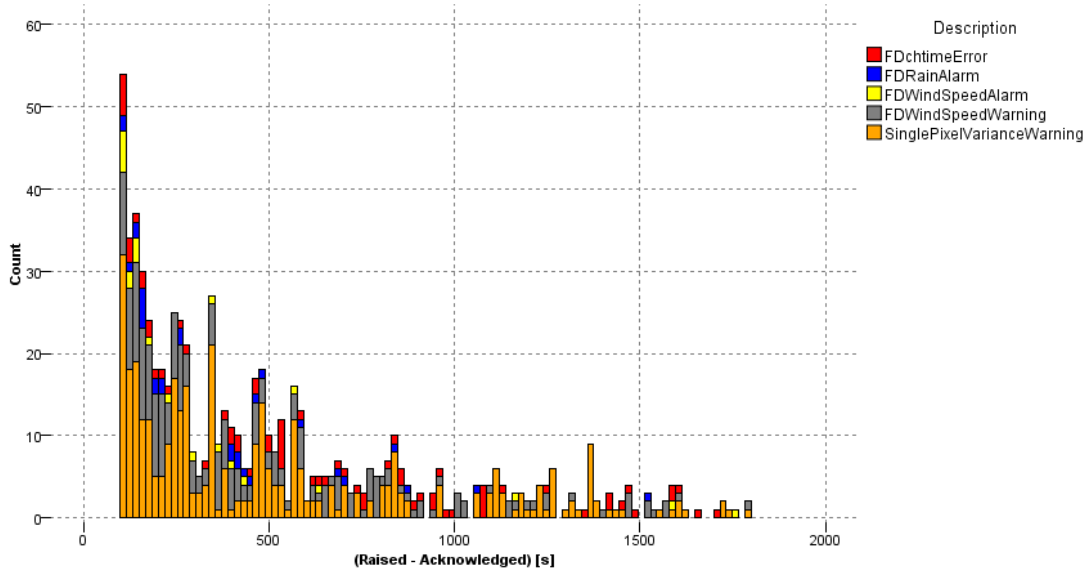

Figure G.1: The stacked histogram of shifters reaction time - difference between the time of acknowledgement and the time when an alarm was raised with wide range bins to show outlier values.

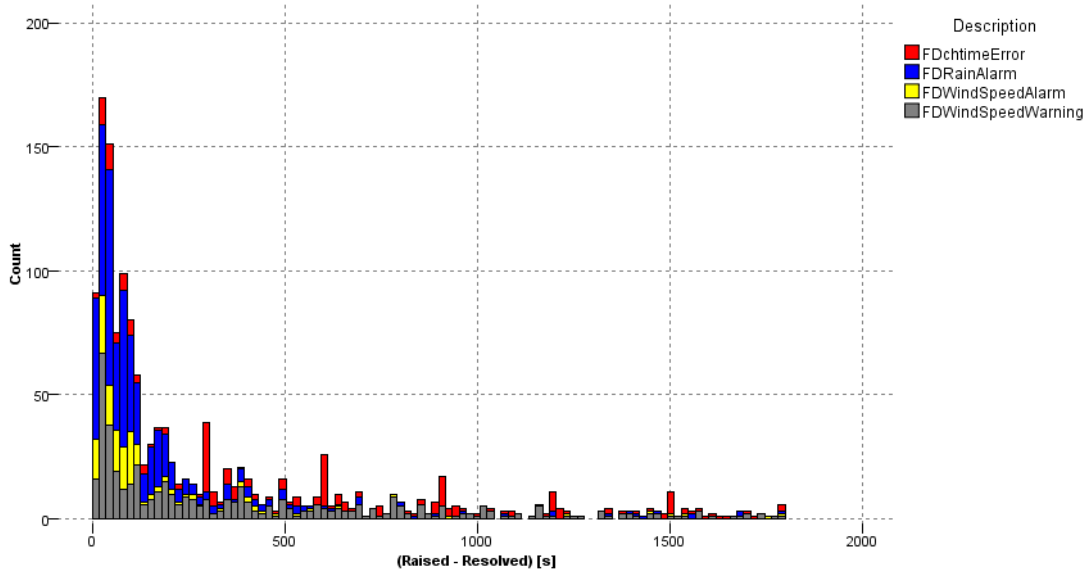

Figure G.2: The stacked histogram of distribution of time between raised time and the time when an alarm is resolved for four types of alarms - FDChtimeError, FDRainAlarm, FDWindSpeedAlarm and FDWindSpeedWarning. Wide range of x-axis is used to show outlier values.

Alarm	Raised	Acknowledged	Solved
FDWindSpeedWarning	581	479	581
FDWinSpeedAlarm	180	123	180
SinglePixelVarianceWarning	3632	1462	3632
FDRainAlarm	610	189	610
FDChtimeError	535	361	535

Table G.1: Summary of raised, acknowledged and solved alarms between period from October 2010 till February 2014.

Bibliography

[1] Wulf, T. *Physikalische Zeitschrift.* 1909, **10**, 152.

[2] Pacini, D. La radiazione penetrante alla superficie ed in seno alle acque. *Il Nuovo Cimento.* 1912 , **VI**(3), 93-100.

[3] Gockel, A. *Physikalische Zeitschrift.* 1910, **11**, 280.

[4] Hess, V.F. *Physikalische Zeitschrift.* 1912, **13**, 1084.

[5] Kolhörster, W. Zur Messung der durchdringenden Strahlung. *Physikalische Zeitschrift.* 1913, **14**, 1153-1156.

[6] Millikan, R.A. High Frequency Rays of Cosmic Origin. *Proceedings of the National Academy of Sciences:* Smithsonian Institution, 1926, **12**, 48-55.

[7] Stanev, T. *High Energy Cosmic Rays.* Second edition. Chichester: Springer, Praxis Publishing, 2004.

[8] Compton, A.H. *Physical Review.* 1933, **43**, 387.

[9] Clay, J. *Proc. Acad. Wetesch.* Amsterdam, 1927, **30**, 633.

[10] Størmer, C. Terrestrial Magnetism and Atmospheric Electricity. *Journal of Geophysical Research.* 1930, **35**, 193-208.

[11] Bothe, W., Kolhörster, W. *Die Natur der Höhenstrahlung* 1929, **17**, 271.

[12] Rossi, B. *Physical Review.* 1934, **45**, 212.

[13] Auger, P., Maze, R. *Compt. Rend. Acad. Sci. (Ser.II)* 1938, **207**, 228.

[14] Anderson, C.D. The Position Electron. *Physical Review* 1933, **43**, 491.

[15] Linsley, J. *Phys. Rev. Lett.* 1963, **10**, 146-148.

[16] Lisley, J., Scarsi, L., Rossi, B. *Phys. Rev. Lett.* 1961, **6**, 458.

[17] Winn, M.M. et al. *J. Phys.* 1986, **G12**, 653.

[18] Lawrance, M., Reid, R., Watson, A. *J. Phys.* 1991, **G17**, 733.

[19] Afanasiev, B.N. et. al. *Proceedings of the Tokyo Workshop on Techniques for the Study of Extremely High Energy Cosmic Rays, edited by M. Nagano: 2003, Institute for Cosmic Ray Research, University of Tokyo, Japan*, p.34.

[20] Chiba, N. et al. (AGASA Collab.) *Nucl. Instrum. Meth.* 1992, **A311**, 338-349.

[21] Bird, D.J. et al. *Astrophys. J.* 1994, **424**, 491.

[22] Abbasi, R.U. et al. (The HiRes Collaboration). *Phys.Lett. B.* 2005, **619**, 271-280. Available from: `http://arxiv.org/abs/astro-ph/0501317v2`.

[23] Tokuno, H. et al. The Telescope Array experiment: Status and prospects. *J. Phys. Conf. Ser.* 2008, **120**, 062027.

[24] Tokuno, H. et al. New air fluorescence detectors employed in the Telescope Array experiment. *Nuclear Instruments and Methods in Physics Research Section A: Accelerators, Spectrometers, Detectors and Associated Equipment.* 2012, **676**, 54-65.

[25] Sasaki, M. et al. (The Ashra Collaboration). *Proceedings of th 30th Internation Cosmic Ray Conference: July 3-11 July 2007, Merida, Mexico,* **3**, p. 1559-1562.

[26] Antoni, T. et al. (KASCADE Collaboration). The cosmic-ray experiment KASCADE. *Nucl. Instr. Meth. A.* 2003, **513**, 429.

[27] Navarra, G. et al. (KASCADE-Grande Collaboration). KASCADE-Grande: A large acceptance, high-resolution cosmic-ray detector up to 10^{18} eV. *Nucl. Instr. Meth. A*. 2004, **518**, 207-209.

[28] Heck, D., Knapp, J., Capdevielle, J.N. et al. CORSIKA: A Monte Carlo Code to Simulate Extensive Air Showers. In: *Forschungszentrum Karlsruhe Report FZKA 6019*, 1998. Available from: `http://web.ikp.kit.edu/corsika/physics_description/corsika_phys.html`

[29] Cortina, J. (The MAGIC Collaboration). Status and First results of the MAGIC Telescope. *Astrophys. Space Sci.* 2005, **297**, 245-255.

[30] Hinton, J. A. (The HESS Collaboration). The status of the HESS project. *New Atron. Rev.* 2004, **48**, 331-337.

[31] Dingus, B.L. et al.(The Milagro collaboration). Milagro-A TeV Observatory for Gamma Ray Bursts. *AIP Conference Proceedings*. 2004, **727**, 131-135.

[32] Abeysekara, A.U. et al. HAWC Collaboration. *Astropart. Phys.* 2012, **35**, 641-650.

[33] Yoshida, T. et al. BESS-Polar experiment. *Adv. Space Res.* 2004, **33**, 10.

[34] Ebisuzaki, T. et al. The JEM-EUSO project: Observing extremely high energy cosmic rays and neutrinos from the International Space Station. *Nucl. Phys. Proc. Suppl.* 2008, **175**, 237-240.

[35] Casolino, M. et al. Launch of the space experiment PAMELA. *Advances in Space Research*. 2008, **42**, 455-466.

[36] Fliescher, S. it Antenna Devices and Measurement of Radio Emission from Cosmic Ray induced Air Showers at the Pierre Auger Observatory. Aachen, 2011. The doctoral thesis. RWTH Aachen University. Faculty of Mathematics, Computer Science and Natural Sciences.

[37] Blümer, J., Engel, R., Hörandel, J.R. Cosmic rays from the knee to the highest energies *Prog. Part. Nucl. Phys.* 2009, **63**, 293, (*Preprint* arXiv:0904.0725 [astro-ph.HE]).

[38] Abraham, J. et al. (Pierre Auger Collaboration) Measurement of the energy of cosmic rays above 10^{18} eV using the Pierre Auger Observatory. *Phys. Lett. B*. 2010, **685**, 239.

[39] Beringer, J. et al. (Particle Data Group) *Phys. Rev. D*. 2012, **86**, 010001.

[40] Hörandel, J.R. Models of the knee in the energy spectrum of cosmic rays. *Astropart. Phys.* 2004, **21**, 241-265.

[41] Maur, M. Improving the Composition Sensitivity of the Pierre Augere Observatory with Additional Scintillators. Karlsruhe, 2012. The diploma thesis. The Karlsruhe Institute of Technology.

[42] Aloisio, R., Berezinsky, V., Gazizov, A. Transition from galactic to extragalactic cosmic rays. *Astropart. Phys.* 2012, **39-40**, 129-143, *Preprint*: arXiv:1211.0494 [astro-ph.HE].

[43] Abraham, J. *et al.* (Pierre Auger Collaboration). Measurement of the Depth of Maximum of Extensive Air Showers above 10^{18} ev. *Phys. Rev. Lett.* 2010, vol. 104, issue 9.

[44] *Science news of Advanced Composition Explorer (ACE).* [viewed 2012]. Available from: `http://www.srl.caltech.edu/ACE/ACENews/ACENews83.html`

[45] Lodders, K. Solar System Abundances and Condensation Temperatures of the Elements. *The Astrophysical Journal* 2003, vol. 591, 1220-1247.

[46] Abreu, P. *et al.* (Pierre Auger Collaboration) The Pirre Auger Observatory II: Studies of Cosmic Ray Composition and Hadronic Interaction models. *Proceedings of the 32th International Cosmic Ray Conference: August 11-18, 2011, Beijing, China*, *Preprint* arXiv:1107.4804.

[47] Drees, M. The top-down interpretation of ultra-high energy cosmic rays. *J. Phys. Soc. Jpn.* 2008, **77**, Supplement B 16.

[48] Nagano, M., Watson A.A. *Rev. Mod. Phys.* 2000, **72**, 689.

[49] Fermi, E. *Physical Review* 1949, **75**, 1169.

[50] Bel, A.R. The acceleration of cosmic rays in shock fronts. Mon. Not. Roy. Astron. Soc. 1978, **182**, 147.

[51] Greisen, K. End to the cosmic-ray spectrum? *Phys. Rev. Lett.* 1966, **16** (17), 748-750.

[52] Zatsepin, G.T., Kuzmin, V.A. Upper limit of the spectrum of cosmic rays. *JETP Lett.(USSR) (Engl. Transl.)* 1966, 4.

[53] Cronin J. *Nuclear Physics B* 2005, **138**, 465.

[54] The Auger Collaboration. The Pierre Auger Observatory Design Report. 1997, Fermilab.

[55] Dembinski, H. Measurement of the ultra-high energy cosmic ray flux from very inclined air showers at the Pierre Auger Observatory. Aachen, 2009. The doctoral thesis. RWTH Aachen University. Faculty of Mathematics, Computer Science and Natural Sciences.

[56] Schmidt, F. *CORSIKA Shower images*. [viewed 2012]. Available from: `http://www.ast.leeds.ac.uk/~fs/showerimages.html`

[57] Heitler, W. *Quantum Theory of Radiation*. Oxford University Press, 1944, Oxford, 2nd edition.

[58] Gaisser, T.K. *Cosmic Rays and Particle Physics*, Cambridge University Press, 1990, Cambridge.

[59] Matthews, J. A Heitler model of extensive air showers. *Astroparticle Physics*. 2004, vol. 22, issue 5-6, p. 387-397.

[60] Greisen, K. *Prog. Cosmic Ray Phys.* 1956, **3**.

[61] Lipari, P. *Phys. Rev. D.* 2009, **79**, 063001.

[62] Gaisser, T.K., Hillas, A.M. *Proceedings of the 15th International Cosmic Ray Conference: 1977, Plovdiv, Bulgaria*, p.358.

[63] Greisen, K., Wilson, J.G. (ed), *Progress in cosmic ray physics III*. 1956, 3.

[64] Unger, M. Shower Profile Reconstruction from Fluorescence and Cherenkov light. *Pierre Auger internal GAP note*. 2006, GAP-2006-010.

[65] Kümpel, D. Geometry Reconstruction of Fluorescence Detectors Revisited. Wuppertal, 2007. The diploma thesis. Bergische Universitat Wuppertal.

[66] OFFLINE PROFILE RECONSTRUCTION, [software]. [accessed 2013]. Available from: `http://www-ik.fzk.de/~munger/FD/ProfileReconstructor.tar.gz`

[67] Aab, A. et al. (Pierre Auger Collaboration). *Contributions to the 33rd International Cosmic Ray Conference, July 2013, Rio de Janeiro, Brazil*, *Preprint* arXiv.:1307.5059[astro-ph.HE].

[68] Abraham, J. et al. (Pierre Auger Collaboration). *Nucl. Instrum. Meth. A.* 2004, **523**, 50.

[69] Abraham, J. et al. (Pierre Auger Collaboration). The fluorescence detector of the Pierre Auger observatory. *Nucl. Instr. and Meth. in Phys. Res. A*. 2010, **620**, 227.

[70] Abraham, J. et al. (Pierre Auger Collaboration). Operations of and Future Plans for the Pierre Auger Observatory. *Proceedings of the 31st International Cosmic Ray Conference: 2009, Lodz, Poland*, *Preprint* arXiv:0906.2354

[71] Allekotte, I. et al. (Pierre Auger Collaboration). *Nucl. Instrum. Meth.* 2007, **A586**, 409.

[72] Abraham, J. et al. (Pierre Auger Collaboration). *Nucl. Instrum. Meth.* 2004, **A523**, 50.

[73] Edge, D.M., Evans, A.C. and Garmston, H.J. *Journal of Physics A*. 1973, **6**, 1612.

[74] Bertou, X. et al. *Nucl. Instrum. Meth.* 2006, **A568**, 839-846.

[75] Abraham, J. et al. Atmospheric effects on extensive air showers observed with the surface detector of the Pierre Auger Observatory. *Astopart. Phys.* 2009, **32**, 89-99.

[76] Bellido, J. Measuring the Energy Scale Stability of the Surface and Fluorescence Detectors. *Pierre Auger internal GAP note*. 2010, GAP-2010-014.

[77] Abraham, J. et al. (Pierre Auger Collaboration). Trigger and aperture of the surface detector array of the Pierre Auger Observatory. *Nucl. Inst. and Methods in Physics Research A* 2010, **613**, 29-39.

[78] Bauleo, P. et al. *Nucl. Instr. & Meth.* 1998, **A406**, 69.

[79] Aglietta, M. et al. (Pierre Auger Collaboration). Response of the Pierre Auger Observatory Water Cherenkov Detectors to Muons. *Proceedings of the 29th International Cosmic Ray Conference: August 03-10, 2005, Pune, India.*, **7**, 83.

[80] Šmída, R. Performance of the fluorescence detector of the Pierre Auger Observatory. Prague, 2009. The doctoral thesis. Charles University in Prague. Faculty of Mathematics and Physics.

[81] Roberts, M.D. et al. (Pierre Auger Collaboration). Calibration of the Pierre Auger fluorescence detector. *Proceedings of the 28th International Cosmic Ray Conference: July 31-August 7, 2003, Tsukuba, Japan. Preprint* arXiv:astro-ph/0308410

[82] Knapik, R. et al. (Pierre Auger Collaboration). The absolute, relative and multi-wavelength calibration of the Pierre Auger observatory fluorescence detectors. *Proceedings of the 30th International Cosmic Ray Conference: July 03-11, 2007, Merida, Mexico.* (*Preprint* arXiv:0708.1924 [astro-ph]).

[83] Kümpel, D. et al. Effect of realistic speed of light on Hybrid Reconstruction. *Pierre Auger internal GAP note*. 2007, GAP-2007-036.

[84] Schmidt, A. et al. New Third Level Trigger for the Fluorescence Telescopes. *Pierre Auger internal GAP note*. 2007, GAP-2007-118.

[85] Gemmeke, H. et al. *IEEE Trans. Nucl. Sci.* 2000, **47**, 371.

[86] Santander, M., Martino, J.R. Impact of FD operation on the PMTs life-time. *Pierre Auger internal GAP note*. 2007, GAP-2007-025.

[87] Fratte Delle C. et al. On the stability of the FD cameras. *Pierre Auger internal GAP note*. 2007, GAP-2007-111.

[88] Fratte Delle, C. et al. On the stability of the FD cameras - update #1. *Pierre Auger internal GAP note*. 2008, GAP-2008-129.

[89] Tomankova, L. Pierre Auger Fluorescence Detector Analysis of Relative Calibration Data. Prague, 2012. The diploma thesis. Czech Technical University in Prague. Faculty of Nuclear Sciences and Physical Engineering.

[90] Bauleo, P. et al. The Generation of Relative Calibration Constants for the FD. *Pierre Auger internal GAP note*. 2009, GAP-2009-076.

[91] Clay, R. et al. Ageing and Other Gain Variations of Auger Fluorescence Detector Photomultipliers. *Pierre Auger internal GAP note*. 2009, GAP-2009-026.

[92] Nečesal, P. Temperature measurement in Coihueco. *Pierre Auger Collaboration meeting*. 2009, Malargüe, Argentina.

[93] Nečesal, P. Temperature in(stability) in Coihueco. *Pierre Auger Collaboration meeting*. 2010, Malargüe, Argentina.

[94] Municipal Affairs Federal Institute (IFAM), Municipal Affairs Secretariat. 2013. Ministry of Interior, Argentina.

[95] Nečesal, P. Temperature Measurement and Calibration Constants. *Seminar of Czech Auger Group.* 2010, Institute of Physics of ASCR, v.v.i., Prague.

[96] Oliveira, M. Measurement of the Number of Muons in Inclined Showers at the Pierre Auger Observatory. Lisbon, 2012. The diploma thesis. Universidade Tecnica de Lisboa, Instituto Superior Tecnico.

[97] Newton, D., Knapp, J., Watson, A.A. *Astropart. Phys.* 2007, **26**, 414.

[98] Hersil, J. et al. *Phys. Rev. Lett.* 1961, **6**, 22-23.

[99] Pesce, R. (Pierre Auger Collaboration). Energy calibration of data recorded with the surface detectors of the Pierre Auger Observatory: an update. 2011, Available from: arXiv:1107.4809[astro-ph.HE].

[100] Cester, R. et al. (Pierre Auger Collaboration). Atmospheric aerosol monitoring at the Pierre Auger Observatory. *Proceedings of the 29th International Cosmic Ray Conference: August 03-10, 2005, Pune, India.* **00**, 101-106.

[101] Prouza, M. et al. (Pierre Auger Collaboration). Systematic study of atmosphere-induced influences and uncertainties on shower reconstruction at the Pierre Auger Observatory. *Proceedings of the 30th International Cosmic Ray Conference: July 03-11, 2007, Merida, Mexico. Preprint* arXiv:0706.1719 [astro-ph].

[102] Abraham, J. et al. (Pierre Auger Collaboration). Calibration and Monitoring of the Pierre Auger Observatory. 2009, *Preprint* arXiv:0906.2358[astro-ph.IM].

[103] Abreu, P. *et al.* (Pierre Auger Collaboration). The Pierre Auger Observatory IV: Operation and Monitoring. 2011, *Preprint* arXiv:1107.4806[astro-ph.IM].

[104] Abraham, J. *et al.* (Pierre Auger Collaboration). it Astropart. Phys. 2010, **33**, 108-129.

[105] NOAA Air Resources Laboratory (ARL). *Technical report* [online]. [viewed May 2014]. Available from: `http://ready.arl.noaa.gov/gdas1.php`

[106] Loudec, K. (2011): Atmospheric aerosols at the Pierre Auger Observatory: characterization and effect on the energy estimation for ultra-high energy cosmic rays. Paris, 2011. The doctoral thesis. Paris Descartes University. Laboratoire De l'Accelerateur Lineaire.

[107] Abreu, P. *et al.* (Pierre Auger Collaboration) The Pierre Auger Observatory V: Enhancements. 2011, *Preprint* arXiv:1107.4807[astro-ph.IM].

[108] Nečesal, P. et al. FD Alarm System. *Pierre Auger internal GAP note.* 2014, GAP-2014-023.

[109] Pierre Auger internal list of alarms. Available from: `http://wiki.auger.org.ar/doku.php?id=monitoring:shifter:alarmlist`

[110] Pierre Auger internal instructions for shifters. Available from: `http://wiki.auger.org.ar/doku.php?id=fd:fd_shift_-_quick_start`

[111] Pierre Auger internal checklist for shifters. Available from: `http://www.auger.org.ar/FD/fd-shift-checklist.html`

[112] Pierre Auger internal alarm web page. Available from: `http://moni.auger.org.ar/pro/FD/Alarms/`

[113] Nečesal, P. Shift Guard software overview, *Auger internal GAP note*. 2014, GAP-2014-024.

[114] Kég, B. et al. Reconstructing $N_{\mu 19}(1000)$ *Auger internal GAP note*. 2011, GAP-2011-054.

[115] Ostapchenko, S. *Nucl Phys. Proc. Suppl.* 2006, **151**, 143.

[116] Werner, K., Liu, F., Pierog, T. *Phys. Rev. C*. 2006, **74**, 044902.

[117] Abreu, P. et al. (Pierre Auger Collaboration). Interpretation of the Depths of Maximum of Extensive Air Showers Measured by the Pierre Auger Observatory. 2013, *Preprint* arXiv:1301.6637.

[118] Trávníček, P. Detection of high-energy muons in cosmic ray showers. Prague, 2004. The doctoral thesis. Charles University in Prague. Faculty of Mathematics and Physics.

[119] Cirelli, M. Indirect Searches for Dark Matter: a status view. 2012, *Preprint* arXiv:1202.1454.

[120] Arkani-Hamed, N. et al. A Therory of Dark Matter. *Phys. Rev. D*. 2009, **79**, 015014. *Preprint* arXiv:0810.0713, doi:10.1103/PhysRevD.79.015014.

[121] Cheung, C. et al. Kinetic Mixing as the Origin of Light Dark Scales. *Phys. Rev. D*. 2009, **80**, 035008. *Preprint* arXiv:0902.3246, doi:10.1103/PhysRevD.80.035008.

[122] Adriani, O. et. al. An anomalous positron abundance in cosmic rays with energies $1.5-100$ GeV. *Nature*. 2009, **458**, 607-609. *Preprint* arXiv:0810.4995, doi: 10.1038/nature07942.

[123] Ackermann, M. *et. al.* (Fermi LAT Collaboration). *Phys. Rev. Lett.* 2012, **108**, 011103. *Preprint* arXiv:1109.0521 [astro-ph.HE].

[124] Ebr, J., Nečesal, P. *Phys. Letters B*. 2013, **725**, 4-5, 185-189.

[125] Landau, L.D., Pomeranchuk I.Y. *Dokl. Akad. Nauk SSSR*. 1953, **92**, 535.

[126] Kalmykov, N.N., Ostapchenko, S.S., Pavlov A.I. *Nucl. Phys. B (Proc. Suppl.).* 1997, **52**, 17.

[127] Kaidalov A.B., Ter-Martirosyan K.A. *Phys. Lett. B.* 1982, **117**, 247.

[128] Ostapchenko S. QGSJET-II: towards reliable description of very high energy hadronic interactions. 2004, *Preprint* arXiv:hep-ph/0412332.

[129] Kaidalov, A.B. et al. *Yad. Fiz.* 1986, **43**, 1282.

[130] Kalmykov, N.N. et al. *Izv. RAN Ser. Fiz.* 1994, **58**, 21.

[131] Sjostrand, T., Mrenna, S., Skands, P. *J. of High Energy Phys.* 2006, 026.

[132] Gribov, V.N., Lipatov, L.N. Deep inelastic ep scattering in perturbation theory. *Sov. J. Nucl. Phys.* 1972, **15**, 438.

[133] Gribov, V.N., Lipatov, L.N. e+e- pair annihilation and deep inelastic ep scattering in perturbation theory. *Sov. J. Nucl. Phys.* 1972, **15**, 675.

[134] Dokshitzer, Yu.L. Calculation of the structure functions for deep inelastic scattering and e+e- annihilation by perturbation theory in quantum chromodynamics. *Sov. Phys. JETP.* 1977, **46**, 641.

[135] Altarelli, G., Parisi, G. Asymptotic freedom in parton language. *Nucl. Phys. B.* 1977, **126**, 298.

[136] Milke, J. et al. Test of Hadronic Interaction Models with Kascade. *Acta Phys. Pol. B.* 2004, **35**, 341-348.

[137] Antoni, T. et al. Test of High-energy Interaction Models Using the Hadronic Core of EAS. *J. Phys. G: Nucl. Part. Phys.* 1999, **25**, 2161-2175.

[138] Werner, K. The hadronic interaction model EPOS. *Nucl. Phys. B (Proc. Suppl.)* 2008, 175-176, 81-87.

[139] Werner, K., Liu, F.M., Pierog, T. *Phys. Rev. C.* 2006, 74.

[140] Pierog, T., Werner, K. 2006, *Preprint* arXiv:astro-ph/0611311

[141] Mariazzi, A.G., Tueros, M.J. Estimating the missing energy of Extensive Air Showers at the Pierre Auger Observatory. *Pierre Auger internal GAP note.* 2013, GAP-2013-026.

[142] Nyklíček, M. *et al. Proceedings of the 31st International Cosmic Ray Conference: 2009, Lodz, Poland.*

[143] Mariazzi, .A.G., Tueros, M.J. A novel method for the determination of the EAS missing energy for golden hybrid events at the Pierre Auger Observatory. *Pierre Auger internal GAP note.* 2010, GAP-2010-131.

[144] Mariazzi, .A.G. (Pierre Auger Collaboration). A new method for determining the primary energy from the calorimetric energy of showers observed in hybrid mode on a shower-by-shower basis. *Proceedings of the 32nd International Cosmic Ray Conference: 2011, August 1118, 2011, Beijing, China. Preprint* arXiv:1107.4804.

[145] Desiati, P. et al. (AMANDA Collaboration). *Proceedings of the 27th International Cosmic Ray Conference: August 8-15, 2001, Hamburg, Germany.* 985.

[146] Schröder, F. et al. *Proceedings of the 27th International Cosmic Ray Conference: August 8-15, 2001, Hamburg, Germany.* 1013.

[147] Achard, P. et al. (L3 Collaboration). *Phys. Lett. B.* 2004, **598**, 15.

[148] Řídký, J., Trávníček, P. *Nucl. Phys. (Proc. Suppl.) B.* 2005, **138**, 295.

[149] Řídký, J. et al. *Proceedings of the 30th International Cosmic Ray Conference: July 3-11, 2007, Merida, Mexico.*, HE 1.6 contr. 812. *Preprint* arXiv:astro-ph/0706.2145.

[150] Beringer, J. et al. (Particle Data Group). *Phys. Rev. D.* 2012, **86**, 010001.

[151] Kalmykov, N.N., Ostapchenko, S.S., Pavlov, A.I. *Nucl. Phys. B (Proc. Suppl.)* 1997, **52**, 17.

[152] Hagiwara, K. et al. (Particle Data Group). *Phys. Rev. D.* 2002, **66**, 010001.

[153] Barbosa, M.J. et al. Determination of the calorimetric energy in extensive air showers. *Astro. Part. Phys.* 2004, **22**, 159. *Preprint* arXiv:astro-ph/0310234v3

[154] Aaij, R. et al. (The LHCb collaboration). Prompt charm production in *pp* collisions at $\sqrt{s} = 7\,\mathrm{TeV}$. 2013, *Preprint* arXiv:1302.2864[hep-ex].

[155] Heck, D. Charmed Particles in CORSIKA. *Report FZKA 7366.* 2008, Forschungszentrum, Karlsruhe.

[156] Nečesal, P. Testing of Interaction Models of Cosmic Radiation at LHC Collider. Prague, 2006. The diploma thesis. Charles University in Prague. Faculty of Mathematics and Physics.

[157] Ebr, J., Nečesal, P., Řídký, J. Separability of primary particles using muon detectors: influence of the soft-particle addition model. *Pierre Auger internal GAP note.* 2014, GAP-2014-072.

[158] Arkani-Hamed, N., Finkbeiner, D.P., Slatyer, T.R., Weiner, N. A Theory of Dark Matter. *Phys. Rev. D.* 2009, **79**, 015014. *Preprint* arXiv:0810.0713.

[159] Cheung, C., Ruderman, J.T., Wang, L.-T., Yavin, I. Kinetic Mixing as the Origin of Light Dark Scales. *Phys. Rev. D.* 2009, **80**, 035008. *Preprint* arXiv:0902.3246.

[160] Kuijer, P.G. Soft physics in Pb-Pb collisions at the LHC. *Hadron Collider Physics Symposium*. 2011, Paris, France.